



HAL
open science

Physical analysis and numerical simulation of the separation phenomenon in over-expanded nozzle flow

Arthur Piquet

► **To cite this version:**

Arthur Piquet. Physical analysis and numerical simulation of the separation phenomenon in over-expanded nozzle flow. Fluids mechanics [physics.class-ph]. Normandie Université; Imperial College London, 2017. English. NNT: 2017NORMIR09 . tel-01689970

HAL Id: tel-01689970

<https://theses.hal.science/tel-01689970>

Submitted on 22 Jan 2018

HAL is a multi-disciplinary open access archive for the deposit and dissemination of scientific research documents, whether they are published or not. The documents may come from teaching and research institutions in France or abroad, or from public or private research centers.

L'archive ouverte pluridisciplinaire **HAL**, est destinée au dépôt et à la diffusion de documents scientifiques de niveau recherche, publiés ou non, émanant des établissements d'enseignement et de recherche français ou étrangers, des laboratoires publics ou privés.



Normandie Université

THÈSE EN CO-TUTELLE

pour obtenir le diplôme de doctorat

Spécialité : Mécanique des Fluides

Préparé au sein du Laboratoire CORIA, UMR 6614 CNRS.

ANALYSE PHYSIQUE ET SIMULATION NUMÉRIQUE DES PHÉNOMÈNES DE DÉCOLLEMENT DE JET DANS LES TUYÈRES SUPERSONIQUES

présentée par

ARTHUR PIQUET

**Thèse soutenue publiquement le 13 Octobre 2017
devant le jury composé de**

Françoise BATAILLE	Professeur, PROMES, France	Rapporteur
Jean-Christophe ROBINET	Professeur, ParisTech, France	Rapporteur
Dany VANDROMME	Professeur, INSA de Rouen, France	Examinateur
Niklas ANDERSSON	Professeur, Chalmers, Suède	Examinateur
Alexandre GEORGES-PICOT	Ingénieur, DGA, France	Examinateur
Abdellah HADJADJ	Professeur, CORIA, France	Directeur
Emile TOUBER	Professeur, Imperial College, UK	Co-encadrant

■ **Thèse dirigée par** Abdellah HADJADJ, CORIA CNRS, FR et co-encadrée par Emile TOUBER, Imperial College of London, UK.





Normandie Université

JOINT SUPERVISION THESIS

for the degree of Doctor of Philosophy

Department : Fluid Mechanics

From CORIA, UMR 6614 CNRS.

PHYSICAL ANALYSIS AND NUMERICAL SIMULATION OF THE SEPARATION PHENOMENON IN OVER-EXPANDED NOZZLE FLOW

by

ARTHUR L. PIQUET

**Thesis submitted in October 13 2017
in fulfillment of the requirements from**

Françoise BATAILLE	Professor, PROMES, France	Reviewer
Jean-Christophe ROBINET	Professor, ParisTech, France	Reviewer
Dany VANDROMME	Professor, INSA of Rouen, France	Examiner
Niklas ANDERSSON	Professor, Chalmers, Sweden	Examiner
Alexandre GEORGES-PICOT	Engineer, DGA, France	Examiner
Abdellah HADJADJ	Professor, CORIA, France	Supervisor
Emile TOUBER	Professor, Imperial College, UK	Co-advisor

■ **Under the supervision of** Abdellah HADJADJ, CORIA CNRS, FR and Emile TOUBER, Imperial College of London, UK.



Imperial College
London



ABSTRACT

Cette thèse, initiée par un programme de coopération franco-britannique entre la DGA et la DSTL, est consacrée à l'étude des phénomènes de décollement de jet au sein des tuyères propulsives sur-détendu. L'aérodynamique des systèmes propulsifs (missile, avion supersonique ou lanceur) est un des domaines de la mécanique des fluides où des progrès décisifs restent à réaliser pour améliorer les performances des ensembles moteurs, en terme de bilan de poussée, de stabilité, de fiabilité et de réduction de nuisances (bruit, émission de polluants, etc.). Les conditions de vols et la complexité des phénomènes caractéristiques n'étant pas reproductibles sur bancs d'essais à l'aide des outils expérimentaux actuelles, l'utilisation de simulation numérique permettrait une étude approfondie et précise des phénomènes mis en jeu. Le besoin d'informations concernant l'instationnarité de l'écoulement s'affirmant de plus en plus, notamment sur les phénomènes basse fréquence dû aux décollements de jets, l'utilisation des simulations numériques aux grandes échelles (LES) permettrait de faire face au coût prohibitif des simulations directes (DNS).

Les tuyères sur-détendu souffrent de charges latérales, caractérisées par des forces instationnaires orthogonales à la direction de l'écoulement. Ils sont causés par le décollement de la couche limite se développant le long de la paroi, provoquant des excursions de chocs importants, parfois asymétrique. Ces phénomènes instationnaires ont déjà été observés expérimentalement et numériquement. Ces instationnarités émergent d'une combinaison de phénomène complexe, tels que les interactions choc/couche limite sur la paroi de la tuyère, les couches de mélange décollées ou les zones de recirculation en aval du décollement, toutes produisant des modes énergétiques à différente fréquence caractéristique et tout particulièrement dans la plage de basse fréquence.

Capter le phénomène de décollement est un véritable défi dû à la nécessité de résoudre plusieurs échelles spatiales et temporelles. L'utilisation des simulations directes (DNS) ou résolu proche paroi (WR-LES) devient difficile compte tenu des ressources en calcul numérique actuelles. Pour parer ce problème, l'utilisation d'une stratégie de modélisation proche paroi est nécessaire. Le modèle de paroi développé par [Kawai & Larsson \(2013\)](#) est intégré à la simulation LES, combiné au modèle de viscosité de [Duprat et al. \(2011\)](#) afin de tenir compte des gradients de pression rencontré tout au long de la tuyère. Le développement d'un code curviligne a également permis de réduire le coût de calcul des simulations cylindriques en utilisant un maillage raffiné proche paroi.

Les résultats obtenus à partir des simulations modélisés (WM-LES) permettent de bien mettre en évidence les phénomènes d'instationnarité menant au problème de charge latérale. Le coût de calcul étant réduit de 40 fois comparé à une simulation résolu proche paroi WR-LES, la production d'une base de donnée basse fréquence devient possible. La comparaison des calculs modélisés aux calculs résolus et aux données expérimentales confirme la bonne implémentation du modèle pour des simulations LES de tuyère propulsive. La caractérisation des différents phénomènes est faite à l'aide d'analyses spectrales effectuées sur la base de donnée permettant de mettre en avant le phénomène basse fréquence rencontré dans les tuyères sur-détendu.

ABSTRACT

The present thesis, sponsored by a Franco-British cooperation program between the DGA and the DSTL, is devoted to the study of separation phenomenon in over-expanded nozzle. The aerothermodynamic of propulsion systems (missile, supersonic aircraft or launcher) is one of the fields of fluid mechanics where important progress remains to be made in order to improve the performance of the engine, in terms of thrust, stability, reliability and pollutant (noise reduction, pollutant emissions, etc.). Since the flight conditions and the complexity of the characteristic phenomena are not reproducible on experimental benches, the use of numerical simulation would allow a thorough and precise study of the phenomena involved. The instationnarity observed in the separation of the boundary layer is becoming a main concern nowadays, especially the low-frequency phenomenon observed in some experiments, the use of large scale simulations (LES) would fit perfectly the computational power allocated on supercomputer compared to the prohibitive cost of direct simulations (DNS).

Over-expanded nozzles are known to suffer from side loads, characterized by undesired unsteady forces orthogonal to the flow direction. They are caused by boundary-layer separation that causes significant and asymmetrical shock excursions within the nozzle. These phenomena have been studied experimentally and numerically. They emerge from a combination of complex unsteady flow phenomena, not yet fully understood, such as shock/boundary-layer interactions at the nozzle walls, detached mixing layers, and large regions of recirculating flow, all producing energetic motions at frequencies one or two orders of magnitudes lower than the characteristic frequency of the incoming turbulence.

Capturing the phenomenon is a real challenge due to the need to resolve at least four decades of time scales, from the energetic scales of the incoming turbulence. This makes both direct (DNS) and wall-resolved large-eddy simulations (WR-LES) rather impractical. Instead, a wall-modelled LES (WM-LES) strategy is employed here, following the approach of [Kawai & Larsson \(2013\)](#) together with the eddy-viscosity modification of [Duprat et al. \(2011\)](#) so as to account for pressure gradients. The WM-LES is found to accurately reproduce the flow topology, as well as the spectral content obtained by a reference WR-LES. The development of a curvilinear code has allowed us to decrease the cost of computation of the simulations by using a stretched mesh close to the wall.

The results obtained from the wall-modeled simulations (WM-LES) allowed us to capture and study the phenomena of instationnarity leading to the problem of side-loads. The WM-LES being about 40 times cheaper, the low-frequency motions may be statistically converged, enabling the study of the very low frequencies. The comparison of the modeled simulations with the resolved simulations and the experimental data confirms the good implementation of the model for LES computations of over-expanded nozzle flow. The characterization of the different phenomena is done through spectral analyses, carried out on the LES database allowing the highlight of the low-frequency phenomenon encountered in the over-expanded nozzle flow.

Contents

Abstract	i
Acknowledgements	v
Symbols	viii
1 Introduction	1
1.1 Nozzle flow	1
1.2 Shock pattern in over-expanded nozzles	4
1.3 Over-expanded nozzle flow unsteadiness	6
1.3.1 The separation phenomenon	7
1.3.2 Origins of fluctuations	8
1.3.3 Side-loads	14
1.3.4 Low-frequency unsteadiness	14
1.4 Scope of the present work	16
2 Governing equations and numerical methods	19
2.1 Governing equations	19
2.1.1 Navier–Stokes equations in Cartesian form	19
2.1.2 Navier–Stokes equations in generalized curvilinear form	20
2.1.3 Large Eddy Simulation	24
2.2 Numerical method	26
2.2.1 Spatial scheme	26
2.2.2 Temporal scheme	30
2.2.3 Stability properties	31
2.2.4 Scalability of the code	32
2.3 Boundary and initial conditions	33
2.3.1 Immersed Boundary Method	33
2.3.2 Initial conditions for turbulent flow	36
2.3.3 Inlet synthetic turbulence injection	37

2.3.4	Perturbation model	38
2.4	Domain decomposition method	39
2.4.1	The singularity issue	39
2.4.2	2D domain decomposition method	40
3	Numerical verification and validation	45
3.1	Vortex advection	45
3.2	Compressible flow over a circular cylinder	49
3.3	Poiseuille flow	50
3.4	Turbulent channel flow at $Re_\tau = 220$	53
3.5	DNS of a turbulent pipe flow at $Re_\tau = 220$	58
3.5.1	Channel vs. pipe flow	60
3.5.2	Cylindrical and generalized curvilinear coordinates code comparison	67
4	Near-wall modeling for LES	71
4.1	DNS of a zero pressure gradient turbulent boundary layer at $Re_\theta = 4200$	71
4.1.1	The hybrid scheme	74
4.1.2	Results	74
4.2	DNS of a turbulent boundary layer under APG / FPG	78
4.3	Near wall modeling	90
4.3.1	<i>A priori</i> test	93
4.3.2	<i>A posteriori</i> test	96
5	Planar nozzle flow	101
5.1	Experimental setup	101
5.2	WR-LES simulation of Olson & Lele (2011)	103
5.3	Wall-Resolved LES	104
5.3.1	Boundary-layer separation analysis	106
5.3.2	Comparison of profiles and boundary layer statistics	108
5.3.3	Shock-wave patterns	115
5.3.4	Asymmetry of the separation line	116
5.4	Wall-Modeled LES	121
5.4.1	Comparison to the WR-LES simulation	123
5.4.2	Side-loads generation	124
5.4.3	Low-frequency unsteadiness	131
5.5	Summary	138

6	Cylindrical nozzle flow	141
6.1	Simulation setup	141
6.2	Incoming boundary layer	143
6.3	Some statistics	147
6.4	Side-loads analysis	150
6.5	Summary	154
7	Conclusion	163
A	Nozzle flow grid	165
A.1	Planar nozzle	166
A.2	Cylindrical nozzle	168
B	NSCBC outflow	175
B.1	NSCBC method	175
B.2	WM-LES of the cylindrical nozzle flow with NSCBC	176
C	Conference paper	177
D	Article	185
	List of Figures	199
	List of Tables	209
	Bibliography	212

Acknowledgements

I would like to thank my advisor, Abdellah Hadjadj, and my co-advisor, Emile Touber, for their advice and support throughout my thesis. During those three years, they have been able to teach me about the physics of fluid dynamics and the different aspects of my Ph.D. subject. I express my gratitude to the committee member; the two reviewers, Professor Bataille and Professor Robinet, for the time they have spent correcting and reviewing my work; the three examiners, Professor Vandromme, Professor Andersson and Alexandre Georges-Picot, for their comments and suggestions.

I am also thankful to the Direction Générale de l'Armement (DGA) and the Defence Science and Technology Laboratory (DSTL) for financially supporting this thesis. I acknowledge the wonderful staff of the Criann supercomputer and the TGCC/CEA for their support on hardware and software optimisation of the code I have developed. Special thank to Guy Moebs and Anne-Sophie Mouronval for their help on parallel programming. I wish to thank Patrick Bousquet-Melou and Beatrice Charton for teaching courses on Parallel Computing and for helping me on HPC issues. I wish to thank Dr. Britton J. Olson for helping me on the simulation of the planar nozzle flow.

My experience at the CORIA of Rouen and at the Imperial College of London was unforgettable, thanks to a great group of researchers and colleagues. Special thank to Dr. Alexandre Georges-Picot for his help and his knowledge on nozzle flows and Vineet Soni for his continuous support during my thesis. I wish to thank my Coria's labmates, Mostafa S. Shadloo, Olivier Roussel, Zebiri Boubakr, Sushank Sharma, Margio Mendez, Nassim Brahmi and Minh Quan Nguyen. I also thank my friends from the Coria, Nicolas Jaouen, Pierre Benard, Umut Guven, Kevin Bioche, Andréa Seltz and Dorian Midou. I also acknowledge my colleagues from the Imperial College of London, Nicolas Alferez, Francis Nwobu and Teddy Szemberg-O'Connor. I personally thank my friend, roommate, and colleague, Bastien Duboc, for helping me in both academic and personal life and for the numerous evening we have spent beating the Binding of Isaac. I also thank my other roommate, Charlotte, for her friendship during my stay in Rouen.

Finally, I would like to acknowledge with gratitude my friends and family – my parents, my sister and my grandparents – for their support and love during those three years.

*“We’ve always defined ourselves by the ability to overcome the impossible.
And we count these moments.
These moments when we dare to aim higher, to break barriers,
to reach for the stars, to make the unknown known.
We count these moments as our proudest achievements.
But we lost all that.
Or perhaps we’ve just forgotten that we are still pioneers.
And we’ve barely begun.
And that our greatest accomplishments cannot be behind us,
because our destiny lies above us.”*

– Christopher Nolan’s *Interstellar*

Symbols

c	speed of sound
C_f	friction coefficient
C_p	heat capacity at constant pressure
C_v	heat capacity at constant volume
e_i	internal energy
e	total energy
f	additionnal force
F	thrust or side loads
Fo	Fourier number
H	enthalpy
H_t	nozzle throat height
k	turbulent kinetic energy
K	kinetic energy
L_x, L_y, L_z	streamwise, wall-normal and spanwise domain length
L_d	nozzle divergent length
M	Mach number
m	mass
N	Number of grid points
Pr	Prandlt number
p	static pressure
Re	Reynolds number
r	heat capacity ratio
R	gas constant
S	entropy
\mathbf{S}	strain rate tensor
St	Strouhal number
t	time
T	temperature
\mathbf{T}	deviatoric stress tensor

u, v, w	velocity
U, V, W	contravariant velocity
x, y, z	cartesian coordinates
ξ, η, ζ	curvilinear coordinates

Greeks

δ	boundary-layer thickness
δ_1, δ^*	displacement thickness
δ_{ij}	Kronecker symbol
ϵ	turbulent eddy dissipation
ε	nozzle area ratio
γ	heat capacity ratio
κ	spatial wave number
λ	thermal conductivity
μ	dynamic viscosity
μ''	second viscosity
μ_b	bulk viscosity
ν	kinematic viscosity
ρ	density
σ	stress tensor
τ	shear stress tensor
θ	momentum thickness

Subscripts

i, j, k	Einstein notation, 1: stream-wise, 2: wall-normal and 3: span-wise direction
∞	freestream flow
0	total/stagnation variable
t	throat based variable
w	wall variable
τ	friction variable
rms	root mean square

Superscripts

+	wall-units normalized variable
---	--------------------------------

Operators

$\vec{\varphi}$ or $\{\varphi\}_i$	vector
------------------------------------	--------

φ or $\{\varphi\}_{ij}$	tensor
$\langle \varphi \rangle$	time averaging
$\bar{\varphi}$	filtered/spatial averaging
$\tilde{\varphi}$	Favre averaging
$\hat{\varphi}$	Fourier transform

Abbreviations

APG	Adverse Pressure Gradient
BL	Boundary-Layer
DNS	Direct Numerical Simulation
FPG	Favourable Pressure Gradient
LES	Large Eddy Simulation
NPR	Nozzle Pressure Ratio
RANS	Reynolds Averaged Numerical Simulation
RMS	Root Mean Square
SRA	Strong Reynolds Analogy
SW	Shock-Wave
TBLE	Thin Boundary Layer Equations
WCNS	Weighted Compact Nonlinear Scheme
WENO	Weighted-Essentially Non-Oscillatory
ZPG	Zero Pressure Gradient

1

Introduction

1.1 Nozzle flow

The nozzle is a central element in supersonic propulsion system. It is mainly used for space launch vehicles but also for satellite stabilization, gas turbines and supersonic propulsion. The basic principle behind rocket propulsion is the Newtonian action-reaction principle, “to every action, there is an equal and opposite reaction”. A rocket engine ejects mass in one direction which creates a force in the opposite direction.

The nozzle is a system that accelerates the gases through a converging-diverging section from a high pressure chamber (fig. 1.1). These gases are often heated during an isobar combustion before getting expanded in the atmosphere through the nozzle. This will deliver the effective thrust to the launcher.

The thrust, noted F_{jet} , produced by the nozzle can be expressed as:

$$F_{\text{jet}} = \dot{m} u_e + (p_e - p_a) A_e, \quad (1.1)$$

where \dot{m} is the mass flow coming from the stagnation chamber, u_e the nozzle exit velocity, p_e the nozzle exit pressure, p_a the ambient pressure and A_e the nozzle exit cross section.

The thrust is made of the Newton’s second law and the force of pressure acting at the exit of the nozzle. The nozzle exit velocity, noted u_e , is governed by the nozzle expansion ratio ε , defined as the ratio between the nozzle exit area and the throat area, *i.e.* $\varepsilon = A_e/A_t$. This ratio changes along the nozzle with a converging section between the combustion chamber and the throat, followed by a diverging section downstream of the throat. The flow inside the nozzle follows the first and second laws of thermodynamics. For isentropic flow, the total pressure and total temperature are conserved along the nozzle. This conservation combined with the second law of thermodynamics and with

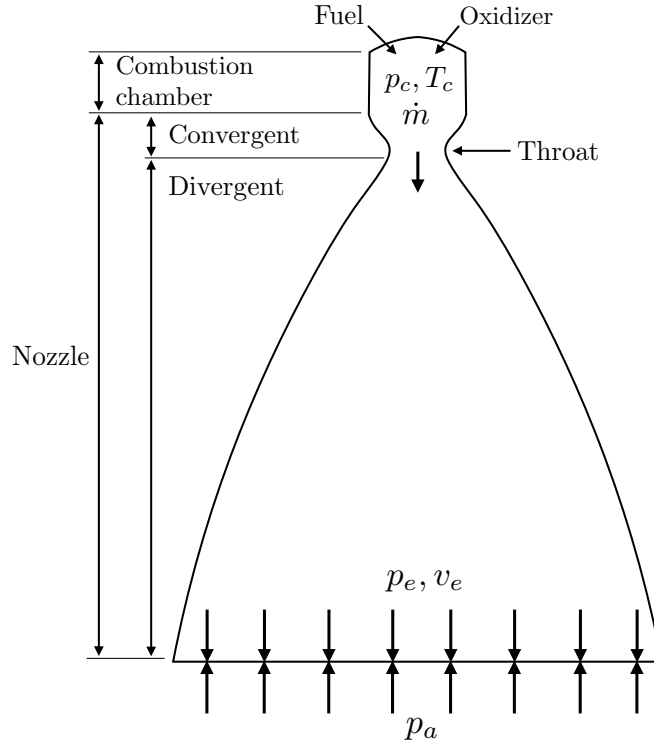


Figure 1.1: Rocket engine diagram

the perfect gas relation gives the isentropic relations (eq. 1.2, 1.3, 1.4):

$$\frac{A}{A_t} = \left(\frac{\gamma+1}{2}\right)^{-\frac{\gamma+1}{2(\gamma-1)}} \frac{\left(1 + \frac{\gamma-1}{2} M^2\right)^{\frac{\gamma+1}{2(\gamma-1)}}}{M}, \quad (1.2)$$

$$\frac{p}{p_c} = \left(1 + \frac{\gamma-1}{2} M^2\right)^{\frac{-\gamma}{\gamma-1}}, \quad (1.3)$$

$$\frac{T}{T_c} = \left(1 + \frac{\gamma-1}{2} M^2\right)^{-1}. \quad (1.4)$$

The velocity is increasing along the converging section. At a specific Nozzle Pressure Ratio (eq. 1.5), the velocity at the throat reaches the sonic state ($M_{throat} = 1$). From this point, the nozzle passes through several states:

- Subsonic-Subsonic, $M_{throat} = 1$: Choked nozzle
- Subsonic-Partially Supersonic, $p_a > p_e$: Over-expanded nozzle
- Subsonic-Supersonic, $p_a = p_e$: Ideally expanded nozzle
- Subsonic-Supersonic, $p_a < p_e$: Under-expanded nozzle

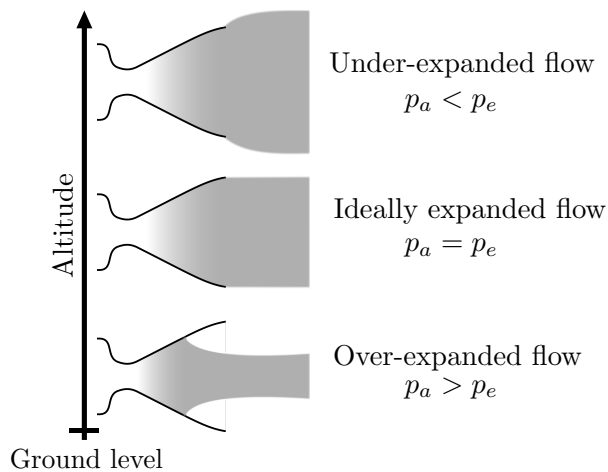


Figure 1.2: Nozzle flow regime during flight.



Figure 1.3: Ariane 5 launch.

$$NPR = \frac{p_c}{p_a}, \quad (1.5)$$

where, p_c is the combustion chamber or total pressure and p_a the ambient pressure.

In practical application, the pressure in the combustion chamber (p_c) is mostly constant. On the other hand, the NPR changes during the flight as the atmospheric pressure (p_a) changes. The atmospheric pressure is decreasing during the ascension of the rocket, while the NPR is increasing (fig. 1.4). At ground level or during the engine start-up, the rocket is usually over-expanded and passes through the ideally and under-expanded regimes during the ascension to space. In space, all nozzles are under-expanded as a result of the extremely low pressure.

As an example, the European rocket launcher, Ariane 5 (fig. 1.3), uses a Vulcain 2 engine with an expansion ratio of $\varepsilon = 58$. The flow is ideally expanded at an altitude of 19 km. From ground level up to this altitude, the flow is over-expanded and then under-expanded at higher altitude.

In terms of efficiency, the maximum thrust is reached when the flow is ideally expanded. When the rocket is over-expanded, the flow is not fully attached but separated from the nozzle wall. Flow separation in rocket nozzle is undesirable and can lead to dynamic loads on the structure, which can cause damage on the nozzle. These unsteady mechanical loads are commonly called side-loads. This phenomenon can also lead to unwanted unsteadiness of the exhaust plume and end-up with an uncontrolled rocket.

An ideal expansion would require to adapt the contour during the rocket ascent. Due to the mechanical complexity, engineers have not yet been successful at designing such

adaptive devices. Most of the actual rockets use two or three stages to launch a satellite. Each stage is designed for a certain range of altitude and avoids highly over/under-expanded regimes. The first stage, used at the ground level, can be designed so that flow separation is reduced at sea level. The nozzle is still running in over-expanded regime at the startup of the engine but for a limited period of time.

1.2 Shock pattern in over-expanded nozzles

Although the operating mode of convergent-divergent nozzles is the same for all supersonic applications, there is, nevertheless, a wide variety of possible flows according to the different nozzle shapes. The geometry of the nozzle has a dominant role on shock patterns and performance. Conical nozzles were the first to be developed due to their simplicity and ease of construction. Generally, these nozzles have a half-angle divergence of 15° to 25° . They are not used for the propulsion of recent rockets because of space limitation and lack of performance. Nevertheless, they are still used for research purposes. Curved nozzles, forming the second family of conventional nozzles, offer advantages over conical nozzles in terms of size and performance. These nozzles can be divided into three categories: TIC, TOC and TOP.

Truncated Ideal Contour (TIC) profile is defined by the method of characteristics (MOC) so that the flow in the divergent section is ideally expanded. The flow at the nozzle exit is uniform for the non-truncated version. In TIC design, the nozzle is truncated slightly before the nozzle exit for space savings which yields a loss of performance due to the non-uniform flow at the exit. These nozzles are often used on the second stage of space launch system in order to save space and to reduce the weight.

Thrust Optimized Contour (TOC) nozzles are designed to deliver the maximum of thrust for a specific NPR. These nozzles are characterized by the presence of an internal shock that starts downstream of the throat due to the high deflection angle. More specific shock patterns are observed in TOC nozzle flows than in TIC nozzle flow.

Thrust Optimized Parabolic (TOP) nozzles are similar to TOC nozzle in terms of concept, except for the nozzle profile that is approximated by a parabola without significant loss of performance. This method is frequently used nowadays for the design of first stage nozzles. As for TOC, TOP nozzles are characterized by the presence of an internal shock.

New nozzle concepts have been developed recently, such as aerospike engines (annular or planar shapes). This type of nozzle has not been used for real space applications.

Depending on the evolution of the nozzle shape and the flow conditions, several shock patterns may appear in over-expanded jet flows (fig. 1.4):

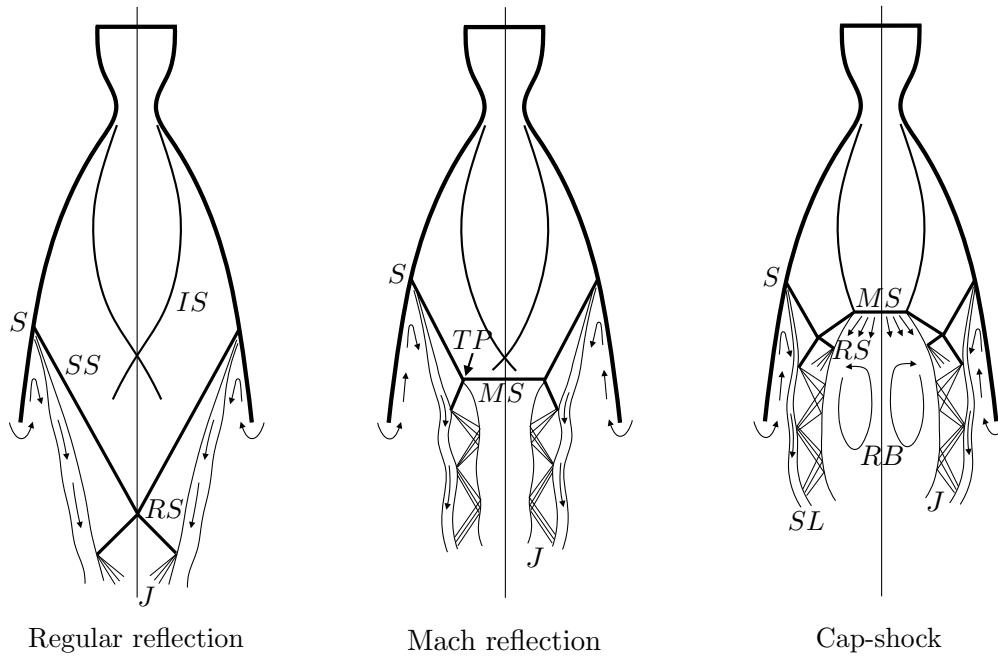


Figure 1.4: Shock patterns in over-expanded nozzle flow; S: separation, SS: separated shock, RS: reflected shock, TP: triple point, IS: internal shock, MS: Mach stem, RB: recirculation bubbles, J: supersonic jet, SL: slip line.

- Regular reflection: The incident shock is reflected on the axis of the nozzle due to high pressure ratios. The regular reflection may be observed in the plume of all nozzle types but only during flight (not observable on ground operation).
- Mach reflection: For lower pressure ratios, the incident shock is reflected on a Mach disk (conical nozzle), or Mach stem (planar nozzle). The Triple Point is where the incident shock, the reflected shock and the Mach disk meet. The Mach disk is characterized by a strong shock which creates a subsonic region downstream.
- Cap-shock pattern: When the nozzle is optimized to deliver a maximum thrust (TOC, TOP), an internal shock appears at the throat region. The internal shock hits the Mach disk forming complex shock patterns inside the nozzle. A subsonic zone with large recirculation bubbles is observed downstream of the Mach disk.

A transition between different shock patterns may occur during flight which produces high dynamic loads on the structure of the nozzle. A hysteresis effect has been observed on many experiments (Chpoun et al. 1995, Frey & Hagemann 1998, Ben-Dor et al. 2002) during transition between regular, Mach reflection and cap shock patterns.

At separation, the upstream boundary layer is deviated away from the wall followed by a mixing/shear layer. Most of the time, the mixing layer downstream of the shock is separated from the wall, *i.e.* Free Shock Separation (FSS). However, in specific conditions

(NPR or nozzle contour), a different type of pattern is expected, commonly called Restricted Shock Separation (RSS). The latter is characterized by a reattachment at the wall with large recirculation bubbles downstream of the Mach disk. The transition between FSS and RSS produces strong side-loads along the wall of the nozzle. This transition happens when the detached shear layer from the FSS jet is close to the wall, reattaching by a “Coanda effect”. Östlund (2002) showed that the transition creates a peak of side-loads for a specific range of NPR. Further studies (Kwan & Stark 2002, Nguyen et al. 2003) demonstrated that the transition is subjected to an asymmetrical behavior of the separation line which increases the unsteadiness of side-loads. Also a hysteresis effect was observed during FSS-RSS transition, which increases the side-loads and the low frequency tone observed in over-expanded nozzle (Frey & Hagemann 1998, Martelli et al. 2010).

- In the case of Free Shock Separation (FSS), the over-expanded jet is completely separated from the wall. A back flow is observed between the exit and the separation location. This recirculated flow increases the unsteadiness of the separation line because of large structures and vortices. A mixing layer is created with Kelvin-Helmholtz instabilities.
- The RSS patterns have been observed in the early 1970’s by Nave & Coffey (1973) during experimental studies of the J-2S rocket engine. Among others, Chen et al. (1994) observed similar behavior in a numerical simulation of the same configuration. They captured a separated flow reattached at the nozzle wall with a large vortex behind the Mach disk.

1.3 Over-expanded nozzle flow unsteadiness

Flow separation occurs in over-expanded nozzle when the boundary layer is subjected to a strong adverse pressure gradient which it cannot withstand. This separation creates an oblique shock and a mixing layer downstream of the separation. The separation line unsteadiness is influenced by different phenomena happening inside the nozzle; the upstream boundary layer turbulence; the mixing layer unsteadiness; the recirculation bubbles downstream of the shock; the trailing-edge noises created by the lip at the nozzle exit. Low-frequency shock oscillations are often seen in this type of flow (Sajben & Kroutil 1980, Bogar et al. 1983, Zaman et al. 2002). The unsteadiness of the separation has an important effect on the side-loads and on the symmetry of the exhaust plume.

Many studies have been performed in the past on separated flow in over-expanded nozzle to understand the influence of different flow parameters on the frequency and amplitude of separation. Summerfield et al. (1954) started in the 1950’s with experimental

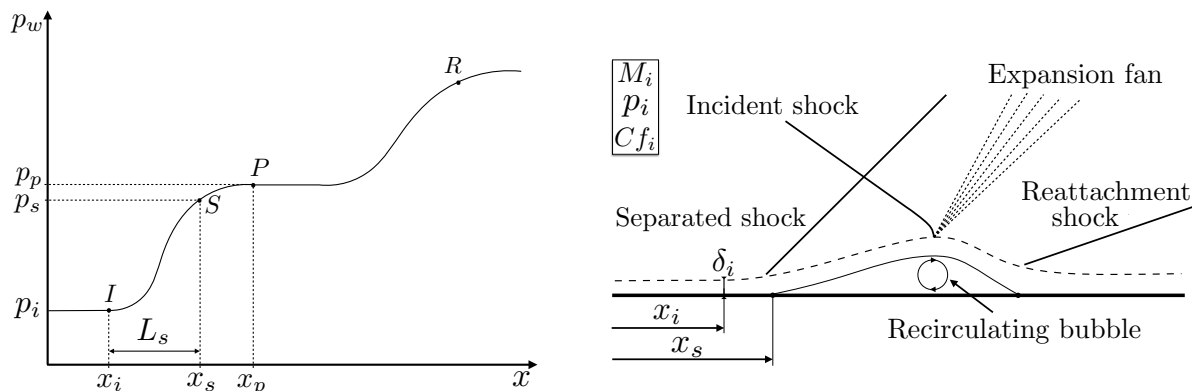


Figure 1.5: Typical wall-pressure distribution (*left*) and schematic representation of SWBLI (*right*); I: start of interaction, S: separation point, P: plateau point, R: reattachment point, L_s : separation length.

work followed by Shmyglevsky (1957), Chapman et al. (1958), Arens & Spiegler (1963), Schmucker (1974), Watanabe et al. (2002), Nguyen et al. (2003), Smalley et al. (2007), Tomita et al. (2009) and Baars & Tinney (2013). Similarly, numerical studies have been done by Chen et al. (1994), Frey & Hagemann (1998), Reijasse (2005), Xiao et al. (2007), Ivanov et al. (2009), Wang (2009) and Olson & Lele (2013). Further studies have been conducted by Östlund (2002) on the effect of the separation on side-loads.

1.3.1 The separation phenomenon

Flow separation under high adverse pressure gradient is a complex phenomenon involving shock waves boundary layer interaction, known as SWBLI. Study on SWBLI started in the 1950's with the case of an incident oblique shock wave impinging a flat plate boundary layer. At that time, the research was only experimental and focused on mean wall pressure distribution. Figure 1.5 shows a typical wall pressure distribution along with a schematic representation of SWBLI. The interaction zone extends from the first wall pressure rise (I) to the point of separation (S). Chapman et al. (1958) observed, from different experimental studies, a general form of the pressure distribution over the interaction zone. They formulate the so-called free interaction theory to predict the pressure distribution and the separation length (L_s) from upstream boundary layer properties: the skin friction coefficient (C_f), the displacement thickness (δ^*) and the incoming Mach number (M_i).

Kistler (1964) has shown an unsteady effect of the separation phenomenon in SWBLI. They investigated a shock-induced turbulent separation from a forward-facing step experimentally. Figure 1.6 shows a typical RMS pressure fluctuation distribution. Kistler (1964) observed that the pressure is intermittent in the region of separation. In the in-

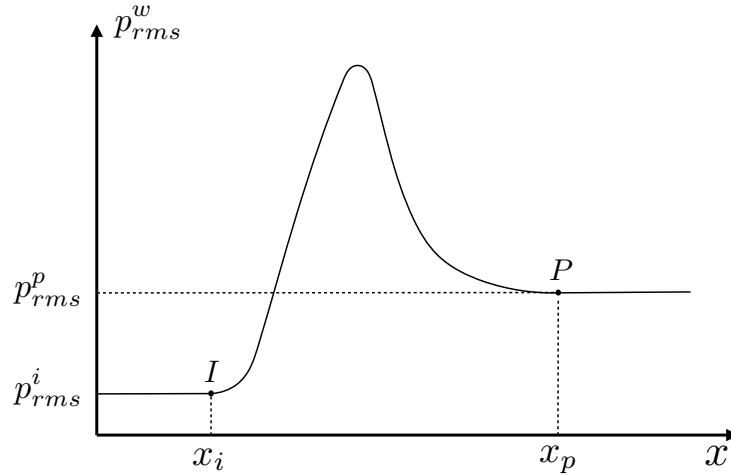


Figure 1.6: Typical rms wall-pressure distribution.

teraction region, near the separation, the pressure oscillates between the mean pressure at the beginning of the interaction (p_i) and the mean pressure at the plateau (p_p). They defined an intermittency region near the separation point where the wall pressure distribution can be modeled as a fraction of p_i and p_p using an intermittency factor $\varepsilon_i(x)$ (eq. 1.6). Thus, ε_i can be computed from the pressure distribution.

$$p(x) = \varepsilon_i(x) p_p + (1 - \varepsilon_i(x)) p_i \quad (1.6)$$

In equation 1.7, Kistler (1964) expressed the mean square fluctuating pressure distribution as a combination of high- and low-frequency phenomena. The high-frequency oscillations are generated by the incoming boundary layer fluctuations $p_{i,rms}$ and the downstream shear layer oscillations $p_{p,rms}$. While the low frequency oscillations are due to the intermittency of the shock wave motion.

$$p_{rms}(x) = \underbrace{\varepsilon_i(x)(1 - \varepsilon_i(x)) (p_p - p_i)^2}_{\text{low frequency part}} + \underbrace{\overbrace{\varepsilon_i(x) p_{p,rms}}^{\text{shear layer}} + \overbrace{(1 - \varepsilon_i(x)) p_{i,rms}}^{\text{boundary layer}}}_{\text{high frequency part}} \quad (1.7)$$

1.3.2 Origins of fluctuations

Previous works on shock-wave/supersonic boundary layer interaction (SWBLI) (Dupont et al. 2006, Piponniau et al. 2009, Toubert & Sandham 2011, Hadjadj 2012, Morgan et al. 2013) suggested that the frequency range is split among four separate zones; a high-frequency zone corresponding to the incoming turbulent boundary layer; two medium-frequency zones, the interaction zone (IZ) with a mixing layer reattaching near the end of the interaction and a relaxation zone downstream of the IZ; a low-frequency zone created by the unsteady reflected shock. The Strouhal number St_L , defined by many SWBLI

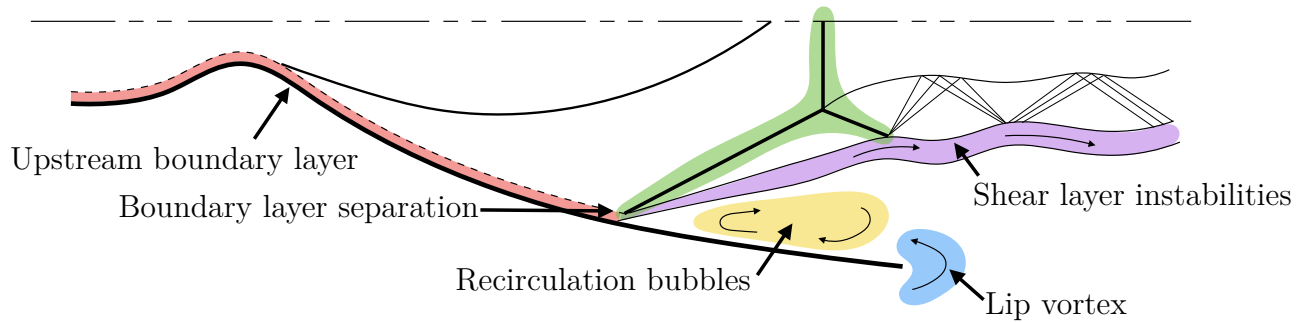


Figure 1.7: Topology of shock unsteadiness in over-expanded nozzle flow (FSS).

simulations (Dupont et al. 2006, Piponnier et al. 2009, Toubert & Sandham 2011), is based on the freestream velocity u_∞ and the interaction length L_I , *i.e.* $St_L = f L_I / u_\infty$. Dupont et al. (2006) captured experimentally the frequency ranges of the different SWBLI phenomenon; the upstream turbulence of the turbulent boundary layer at $St_L > 10$; the mixing layer unsteadiness and the relaxation zone in the range $0.5 \leq St_L \leq 5$; the low-frequency tone of the separation line spanning the range $0.02 \leq St_L \leq 0.1$. The conclusions on the origin of the low frequency motion of the reflected shock is still in debate, whether the shock motion is caused by a mechanism from the upstream or downstream flow condition.

In the case of nozzle flow, the separation unsteadiness originates from more complex phenomena compared to the SWBLI study. Unlike SWBLI, the boundary layer separates completely downstream of the interaction zone, creating a mixing layer and large recirculation bubbles downstream. Figure 1.7 shows the topology of the different phenomena happening in over-expanded nozzle flow.

1.3.2.1 Upstream boundary layer

In real configurations, the flow starts in the combustion chamber which creates a boundary layer along the walls. In over-expanded nozzle flow, the boundary layer is attached to the wall and evolves up to the separation. The boundary layer is characterized by three-dimensional turbulent structures happening between the external free-stream and the no-slip wall condition. The largest eddies are of the size of the boundary layer thickness, thus the maximum energy of the boundary layer spectrum is localized at a Strouhal number of unity, where $St_\delta = f \delta / u_\infty$. The energy of these large scale eddies is transferred through a cascade to small scale eddies. The smallest eddies are then dissipated by viscosity at the Kolmogorov scale. The transfer of energy in the inertial subrange, *i.e.* between the largest and smallest eddies, can be approximated by an universal inertial subrange equation, *i.e.* $\kappa^{-5/3}$, where κ is the wave number (Pope 2000).

In DNS of SWBLI at $M_\infty = 1.3$, Pirozzoli et al. (2010) showed that pressure spectra

upstream of the separation are characterized by a large peak of energy above Strouhal number in the range close to unity and by the absence of low-frequency oscillations. The supersonic boundary layer upstream of separation is composed of a thin subsonic layer that could propagate upstream disturbances. However, in practical application and for high Reynolds number, the subsonic layer thickness is too small to allow perturbations to propagate far upstream.

The state of the incoming boundary layer, *i.e.* the Reynolds number or the friction coefficient, is an important factor for the location of the separation. Verma & Manisankar (2014) observed that given the state of the boundary layer at the throat, *i.e.* laminar or turbulent, the separation location could be shifted downstream or upstream.

Dussauge & Piponnier (2008) demonstrated that the superstructures of the outer region of the boundary layer, captured by Adrian *et al.* (2000), could also play an important role on the unsteadiness of the separation. Those superstructures of length up to 30δ could be advected in the low-speed recirculating area increasing lower-frequency phenomena.

1.3.2.2 Boundary layer separation

Boundary layer separation occurs when the incoming boundary layer is subjected to a strong adverse pressure gradient. A shear layer is created downstream of the separation that deviates the incoming boundary layer away from the wall and creates an oblique shock, called separated shock, which hits the internal shock at the so-called Triple Point. The shock pattern near the separation is close to the one observed in SWBLI simulations or in FSS experiments, commonly called “lambda shock pattern”. As observed in the Mach reflection pattern from figure 1.4, a reflected shock arises from the triple point that realigns the deviated flow downstream of the separated shock. Simpson (1989) demonstrated that the shape of the nozzle could also influence the separation and its position in the divergent section, especially for strong streamwise curved wall.

1.3.2.3 Shear layer instabilities

Due to the difference of velocity between the supersonic jet and the recirculation zone, a shear (or mixing) layer is observed downstream of the separation. This mixing layer can either be planar or cylindrical according to the shape of the nozzle. Instabilities in shear layer have been observed in the past (Brown & Roshko 1974, Lasheras & Choi 1988, Lesieur 2012) and are characterized by turbulent instabilities and large coherent structures. The eddies observed in shear layer are similar to those produced by Kelvin-Helmholtz instability (fig. 1.8).

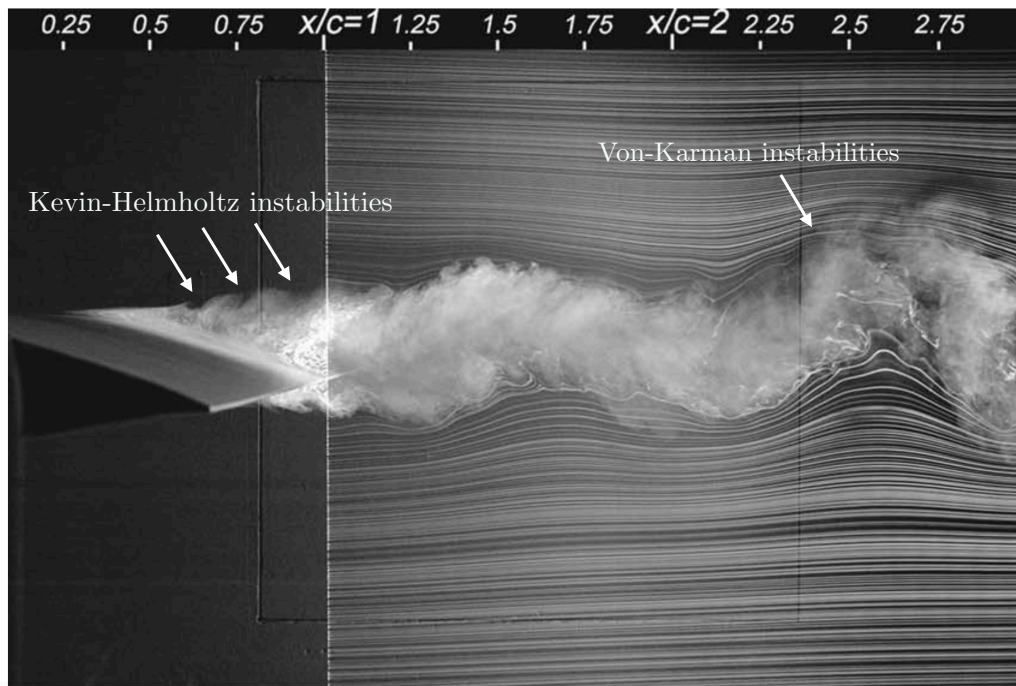


Figure 1.8: Representation of Kelvin-Helmholtz instability observed downstream of the separation over an airfoil; Extracted from [Yarusevych et al. \(2006\)](#).

Brown & Roshko (1974) were the first to study the Kelvin-Helmholtz instability and showed the importance of these structures on the turbulent mixing process, *i.e.* heat transfer, combustion or acoustic waves. Lesieur (2012) has shown the bi-dimensional aspect of the vortex structures in Kelvin-Helmholtz instabilities where two types of vortex can be described.

The primary cylindrical bi-dimensional vortices are characterized by strong vorticities. These vortices are representative of the large-scale organization of the shear layer and result from the difference in speed between the two fluids. These structures are convected at an averaged speed computed by $u_{sl} = (u_1 + u_2)/2$, where u_1 and u_2 are the “lower” and “upper” velocities, respectively. In nozzle flows, the “lower” velocity is the one captured in the recirculating zone while the upper is the internal jet velocity. The size and spacing between the structures increase with time. This process, linked to Kelvin-Helmholtz instability, is responsible for the thickening of the shear layer.

A second type of vortices are superimposed to the primary ones and are under the effect of the positive strain created by the spanwise vortex tubes (Lasheras & Choi 1988). The weak perturbed vorticity existing on the braids is stretched, leading to the formation of vortex tubes whose axes align with the direction of maximum positive strain.

The Strouhal number associated to the shear layer instability is defined based on the thickness of the vorticity field δ_ω where $St_{sl} = f \delta_\omega / u_{sl}$. Similarly to the boundary layer, the St_{sl} is close to unity inside the shear layer. Using the boundary layer Strouhal

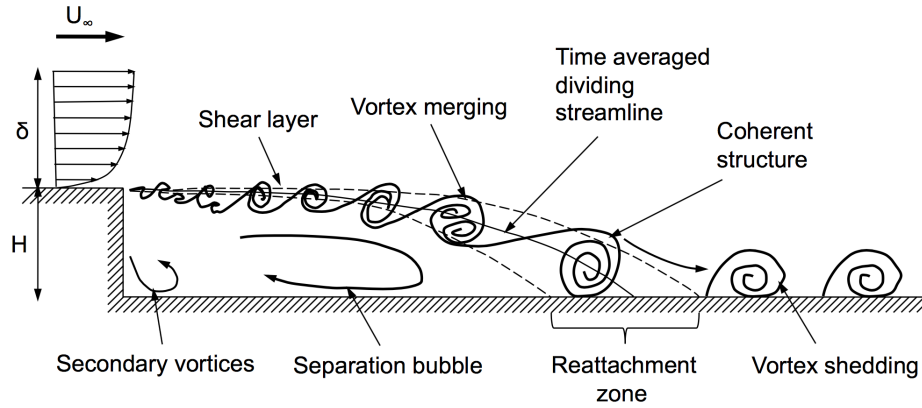


Figure 1.9: Representation of the recirculating area captured in a backward facing step; Extracted from [Rajasekaran \(2011\)](#).

number, *i.e.* $St_\delta = f\delta/u_\infty$, the fluctuations are in the range of 0.05-0.2 as observed by Dupont et al. (2006), Piponniau et al. (2009) and Touber & Sandham (2011).

Among the unsteady phenomena produced in the shear layer, a “flapping” phenomenon is also observed. This phenomenon is characterized by an intermittent lateral oscillation of the shear layer. Viets (1975) has made an experimental nozzle flow characterized by a significant unsteadiness of the main supersonic jet. This unsteadiness arises because the jet is close enough to the walls which produces an unstable jet and may possibly oscillate between the two walls. This flapping has an important impact on the symmetry of the flow.

1.3.2.4 Recirculation bubbles

Regardless of the shock pattern is FSS or RSS, a recirculation bubble is observed downstream of the separation. For the FSS pattern, the recirculation zone extends from the separation to the nozzle exit and is composed of a large recirculation bubble characterized by low frequency oscillations. Many studies (Eaton & Johnston 1981, Kiya & Sasaki 1983, Simon et al. 2007, Boccaletto 2011) have been done to characterized recirculation areas, also called “dead water” region. They all pointed out a cycle of expansion and contraction of the recirculation bubble. Simon et al. (2007) showed that the latter exhibits large oscillations in the low-frequency as well as in the high-frequency regimes. Some fluctuations emanate from the large vortices, or bubbles, created between the shear layer and the wall while the high-frequency oscillations are created by the pressure waves emanating from the vortices of the mixing layer. Most of the energy captured in the recirculating area, *i.e.* the lower frequencies, are defined by the “breathing” phenomenon created by an imbalance state between the flow from the shear layers and the backflow captured at the lip of the nozzle. This “breathing” phenomenon is the oscillating effect

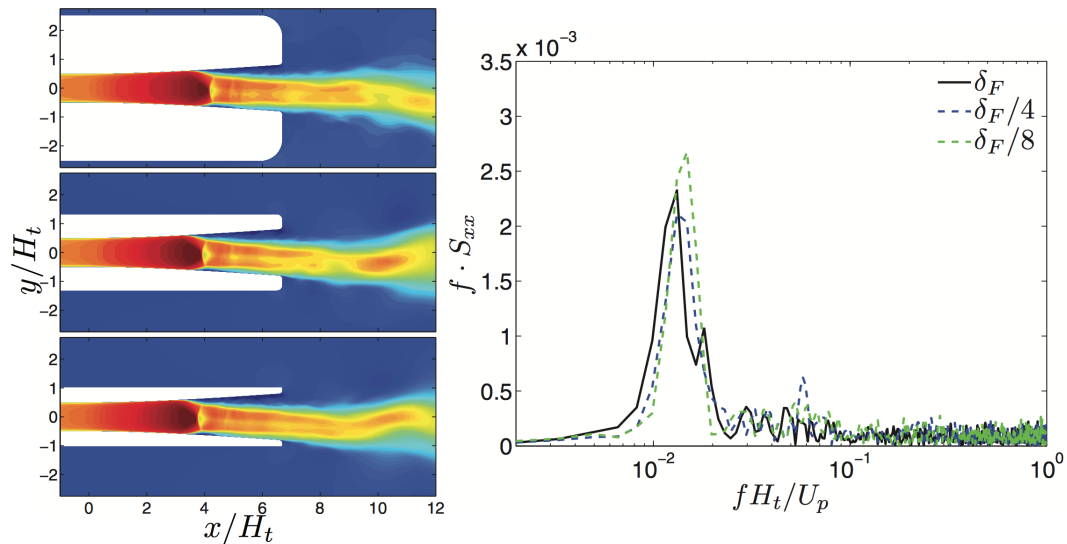


Figure 1.10: Parametric study of the flange width effects on lip vortices; Extracted from [Olson & Lele \(2013\)](#).

coming from the backflow at the exit which perturbs the dynamic of the recirculating bubbles. The study of [Kiya & Sasaki \(1983\)](#) showed that the size of the bubbles are increased due to an accumulation of angular momentum in the recirculation zone. When the large eddies reach a critical size, a part of the energy is released through smaller vortices, thereby decreasing the volume of the recirculating area. This energy cycle and the release of vortices lead to the “breathing” of the bubbles.

1.3.2.5 Lip vortex

The backflow acting in the recirculating area produces a small bubble at the nozzle lip. This vortex is influenced by the external flow, the mixing layer and the shape of the lip. Actually, the geometry of the lip has a major impact on the size/frequency of the lip vortex. [Ponton & Seiner \(1992\)](#) and [Pilinski \(2002\)](#) have shown the effects of nozzle lip thickness/shape on the trailing-edge noises for both over- and under-expanded nozzle flow. Both frequency and amplitude of acoustic waves are increased, while decreasing the lip thickness. [Pilinski \(2002\)](#) demonstrated that over a lip flange of thickness $0.1R_e$, where R_e is the exit radius, the effect of the length is moderate and similar to an infinite flange. [Olson \(2012\)](#) found similar results in their LES of a planar over-expanded nozzle flow.

The trailing-edge noises created by the lip are often the dominant frequency captured in the atmosphere as it propagates downstream of the exit. The sound created by the nozzle is assimilated to a screech emanating from these trailing-edges. The screech is more pronounced in the case of under-expanded nozzle as the flow at the lip is mostly supersonic increasing thereby the vorticity strength of the lip vortices. For over-expanded

nozzle, the flow is mostly subsonic at the lip so the effect of trailing-edge is mild.

1.3.3 Side-loads

Side-loads have been observed in many nozzle flows during experiments and simulations because of their impact on mechanical loads. The forces applying on the side of the nozzle, *i.e.* F_y and F_z , are non-uniform in space and unsteady in time. Side-loads originate from:

- Asymmetrical behavior of the separation line
- Transition shock patterns, regular to Mach reflexion or FSS to RSS
- Pressure fluctuations in the separated region and in the recirculating area region
- Vortices developing in the recirculating area and at the exit lip

Finally, a two-way coupling exists between the side-loads and the mechanical deformation of the nozzle structure that could deviate the flow along the walls and could modify the shock patterns. Side-loads are computed as follows:

$$\vec{F} = \oint_S (p_w - p_a) \vec{n} ds \quad (1.8)$$

where A the surface of the nozzle, p_w the wall-pressure, p_a the atmospheric pressure and \vec{n} the normal vector from the surface element s .

Side-loads are important for the lifetime and safety margin of a launcher. Nave & Coffey (1973) and Östlund (2002) have shown that the nozzle structure is affected by dynamical effects, *i.e.* turbulence and acoustic waves, which plays a dominant role in side-loads amplification. Depending on the nozzle geometry, the following behavior happens:

- For nozzle with high angle of deflection, the asymmetrical behavior of the separation line is reduced,
- For asymmetrical flow, the amplitude of side-loads is proportional to the asymmetrical surface,
- Amplitude of side-loads is reduced for high angle of deflection,
- The main tone of side-loads can reach the mechanical resonance of the nozzle structure which could lead to resonance failure.

1.3.4 Low-frequency unsteadiness

The unsteady shock-wave position in over-expanded nozzle flow contains highly energetic low-frequency modes. These modes are considered dangerous for the lifespan and reusability of the nozzle. Similarly, they can impact the stability of the downstream

exhaust plume leading to unstable thrust. The low-frequency unsteadiness has been revealed in many configurations, such as ducts (Salmon et al. 1983, Sajben et al. 1984, Weiss et al. 2010), wind tunnels (Dupont et al. 2006) or ramps (Ganapathisubramani et al. 2007). The identification of the origin of low-frequency modes and the physical mechanism that drive this unsteadiness has been studied in the literature over the past decades.

A lot of experimental work has been carried out to understand the unsteadiness of shocks in nozzle flows. Bogar et al. (1983) were the first to capture and study the unsteady motion of the shock in an experimental diffuser. They observed that the low-frequency modes of transonic diffuser were inversely proportional to the shock-to-exhaust distance. Similarly, Zaman et al. (2002) performed experimental investigations of the transonic tones in transonic diffusers. They concluded that the low-frequency modes were stimulated by the unsteadiness of the separated flow, serving as a source of perturbation. Oppositely to the mechanism of Bogar et al. (1983), they proposed a similar mechanism to that involved in longitudinal acoustic resonance, where the low-frequency mode corresponds to the case when one-quarter wavelength is fitted within the approximate distance from the foot of the shock to the nozzle exit. Handa et al. (2003) investigated experimentally and theoretically the shock wave oscillation in transonic diffusers. Using their theoretical solver, they proposed that the oscillations were governed by the geometrical shape of the diffuser and the Mach number in front of the shock wave. Nevertheless, they observed that the acoustic resonance, which was not taken into account in their theory, is an important mechanism for determining the shock wave oscillation. Lastly, Papamoschou & Johnson (2006) experimented the low-frequency phenomenon in planar nozzle flow. They captured interesting flow patterns and motions when the nozzle was considered transonic ($M_j \sim 1$). In a recent review of Clemens & Narayanaswamy (2014) on the low-frequency modes, they showed that two mechanisms, upstream and downstream perturbations, were at work in the low-frequency phenomenon. The upstream perturbations coming from the turbulent boundary layer were a source of fluctuations in weakly separated flow. They explained that the upstream momentum fluctuations could seed the shear layer with disturbances that grow and lead to large-scale flapping. On the contrary, for strongly separated flows, the downstream mechanism dominates as explained by Bogar et al. (1983), Zaman et al. (2002), Handa et al. (2003).

In the field of numerical simulation of nozzle flows and its application to low-frequency unsteadiness, very few studies can be found in literature. Most of the existing simulations from the literature use Detached Eddy Simulations (DES) to capture the low-frequency modes. The benefits of DES is the ability to perform simulation of over-expanded flow at high Reynolds number. On the contrary, the thin boundary layer developing along

the wall is computed by the RANS calculation which do not solve in detail the turbulent aspect of the boundary layer towards separation. Thus, the unsteady phenomena linked to the shock-wave boundary layer interaction are not correctly captured. Deck (2009) performed a DDES of LEA TOC nozzle and studied the low-frequency oscillations of the separation. The flow features a restricted shock separation (RSS). They found similar pressure distributions to the actual experiment but some discrepancy has been found for the oscillatory motion of the shock. Following the work of Deck (2009), Martelli et al. (2016) have simulated the same nozzle geometry using the DDES approach. They used Fourier and wavelet analysis to characterize the shock motion in the time-frequency space. Recently, Olson & Lele (2013) performed a Large Eddy Simulation (LES) of the planar nozzle flow from Papamoschou & Johnson (2006). They have been able to capture in detail the separation phenomenon and the unsteadiness leading to the low-frequency oscillations observed by Papamoschou & Johnson (2006). They concluded that the low-frequency mechanism was driven by a feedback mechanism, similarly to the one presented by Zaman et al. (2002). Due to high cost of computation of the LES, they have not been able to simulate enough physical time and observed a lack of convergence in their frequency study.

1.4 Scope of the present work

Over-expanded flow separation are characterized by complex phenomena occurring inside of the nozzle due to the shock/BL interaction. These phenomena interact with each others to form a highly complex system of acoustic, thermal and turbulent effects. Many studies have been performed in the last 60 years to understand and ultimately control the separation phenomenon. Even though, each phenomenon taken separately is highly documented and understood, *i.e.* supersonic jet, mixing layer, recirculating flow, vortices or shock patterns, the combination of all of these phenomena in a complex geometry is still an open research area, *i.e.* the impact of the incoming boundary layer on the separation, the prediction of the separation line location, the asymmetry of the exhaust plume or the fluid-structure coupling.

In numerical studies, nozzle flows are complex to solve due to the geometry, the presence of shock or the small boundary layer developing along the wall that needs to be captured. In the past, LES or RANS computations have been performed on planar or cylindrical flow but the frequency analysis of the internal flow is not fully documented to allow better prediction of the side-loads. To the best of the author's knowledge, no LES has been carried on separated cylindrical nozzle flow so far. Most of the numerical studies use either RANS or DES that do not necessarily capture the range of unsteadiness

observed in a separated nozzle flow.

The present thesis aims to study the boundary layer separation and the low-frequency modes inside an over-expanded nozzle (cylindrical or planar) using Large Eddy Simulation.

2

Governing equations and numerical methods

This chapter presents the governing equations in both Cartesian and generalized curvilinear form along with the numerical methods used to perform the simulations. Meanwhile, a parallel strategy for a domain decomposition technique in an overlapping grid is developed.

2.1 Governing equations

2.1.1 Navier–Stokes equations in Cartesian form

The three-dimensional compressible Navier–Stokes equations are defined by the conservation of mass, momentum and energy. In Cartesian coordinates $x_i = (x, y, z)$, they are expressed as:

$$\frac{\partial \rho}{\partial t} + \frac{\partial \rho u_j}{\partial x_j} = 0, \quad (\text{Continuity})$$

$$\frac{\partial \rho u_i}{\partial t} + \frac{\partial \rho u_i u_j}{\partial x_j} = -\frac{\partial p}{\partial x_i} + \frac{\partial \tau_{ij}}{\partial x_j}, \quad (\text{Momentum})$$

$$\frac{\partial \rho e}{\partial t} + \frac{\partial (\rho e + p) u_j}{\partial x_j} = \frac{\partial \tau_{ij} u_i}{\partial x_j} - \frac{\partial \dot{q}_j}{\partial x_j}, \quad (\text{Energy})$$

where ρ is the density, u_i the velocity vector, p the pressure, T the temperature, e the total energy, τ_{ij} the viscous stress tensor and \dot{q}_i the heat diffusion flux.

The perfect gas state is considered with

$$p = \rho r T, \quad (2.1)$$

The total energy is expressed as:

$$e = e_i + K = C_v T + \frac{1}{2}(uu + vv + ww), \quad (2.2)$$

the shear stress tensor:

$$\tau_{ij} = 2\mu S_{ij} + \mu'' \delta_{ij} \frac{\partial u_k}{\partial x_k}, \quad (2.3)$$

$$S_{ij} = \frac{1}{2} \left(\frac{\partial u_i}{\partial x_j} + \frac{\partial u_j}{\partial x_i} \right), \quad (2.4)$$

and the heat diffusion flux:

$$\dot{q}_j = -\lambda \frac{\partial T}{\partial x_j}. \quad (2.5)$$

The viscous stress tensor is composed of a viscous part and a dilatational part, where S_{ij} denotes the strain rate tensor and μ'' the second viscosity. On the assumption of a Newtonian fluid, the second viscosity can be expressed by the relation of Stokes (2.6) where μ_b denotes the bulk viscosity:

$$\mu_b = \mu'' + \frac{2}{3}\mu. \quad (2.6)$$

The dynamic viscosity follows the Sutherland law:

$$\mu(T) = \mu_{ref} \frac{T^{2/3}}{S + T}, \quad \text{with } S = 110.4K, \quad (2.7)$$

where the constant μ_{ref} depends on the fluid parameters.

The Prandtl number P_r is taken equal to 0.72, the heat capacity ratio $\gamma = 1.4$, the viscosity constant $\mu_{ref} = 1.456 \times 10^{-6} [kg \ m^{-1} s^{-1}]$, the bulk viscosity $\mu_b = 0 [kg \ m^{-1} s^{-1}]$ and the specific gas constant $r = 287 [m^2 K^{-1} s^{-2}]$.

2.1.2 Navier–Stokes equations in generalized curvilinear form

In order to compute arbitrary geometries, the structured code has been developed in a generalized curvilinear coordinates. This implies a transformation from a computational space to a physical space. The code uses the computational space to perform the simulation, where the mesh can be seen as a hexahedral domain. The computational space needs additional information to reconstruct the physical space by using the mapping

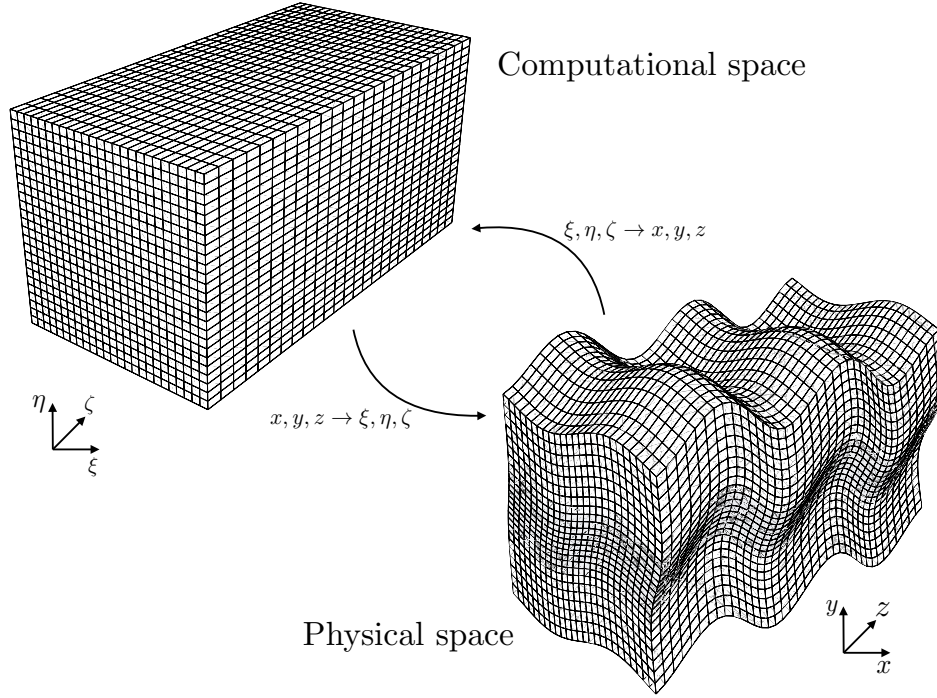


Figure 2.1: Transformation between physical and computational space.

transformations:

$$\begin{aligned}
 \xi &= \xi(x, y, z), \\
 \eta &= \eta(x, y, z), \\
 \zeta &= \zeta(x, y, z).
 \end{aligned}
 \tag{2.8}$$

By applying the chain rule, the partial derivative of any quantity φ can be written as:

$$\begin{aligned}
 \frac{\partial \varphi}{\partial x} &= \xi_x \frac{\partial \varphi}{\partial \xi} + \eta_x \frac{\partial \varphi}{\partial \eta} + \zeta_x \frac{\partial \varphi}{\partial \zeta}, \\
 \frac{\partial \varphi}{\partial y} &= \xi_y \frac{\partial \varphi}{\partial \xi} + \eta_y \frac{\partial \varphi}{\partial \eta} + \zeta_y \frac{\partial \varphi}{\partial \zeta}, \\
 \frac{\partial \varphi}{\partial z} &= \xi_z \frac{\partial \varphi}{\partial \xi} + \eta_z \frac{\partial \varphi}{\partial \eta} + \zeta_z \frac{\partial \varphi}{\partial \zeta}.
 \end{aligned}
 \tag{2.9}$$

The terms ξ_i , η_i and ζ_i , called the metrics, can be cast in a 3×3 matrix where $\xi_i = \partial \xi / \partial x_i$. The metrics represent the transformation from physical to computational space. The ξ , η and ζ parameters vary from 0 to N_x , N_y and N_z respectively.

$$\begin{pmatrix} \xi_x & \xi_y & \xi_z \\ \eta_x & \eta_y & \eta_z \\ \zeta_x & \zeta_y & \zeta_z \end{pmatrix} \quad (\text{Metrics})$$

In general, the transformation from physical space to computational space, *i.e.* ξ_x , is not known a priori and the physical mesh is directly described by the x , y and z space coordinates. It is then common to use the inverse of the metrics, *i.e.* x_ξ , by numerically deriving the physical mesh coordinates through a finite difference scheme. The relation between the metrics and their inverse is described as follow:

$$\begin{pmatrix} \xi_x & \xi_y & \xi_z \\ \eta_x & \eta_y & \eta_z \\ \zeta_x & \zeta_y & \zeta_z \end{pmatrix} = \begin{pmatrix} x_\xi & x_\eta & x_\zeta \\ y_\xi & y_\eta & y_\zeta \\ z_\xi & z_\eta & z_\zeta \end{pmatrix}^{-1}. \quad (2.10)$$

By computing the inverse of the following matrix, one can find the relation to compute the metrics, where J is the Jacobian of the metrics (2.12). J is a representation of the volume of each cell in the computational space.

$$\begin{pmatrix} \xi_x & \xi_y & \xi_z \\ \eta_x & \eta_y & \eta_z \\ \zeta_x & \zeta_y & \zeta_z \end{pmatrix} = \frac{1}{J} \begin{pmatrix} (y_\eta z_\zeta - y_\zeta z_\eta) & (z_\eta x_\zeta - z_\zeta x_\eta) & (x_\eta y_\zeta - x_\zeta y_\eta) \\ (y_\zeta z_\xi - y_\xi z_\zeta) & (z_\zeta x_\xi - z_\xi x_\zeta) & (x_\zeta y_\xi - x_\xi y_\zeta) \\ (y_\xi z_\eta - y_\eta z_\xi) & (z_\xi x_\eta - z_\eta x_\xi) & (x_\xi y_\eta - x_\eta y_\xi) \end{pmatrix} \quad (2.11)$$

$$J = x_\xi(y_\eta z_\zeta - y_\zeta z_\eta) + x_\eta(y_\zeta z_\xi - y_\xi z_\zeta) + x_\zeta(y_\xi z_\eta - y_\eta z_\xi) \quad (2.12)$$

The governing equation can be transformed from physical to computational space by replacing each derivative by their curvilinear form (Eq. 2.9). For instance, the continuity equation can be written as:

$$\frac{\partial \rho}{\partial t} + \xi_j \frac{\partial \rho u_j}{\partial \xi} + \eta_j \frac{\partial \rho u_j}{\partial \eta} + \zeta_j \frac{\partial \rho u_j}{\partial \zeta} = 0, \quad (2.13)$$

with $\xi_i = (\xi_x, \xi_y, \xi_z)$.

Equation 2.13 is written in a non-conservative form. The strong conservative form of this equation can be found using the metric relations and the Jacobian definition. One can find:

$$J \frac{\partial \rho}{\partial t} + \frac{\partial \rho J \xi_j u_j}{\partial \xi} + \frac{\partial \rho J \eta_j u_j}{\partial \eta} + \frac{\partial \rho J \zeta_j u_j}{\partial \zeta} = 0. \quad (2.14)$$

To simplify the previous equation, the term $U = J \xi_j u_j$ is called the contravariant velocity. The contravariant velocities can be seen as the projection of the velocity components on the computational space:

$$\begin{aligned}
U &= J(\xi_x u + \xi_y v + \xi_z w), \\
V &= J(\eta_x u + \eta_y v + \eta_z w), \\
W &= J(\zeta_x u + \zeta_y v + \zeta_z w).
\end{aligned} \tag{2.15}$$

Finally, the strong conservative form of the generalized curvilinear equations are:

$$J \frac{\partial \rho}{\partial t} + \frac{\partial \rho U_j}{\partial \xi^j} = 0, \tag{Continuity}$$

$$J \frac{\partial \rho u_i}{\partial t} + \frac{\partial \rho u_i U_j}{\partial \xi^j} = - \frac{\partial J \xi_i^j p}{\partial \xi^j} + \frac{\partial J \xi_j^k \tau_{ij}}{\partial \xi^k}, \tag{Momentum}$$

$$J \frac{\partial \rho e}{\partial t} + \frac{\partial (\rho e + p) U_j}{\partial \xi^j} = \frac{\partial J \xi_i^k u_j \tau_{ij}}{\partial \xi^k} - \frac{\partial J \xi_j^k \dot{q}_j}{\partial \xi^k}, \tag{Energy}$$

$$\tau_{ij} = \mu \left(\xi_i^l \frac{\partial u_j}{\partial \xi^l} + \xi_j^l \frac{\partial u_i}{\partial \xi^l} \right) + \mu'' \delta_{ij} \xi_m^l \frac{\partial U_m}{\partial \xi^l}, \tag{2.16}$$

$$\dot{q}_j = -\lambda \xi_j^l \frac{\partial T}{\partial \xi^l}, \tag{2.17}$$

where $\xi^i = (\xi, \eta, \zeta)$ for consistency.

The generalized form of the equations contains three times more terms than the Cartesian ones, implying an extra computational time.

2.1.3 Large Eddy Simulation

The approach of large-eddy simulation, or LES, is to reduce the computational cost by ignoring the smallest length scales. The large-scale turbulence is resolved while the small eddies are modeled by an additional term in the Navier–Stokes equations. The separation of scale is bound by the computational grid resolution. In practice, the Kolmogorov scale is proportional to the local Reynolds number.

$$\frac{L}{\eta} \sim Re^{3/4} \quad (2.18)$$

where Re is the Reynolds number, L a characteristic length scale and η the Kolmogorov scale.

For high Reynolds number, the number of points needed for a practical simulation can be unfeasible with the current computational power. It is common to use a subgrid model to compute such flows. Based on the Nyquist theorem, no scale smaller than $2\Delta x$ can be captured. Equivalently, these high wavenumbers can be cut off by the grid resolutions where the cutoff wavenumber is $\hat{k}_c = \pi/\Delta x$.

A spatial-scale filtering is introduced using the convolution product:

$$\bar{\varphi} = \int_D G(\vec{x} - \vec{z}; \bar{\Delta}) \varphi(\vec{z}) d^3\vec{z}, \quad (2.19)$$

where φ is any vector field, G the convolution filter kernel and $\bar{\Delta}$ the characteristic cutoff length scale. The convolution filter kernel can be any filter function but is often assimilated to a top-hat function.

The spatial-scale filter (2.19) is applied to the Navier–Stokes equations, where $\tilde{\varphi} = \overline{\rho\varphi}/\bar{\rho}$ is the Favre-averaging, $\varphi'' = \varphi - \tilde{\varphi}$ the Favre-fluctuation and $\varphi' = \varphi - \bar{\varphi}$ the Reynolds-fluctuation:

$$\frac{\partial \bar{\rho}}{\partial t} + \frac{\partial \bar{\rho} \tilde{u}_j}{\partial x_j} = 0, \quad (\text{Continuity})$$

$$\frac{\partial \bar{\rho} \tilde{u}_i}{\partial t} + \frac{\partial \bar{\rho} \tilde{u}_i \tilde{u}_j}{\partial x_j} = -\frac{\partial \bar{p}}{\partial x_i} + \frac{\partial \bar{\tau}_{ij}}{\partial x_j} - \frac{\partial \overline{\rho u_i'' u_j''}}{\partial x_j}, \quad (\text{Momentum})$$

$$\frac{\partial \bar{\rho} \tilde{e}}{\partial t} + \frac{\partial (\bar{\rho} \tilde{e} + \bar{p}) \tilde{u}_j}{\partial x_j} = \frac{\partial \bar{\tau}_{ij} \tilde{u}_i}{\partial x_j} - \bar{q}_j - \frac{\partial \overline{\rho e'' u_j''}}{\partial x_j} - \frac{\partial \overline{p' u_j'}}{\partial x_j} - \frac{\partial \overline{\tau'_{ij} u_i'}}{\partial x_j}, \quad (\text{Energy})$$

$$\bar{q}_j = -\bar{\lambda} \frac{\partial \bar{T}}{\partial x_j} - \overline{\lambda' \frac{\partial T'}{\partial x_j}}. \quad (2.20)$$

The subgrid viscous term $\bar{\tau}_{ij}$ can also be split up into a filtered part and a fluctuation

part. Some of the SGS terms are negligible compared to others. For instance, the subgrid-scale pressure terms and viscous terms are known to be relatively small compared to the other terms. The subgrid-scale stress tensor $\overline{\rho u_i'' u_j''}$ and the subgrid-scale Reynolds heat flux $\overline{\lambda' \partial T' / \partial x_j}$ which comes from the filtered equations, are known as the SubGrid-Scale terms (or SGS).

The most common approach is to model those terms by an eddy viscosity approach such as:

$$\overline{\rho u_i'' u_j''} = \tau_t = 2\mu_t \overline{S_{ij}} + \mu_t'' \delta_{ij} \frac{\partial \overline{u_k}}{\partial x_k}, \quad (2.21)$$

$$\overline{\lambda' \frac{\partial T'}{\partial x_j}} = \lambda_t \frac{\partial \overline{T}}{\partial x_j} = \frac{\mu_t C_p}{Pr_t} \frac{\partial \overline{T}}{\partial x_j}. \quad (2.22)$$

Many models to compute the subgrid-scale viscosity exist in literature. The WALE model has been used because of its ability to simulate wall-bounded flow.

2.1.3.1 WALE eddy viscosity model

Due to the fact that the nozzle flow simulations are wall-bounded flow, the behavior of μ_t needs to be equal to zero when there is no energy near the cutoff frequency and needs to decrease near the wall since the slope m of the kinetic energy spectrum $\widehat{E}(\widehat{k}) \propto \widehat{k}^{-m}$ is larger in the wall than outside of the boundary layer. Using the Kolmogorov spectrum $\widehat{E}(\widehat{k}) \propto C_K \epsilon^{2/3} \widehat{k}^{-5/3}$, one can find:

$$\mu_t = \frac{2}{3} \rho C_K^{-3/2} \sqrt{\frac{\widehat{E}(\widehat{k}_c)}{\widehat{k}_c}}. \quad (2.23)$$

The WALE model (Nicoud & Ducros 1999) has been developed to handle wall-bounded flow and transitional problem. The form of the eddy viscosity term can be expressed as follows:

$$\mu_t = \rho (C_m \Delta)^2 \frac{(S_{ij}^d S_{ij}^d)^{3/2}}{(S_{ij} S_{ij})^{5/2} + (S_{ij}^d S_{ij}^d)^{3/2}}, \quad (2.24)$$

$$S_{ij}^d = \frac{1}{2} \left(\left(\frac{\partial u_i}{\partial x_j} \right)^2 + \left(\frac{\partial u_j}{\partial x_i} \right)^2 \right) - \frac{1}{3} \delta_{ij} \left(\frac{\partial u_k}{\partial x_k} \right)^2, \quad (2.25)$$

where $C_m = \sqrt{10.6} C_s$ is a model constant, proportional to the LES Smagorinsky's constant C_s defined by $C_s = \frac{1}{\pi} \left(\frac{3C_K}{2} \right)^{-5/4}$ and S_{ij}^d an operator based on the traceless symmetric part of the square of the velocity gradient. In a shear layer, the term $S_{ij}^d S_{ij}^d$ tends to zero near the wall to conserve the property of wall-bounded flow. The WALE

model has the advantage of reproducing the asymptotic scaling in $O(y^3)$ of the eddy viscosity near the wall. This model has been written in generalized curvilinear coordinates using equation 2.9.

2.2 Numerical method

A new code has been developed to handle the curvilinear equations in 3D. The code is based on an existing inhouse code developed by Abdellah Hadjadj and co-workers at the Coria laboratory in Rouen. The code, called ChocWaves for Compressible High-Order Code using Weno AdaptatiVE Stencils, is a Cartesian explicit Navier–Stokes solver with WENO / Central scheme for space discretization and compact RK3 for time integration. It uses the Immersed Boundary Method (IBM) to simulate a flow with complex geometries. The code is fully parallelized with the MPI/OMP library and uses HDF5 library for IO.

The version of the code developed in this thesis is a curvilinear explicit finite-difference Navier–Stokes solver with WCNS / Central / Hybrid scheme for space discretization and RK4 for time integration. The code uses the HDF5 library for IO and the MPI library for parallelization. The scalability of the solver has been tested on more than 20k CPUs and shows good scalability even for large number of nodes (sec. 2.2.4).

2.2.1 Spatial scheme

Due to the conservative form of the equations written in curvilinear coordinates, the spatial scheme deals with issues of freestream preservation and metric cancelation. These errors arising from the finite-difference discretization of the terms in strong-conservative form can lead to unphysical behavior of the flow and numerical instability. Visbal & Gaitonde (1999) have proved that using the same scheme as those employed for the fluxes to compute the metrics can force the cancellation of the metrics. They also proposed a new way of computing the metrics to improve the freestream preservation in general 3-D meshes (Visbal & Gaitonde 2002). In this case, the metrics are computed as:

$$\begin{pmatrix} \xi_x & \xi_y & \xi_z \\ \eta_x & \eta_y & \eta_z \\ \zeta_x & \zeta_y & \zeta_z \end{pmatrix} = \frac{1}{J} \begin{pmatrix} ((y_\eta z)_\zeta - (y_\zeta z)_\eta) & ((z_\eta x)_\zeta - (z_\zeta x)_\eta) & ((x_\eta y)_\zeta - (x_\zeta y)_\eta) \\ ((y_\zeta z)_\xi - (y_\xi z)_\zeta) & ((z_\zeta x)_\xi - (z_\xi x)_\zeta) & ((x_\zeta y)_\xi - (x_\xi y)_\zeta) \\ ((y_\xi z)_\eta - (y_\eta z)_\xi) & ((z_\xi x)_\eta - (z_\eta x)_\xi) & ((x_\xi y)_\eta - (x_\eta y)_\xi) \end{pmatrix}. \quad (2.26)$$

The WENO (Weighted Essentially NonOscillatory) scheme applies a weighted averaging procedure directly to the flux. It is then impossible both to evaluate the discretization scheme used on the metrics and to force the freestream preservation. Thus, the WENO

scheme can only be used in the non-conservative form of the Euler equations which do not impose global conservation on the set of equations. Deng & Zhang (2000) developed a fifth-order Weighted Compact Nonlinear scheme (WCNS) where the conservative variables are interpolated using a weighted averaging procedure similar to the WENO scheme. In this formulation, the freestream condition can be imposed because the metrics are evaluated by the same numerical finite-difference scheme used in the WCNS. Nonomura et al. (2010) compared WENO and WCNS schemes on curvilinear grid and proved that the WCNS imposes the freestream preservation. Nonomura & Fujii (2013) developed a compact form of the WCNS scheme to reduce the stencil and found a new technique for freestream preservation of the WENO scheme (Nonomura et al. 2015). All the above schemes have been validated (see chapter 3).

2.2.1.1 Convective terms

The convective terms can be discretized using different methodology, by a local conservative central difference scheme, by a WCNS scheme or by a hybrid scheme.

Conservative central difference scheme

Following the work of Pirozzoli (2010), the standard central difference formulas can be applied to the convective term by using a split form which improves the stability and the energy preservation properties. The convective term is discretized by a conservative finite-difference scheme:

$$\frac{\partial \varphi}{\partial \xi} = F_{i+1/2} - F_{i-1/2}, \quad (2.27)$$

where $F_{i+1/2}$ is the numerical flux.

The 6th-order form of the central finite-difference scheme is used to match the WCNS's order (5th-order). The numerical flux is computed using a generalized curvilinear Euler equation by the following (for the x -component):

$$F_{i+1/2} = 2 \sum_{l=1}^6 a_l \sum_{m=0}^{l-1} (f, g, h)_{j-m,l}, \quad (2.28)$$

$$(f, g, h)_{j,l} = \frac{1}{8} (f_j + f_{j+l})(g_j + g_{j+l})(h_j + h_{j+l}), \quad (2.29)$$

where $a_1 = 3/4$, $a_2 = a_3 = -3/20$, $a_4 = a_5 = a_6 = 1/60$ and (f, g, h) represents variables used in the curvilinear Euler equation $((f, g, h) = (\rho, \vec{u}, \vec{U}))$.

WCNS scheme

The WCNS has been implemented into the code to take care of the freestream preservation in generalized curvilinear coordinates using the work of Deng & Zhang (2000) and Nonomura et al. (2010). The WCNS is using a 5th-order discretization with the generalized curvilinear coordinates of the Euler's equations.

Let us consider the Euler equations:

$$J \frac{\partial \vec{Q}}{\partial t} + \sum_{j=1}^3 \frac{\partial \vec{E}_j}{\partial \xi^j} = 0, \quad (2.30)$$

where \vec{Q} is the conservative vector $\vec{Q} = (\rho, \rho u, \rho v, \rho w, \rho e)^t$ and \vec{E}_j is convective terms $\vec{E}_j = (\rho U_j, \rho u U_j + J \xi_x^j p, \rho v U_j + J \xi_y^j p, \rho w U_j + J \xi_z^j p, (\rho e + p) U_j)^t$.

For consistency, the curvilinear coordinates are defined by $\xi^i = (\xi, \eta, \zeta)$.

The spatial derivative $\partial E / \partial \xi^j$ can be evaluated by a sixth-order midpoint to computational-node difference scheme,

$$\frac{\partial E}{\partial \xi} = \frac{75}{64} (E_{i+1/2}^{\text{WCNS}} - E_{i-1/2}^{\text{WCNS}}) - \frac{25}{384} (E_{i+3/2}^{\text{WCNS}} - E_{i-3/2}^{\text{WCNS}}) + \frac{3}{640} (E_{i+5/2}^{\text{WCNS}} - E_{i-5/2}^{\text{WCNS}}), \quad (2.31)$$

where $E_{i+1/2}^{\text{WCNS}}$ is the WCNS numerical flux calculated at a midpoint.

The WCNS weighted averaging procedure is applied to the characteristic variables W_i , to find the left and right interpolated fluxes, $Q_{i+1/2}^{\text{WCNS},L}$ and $Q_{i+1/2}^{\text{WCNS},R}$, respectively. The transformation from conservative to primitive variables is detailed in the following equations:

$$J \frac{\partial Q}{\partial t} + A_j \frac{\partial Q}{\partial \xi^j} = 0, \quad (2.32)$$

$$A_j = \frac{\partial E_j}{\partial Q} = R \Lambda L, \quad (2.33)$$

where A is the flux Jacobian, L the left eigenvector, R the right eigenvector and Λ the diagonal matrix with the eigenvalues of A . By definition, $L = R^{-1}$. The transformation from conservative to characteristic is defined by the following equation:

$$W_{i,m} = L_{i^*,m} Q_i, \quad (2.34)$$

where i^* denotes the Roe's averaging procedure (Roe 1981) at the i th grid point bounded by $(i, i+1)$ and m the m th characteristic variable.

The weighted averaging procedure $W_{i,m} \Rightarrow W_{i+1/2,m}^{\text{WCNS},L}$, similar to the WENO procedure, is detailed in Appendix B of Nonomura et al. (2010). Finally, the left and the right conservative variables can be reconstructed from characteristic variables by:

$$Q_{i+1/2}^{\text{WCNS},L} = \sum_m W_{i+1/2,m}^{\text{WCNS},L} R_{i^*,m}. \quad (2.35)$$

The WCNS numerical flux $E_{i+1/2}^{\text{WCNS}}$ from equation 2.31 can be reconstructed by the Roe's flux difference splitting Roe (1981):

$$E_{i+1/2}^{\text{WCNS}} = \frac{1}{2} \left(E_{\star} \left(Q_{i+1/2}^{\text{WCNS},L} \right) + E_{\star} \left(Q_{i+1/2}^{\text{WCNS},R} \right) - R_{i^*} \Lambda_{i^*} L_{i^*} \left(Q_{i+1/2}^{\text{WCNS},R} - Q_{i+1/2}^{\text{WCNS},L} \right) \right), \quad (2.36)$$

where i^* denotes the Roe's averaging procedure at the i th grid point bounded by (L, R) .

The left and right fluxes $E \left(Q_{i+1/2}^{\text{WCNS},L/R} \right)$ are computed using the interpolated metrics from the following sixth-order Lagrange interpolation scheme:

$$\begin{aligned} (J\xi_x)_{i+1/2}^{\text{WCNS}} &= \frac{75}{128} \left((J\xi_x)_i + (J\xi_x)_{i+1} \right) \\ &- \frac{25}{256} \left((J\xi_x)_{i-1} + (J\xi_x)_{i+2} \right) + \frac{3}{256} \left((J\xi_x)_{i-2} + (J\xi_x)_{i+3} \right). \end{aligned} \quad (2.37)$$

In order to preserve the freestream, the metrics are discretized by the same computational-node to midpoint interpolation scheme (Eq. 2.31) and the same midpoint interpolation scheme (Eq. 2.37).

Hybrid scheme

Due to the high dissipation of the shock-capturing WCNS / WENO scheme, a hybrid scheme has been developed. The hybrid scheme acts as a switch between the WCNS scheme and the centered difference scheme. Thus, the numerical dissipation of the WCNS scheme can be confined in shocked regions and the centered difference can be applied in free-shock region to ensure accuracy and stability. The hybrid scheme is defined by:

$$\frac{\partial \varphi}{\partial x}^{\text{Hybrid}} = (1 - \Theta) \frac{\partial \varphi}{\partial x}^{\text{Centered}} + \Theta \frac{\partial \varphi}{\partial x}^{\text{WCNS}}. \quad (2.38)$$

The difficulty of hybrid scheme is to locate the shock regions where high gradient of pressure, velocity or temperature can affect the stability of the centered scheme. Ducros et al. (1999) proposed a shock sensor based on the Jameson's sensor (Jameson et al. 1981):

$$\theta = \frac{(\vec{\nabla} \cdot \vec{u})^2}{(\vec{\nabla} \cdot \vec{u})^2 + (\vec{\nabla} \times \vec{u})^2 + \varepsilon}, \quad (2.39)$$

where $\varepsilon = 10^{-30}$ is a positive real number chosen to prevent numerical divergence.

The ε coefficient has been changed by Pirozzoli (2011a) to improve the original formulation for wall-bounded flow. In their case, they set $\varepsilon = (u_{\infty}/\delta_0)^2$. Several tests, using

the shock tube problem (Riemann problem), have been done with this new parameter but provide unstable results in shock region. The Ducros sensor is a coefficient varying between 0 and 1. However, in our code, we set the coefficient Θ as a switch equal to 0 or 1 where θ_0 is the limiter value (configured with *a-priori* test):

$$\begin{cases} \Theta = 1, & \text{if } \theta > \theta_0 \\ 0, & \text{otherwise} \end{cases} \quad (2.40)$$

2.2.1.2 Viscous terms

The viscous terms in the curvilinear Navier–Stokes have been discretized by a 4th-order central scheme. To improve the stability of the code, each derivative is separated into two derivatives by a Laplacian operator. As an example, the first viscous term written with a Laplacian operator, from equation 2.16, gives:

$$\frac{\partial(\mu \xi_x J \xi_x) \frac{\partial u}{\partial \xi}}{\partial \xi} = \frac{\partial(\mu \xi_x J \xi_x)}{\partial \xi} \frac{\partial u}{\partial \xi} + \mu \xi_x J \xi_x \frac{\partial^2 u}{\partial \xi^2}. \quad (2.41)$$

Equations 2.42 and 2.43 show the 4th-order central scheme for the first derivative and the second derivatives, respectively.

$$\frac{\partial \varphi}{\partial \xi} = \frac{-\varphi_{i+2} + 8(\varphi_{i+1} - \varphi_{i-1}) + \varphi_{i-2}}{12}, \quad (2.42)$$

$$\frac{\partial^2 \varphi}{\partial \xi^2} = \frac{-(\varphi_{i+2} + \varphi_{i-2}) + 16(\varphi_{i+1} + \varphi_{i-1}) - 10\varphi_i}{12}. \quad (2.43)$$

Because of the high number of viscous terms to be computed, a special care has been taken with the viscous subroutine in term of optimisation. The averaged consumption of this routine is around 40% per iteration (sec. 2.2.4).

2.2.2 Temporal scheme

The governing equations are advanced in time by an explicit 4th-order Runge-Kutta (RK4) method. This RK4 scheme is overly used by many for its broad stability properties. The scheme uses four sub-integrations and two temporary arrays. A low-storage method has been developed by Williamson (1980) to remove one temporary array. The large amount of memory available nowadays on high performance supercomputer does not require the integration of the low-storage method. The RK4 is described as follows, where Δt is the time step:

$$\frac{\partial F(t, \vec{x})}{\partial t} = Q(t, \vec{x}), \quad (2.44)$$

$$\begin{aligned}
& \bullet F^{n+1/4} = F^n + \frac{\Delta t}{6} Q(F^n) \\
& F_1^* = F^n + \frac{\Delta t}{2} Q(F^n) \\
& \bullet F^{n+2/4} = F^{n+1/4} + \frac{\Delta t}{3} Q(F_1^*) \\
& F_2^* = F^n + \frac{\Delta t}{2} Q(F_1^*) \\
& \bullet F^{n+3/4} = F^{n+2/4} + \frac{\Delta t}{3} Q(F_2^*) \\
& F_3^* = F^n + \Delta t Q(F_2^*) \\
& \bullet F^{n+1} = F^{n+3/4} + \frac{\Delta t}{6} Q(F_3^*)
\end{aligned} \quad (2.45)$$

2.2.3 Stability properties

The drawback of time-explicit schemes comes from the constraint applied on the time step for stability purpose. To avoid the divergence of the temporal scheme, two parameters have been used to compute the time step Δt . From the von Neumann analysis, one can find the Courant-Friedrichs-Lewy condition on the convection terms and the Fourier condition on the viscous terms. For a first-order time advancement and a first-order spatial discretization, the von Neumann analysis gives a critical CFL equals to unity and a critical Fourier number of 0.5. By increasing the accuracy of the schemes, both temporally and spatially, one can find a higher critical CFL/Fourier conditions.

For the 3D curvilinear equations, the minimal physical time step Δt is computed by:

$$C_{\Delta t} = \frac{1}{J} \left(\sum_i |u\xi_i| + \sum_i |v\eta_i| + \sum_i |w\zeta_i| + c \sum_{i=1}^3 \left(\sum_{j=1}^3 |\xi_i^j| \right) + \frac{1}{\gamma \text{Fo} J} \left(\frac{\mu}{Pr} + \frac{\mu_t}{Pr_t} \right) \left(\sum_{i=1}^3 |\xi_i^{i^2}| \right) \right), \quad (2.46)$$

$$\Delta t = \min \left(\frac{\text{CFL}}{C_{\Delta t}} \right), \quad (2.47)$$

where CFL is a parameter of stability depending on the numerical schemes used and Fo the critical Fourier number.

Core	Wallclock time ($\mu s/N_{step}/N_{cells}$)	Speedup
8 (2x2x2)	-	-
32 (2x4x4)	21.6	0.53
64 (4x4x4)	20.3	1
128 (8x4x4)	21.8	2.2
256 (8x8x4)	23.4	4.6
512 (8x8x8)	22.9	9.0

Table 2.1: Strong scalability test of the curvilinear code.

N_{pt} per process	Wallclock time ($\mu s/N_{step}/N_{cells}$)
16^3	25.9
32^3	22.9
48^3	21.1
64^3	20.5
80^3	20.1
96^3	20.0
128^3	-

Table 2.2: Grid size per process scaling.

2.2.4 Scalability of the code

To demonstrate the performance of the code and its adaptability on large clusters, both weak and strong scaling benchmarks have been carried out on the TGCC-Curie from the CEA in Saclay, France. For information, the cluster uses 5040 nodes with 2 Intel octo-core E5-2680 and 64GB of memory. To be representative, the code has been executed with the WENO scheme, the LES model and all of the IO subroutine activated.

Table 2.1 shows the strong scalability where the total domain size is kept constant ($N = 16.7M$ cells) while the MPI discretization is increased. The 64 cores run is taken as a reference. At 8 cores, the memory allocation per process is over the limit per node, *i.e.* $< 64GB$. Because of the 3D MPI decomposition, the best efficiency, in terms of communication, is obtained when the domain shape per process is close to a cube, *i.e.* $N_x^{/cores} = N_y^{/cores} = N_z^{/cores}$. From the results, it can be seen that the cubic discretization leads to the best performance.

Table 2.2 shows the scaling of the optimum grid size per process. The optimum grid size per process finds the optimum balance between the efficiency of the code and the memory used per process. In this test, the MPI discretization is kept constant ($N_{cores} = 512$) and the number of points per process is increased. Again, the cube of 128 points per side overloads the node memory limitation of 64GB. The optimum grid size is the 48^3 cube which gives an efficient scalability and a reasonable memory allocation.

Core	Wallclock time ($\mu s/N_{step}/N_{cells}$)	Speedup
256	21.1	1.0
512	21.2	2.0
1024	21.2	4.0
2048	21.3	8.1
4096	21.4	16.2
8192	21.5	32.5
16384	23.9	72.3

Table 2.3: Weak scaling test of the curvilinear code

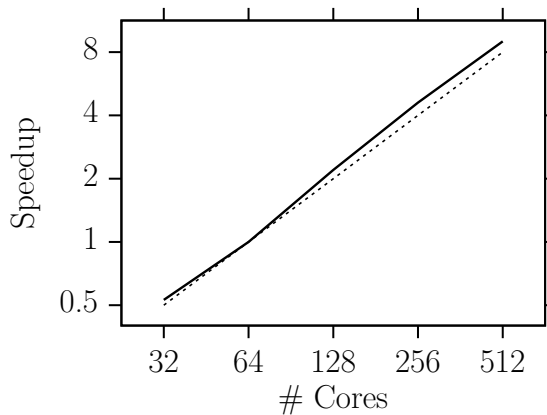
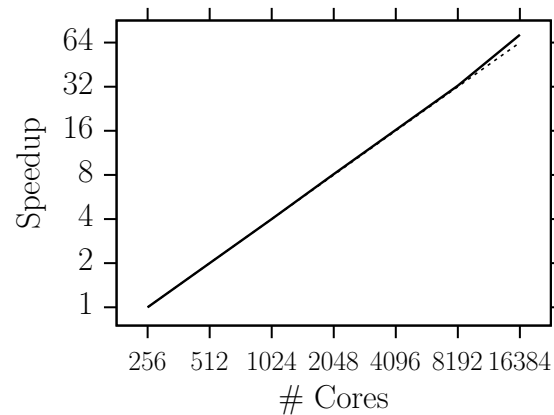


Figure 2.2: Strong scaling on the TGCC-Curie with a constant grid of 16.7 millions cells.

Figure 2.3: Weak scaling on the TGCC-Curie with a constant grid size per process of 48^3 .

Lastly, table 2.3 shows the weak scalability where the grid size per process is constant (48^3) while the number of cores is increased. The results give a linear scaling up to 8192 cores. Over 8000 cores, the cluster depends highly on internal nodes communication and the efficiency is decreasing because of the high number of MPI communication within the machine.

2.3 Boundary and initial conditions

2.3.1 Immersed Boundary Method

ChocWaves code uses the structured coordinate form of the equations. Any complex geometries need to be reconstructed using the so-called, Immersed Boundary Method. This method, originally developed by Peskin (1972), is overly used in CFD for the simulation of complex fluid-structure interaction. The next lines are set to explain in details the method and the improvement made on the interpolation. This method is a matter of discussion because it has been used for the validation of the domain decomposition method (sec. 2.4). This method has also been compared with the Brinkman penalization

method (BPM) on a paper published in *Computers & Fluids* journal (Piquet et al. 2016) (appendix D).

With the IBM, the Cartesian grid is first decomposed into solid and fluid cells. The solid cells are then split up into ghost and pure solid cells (the number of ghost cell depends on the scheme used for spatial discretization). The Immersed Boundary Method is applied only on the ghost cells. Figure 2.4 shows IBM mask distribution for a pipe flow.

For each ghost point, corresponding image points are created in the fluid from the surface of the geometry. Since the image points lie in the fluid, 3D interpolation is necessary (cell data to point data). The tri-linear interpolation method is used to interpolate the value in the fluid Nam & Lien (2014). For points near the wall surrounded by one or more ghost points, simple tri-linear interpolation is not possible and will cause an ill-posedness problem. Nam & Lien (2014) suggested an interpolation between fluid points and skin geometry since parameters at the wall are known. For clarity, figure 2.5 is represented in 2D. It shows the interpolation method for both cases: full surrounded image point and near wall image point.

For the 3D Bi-linear interpolation method, the generic flow variable (ϕ) can be calculated with:

$$\phi(x, y, z) = C_1xyz + C_2xy + C_3xz + C_4yz + C_5x + C_6y + C_7z + C_8. \quad (2.48)$$

The eight weighting coefficients, noted C_i , are evaluated from the generic variables of the eight surrounding points by solving this algebraic system:

$$\begin{bmatrix} C_1 \\ \dots \\ C_8 \end{bmatrix} = \begin{bmatrix} x_1y_1z_1 & x_1y_1 & x_1z_1 & y_1z_1 & x_1 & y_1 & z_1 & 1 \\ \dots & \dots \\ x_8y_8z_8 & x_8y_8 & x_8z_8 & y_8z_8 & x_8 & y_8 & z_8 & 1 \end{bmatrix}^{-1} \begin{bmatrix} \phi_1 \\ \dots \\ \phi_8 \end{bmatrix}. \quad (2.49)$$

This 8x8 Vandermonde matrix is inverted for each ghost cell of the grid at the start of the simulation using Lapack library. The following equation shows the Vandermonde matrix when a point, or more, (noted B) lies in a ghost cell:

$$\begin{bmatrix} C_1 \\ \dots \\ C_8 \end{bmatrix} = \begin{bmatrix} x_1y_1z_1 & x_1y_1 & x_1z_1 & y_1z_1 & x_1 & y_1 & z_1 & 1 \\ \dots & \dots \\ x_By_Bz_B & x_By_B & x_Bz_B & y_Bz_B & x_B & y_B & z_B & 1 \end{bmatrix}^{-1} \begin{bmatrix} \phi_1 \\ \dots \\ 0 \end{bmatrix}. \quad (2.50)$$

In isothermal case, u_1, u_2, u_3 and T are imposed by the previous method and p is set to zero gradient-normal. The gradient condition can be expressed as follows using the

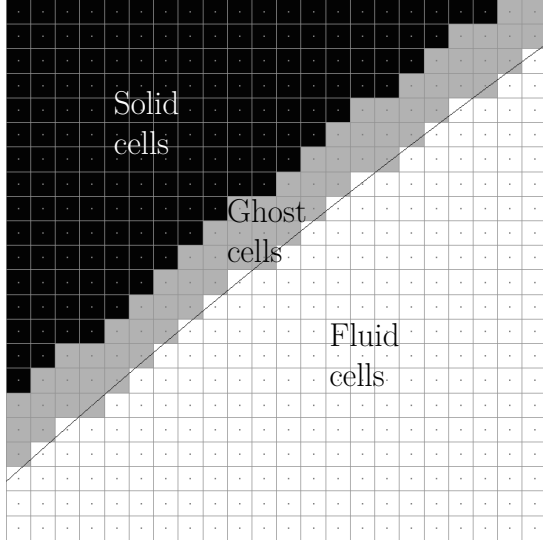


Figure 2.4: Immersed Boundary Method for a pipe geometry; Black, grey and white color represent pure solid cells, ghost cells and fluid cells, respectively.

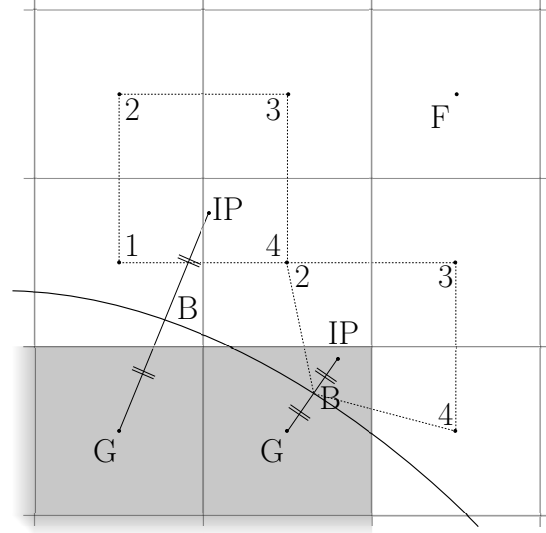


Figure 2.5: Bi-linear interpolation for the IBM demonstrating the two interpolations method (ghost cells close to the wall).

wall-normal vector $\vec{n} = \{n_x, n_y, n_z\}$:

$$\begin{aligned} \frac{\partial \phi(x, y, z)}{\partial \vec{n}} = & C_1(y_B z_B n_x + x_B z_B n_y + x_B y_B n_z) + C_2(y_B n_x + x_B n_y) \\ & + C_3(z_B n_x + x_B n_z) + C_4(y_B n_y + z_B n_z) + C_5 n_x + C_6 n_y + C_7 n_z = \vec{0}. \end{aligned} \quad (2.51)$$

As a result, the corresponding Vandermonde matrix becomes:

$$\begin{bmatrix} x_1 y_1 z_1 & x_1 y_1 & x_1 z_1 & y_1 z_1 & x_1 & y_1 & z_1 & 1 \\ \dots & & & & & & & \\ (y_B z_B n_x + & (y_B n_x + & (z_B n_x + & (y_B n_y + & & & & \\ x_B z_B n_y + & x_B n_y) & x_B n_z) & z_B n_z) & n_x & n_y & n_z & 0 \\ x_B y_B n_z) & & & & & & & \end{bmatrix}^{-1} \begin{bmatrix} \phi_1 \\ \dots \\ 0 \end{bmatrix}. \quad (2.52)$$

Once the flow variables at the image point (ϕ_i) are interpolated, the isothermal/no-slip wall boundary conditions (equation 2.53) will determine the values of the non-conserved variables (T, p, u, v, w) at the ghost cells. Nam & Lien (2014) proposed their method for adiabatic wall and used conserved variables. In our case, non-conserved variables have been used to apply the isothermal condition. In the case where wall informations are needed, we simply impose the following parameters $\vec{v} = \vec{0}$, $T = T_w$, $\frac{\partial p}{\partial \vec{n}} = \vec{0}$.

$$u_g = -u_i, \quad v_g = -v_i, \quad w_g = -w_i, \quad T_g = 2T_w - T_i, \quad p_g = p_i \quad (2.53)$$

2.3.2 Initial conditions for turbulent flow

To initialize the flow field in the case of a wall-bounded turbulent flow, one can use the so-called Klein method (M. Klein & Janicka 2003). This method generates an artificial turbulent flow based on first- and second-order statistics. A set of autocorrelated filters is used to smooth a random field which is then projected on the Reynolds stress tensor to calculate the fluctuating velocity field. Temperature (Eq. 2.54) and pressure (Eq. 2.55) fields are then computed from the fluctuating velocity field using the strong Reynolds analogy formulation (SRA) (Touber & Sandham 2009).

$$\frac{T'}{\langle T \rangle} = (\gamma - 1) Ma^2 \frac{u'}{\langle u \rangle}, \quad (2.54)$$

$$\frac{\rho'}{\langle \rho \rangle} = -\frac{T'}{\langle T \rangle}. \quad (2.55)$$

The one-dimensional filter (Eq. 2.56) uses a Gaussian function similar to the auto-correlation function in order to reconstruct an isotropic turbulent field. The use of the exponential auto-correlation function leads to a spectrum energy-decay rate of -2 instead of the expected -5/3 law.

For each direction, the filter sizes are calculated by $N_{F_i} = 2\Lambda_i/\Delta x_i$ (Touber & Sandham 2009), where Λ_i is the integral length scale and Δx_i the grid spacing. The three-dimensional filter is obtained by the convolution of three one-dimensional filters (Eq. 2.57).

$$b_k = \frac{\exp\left(-\frac{\pi}{2} \frac{k^2}{n^2}\right)}{\sqrt{\sum_{j=-N}^N \exp\left(-\frac{\pi}{2} \frac{k^2}{n^2}\right)^2}}, \quad (2.56)$$

$$b_{ijk} = b_i b_j b_k. \quad (2.57)$$

The spatially correlated function is computed by:

$$\mathcal{U}_i(x, y, z) = \left(\sum_{i'=-N_{F_x}}^{N_{F_x}} \sum_{j'=-N_{F_y}}^{N_{F_y}} \sum_{k'=-N_{F_z}}^{N_{F_z}} b_{ijk}(i', j', k') \mathcal{R}_i(x + i'\Delta x, y + j'\Delta y, z + k'\Delta z) \right), \quad (2.58)$$

where \mathcal{R}_i is the random fields for each i -direction.

The velocity field is then reconstructed by:

$$u_i = \langle u_i \rangle + \sum_{j=1}^3 a_{ij} \mathcal{U}_j, \quad (2.59)$$

$$a_{ij} = \begin{pmatrix} \sqrt{R_{11}} & 0 & 0 \\ R_{21}/a_{11} & \sqrt{R_{22} - a_{21}^2} & 0 \\ R_{31}/a_{11} & (R_{22} - a_{21} a_{31})/a_{22} & \sqrt{R_{33} - a_{31}^2 - a_{32}^2} \end{pmatrix}, \quad (2.60)$$

where $R_{ij} = \langle u'_i u'_j \rangle$ is the Reynolds stress tensor given from previous simulations or from experimental results.

2.3.3 Inlet synthetic turbulence injection

M. Klein & Janicka (2003) have proposed an algorithm for generating inflow data from their spatial method (sec. 2.3.2). They generate a new three-dimensional spatially correlated flow field at each time step with the method described in section 2.3.2. At each time step, they discard the first y - z plane and shift the whole random data field in x -direction with $\mathcal{R}_i(x, y, z) := \mathcal{R}_i(x + \Delta x, y, z)$. This approach is easily adaptable to the code but creates uncorrelated time signal at the inlet of the domain.

Following the work of Klein, Xie & Castro (2008) have implemented an inflow boundary condition that uses an autocorrelation function in space and time. The time correlation is created by an exponential function based on two weight factors. They also improved the efficiency of the previous method of M. Klein & Janicka (2003) by generating only one set of two-dimensional random data field. The spatially correlated function is then computed by:

$$\mathcal{U}_i(y, z) = \left(\sum_{i'=-N_{Fx}}^{N_{Fx}} \sum_{j'=-N_{Fy}}^{N_{Fy}} \sum_{k'=-N_{Fz}}^{N_{Fz}} b_{ijk}(i', j', k') \mathcal{R}_i(i' \Delta x, y + j' \Delta y, z + k' \Delta z) \right). \quad (2.61)$$

The time correlation is applied on the random data \mathcal{R} using:

$$\mathcal{R}(t + \Delta t, y, z) = \mathcal{R}(t, y, z) \exp\left(-\frac{\pi \Delta t}{2\tau}\right) + \mathcal{R}^*(y, z) \sqrt{1 - \exp\left(-\frac{\pi \Delta t}{\tau}\right)}, \quad (2.62)$$

where $\mathcal{R}^*(y, z)$ is a new set of random data, $\tau = t_L / \langle u \rangle$ the Lagrangian timescale, t_L the integral time scale and $\langle u \rangle$ the local averaged velocity.

Equation 2.62 satisfies a time correlation function of exponential form with a variance equal to unity. The time correlation generates a spectrum energy-decay rate of -2 instead of the expected -5/3 law (Touber & Sandham 2009).

In order to avoid repetitive pattern of the inflow data, the random numbers are generated by the Mersenne Twister generator (Matsumoto & Nishimura 1998) using an uniformly-distributed function. It has a very long period of 2^{19937} that assure a fast generation of high-quality pseudorandom integers. The method have been parallelized

for MPI by controlling seed generation.

2.3.4 Perturbation model

In section 4.1, we enforce the transition of an incoming laminar boundary layer using a perturbation model proposed by Rai et al. (1995) and Pirozzoli et al. (2004). To induce laminar-to-turbulent flow transition, the wall-normal velocity component at the wall emulates a region of blowing and suction following:

$$v(x, z, t) = A u_\infty f(x) g(z) h(t), \quad x_a < x < x_b, \quad (2.63)$$

where A is the amplitude of the fluctuation applied in the range $x \in [x_a, x_b]$.

The functions f and g are spatial correlation functions in streamwise and spanwise direction, respectively. h is a temporal function expressed as a sum of multiple sine function with a randomized phase offset.

$$f(x) = 4 \sin\left(\theta(1 - \cos(\theta))/\sqrt{27}\right), \quad (2.64)$$

$$g(z) = \sum_{l=1}^{l_{max}} Z_l \sin(2\pi l(z/L_z + \phi_l)), \quad (2.65)$$

$$h(t) = \sum_{m=1}^{m_{max}} T_m \sin(\beta t + 2\pi \phi_m), \quad (2.66)$$

where ϕ_l and ϕ_m are random numbers, β the fundamental frequency of the disturbance, L_z the spanwise length, $\theta = 2\pi(x - x_a)/(x_b - x_a)$ and Z_l and T_m are computed by solving $\sum_{l=1}^{l_{max}} Z_l = 1$, $Z_l = 1.25 Z_{l+1}$ and $\sum_{m=1}^{m_{max}} T_m = 1$, $T_m = 1.25 T_{m+1}$, respectively.

We have found that, by using the model presented in section 4.1, the amplitude of the fluctuations was modified depending on the random number generated. Mathematically, one can find that the rms of equations 2.65 and 2.66 are not equal to one ($h_{rms} \neq 1$ and $g_{rms} \neq 1$) and change depending on ϕ_l and ϕ_m .

To normalize this model, we have added a function to g and h so that their respective rms are equal to one. This modified model has been used in section 4.2.

$$g_{\text{mod}}(z) = \frac{g(z)}{g_{rms}}, \quad (2.67)$$

$$h_{\text{mod}}(t) = \frac{h(t)}{h_{rms}}, \quad (2.68)$$

where $\varphi_{rms} = \sqrt{\langle \varphi' \varphi' \rangle}$ is computed at the initialization of the code.

2.4 Domain decomposition method

2.4.1 The singularity issue

The study of shock unsteadiness in over-expanded cylindrical nozzle flow deals with cylindrical coordinates. To perform simulations in cylindrical coordinates, one can use a purely cylindrical code or a generalized curvilinear code. The advantage of the generalized curvilinear coordinates is that the grid can be distorted in the streamwise direction and fit the wall along the θ -direction. Nozzle flow simulation handles divergent and convergent region where the grid changes in the streamwise direction.

On the other hand, the fully cylindrical coordinates create a singularity at the axis centerline. The singularity arises from the terms $1/r^n$ in the cylindrical Navier–Stokes equations, where $n = 1, 2$ and r is the radial direction. For example, the Laplace operator in cylindrical coordinates is:

$$\nabla^2 \equiv \frac{\partial^2}{\partial r^2} + \frac{1}{r} \frac{\partial}{\partial r} + \frac{1}{r^2} \frac{\partial^2}{\partial \theta^2} + \frac{\partial^2}{\partial z^2}. \quad (2.69)$$

The terms using the first radial derivative and the second polar derivative are both singular at $r = 0$.

The other drawback of fully cylindrical coordinates is the time-step reduction at the axis. The volume of the cells at the axis are generally smaller than the cell along the circumference because of the small $r \Delta \theta$ value near the axis.

A validation case consists in the simulation of a turbulent pipe flow with the generalized curvilinear code (sec. 3.5). The results with the fully cylindrical coordinates are not accurate compared to the literature. To avoid the singularity issue, several numerical methods have been proposed (Constantinescu & Lele 2002, Verzicco & Orlandi 1996, Mohseni & Colonius 2000). Many of these methods use pseudo spectral finite-volume code. These methods give accurate results but require the development of pseudo spectral methods. An alternative approach is to use a domain decomposition method.

The basic idea behind the domain decomposition (DD) methods is to split a boundary value problem, defined on a domain Ω , into smaller boundary value problems defined on subdomains Ω_i , where $\cup \Omega_i = \Omega$. The advantage of DD method is its adaptability on the meshing of complex geometries. The domain can be split up into several subdomains using different grids in order to avoid strongly deformed grid cells.

The connection between the subdomains depends only on the boundary conditions. The subdomains overlap each others and interpolations are performed on the overlapping region to feed the boundary conditions.

2.4.2 2D domain decomposition method

For the nozzle simulations, a custom DD method has been developed. The domain Ω is a cylinder grid containing two overlapping meshes Ω_1 and Ω_2 , representing a Cartesian grid and a hollow cylinder grid, respectively. Figure 2.6 shows the subdomains. The three-dimensional mesh is created so that the cells in the streamwise direction overlap at each i indice. The domain decomposition method is then reduced to two dimensions, $r - \theta$. With this method, the mesh can be curved in the streamwise direction but exclusively in the same way for both subdomains.

The internal Cartesian grid Ω_1 does not use the cylindrical coordinates and thus, the singularity issue and the small volume cells at the axis do not appear with this method.

The code works independently for each subdomains using their own MPI communicators. The method uses an initialization phase to optimize the computation (algorithm 1). At each iteration (RK-step), the overlapping ghost cells (boundary condition) are updated by an interpolation from the other subdomain following algorithm 2. Since the method is reduced to 2D, a simple bi-linear interpolation is used to interpolate the values.

The physical size of the internal Cartesian subdomain must be in a range $R^{\Omega_1}/R(x) \in [0, \sqrt{2}/2]$ to actually work, where $\Omega_1 = \{(y, z) \in [-L_y^{\Omega_1}, L_y^{\Omega_1}] \times [-L_z^{\Omega_1}, L_z^{\Omega_1}]\}$. We chose the value of $R^{\Omega_1}/R(x) = 0.6$ in order to be away from the wall and to avoid interpolation in the boundary layer where the resolution of the internal grid is not sufficient to capture the inner layer of the boundary layer ($\Delta R^{+\Omega_1} \gg \Delta R^{+\Omega_2}$). The internal radius of the hollow cylinder $R_i^{\Omega_2}$ is generated so that the two subdomains overlap ($R_i^{\Omega_2} < R^{\Omega_1}$). One cell size is subtracted to the internal radius to avoid cross-interpolation. The internal radius of the hollow cylinder is $R_i^{\Omega_2} = R^{\Omega_1} - \Delta y^{\Omega_1}$. The hollow cylinder is bounded by $\Omega_2 = \{(r, \theta) \in [R_i^{\Omega_2}, R(x)] \times [0, 2\pi]\}$. Figures 2.7, 2.8 and 2.9 explain the process of initialization and interpolation from algorithm 1 and 2.

The turbulent pipe flow at $Re_\tau = 220$ has been used to validate the domain decomposition method (Sec. 3.5.2).

Algorithm 1 DD method subroutine

- 1: **procedure** INITIALIZATION
 - 2: Split MPI_COMM_WORLD communicator for each subdomains
 - 3: Ω_1 *communicator* / Ω_2 *communicator*
 - 4: Generate Ω_1 grid / Generate Ω_2 grid
 - 5: Scan Ω_2 grid for overlapping cell / Scan Ω_1 grid for overlapping cell
 - 6: Save overlapping cell indices into an array for optimization
 - 7: Save MPI ranks
 - 8: Share to all the matrix of communication (MPI_AllGather)
-

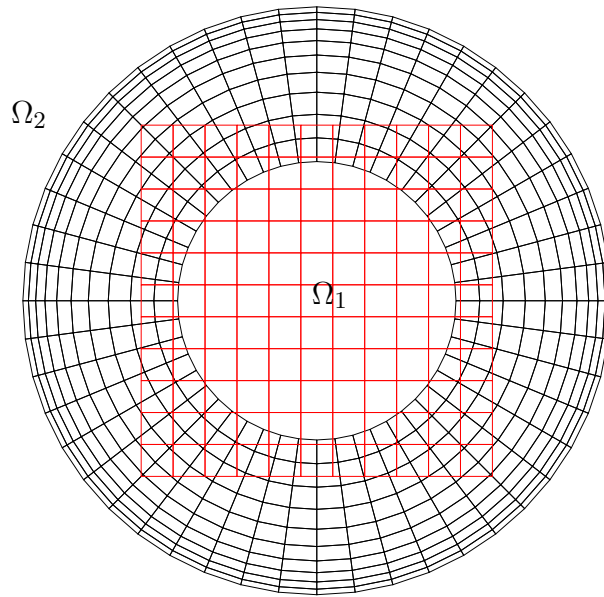


Figure 2.6: Representation of the domain decomposition method showing every 5th grid line.

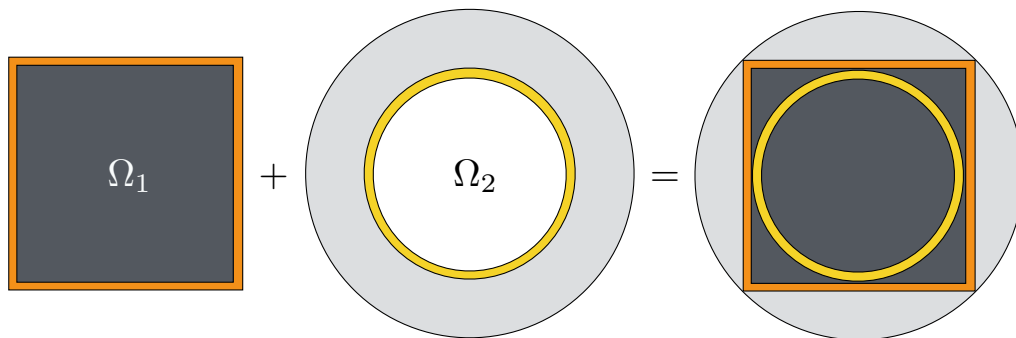


Figure 2.7: Global discretization of the DD method; *Orange*: overlapping ghost point from subdomain Ω_1 , *Yellow*: overlapping ghost point from subdomain Ω_2 .

Algorithm 2 DD method subroutine

- 1: **procedure** INTERPOLATION
 - 2: *Asynchronous Send/Recv to avoid deadlock state*
 - 3: **if** process contains overlapping cells from other process **then**
 - 4: Bi-linear interpolation of the primitive variables
 - 5: MPI_Send the array to the other subdomain
 - 6: **if** process contains overlapping boundary condition **then**
 - 7: MPI_Recv the interpolated values from the other subdomain
-

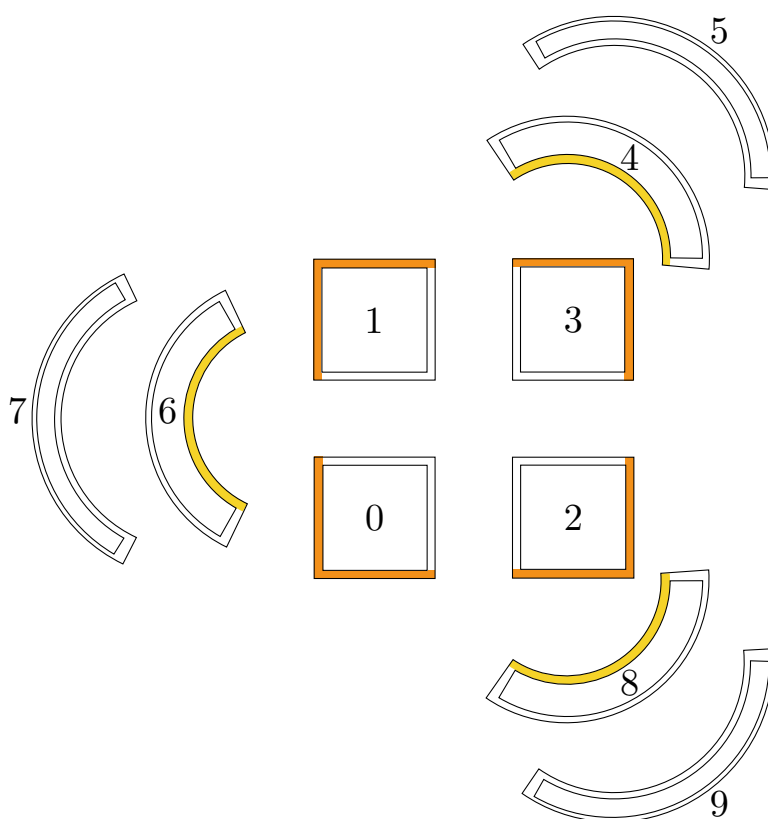


Figure 2.8: Example of MPI discretization of the DD method; *Orange*: overlapping ghost point from subdomain Ω_1 , *Yellow*: overlapping ghost point from subdomain Ω_2 .

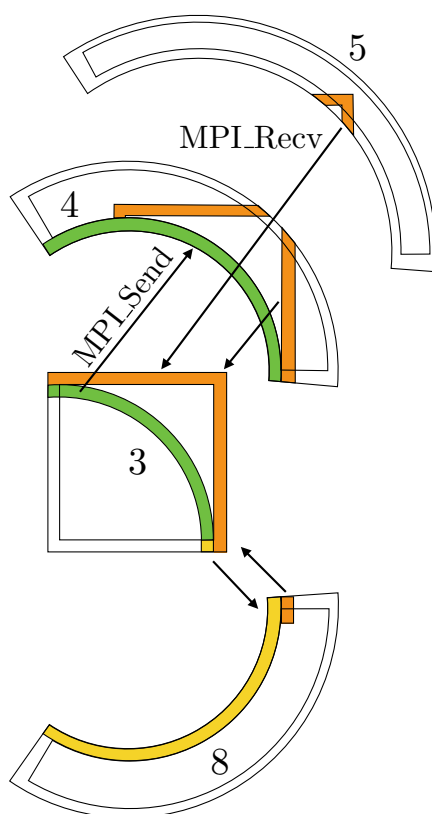


Figure 2.9: Example of *Send/Recv* request for the DD method. View from process 3.

3

Numerical verification and validation

This chapter is dedicated to the validation and verification of the newly developed code. The validation consists of simulating 2D and 3D test cases for the compressible Navier–Stokes equations. First, the simulation of a vortex advection is conducted to verify the correct implementation of the curvilinear equations (sec. 2.1.2) as well as the central scheme (sec. 2.2.1.1); Then, the simulation of a compressible flow over a circular cylinder is achieved in order to validate the WCNS scheme with non-orthogonal grid (sec. 2.2.1.1); Lastly, the simulation of the well-known Poiseuille flow is conducted in order to cross-check the implementation of the curvilinear equation for wall-bounded flow at constant viscosity.

Some of the validation cases have been compared against experimental results or previous numerical simulations; A simulation of a turbulent channel flow has been carried out to confirm the ability of the code to simulate turbulent flow, while a simulation of a pipe flow has also been made to validate the domain decomposition method implemented for cylindrical geometries (sec. 2.4).

3.1 Vortex advection

The first test case consists in the advection of a circular, homentropic, zero circulation vortex. This test is widely used in literature (Visbal & Gaitonde 2002, Kawai & Lele 2008). A curvilinear grid has been generated through the analytical function from Kawai & Lele (2008) (fig. 3.1):

$$x(\xi, \eta) = x_{min} + \frac{\xi}{N_\xi} L_x + A_\xi \sin\left(2\pi \frac{\eta}{N_\eta}\right), \quad (3.1)$$

$$y(\xi, \eta) = y_{min} + \frac{\eta}{N_\eta} L_y + A_\eta \sin\left(4\pi \frac{\xi}{N_\xi}\right), \quad (3.2)$$

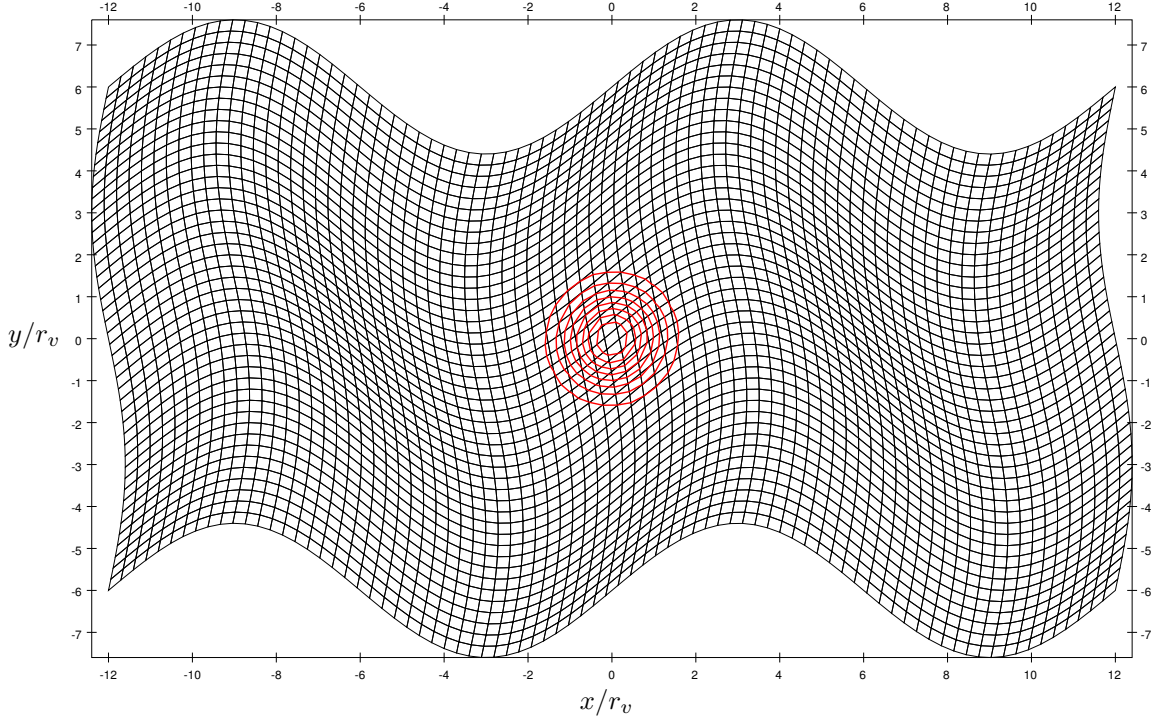


Figure 3.1: Grid of the vortex test case

where $x_{min} = -12r_v$, $L_x = 24r_v$, $y_{min} = -6r_v$, $A_\xi = 0.4r_v$ and $A_\eta = 1.6r_v$.

The vortex is initialized using the same parameters as Pirozzoli (2011b):

$$\frac{u(x, y)}{u_\infty} = 1 - \frac{M_v}{M_\infty} \frac{y - y_0}{r_v} \exp((1 - \hat{r}^2)/2), \quad (3.3)$$

$$\frac{v(x, y)}{u_\infty} = \frac{M_v}{M_\infty} \frac{x - x_0}{r_v} \exp((1 - \hat{r}^2)/2), \quad (3.4)$$

$$\frac{\rho(x, y)}{\rho_\infty} = \left(1 - \frac{\gamma - 1}{2} M_v^2 \exp(1 - \hat{r}^2)\right)^{1/(\gamma - 1)}, \quad (3.5)$$

$$\frac{p(x, y)}{p_\infty} = \left(1 - \frac{\gamma - 1}{2} M_v^2 \exp(1 - \hat{r}^2)\right)^{\gamma/(\gamma - 1)}, \quad (3.6)$$

where $\hat{r} = \sqrt{((x - x_0)^2 + (y - y_0)^2)}/r_v$, r_v is the radius of the vortex core, M_v the vortex Mach number and M_∞ the free-stream Mach number.

The number of grid points is set to $N_\xi = 81$ and $N_\eta = 45$. Periodic boundary condition is applied at left and right sides. The vortex and the free-stream Mach numbers are set to $M_v = 0.5$ and $M_\infty = 0.5$, respectively. This is equivalent to a strongly compressible vortex.

The simulations are run until $tu_\infty/r_v = 720M_v$ which corresponds to fifteen flow

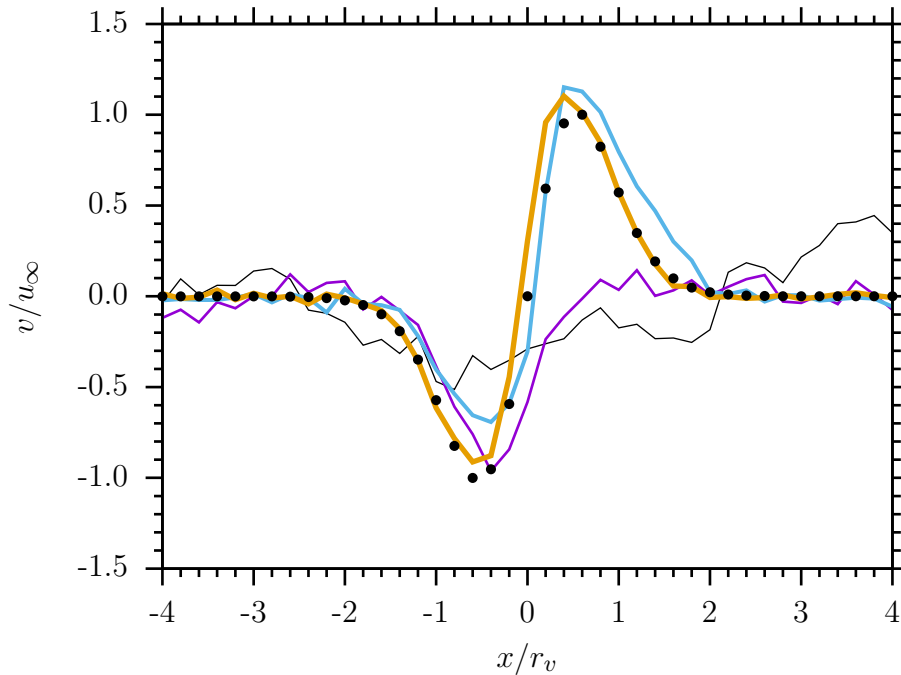


Figure 3.2: Comparison of centered schemes with different order of accuracy; —: 2th order, —: 4th order, —: 6th order, —: 8th order, ·: Exact solution.

through time. Figure 3.2 shows a comparison between different order of accuracy of the centered scheme presented in section 2.2.1. The numerical solutions for the 2th- and the 4th-order centered schemes exhibits an oscillatory behavior while 6th- and 8th-order centered schemes highlight better results.

Hybrid scheme has also been applied to this test case. Since the hybrid sensor was unable to activate the WENO scheme due to the smooth solution, the result was comparable to the centered solution. One can conclude that the implementation of the Euler equations in the code is properly done as observed by the accurate results from high-order schemes. For the next simulations, the 6th-order centred scheme will be used to discretize the convective terms, unless otherwise specified.

3.1.0.1 Cylindrical grid

The previous test case uses an orthogonal grid. In order to validate the implementation of the curvilinear terms, the advection of a zero circulation homentropic vortex is conducted. At the center, the skewness angle of the cells becomes critical and boundary conditions are difficult to apply. Periodicity along the circumference is not possible and thus, the zero-gradient boundary condition is applied along the circumference. Periodicity is used

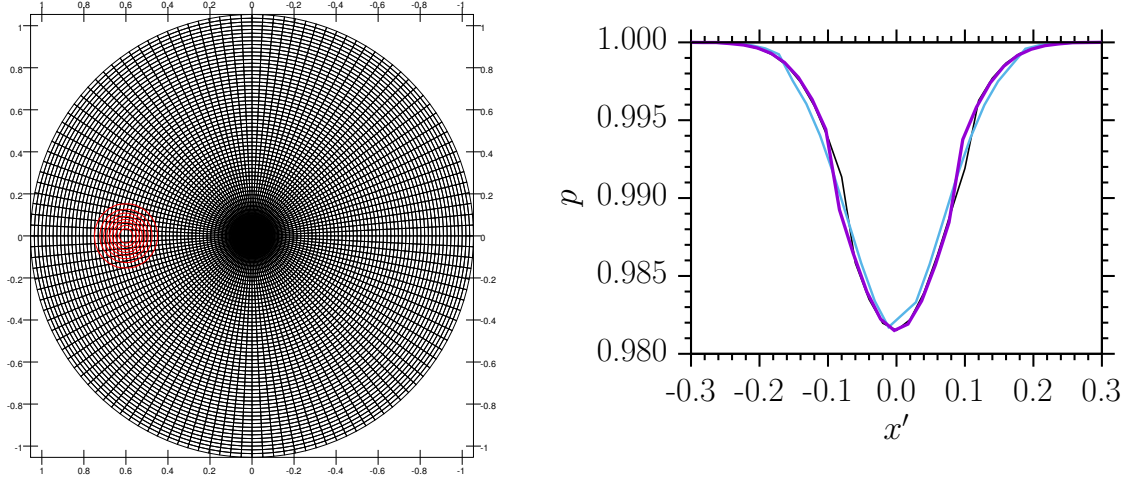


Figure 3.3: Grid of the cylindrical vortex test case (*left*) and shifted pressure distribution at different time step (*right*); $-$: $t^* = 0$, $-$: $t^* = 5.9$, $-$: $t^* = 11.8$.

in the θ -direction. The grid (Fig. 3.3) has been generated by:

$$x(\xi, \eta) = R \frac{\xi}{N_\xi} \cos(2\pi \frac{\eta}{N_\eta}), \quad (3.7)$$

$$y(\xi, \eta) = R \frac{\xi}{N_\xi} \sin(2\pi \frac{\eta}{N_\eta}), \quad (3.8)$$

where R is the radius of the external BC.

The flow is initialized with the same parameters from equations 3.3, 3.4, 3.5 and 3.6 with $x_0 = -0.6R$ and $y_0 = 0$. The vortex is advected from left to right passing through the center of the mesh (fig. 3.4).

The pressure field distribution at different time step $t^* = tu_\infty/r_v$ is shown in figure 3.3. The x-axis is shifted for the sake of comparison, where $x' = x - tu_\infty + 0.6$. The final solution shows good accuracy compared to the initial flow field. The property of the singularity at the axis in finite-differences solver does not lead to a spurious solution of the flow as it would do in finite-volumes code due to the infinite flux at the axis. Nonetheless, the singularity can cause spurious oscillations due to the small volume at the center. One can observe that the second solution ($t^* = 5.9$) from figure 3.3 is slightly different from the initial and final solutions due to the highly irregular mesh at the center. Thus, a particular axis treatment near the center in finite-differences formulation is needed (sec. 2.4).

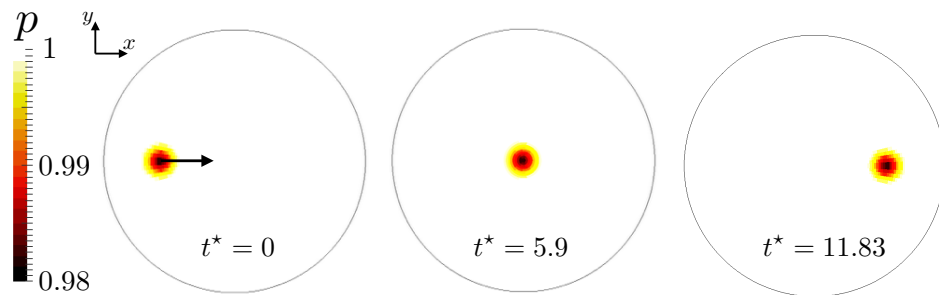


Figure 3.4: Pressure field contour at different time step.

3.2 Compressible flow over a circular cylinder

The description of this test case can be found in Burbeau & Sagaut (2002). A circular cylinder of radius R is placed in a viscous compressible flow at Mach 2 and $Re = 100$. A detached curved shock is formed ahead of this cylinder, while a viscous wake is established downstream. This test case can validate the implementation of the 2D viscous terms in generalized curvilinear coordinates. Burbeau & Sagaut (2002) used a bidimensional unstructured meshes with high-order discontinuous Galerkin method. The curvilinear grid (Fig. 3.5) used for this simulation has been generated by:

$$x(\xi, \eta) = \left(R + (R_a - R) \left(1 + \tanh(r_v(\xi/N_\xi - 1))/\tanh(r_v) \right) \right) \cos\left(2\pi \frac{\eta}{N_\eta}\right), \quad (3.9)$$

$$y(\xi, \eta) = \left(R + (R_a - R) \left(1 + \tanh(r_v(\xi/N_\xi - 1))/\tanh(r_v) \right) \right) \sin\left(2\pi \frac{\eta}{N_\eta}\right), \quad (3.10)$$

where $R_a = 25R$ is the external radius and $r_v = 3.0$ the stretching parameter.

A stretching functions has been used along r-direction to account for the viscous effect along the cylinder wall. The number of grid points is set to $N_\xi = 128$ and $N_\eta = 256$, giving 32,768 cells. The boundary layer is highly resolved in our case compared to the unstructured mesh of Burbeau ($N = 7,478$). The WENO-like scheme (WCNS) is used to account for the presence of shock waves. Periodic boundary condition is used in the θ -direction while adiabatic no-slip condition is applied along the external cylinder.

The obtained results are quite comparable to Burbeau & Sagaut (2002). The bow shock is well captured and gives the same angle of deflection. The solution of Burbeau & Sagaut (2002) was made to show the robustness of their Galerking methods applied to unstructured meshes. Figure 3.6 shows the Mach field contour extracted at a steady state. Our code solution seems more accurate than Burbeau's solution. The boundary layer and the shock seem to be more resolved. The solution of Burbeau & Sagaut (2002) has been simulated on an unstructured mesh while we have used a body-fitted mesh. The number of cell used in the paper of Burbeau & Sagaut (2002) is lower than the one used

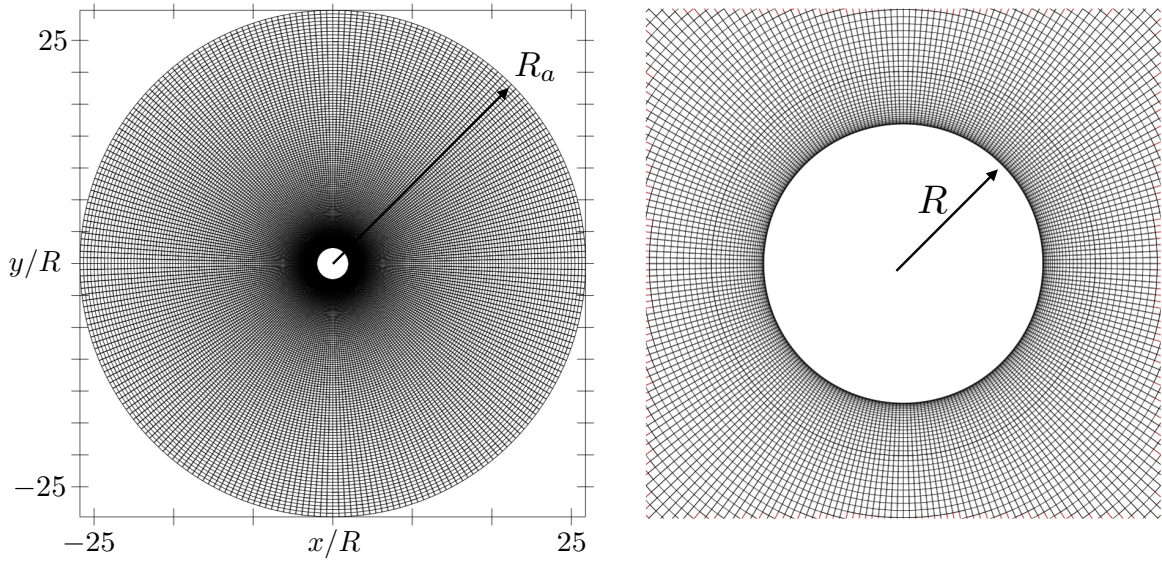


Figure 3.5: Grid of the compressible flow over a circular cylinder test case

in our structured mesh which can be the source of those differences.

3.3 Poiseuille flow

The Poiseuille flow from Schlichting & Gersten (2003) is used as a test case for further validation. The analytical solution is used as a reference solution. The laminar fully-developed boundary layer solution in two-dimensional flow is obtained for the case of steady flow in a channel with two parallel flat walls where the pressure gradient is equal to:

$$\frac{dp}{dx} = \mu \frac{d^2 u}{dy^2}. \quad (3.11)$$

In our simulation, the pressure gradient is imposed by an external force, $F = dp/dx$. Using the boundary condition, $u = 0$, one can find the following velocity profile:

$$u(y) = -\frac{1}{2\mu} \frac{dp}{dx} (h^2 - y^2) = -\frac{F}{2\mu} (h^2 - y^2), \quad (3.12)$$

where $L_y = 2h$ is the height of the channel.

Both velocity and temperature profiles are summarized as follows:

$$u(y) = u_m \left(1 - \frac{y^2}{h^2}\right), \quad (3.13)$$

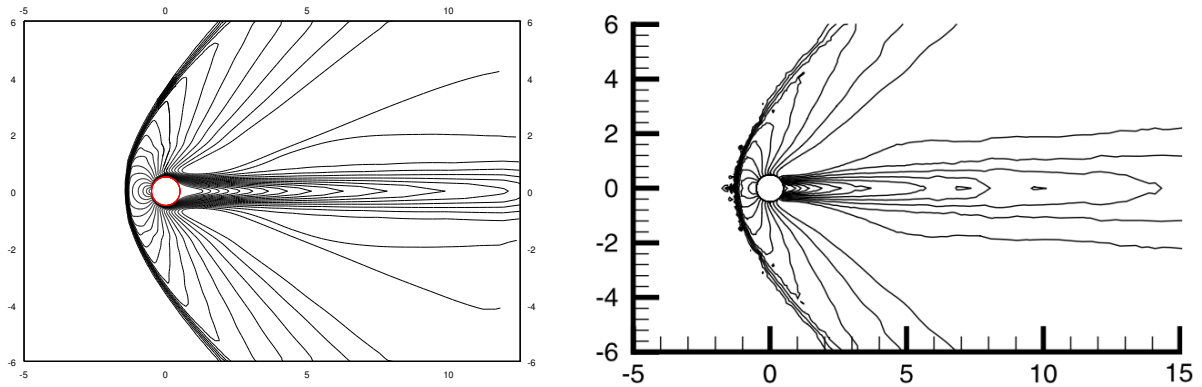


Figure 3.6: Mach number contours; *Left*: current simulation, *Right*: Burbeau & Sagaut (2002)

$$T(y) = T_w + (T_m - T_w) \left(1 - \frac{y^4}{h^4}\right), \quad (3.14)$$

where $u_m = -\frac{F h^2}{2\mu}$ denotes the velocity at the centre of the channel flow and $T_m - T_w = \frac{\mu u_m^2}{3\lambda}$ is the rise of temperature at the centre of the channel.

In order to activate the curvilinear terms of the code, two meshes are computed (Fig. 3.7). Mesh 1 is computed in the Cartesian coordinates and mesh 2 is inclined by an angle α following equations 3.15 and 3.16. The number of grid points is set to $N_\xi = 20$ and $N_\eta = 128$. The streamwise dimension is not important in this test case since the solutions are fully-developed (one dimensional). Periodic boundary condition and isothermal no-slip condition are applied in the streamwise and spanwise direction, respectively.

$$x(\xi, \eta) = \cos(\alpha)(\xi/N_\xi L_x - \eta/N_\eta 2h), \quad (3.15)$$

$$y(\xi, \eta) = \sin(\alpha)(\xi/N_\xi L_x + \eta/N_\eta 2h). \quad (3.16)$$

The flow is initialized with a uniform flow field at a velocity u_m and a temperature T_w . The results from figure 3.8 are showing excellent agreement between the current simulation and the analytical solution in terms of both velocity and temperature fields.

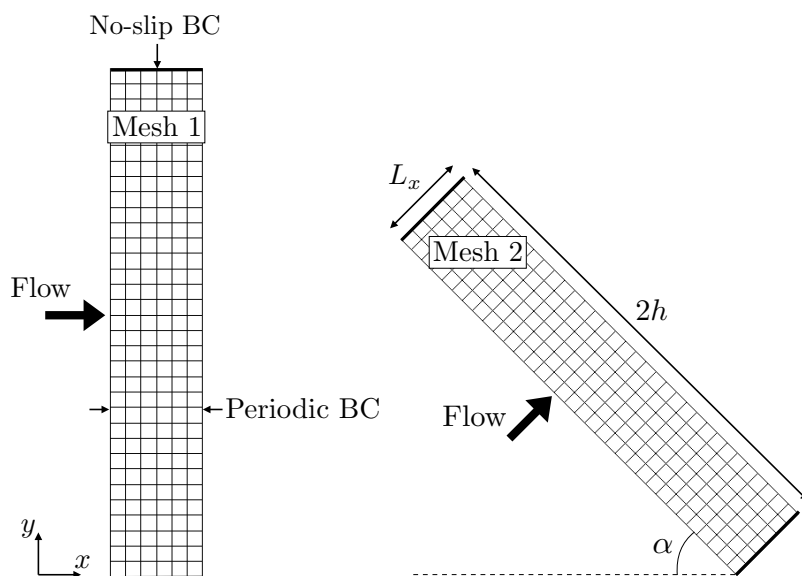


Figure 3.7: Grid representation for Mesh 1 (*left*) and Mesh 2 (*right*) showing every 4th grid-line

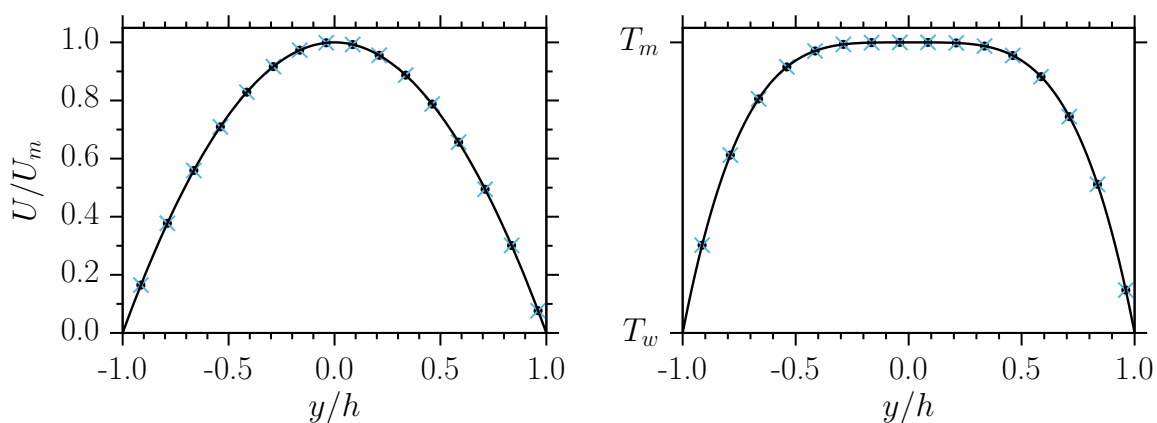


Figure 3.8: Streamwise velocity solution (*left*) and temperature solution (*right*) along the spanwise direction; —: Poiseuille analytical solution, •: Mesh 1, ×: Mesh 2.

3.4 Turbulent channel flow at $Re_\tau = 220$

A turbulent channel flow at a friction Reynolds number of 220 is performed to complete the full validation and verification of the code.

Direct Numerical Simulation of turbulent channel flow between isothermal walls is performed. It is one of the simplest test case of turbulent flow due to the simplicity of the geometry and the boundary conditions. Turbulent statistics can be explored to study near-wall turbulence behavior, such as first-order statistic ($\phi' = \phi - \langle \phi \rangle$) or second-order statistic ($\langle \phi'_i \phi'_j \rangle$).

3.4.0.1 Test case description

As in H. Foysi & Friedrich (2004), the flow is periodic in both x - (streamwise) and z -directions (spanwise). Figure 3.9 shows the actual configuration and table 3.1 summarizes the grid and geometry parameters.

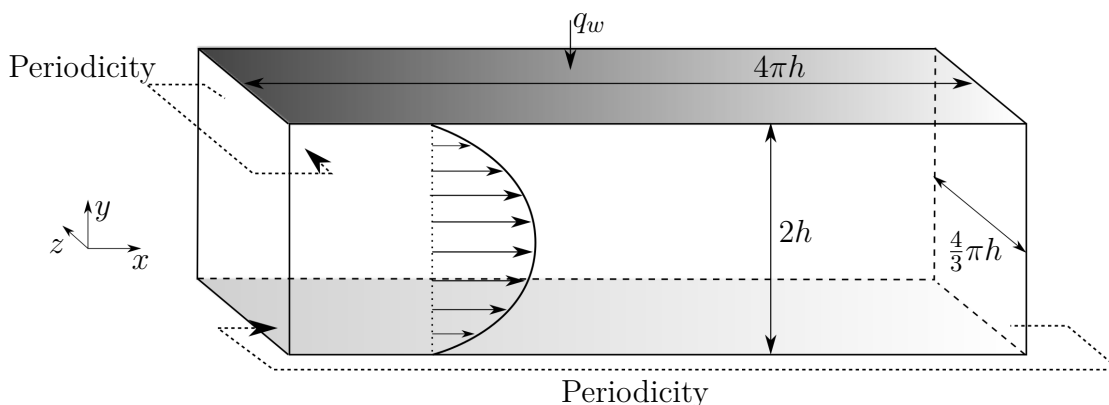


Figure 3.9: Configuration of the channel flow.

L_x	L_y	L_z	N_x	N_y	N_z	h
$4\pi h$	$2h$	$4/3\pi h$	192	150	128	6.84355 mm

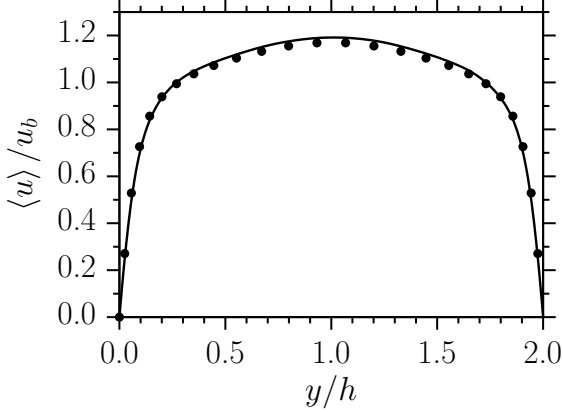
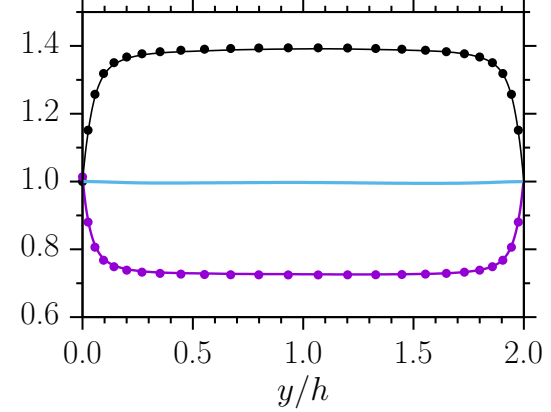
Table 3.1: Channel flow domain properties

This simulation uses a centred 6th-order scheme for convective terms and the 4th-order scheme for the viscous terms. The grid is regularly spaced in the x - and z -direction and the wall-normal direction grid is stretched in order to capture the viscous sublayer. A grid sensitivity study has been conducted by H. Foysi & Friedrich (2004), resulting in the parameters shown in table 3.1. Flow properties are summarized in table 3.2.

The fully-developed boundary layer is supersonic and the Mach number is set to 1.5. The initial averaged velocity field follows a fully-developed profile extracted from H. Foysi

Re	Re_τ	u_τ	M	u_b	T_w
3000	220	35 m/s	1.5	680 m/s	500 K

Table 3.2: Channel flow properties

Figure 3.10: Averaged velocity profile along the wall-normal direction; \bullet : H. Foysi & Friedrich (2004).Figure 3.11: Averaged temperature (—), pressure (—) and density (—) profile along the wall-normal direction; \bullet : H. Foysi & Friedrich (2004).

& Friedrich (2004). The Klein method (sec. 2.3.2) has been used to initiate the turbulent fluctuations. The Reynolds number and averaged parameters are calculated as:

$$\rho_m = \frac{1}{h} \int_0^h \rho dy, \quad u_b = \frac{1}{\rho_m h} \int_0^h \rho u dy, \quad Re = \frac{\rho u_b h}{\mu} \quad \text{and} \quad Re_\tau = \frac{\rho_w u_\tau h}{\mu_w}.$$

Since the flow is periodic in the streamwise direction, the pressure drops because of the wall friction. To account for the pressure drop, additional terms in the momentum and energy equations are used as in (H. Foysi & Friedrich 2004, Taieb 2010). These terms are applied to counteract the friction forces acting along the wall. Equation 3.17 shows the formulation of this term added to the [Momentum](#) and [Energy](#) equation.

$$f_x = \frac{\left(\langle \sigma_{12} \rangle \Big|_{y=0} - \langle \sigma_{12} \rangle \Big|_{y=2h} \right)}{2h\rho_m} = \frac{\tau_w}{h\rho_m}. \quad (3.17)$$

3.4.0.2 Statistical results

All the statistics have been averaged over approximately 150 non-dimensional time unit where $t^* = t u_b / L_x$. Several probes are located along the spanwise direction (y) to collect data for scatter plots.

Figure 3.10 shows the averaged velocity profile compared to the DNS of H. Foysi & Friedrich (2004). Temperature, pressure and density profiles are shown in figure 3.11. As expected, the pressure is constant along y -direction.

The law of the wall is represented in figure 3.12 with normalized velocity based on

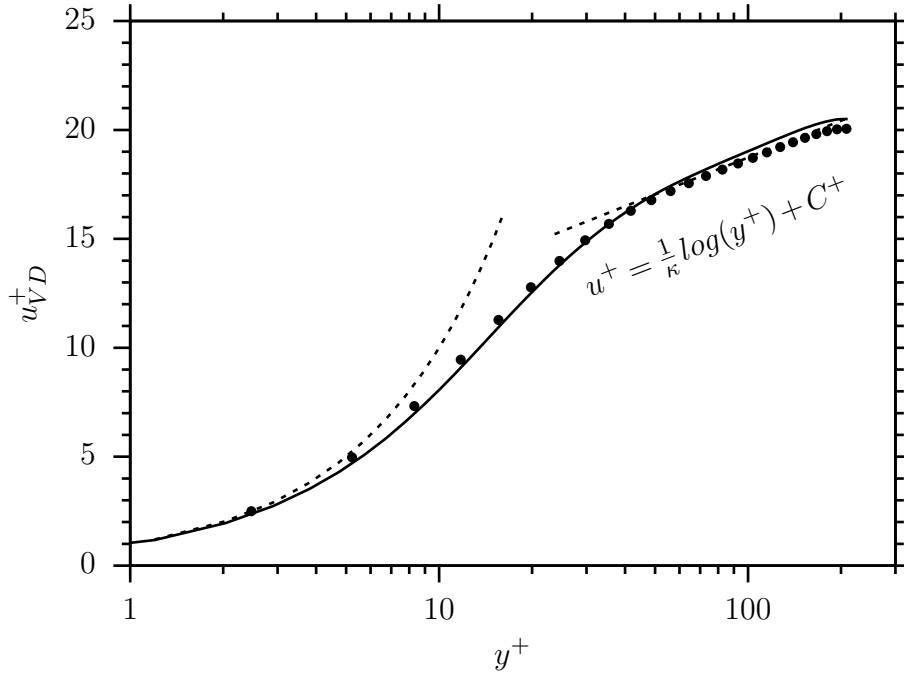


Figure 3.12: Van Driest velocity profile along the wall-normal direction; \bullet : H. Foysi & Friedrich (2004), $--$: viscous sublayer and logarithmic law.

Van-Driest formulation (eq. 3.19). The wall unit normalization is based on local wall quantities. The wall unit length y^+ is given by:

$$y^+ = \frac{\rho_w u_\tau y}{\mu_w}, \quad (3.18)$$

where $u_\tau = \sqrt{\tau_w/\rho_w}$ is the friction velocity.

A semi-local wall normalization, y^* , can also be used which depends on the local averaged properties (eq. 3.20). Several other scaling laws have been made to normalize as much as possible the law of the wall for compressible flow such as the density normalization used by H. Foysi & Friedrich (2004).

$$u_{VD}^+ = \int_0^{u^+} \left(\frac{\rho}{\rho_w} \right) du^+ \quad (3.19)$$

$$y^* = \frac{1}{\langle \nu \rangle} \sqrt{\frac{\tau_w}{\langle \rho \rangle}} \quad (3.20)$$

Figure 3.13 shows contour of different instantaneous fields after 150 non-dimensional time unit. The coherent structures of turbulence are highlighted.

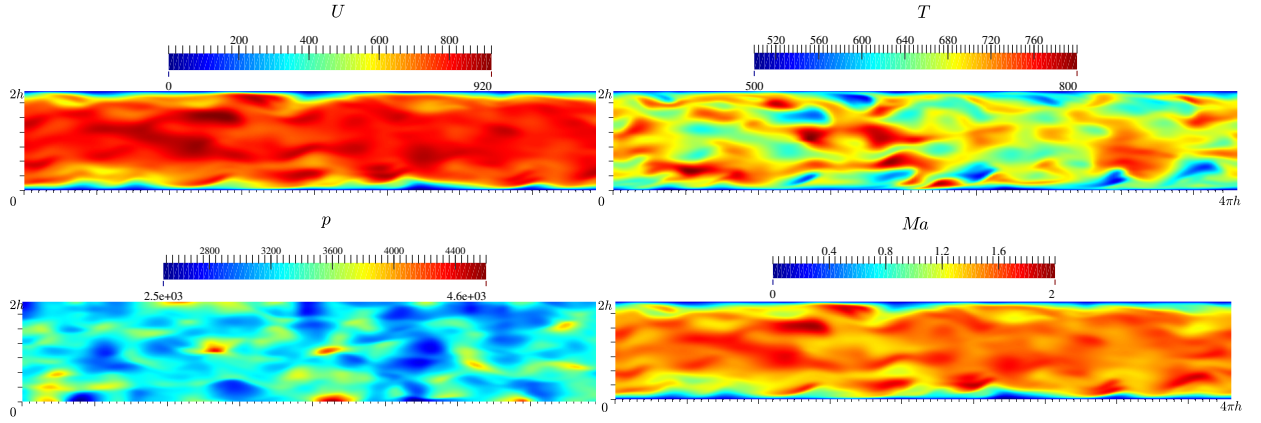


Figure 3.13: Instantaneous contours in the x - y plane at $z = L_z/2$; *Top left*: Streamwise velocity, *Top right*: Temperature, *Bottom left*: Pressure, *Bottom right*: Mach number.

3.4.0.3 Scatter plots

In 1962, Morkovin studied the correlations between different fluctuating quantities (Morkovin 1962). These correlations are known as SRA for 'Strong Reynolds Analogy'. Figure 3.14 shows the scatter plots from $t^* \approx 0$ to $t^* \approx 150$ at different y^+ coordinates.

At $y^+ \sim 10$, both temperature and density fluctuations are correlated with the streamwise velocity fluctuations. For $y^+ \sim 1$, fluctuations are still correlated but the slope is reduced accordingly to equation 3.21. On the other hand, at the centerline of the channel, the fluctuations are independent of each other and the SRA equations are no longer valid in the outer layer. P. Huang & Bradshaw (1995) have proposed a new equation using the total temperature to improve the correlation when the isothermal boundary condition are used:

$$\frac{T'}{\langle T \rangle} \approx \left[\frac{1}{Pr_t \left(\frac{\partial \langle T_0 \rangle}{\partial \langle T \rangle} - 1 \right)} \right] (\gamma - 1) Ma^2 \frac{u'}{\langle u \rangle}. \quad (3.21)$$

3.4.0.4 Turbulence structure

G.N. Coleman & Moser (1995) have studied the 'streaks' structure for isothermal channel flow. These streaks represent the vortex motion happening along the wall. Figure 3.15 shows the fluctuating velocity field at different position in the wall-normal direction. Those streaks, predicted by G.N. Coleman & Moser (1995), can be seen in the buffer layer of the boundary layer, where the viscous sublayer is connected to the log-law layer.

At $y^+ \sim 10$, the velocity fluctuations are maximum (fig. 3.17) and the streaks are clearly visible. Vortices are convected by the flow, creating the streak motions. Figure 3.16 shows the process of streaks structure. The red values of figure 3.15 represent the 'ejection' process and the blue one, the 'sweep' process. In the laminar sublayer ($y^+ < 5$), the viscous effect is dominant compared to the convection ($Re < 1$) and thus, the flow is

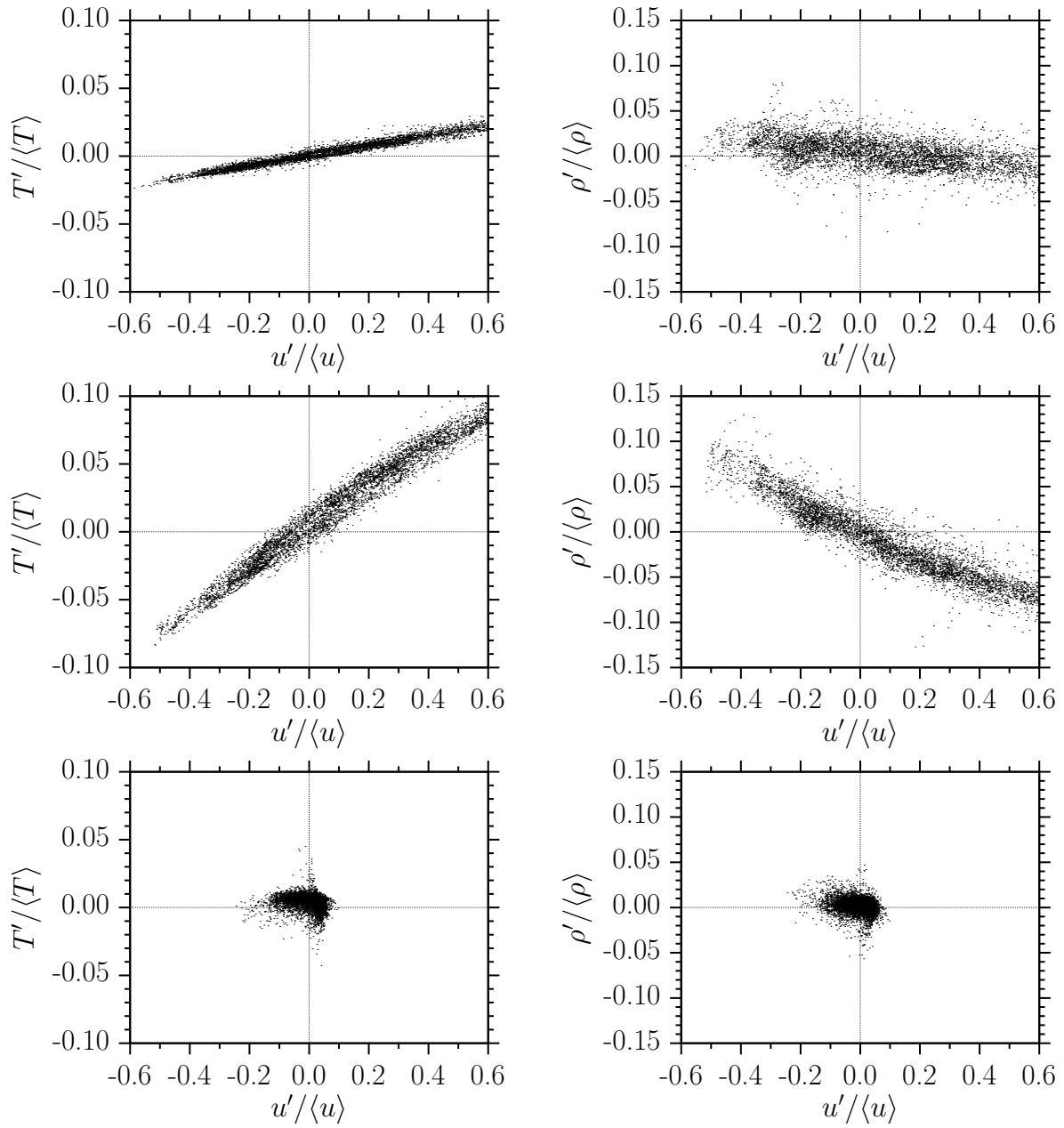


Figure 3.14: Scatter plots of different fluctuating quantities at different y^+ . *Left*: Temperature fluctuation; *Right*: Density fluctuation, *Top*: $y^+ \sim 1$, *Middle*: $y^+ \sim 10$, *Bottom*: $y^+ \sim 200$.

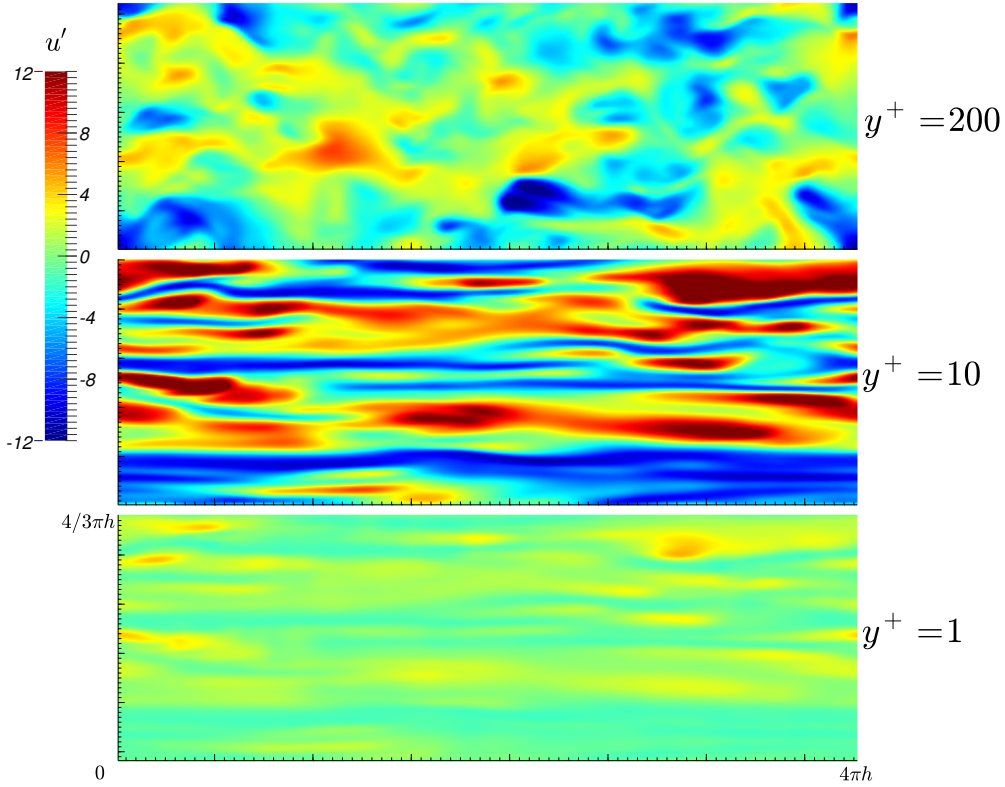


Figure 3.15: Instantaneous contours of the fluctuating streamwise velocity in x - z plane at $t^* \approx 150$ for different y^+

dominated by the viscosity, creating a vorticity component in the velocity field. In the streamwise direction, the flow is separated into two regions: a low speed region where $\partial u'/\partial y > 0$ and a high speed region where $\partial u'/\partial y < 0$. The 'streaks' can be seen as a rolling motion where particles are ejected from the viscous sublayer to the outer layers in the low speed region and are swept from the outer layer to the high speed region.

Another way to characterize the streaks is the Q-criterion or the vorticity. The latter represents the spinning motion of a fluid $\vec{\omega} = \vec{\nabla} \times \vec{u}$. The Q-criterion is commonly used to visualize the vortex streaks.

$$Q = \frac{1}{2} (\Omega_{ij} \Omega_{ij} - S_{ij} S_{ij}) \quad (3.22)$$

The Reynolds stress along the wall-normal direction is plotted in figure 3.17. It shows a good agreement of our DNS with the results of H. Foyi & Friedrich (2004), which gives confidence on our newly developed code.

3.5 DNS of a turbulent pipe flow at $Re_\tau = 220$

In this section, a comparison has been made between channel and pipe flows at similar friction Reynolds number to understand the influence of the geometry on the turbulent

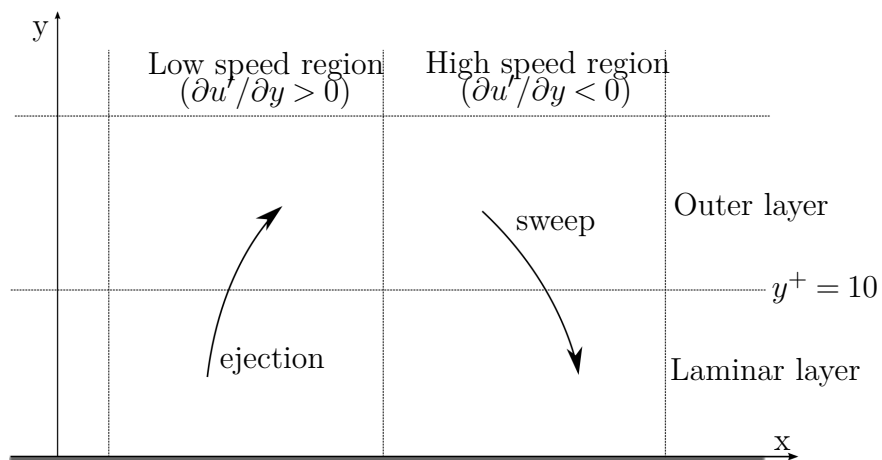
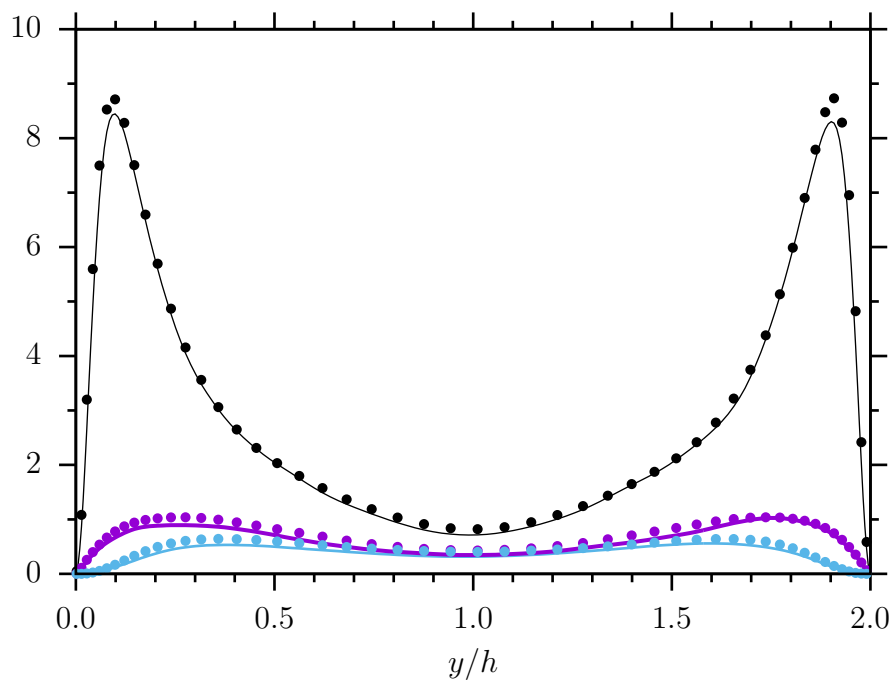


Figure 3.16: Outer/inter process interaction near the wall

Figure 3.17: Reynolds stress tensor along y -direction along the wall-normal direction; $-$: $\langle \rho \widetilde{u''u''} \rangle / \tau_w$, $-$: $\langle \rho \widetilde{v''v''} \rangle / \tau_w$, $-$: $\langle \rho \widetilde{w''w''} \rangle / \tau_w$, \bullet : H. Foyssi & Friedrich (2004).

boundary layer. Also, the pipe flow simulations have been used to validate the correct implementation of the domain decomposition method.

3.5.1 Channel vs. pipe flow

Direct Numerical Simulation of fully developed supersonic and non-swirling turbulent pipe flow at $Re_\tau = 210$ has been done using the Immersed Boundary Method (sec. 2.3.1). The boundary layer turbulence is initialized by the Klein method similarly to the channel flow simulation (sec. 3.4). Comparison between channel and pipe flow will explore their similarities and differences. Transverse curvature of the wall and compressibility effect will be investigated through mean flow quantities and higher order statistics to reveal their effects on the boundary layer.

Several experimental and numerical simulations have been conducted on incompressible pipe flows. Over the past two decades, both DNS and LES were used to simulate pipe flow at various diameter-based Reynolds numbers using, for the most part, cylindrical coordinates. Eggels et al. (1994) were the first to simulate the pipe flow at $Re_D = 5300$ in DNS. The domain was $10R$ in the axial direction with $96 \times 128 \times 256$ along r, θ, z directions, respectively. Orlandi & Fatica (1997) and Fukagata & Kasagi (2002) used the data created by Eggels et al. (1994) to perform pipe flow experiment. Loulou P. (1997) have computed the same Re_D using a hybrid B-spline spectral method creating an online database for the incompressible pipe flow simulation. Higher Reynolds number simulations have been done by Wagner et al. (2001) and Veenman (2004) reaching $Re_D = 10300$. $Re_\tau = 1050$ pipe flow simulation has been proposed by Satake et al. (2000). They used 402 millions grid points with a streamwise dimension of $15R$. More recently, Wu & Moin (2008) performed a turbulent pipe flow simulations using 630 million grid points at $Re_D = 44000$. They used second-order finite-difference methods and validated their results with experimental data from Princeton Superpipe at $Re_D = 41727$.

For compressible pipe flow, only few simulations have been performed in the past. For instance, Nieuwstadt & Bradshaw (1997) have demonstrated that high order statistics fail to collapse data of compressible channel and pipe flow. Reynolds number effects on pipe and channel flow have been presented by Wosnik et al. (2000). Ghosh et al. (2010) compared the channel and pipe flow statistics. Based on the configuration of Foyi et al. (2004), with $Re_\tau = 245$ and $\langle M_a \rangle = 1.3$, they have been able to compare their data and highlight similarities and differences between fully-developed turbulent channel and pipe flow. Ghosh et al. (2008) also performed DNS of pressure gradient effects in fully developed boundary layer using nozzle and diffuser geometry.

Experiments on compressible/incompressible pipe flows have started half-century ago. At this time, they proposed several laws of the wall, completing the theory initialized by

Millikan. Hinze (1959) summarized these studies. Barenblatt et al. (1997) proposed a power law with coefficients contradicting the universal logarithmic law. In 1998, Princeton Superpipe facility performed experimental fully developed pipe flow measurements. They collected data from $Re_D = 31577$ to $Re_D = 35.2 \times 10^6$. For compressible and supersonic pipe flow, no data are yet present due to the difficulty to measure precisely supersonic flow at low Reynolds number.

3.5.1.1 Flow configurations and parameters

Table 3.3 presents the size of the computational domains, the number of grid points and the dimensionless grid spacing for both channel and pipe flow simulation. Due to the difficulty to express cylindrical wall units in a Cartesian grid, a space averaged Δr^+ is calculated on the first layer near the wall. Grid spacing for the pipe flow has : $\Delta r_{min}^+ = 0.01$, $\Delta r_{max}^+ = 1.54$, $\overline{\Delta r^+} = 0.74$, *i.e.* $\Delta r^+ = \rho_w \Delta r u_\tau / \mu_w$.

Flow parameters are summarized in Table 3.4. The Reynolds number, $Re = \rho_b u_b h / \mu_w$, is characterized by the bulk density, the bulk velocity ($u_b = 1 / (\rho_m h) \int_0^h \rho u dy$), the channel/pipe half width/radius and the viscosity at the wall. For both channel and pipe flow simulations, the friction Reynolds number, $Re_\tau = \rho_w u_\tau R / \mu_w$, is set to 210. The results of the channel flow are presented in the previous section. For fully-developed channel/pipe flow, the additional force is expressed as:

$$\begin{aligned} \rho f_x|_{\text{channel}} &= -\frac{\partial \langle p \rangle}{\partial x} = \langle \tau_w \rangle / h \\ \rho f_x|_{\text{pipe}} &= -\frac{\partial \langle p \rangle}{\partial x} = 2 \langle \tau_w \rangle / R \end{aligned} \quad (3.23)$$

The initial flow field is perturbed using the Klein method (Klein et al. 2003). Channel flow mean profiles (Foyi et al. 2004, Case M1.5) for $\langle u_i \rangle$, $\langle T \rangle$, $\langle p \rangle$, $\langle u'_i u'_j \rangle$ are used to initiate the pipe flow profile using a Cartesian to cylindrical transformation. The walls are considered as isothermal and set to 500K.

$$\begin{aligned} \langle v \rangle &= \sin \theta \langle u_r \rangle + \cos \theta \langle u_\theta \rangle \\ \langle w \rangle &= \cos \theta \langle u_r \rangle + \sin \theta \langle u_\theta \rangle \\ \langle v'v' \rangle &= \sin^2 \theta \langle u'_r u'_r \rangle + 2 \cos \theta \sin \theta \langle u'_r u'_\theta \rangle + \cos^2 \theta \langle u'_\theta u'_\theta \rangle \\ \langle u'v' \rangle &= \sin \theta \langle u'_x u'_r \rangle + \cos \theta \langle u'_x u'_\theta \rangle \end{aligned} \quad (3.24)$$

Statistics are obtained after averaging in time and space (streamwise-direction) during 200 non-dimensional times ($t^* = t u_b / L_x$) which is enough to allow the information to travel 200 times through the channel/pipe length at the bulk velocity.

	$L_x \times L_y \times L_z$	$n_x \times n_y \times n_z$	$\Delta x^+, \Delta y^+, \Delta z^+$
Channel	$4\pi h \times 4/3\pi h \times 2h$	192 x 150 x 128	13.5, 0.79, 6.87
Pipe	$4\pi R \times 2R \times 2R$	192 x 540 x 540	13.5, 0.74, 0.74

Table 3.3: Computational domains and grids

	Re_τ	Re	M	u_τ	M_τ	B_q	t^*
Channel	211	2908	1.5	35.83	0.08	0.048	209
Pipe	210	3044	1.57	35.97	0.08	0.045	196

Table 3.4: Flow parameters for channel/pipe flows

3.5.1.2 Mean quantities

Figure 3.18 shows the Van Driest velocity profiles of both channel and pipe flows at $Re_\tau = 210$. The Van Driest transformation, equation 3.27, accounts for the change of density. The results show an increase of velocity in the outer layer of the pipe ($y^+ > 30$).

$$u^+ = \frac{1}{\kappa} \log y^+ + C^+, \quad (3.25)$$

$$u^+ = A y^{+n}, \quad (3.26)$$

$$u_{VD}^+ = \int_0^{\langle u \rangle^+} (\langle \rho \rangle / \rho_w)^{1/2} d\langle u \rangle^+. \quad (3.27)$$

One way to represent the outer layer effect is to study the overlap layer where the universal log-law applies (Equation 3.25). For compressible flow, it has been seen that the overlap layer can be assimilated by the power-law (Equation 3.26). A contradiction exists in the literature whether this law can be applied or not. Barenblatt et al. (1997) were the first to propose an incomplete power law where the power exponent and multiplicative factor depend on the flow Reynolds number. They found that for a pipe flow at $Re = 4000$, the power law was as accurate as the logarithmic law. Following their path, Zagarola & Smits (1998) affirmed that the power law and log law were similar to characterize the overlap layer in velocity distribution for low Reynolds number ($Re_\tau < 5000$). More recently, McKeon et al. (2004) found a log-law validation in the inertial sublayer and affirmed the power law legitimacy in the overlap layer ($0.12Re_\tau < 600$).

Based on the present simulation ($Re_\tau = 210$), the ability of the power law to characterize the overlap layer for low Reynolds number is not evident. Looking at γ^+ for the log-law and β^+ for the power-law might bring more clarifications. These two parameters are based on the variation of the mean Van Driest profiles. In the overlap layer, these

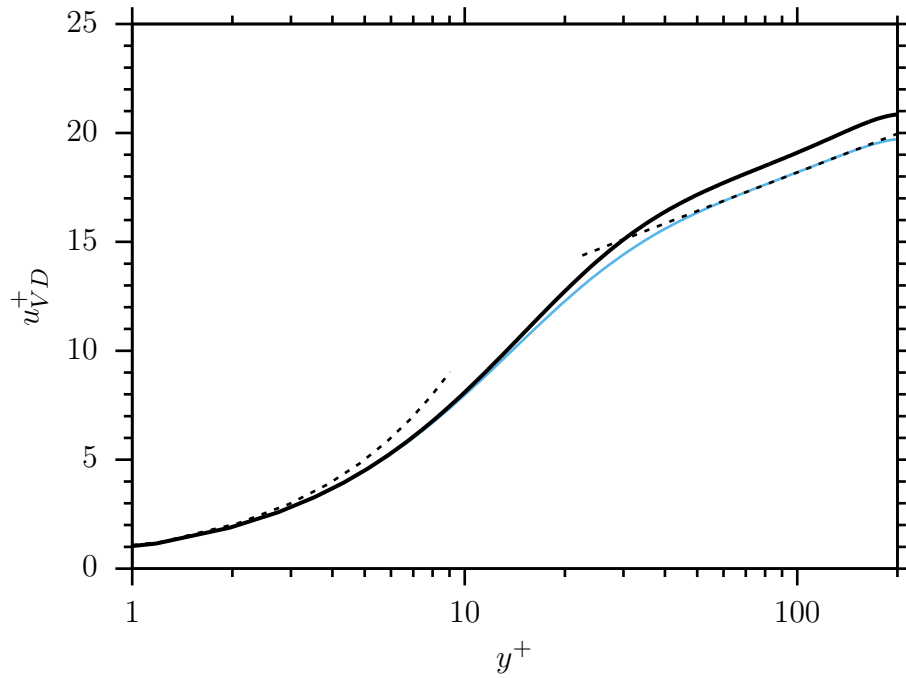


Figure 3.18: Velocity profiles with the Van Driest transformation; —: channel flow, - -: pipe flow.

parameters will be constant with a value of $1/\kappa$ for γ^+ and n for β^+ if they fit with their respective laws.

Figure 3.19 confirms the universal log-law for channel flow since γ^+ is constant in the overlap region giving the Von Karman constant of 0.4. For the pipe flow, a slightly slope exist in the overlap region. One can affirm that the slope for the power-law is not as strong as the slope for the log-law and conclude by a better adaptability of the power-law for pipe flow in the overlap layer. The adaptability of the power-law in the overlap region is not straightforward.

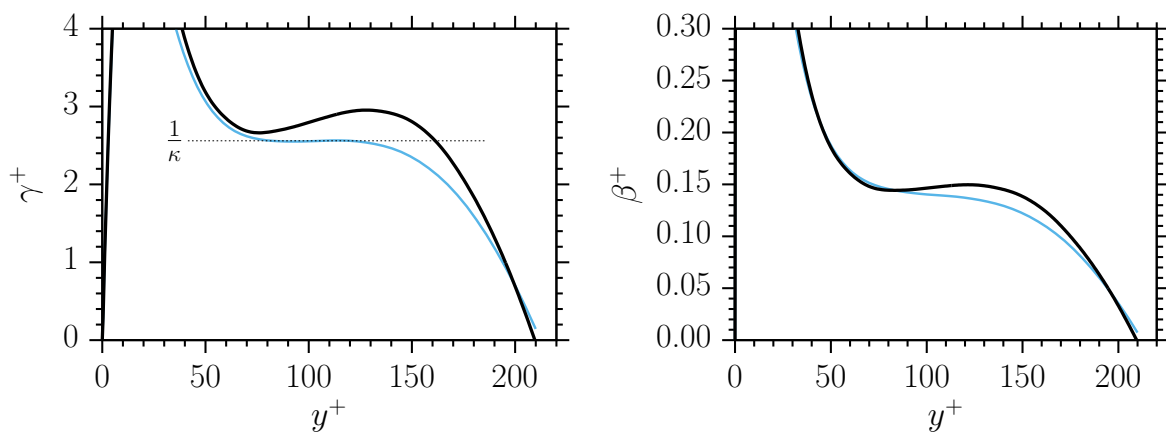


Figure 3.19: Profiles of $\gamma^+ = y^+(du^+/dy^+)$ according to the log-law definition (*left*) and $\beta^+ = (y^+/u^+)(du^+/dy^+)$ according to the power-law definition (*right*); Line types as in figure 3.18.

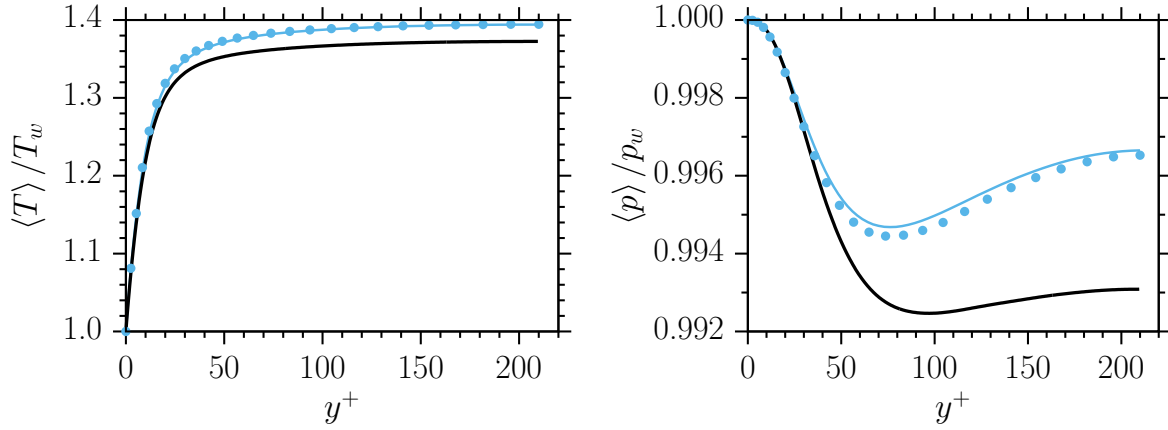


Figure 3.20: Averaged temperature (*left*) and pressure (*right*) along the wall-normal direction; Line colors as in figure 3.18, •: Channel flow of Foysi et al. (2004).

Figure 3.20 shows a decrease of 10% of temperature and 2% of pressure in the central part of the pipe compared to channel flow profile. By integrating the radial/wall-normal mean velocity equation in both flows, the following expression is found:

$$\langle p \rangle = \langle p_w \rangle - \langle \rho \widetilde{v'' v''} \rangle, \quad (\text{Channel})$$

$$\langle p \rangle = \langle p_w \rangle - \langle \rho \widetilde{v'' v''} \rangle - \overbrace{\int_0^r \frac{\langle \rho \widetilde{v'' v''} - \langle \rho \widetilde{w'' w''} \rangle}{R-r} dr}^1. \quad (\text{Pipe})$$

The decay of pressure in the core is caused by the last term of the above equation (1), resulting from the transverse curvature terms in the cylindrical coordinates. The same behavior for temperature can be found by integrating the total energy equation in both cases.

3.5.1.3 Rms fluctuations profiles

Rms velocity fluctuations are investigated through non-dimensional Reynolds stress distribution. The streamwise velocity fluctuations is shown in figure 3.21, $R_{xx}^+ = \langle \rho \widetilde{u'' u''} \rangle / (\rho_w u_\tau^2)$. Figure 3.21 describes wall-normal and span-wise Reynolds stress. Near the wall, the rms velocity fluctuations collapse for both flows. Differences start to appear in the overlap layer and in the core of the flow. For both streamwise and spanwise RMS velocity fluctuations, a decay appears at the peak position ($y^+ = 30$), while the opposite happens for the wall-normal component. Furthermore, differences exist in the core of the pipe/channel for the three components of the autocorrelated velocity fluctuation.

Figure 3.22 shows the dimensionless turbulent shear stress, $R_{xy}^+ = \langle \rho \widetilde{u'' v''} \rangle / (\rho_w u_\tau^2)$. A relationship exists between different quantities such as::

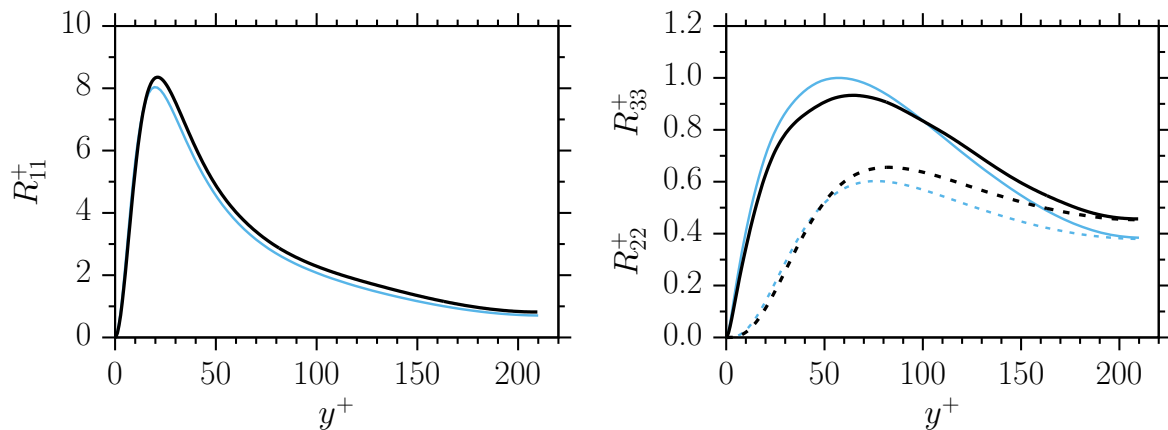


Figure 3.21: Reynolds stress tensor along the wall-normal direction, streamwise (*left*), wall-normal and spanwise (*right*); Line colors as in figure 3.18, --- : R_{22}^+

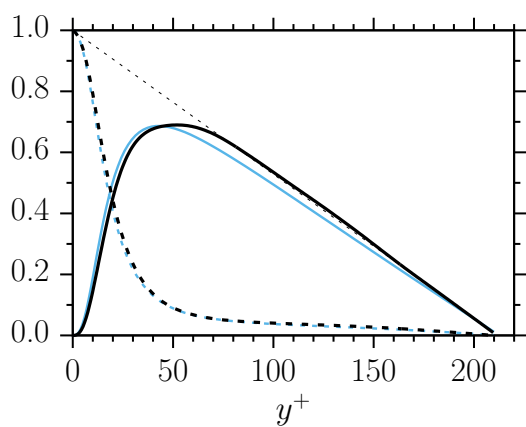


Figure 3.22: Shear stress tensor along the wall-normal direction; Line colors as in figure 3.18; — : $-R_{12}^+$; --- : $\frac{\langle \mu \rangle}{\mu_w} \frac{\partial u^+}{\partial y^+}$.

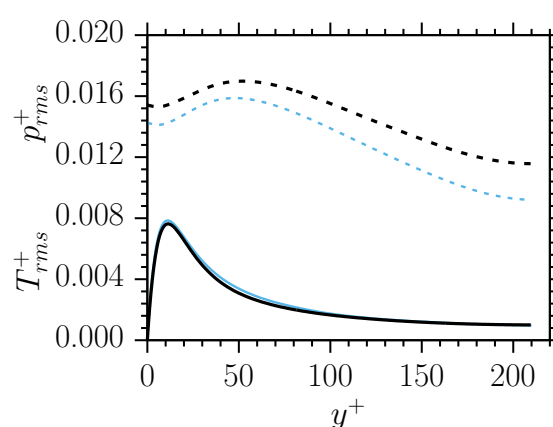


Figure 3.23: Normalized pressure rms (—) and temperature rms (---); Line colors as in figure 3.18.

$$1 - \frac{y^+}{Re_\tau} = \frac{\langle \mu \rangle}{\langle \mu_w \rangle} \frac{\partial u^+}{\partial y^+} - \frac{\langle \rho \rangle \widetilde{u'' v''}}{\tau_w}. \quad (3.28)$$

Rms pressure and temperature are shown in figure 3.23. Rms temperature fluctuations are the same for both cases while differences appear for rms pressure fluctuations. One can notice that, close to the wall, the rms pressure fluctuations for the pipe flow are roughly 8.5% higher than for the channel flow.

3.5.1.4 Turbulent kinetic energy budget

Turbulent energy can be seen as a transfer (cycle) of energy between the mean kinetic energy ($K = 1/2 \widetilde{u_i u_i}$), the turbulent kinetic energy ($k = 1/2 \widetilde{u_i'' u_i''}$) and the internal energy ($\widetilde{u} = C_v \widetilde{T}$). Each of these energies can be decomposed into several terms from averaged equation (Favre averaging). Energy transfers for wall-bounded compressible turbulent flow are summarized in figure 3.24.

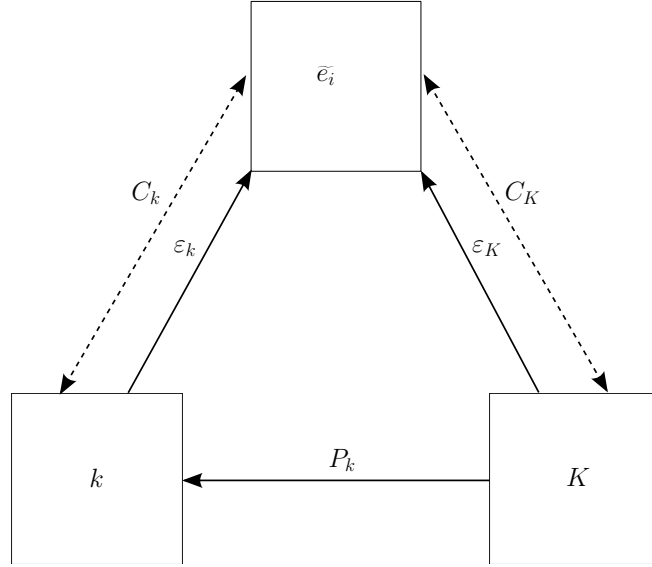


Figure 3.24: Energy transfer of compressible turbulent flow between internal, mean kinetic and turbulent kinetic energy. The dashed lines represent the compressible terms.

The transport equation for turbulent kinetic energy (TKE) is given by:

$$\begin{aligned} \frac{\partial \langle \rho \rangle k}{\partial t} = & \underbrace{-\langle \rho \rangle \widetilde{u_i'' u_j''} \frac{\partial \widetilde{u_i}}{\partial x_j}}_{P_k} - \underbrace{\left\langle \tau'_{ij} \frac{\partial u_i''}{\partial x_j} \right\rangle}_{\varepsilon_k} + \underbrace{\left\langle p' \frac{\partial u_j''}{\partial x_j} \right\rangle}_{C_{k1}} + \underbrace{\left\langle u_i'' \right\rangle \frac{\partial \langle \tau'_{ij} \rangle}{\partial x_j}}_{C_{k2}} - \underbrace{\left\langle u_j'' \right\rangle \frac{\partial \langle p \rangle}{\partial x_j}}_{C_{k3}} \\ & + \frac{\partial}{\partial x_j} \left(\underbrace{-\langle \rho \rangle \widetilde{u_j} k}_{D_k} - \underbrace{\langle \rho \rangle \widetilde{u_j'' u_i'' u_i''} / 2}_{D_t} - \underbrace{\langle p' u_j'' \rangle}_{D_{p'}} + \underbrace{\langle \tau'_{ij} u_i'' \rangle}_{D_{\tau'}} \right). \end{aligned} \quad (3.29)$$

The different terms in the TKE equation are: (P_k): Production of k; (ε_k): Dissipation of k; (C_{k1}): Pressure fluctuation strain; (C_{k2}): Viscous compressibility effect; (C_{k3}): Pressure compressibility effect; (D_k): Diffusion of k; (D_t): Turbulent diffusion; ($D_{p'}$): Pressure fluctuation diffusion and ($D_{\tau'}$): Viscous fluctuation diffusion. The terms of TKE are scaled by $\rho_b u_b^3 / h$.

Figure 3.25 shows the turbulent kinetic budget with the classical term of Production and Dissipation. The production of kinetic energy is reduced in the buffer layer compared to the channel flow. Similarly, the dissipation and the diffusion in the pipe flow decrease at the vicinity of the wall. At the contrary, the pressure terms are kept the same in the boundary layer between pipe and channel flow (fig. 3.26). The compressibility effects are kept the same between the pipe and the channel flow with a peak of energy in the buffer layer of the boundary layer.

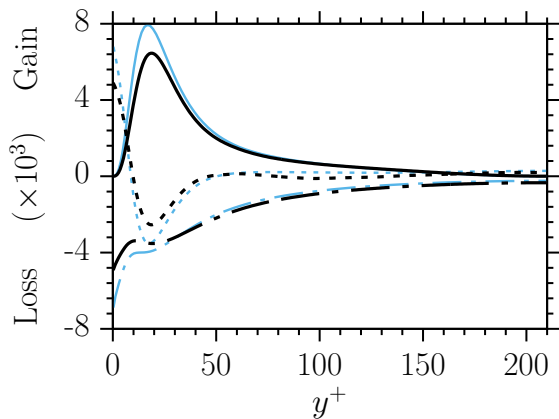


Figure 3.25: Turbulent kinetic budget; Line colors as in figure 3.18; —: P_k^+ , --- : D_k^+ , -·-: ε_k^+ .

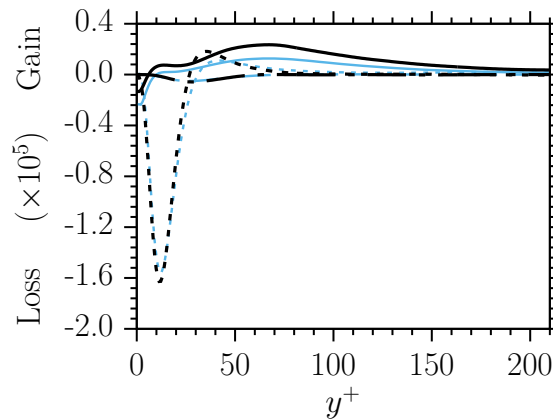


Figure 3.26: Compressible terms of TKE; Line colors as in figure 3.18; —: C_{k1}^+ , --- : C_{k2}^+ , -·-: C_{k3}^+ .

	Re_τ	Re	M	M_τ	T_w
Pipe flow (Sec. 3.5.1)	210	3044	1.57	0.08	500
Ghosh et al. (2010)	245	3180	1.3	0.077	220

Table 3.5: Differences between the pipe flow from section 3.5.1 and Ghosh et al. (2010) simulation.

3.5.2 Cylindrical and generalized curvilinear coordinates code comparison

As discussed before, the results of the DNS of supersonic fully-developed pipe flow are in agreement with the previous study of Ghosh et al. (2010). The drawback of using a Cartesian code with cylindrical shape geometry is the number of points needed. Since the mesh stretching is not practical, a uniform grid spacing is used. Thus, the grid spacing at the center of the pipe is dictated by the grid spacing near the wall, *i.e.* for BL requirements ($\Delta y^+ < 1$). The second drawback of the Cartesian grid is the time-step reduction. The time-step is enforced by the axis cells where the velocity is maximal.

By using a cylindrical coordinates code, one can reduce the number of points. As discussed in section 3.5.1, the cylindrical coordinate system creates a singularity at the axis centerline. The time-step is dictated by the cell near the axis where the velocity is maximal and the volume of the cell minimal ($\Delta\theta r$). A first DNS simulation has been performed using the fully cylindrical coordinates combined with a specific boundary condition for the axis. The obtained results were inaccurate. Thus, an alternative solution using the domain decomposition method is used to simulate cylindrical grid using generalized curvilinear coordinate system.

This section focuses on the comparison of the DNS of supersonic fully-developed pipe flow using the fully-cylindrical coordinates and the domain decomposition method. Those

		N/N_{Cart}	$\langle \Delta t \rangle / \langle \Delta t \rangle_{\text{Cart}}$
Cartesian coordinates	$N_x \times N_y \times N_z = 192 \times 540 \times 540$	-	-
Cylindrical coordinates	$N_x \times N_r \times N_\theta = 192 \times 80 \times 192$	0.05	0.15
DD method	$N_x \times (N_y \times N_z, N_r \times N_\theta)$ 192 x (60 x 60 , 36 x 192)	0.04	4.3

Table 3.6: Details of computational domains and time step values.

two cases are compared to the results of Ghosh et al. (2010). The pipe flow parameters of Ghosh et al. (2010) are a bit different from the previous pipe flow simulation (sec. 3.5.1). Table 3.5 summarizes the main differences. The next simulations (fully-cylindrical coordinates and domain decomposition method) are done using the same parameters as Ghosh et al. (2010).

Table 3.6 shows the details of the grid for each simulation. The number of points for the fully cylindrical simulation and for the DD simulation is highly reduced compared to the Cartesian simulation. For the fully cylindrical grid, the time-step is highly reduced due to the small axis cell volume ($\Delta\theta r$). In the other hand, the DD method includes both advantages, the reduced grid size and the increased time step. Grids are presented in figure 3.27.

Figure 3.28 shows the profiles of mean velocity and temperature for each method compared with Ghosh et al. (2010) data. On the first order statistics, *i.e.* time average of the primitive variables, the solution of the fully-cylindrical method is largely underestimated in the inner layer of the boundary layer. In both methods, the flow is dictated by an additional force following the same formulation as previously discussed (eq. 3.23). In the fully-cylindrical method, the friction Reynolds number is underestimated despite the correct additional force formulation. A second simulation has been made to conserve the friction Reynolds number but led to an over-prediction of the centerline velocity, *i.e.* over-prediction of the Reynolds number.

On the other hand, the results from the DD method are close to the solution of Ghosh. The overlapping zone can be seen in the figure 3.28, where the two solutions from each grid, *i.e.* the internal Cartesian grid Ω_1 and the external hollow cylinder grid Ω_2 , overlap each other. One can notice no spurious oscillations emanating from the overlapping zone meaning that the interpolation between the two grids is satisfactory.

In figure 3.29, the second order statistics (R_{ii}) are plotted. Again, the solution of the fully-cylindrical method is not suitable compared to the DD method solution. The solution of the DD method is close to Ghosh et al. (2010) and proves once again the suitability of the DD method.

This section aimed to validate the domain decomposition method implemented to

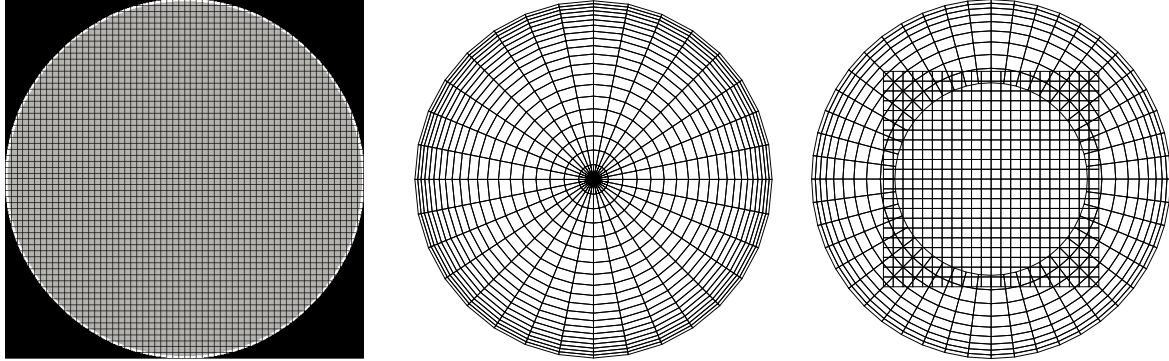


Figure 3.27: Grid representation for the cartesian coordinates (IBM) showing every 9th grid-lines (*left*), the fully-cylindrical coordinates showing every 4th grid-lines (*middle*) and the DD method showing every 3rd grid-lines (Ω_1) and 4th grid-lines (Ω_2) (*right*).

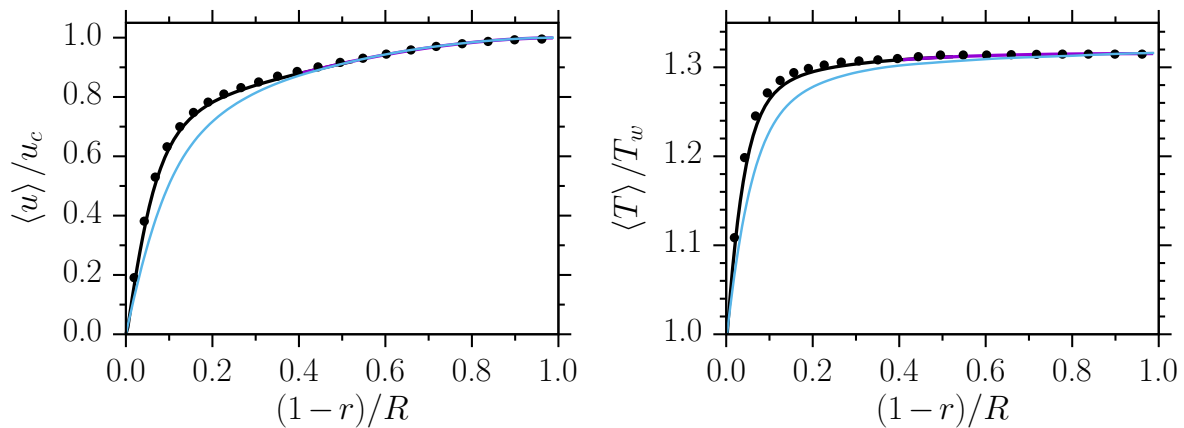


Figure 3.28: Mean velocity (*left*) and mean temperature (*right*) profile along the wall-normal direction; —: DD method (—: Ω_1 and —: Ω_2), —: Fully-cylindrical method, •: Ghosh et al. (2010).

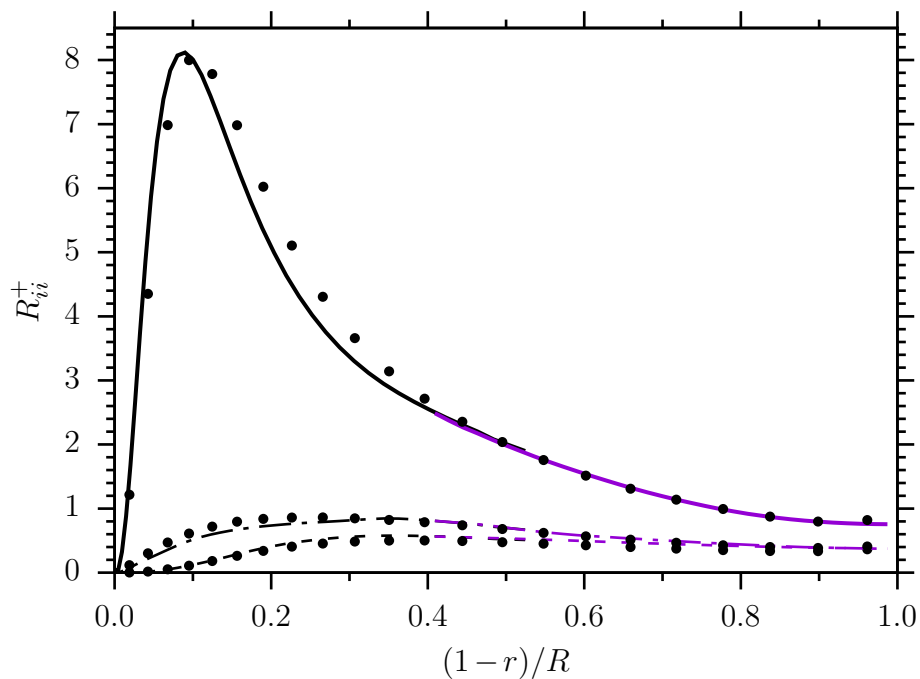


Figure 3.29: Normalized Reynolds stress tensor along the wall-normal direction; Line colors as in figure 3.28, —: R_{11}^+ , -- : R_{22}^+ , -·-·: R_{33}^+ .

avoid the singularity issue in cylindrical coordinate system. The solutions of the DNS using the domain decomposition show good agreement with the previous DNS of Ghosh et al. (2010). The connection between the two sub-domains do not produce spurious oscillations, even for higher-order statistics.

4

Near-wall modeling for LES

A wall model need to be implemented in order to capture the low-frequency oscillation of the separation phenomena in nozzle flow simulation with a reasonable computational efforts. The wall model must be able to simulate high-Reynolds number boundary layer subjected to pressure gradient. So far, DNS of wall-bounded flow has been performed in a fully-developed state (sec. 3.4 and 3.5). In an actual nozzle flow, the boundary layer starts developing in the combustion chamber upstream of the throat and most of the time reaches the fully-developed state before the nozzle throat. Generally, the boundary layer in supersonic nozzles is thin compared to the nozzle throat section.

In this chapter, a wall model has been developed and tested through a DNS of a spatially evolving compressible boundary layer subjected to pressure gradient. First, a comparison of an existing DNS by Pirozzoli et al. (2004) has been done to create a developing boundary layer; then, this DNS has been used to perform a DNS of a turbulent boundary layer under an adverse and favorable pressure gradient; lastly, the DNS of the non-equilibrium boundary layer will be used to validate the implementation of the wall model in *a priori* and *a posteriori* simulations.

4.1 DNS of a zero pressure gradient turbulent boundary layer at $Re_\theta = 4200$

A spatially-evolving supersonic boundary layer over an adiabatic flat plate is simulated to study freestream turbulence and to develop a suitable wall model for the nozzle simulations. This simulation follows the case of Pirozzoli et al. (2004) in terms of domain sizes and inlet quantities.

Rai & Moin (1993) were the first to simulate a compressible growing boundary layer at Mach 2.25. They showed the similarities of the inner layer turbulence compared to

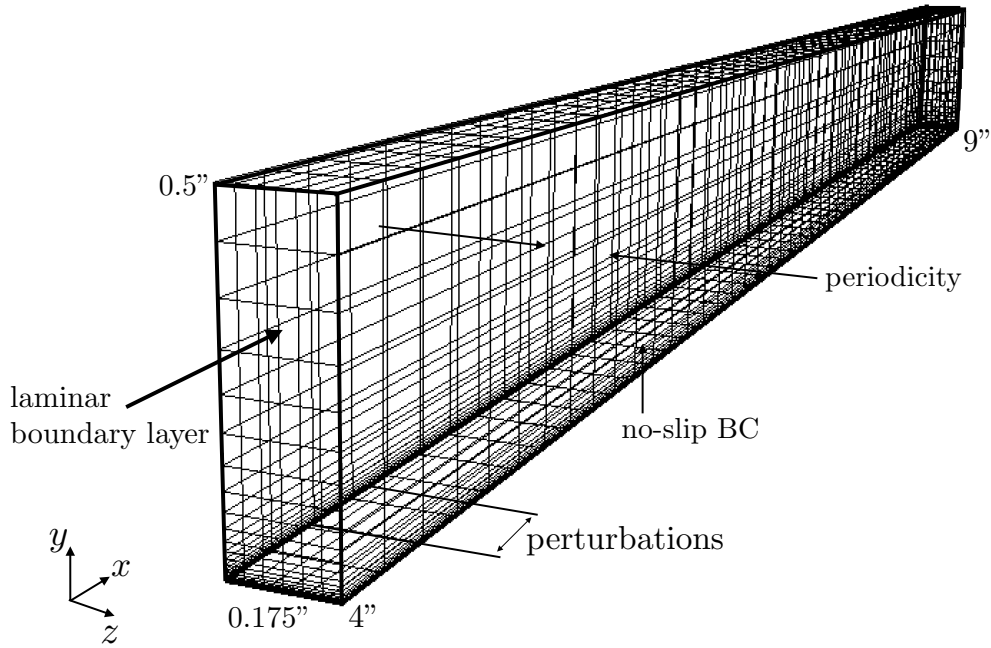


Figure 4.1: Computational domain for the DNS of the transition laminar/turbulent, perturbation model extends from $x = 4.5''$ to $x = 5''$

the incompressible boundary layer results. The same simulation has been done by others. Guo & Adams (1994) showed the influence of the compressibility on the boundary layer by studying the terms of dilatational dissipation and pressure-dilatation correlation. Maeder et al. (2001) studied the influence of the Mach number on the turbulence. They showed that compressibility effects on turbulence statistics are small up to a Mach number of 5. Finally, Pirozzoli et al. (2004) showed that compressible turbulence exhibits close similarities with the incompressible case. They exhibited the good prediction of the Van Driest transformation compared to the incompressible velocity profile and the similarities of the Crocco-Busemann relation to the compressible temperature profile.

An incoming laminar boundary layer at $M_\infty = 2.25$ is evolving along an adiabatic flat plate. At a given Reynolds number, a laminar compressible boundary layer profile is created using the laminar boundary layer equations from White's book (White & Corfield 2006). Both velocity and temperature profiles are used, while pressure is kept constant along the wall-normal direction. The incoming Reynolds number is set to $Re = 2.54 \times 10^6$ (at $x = 4''$) in order to be in a turbulent state ($Re_{\text{turbulent}}^{\text{plate}} > 2 - 5 \times 10^6$). The incoming laminar boundary layer shifts to a turbulent flow during a transition state. In fact, the transition might occur: small upstream perturbations, surface roughness, ... It is common to use a perturbation model to force the transition from laminar to turbulent.

The computational domain extends from $x_{in} = 4''$, corresponding to $Re_x = 2.54 \times 10^6$ to $x_{out} = 9''$. The normal direction extends up to $0.5''$ and the grid is stretched with

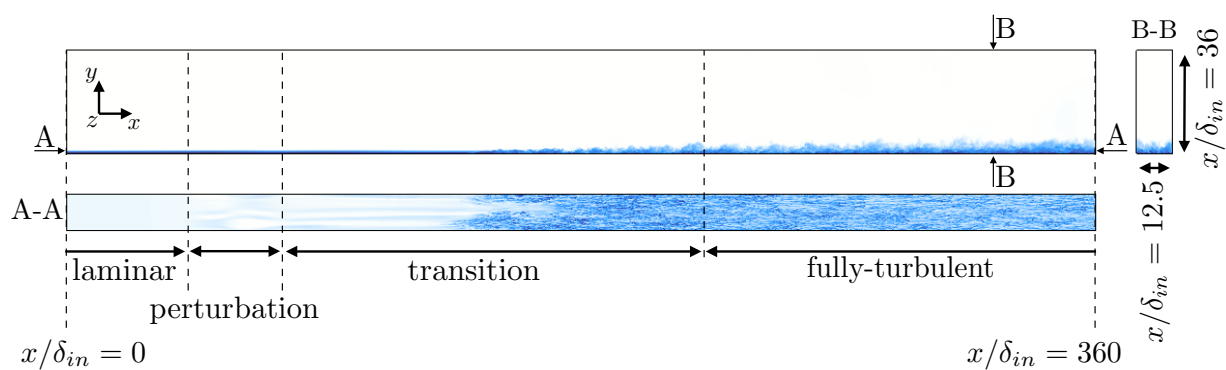


Figure 4.2: Side view of Mach number contour field; Linear black/blue colormap from $M = 0$ to $M = 2.25$, reverse linear colormap for $A - A$ view.

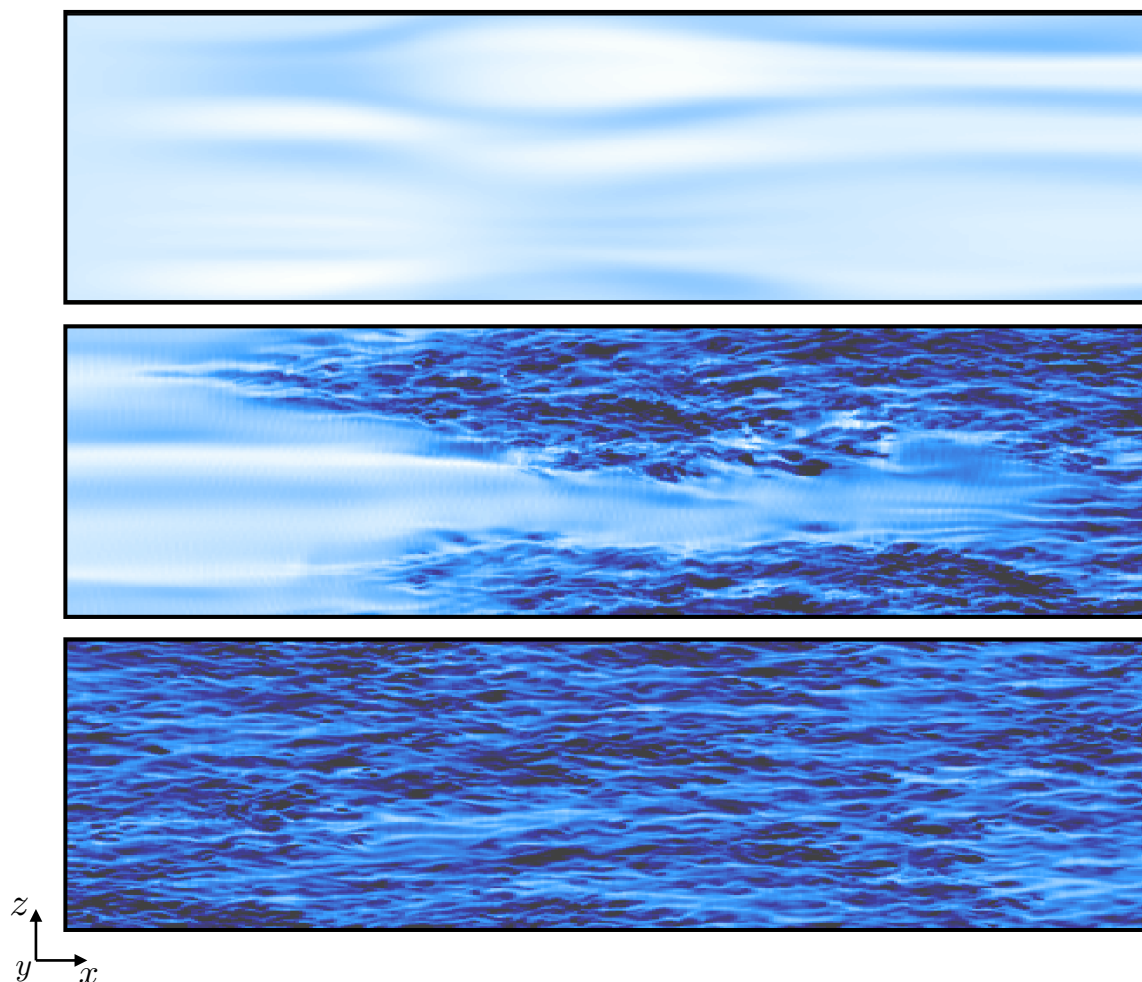


Figure 4.3: Mach number contour field at $y^+ = 15$ at different x -locations; *top*: closed to the perturbation model, *middle*: at the transition, *bottom*: in the fully-turbulent zone; Linear blue/black colormap from $M = 0$ to $M = 1$

a minimum spacing near the wall of $\Delta y_{min}^+ \sim 1$. The spanwise direction of the domain is $0.175''$. The number of points is $N_x \times N_y \times N_z = 3584 \times 128 \times 256$. The freestream flow is set at Mach 2.25 and at a static temperature of $169K$. The momentum thickness Reynolds number post the transition is equal to $Re_\theta = 4260$ ($Re_x = 4.5 \times 10^6$).

The perturbation model is similar to the one implement by Guarini et al. (2000). The region of perturbation extends from $x = 4.5''$ to $x = 5''$. The random numbers are created by a normal/gaussian distribution using the Mersenne Twister random number generator with a cycle of $2^{19937} - 1$ to avoid repetitive patterns. The perturbation model follows the specification of Pirozzoli et al. (2004) as follow:

$$v(x, z, t) = Au_\infty f(x)g(z)h(t), \quad x_a < x < x_b, \quad (4.1)$$

where the parameters are defined in section 2.3.4.

4.1.1 The hybrid scheme

To avoid excessive numerical dissipation inherent to the WENO scheme, an hybrid strategy was used to better capture the boundary layer turbulence with precision (see Sec. 2.2.1).

As it can be seen in figure 4.4, the WENO scheme underestimates the friction coefficient, while the 6th order and hybrid schemes exhibit better solutions. Note that the 6th order centered scheme is not stable.

Figure 4.4 shows different solutions of the friction coefficient for different perturbation amplitude (A) and frequency (f). By increasing the amplitude or the frequency of the perturbation model, the transition zone moves upstream toward the perturbation zone. At a certain point, the transition zone reaches the perturbation zone (blue curve).

4.1.2 Results

Statistics have been averaged in space and time during 10 characteristic time and compared to the DNS data of Pirozzoli et al. (2004). In figure 4.4, the friction coefficient C_f shows the transition zone of the boundary layer from laminar to turbulent, with $C_f = \tau_w / (0.5 \rho_\infty u_\infty^2)$. It points out the perturbation zone (around $Re_x = 3 \times 10^6$), the transitional zone (from $Re_x = 3.8 \times 10^6$ to $Re_x = 4.5 \times 10^6$) and the zone of fully turbulent flow (downstream of $Re_x = 4.5 \times 10^6$). The friction coefficient in the turbulent zone shows a good agreement with the theoretical law Pirozzoli et al. (2004).

For the turbulent region ($Re_x = 4.8 \times 10^6$), the normalized Van Driest velocity is plotted and compared to the classical log-law formulation, to the results of Pirozzoli et al. (2004) and to a previous DNS of Gatski & Erlebacher (2002) in figure 4.6. The

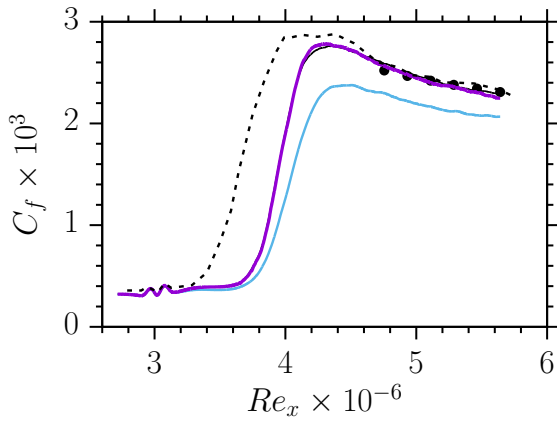


Figure 4.4: Friction coefficient along the x -direction for different convective schemes; —: Hybrid scheme, —: WENO-5th, —: Centered-6th, - - : Pirozzoli et al. (2004), •: Theoretical friction coefficient.

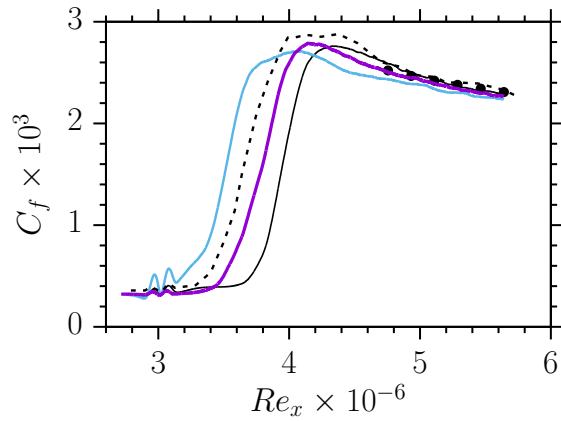


Figure 4.5: Friction coefficient along the x -direction for different parameters of the perturbation model; —: $A = 0.04$ and $f = 75$ kHz, —: $A = 0.08$ and $f = 75$ kHz, —: $A = 0.04$ and $f = 150$ kHz, - - : Pirozzoli et al. (2004), •: Theoretical friction coefficient.

solution shows a close similarity to the theoretical log-law with constant $\kappa = 0.41$ and $C^+ = 5.2$. It also shows good agreement with previous DNS data.

The averaged temperature field is plotted in figure 4.7. The adiabatic wall temperature is correctly captured and exhibits an overshoot of less than 2%. The theoretical temperature profile can be computed by the Crocco–Busemann relation (Pirozzoli et al. 2004). The computed recovery temperature is of the same order of magnitude (approximately 1%). The pressure profile is given in figure 4.8. The assumption in boundary layer theory is that the pressure is constant in the wall-normal direction, *i.e.* $dp/dy = 0$. In turbulent boundary layer, the pressure decreases in the outer layer due to the transverse fluctuating velocity as explained previously in section 3.5 and 3.5.1. Nevertheless, the wall-normal pressure term in the turbulent boundary layer equations is still negligible.

Figure 4.9 shows the normal Reynolds stress components and the shear stress tensor compared to the DNS data of Pirozzoli. Good agreement is obtained from the normal Reynolds stress figures. However, the magnitude of the streamwise components is slightly over-predicted in our case (approximately 8%). Pirozzoli uses the Reynolds fluctuating field, *i.e.* $\langle \rho \rangle \langle u'_i u'_i \rangle$. In our simulation, the Favre averaging operator, *i.e.* $\langle \rho \rangle \widetilde{u''_i u''_i}$ has been used. The difference between the two formulations results in an extra-term $\langle \rho' u'_i u'_i \rangle$ which is not negligible in the outer layer. The shear stress tensor shows a good agreement with the results of Pirozzoli and confirms their findings on the fact that the density scaled Reynolds stress does not exceed unity as predicted by Maeder et al. (2001). Similarly, the total stress, *i.e.* dash line, is slightly constant in the inner layer as expected.

Lastly, the turbulent kinetic energy budget is displayed in figure 4.10. As in section

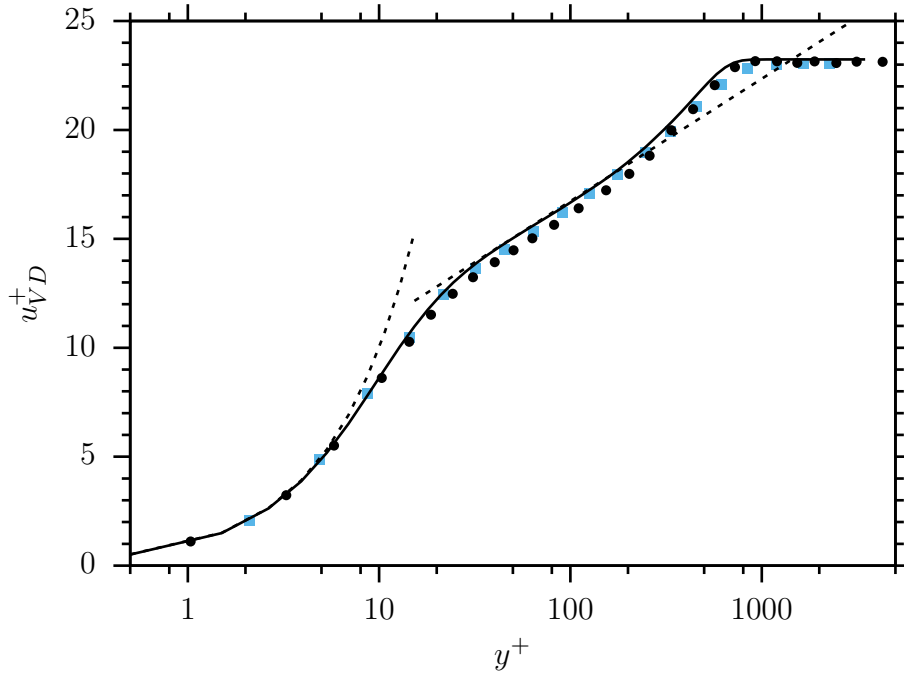


Figure 4.6: Van Driest normalized velocity at $Re_x = 5 \times 10^6$; ●: Pirozzoli et al. (2004), ■: Gatski & Erlebacher (2002), -- : Log-wall with $C^+ = 5.5$.

3.5.1, the kinetic energy equation can be written as a sum of several terms, including the production P , the advection D_k , the dissipation ε , the viscous diffusion D , the turbulent transport T and the pressure dilatation C_k . It shows a qualitatively converged solution compared to Pirozzoli. However, the production term is larger than the one simulated by Pirozzoli while the dissipation term is slightly underestimated. In the vicinity of the wall, the dissipation is over predicted but closer to the results found by Gatski & Erlebacher (2002).

In this test case, a spatially developing supersonic boundary layer has been simulated and compared with the results of Pirozzoli et al. (2004). The simulation shows close similarities with the previous DNS of Pirozzoli. It proves the accuracy of the code to simulate turbulent boundary layers using hybrid schemes. This test case will be used in the next simulation (sec. 4.2) in order to develop a wall-model for the nozzle simulations.

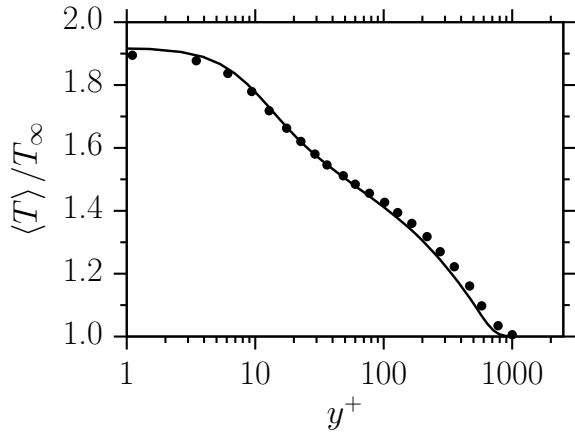


Figure 4.7: Averaged temperature at $Re_x = 5 \times 10^6$; \bullet : Pirozzoli et al. (2004).

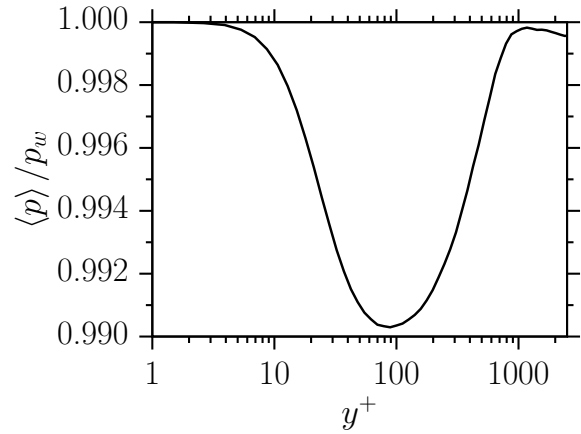


Figure 4.8: Averaged pressure at $Re_x = 5 \times 10^6$.

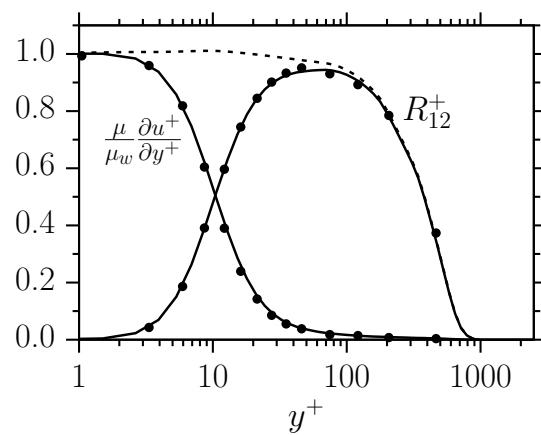
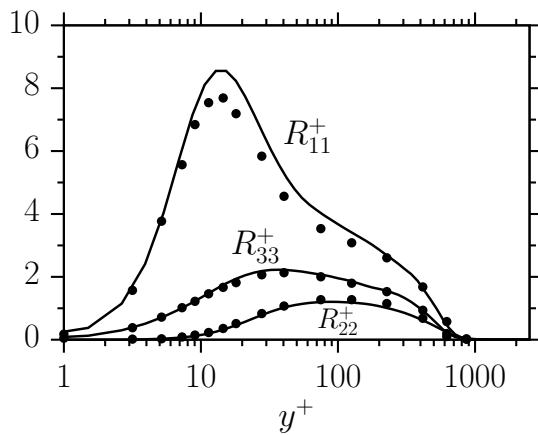


Figure 4.9: Streamwise, wall-normal and spanwise Reynolds stress tensor (*left*) and normalized shear tensor terms (*right*) at $Re_x = 5 \times 10^6$; \bullet : Pirozzoli et al. (2004).

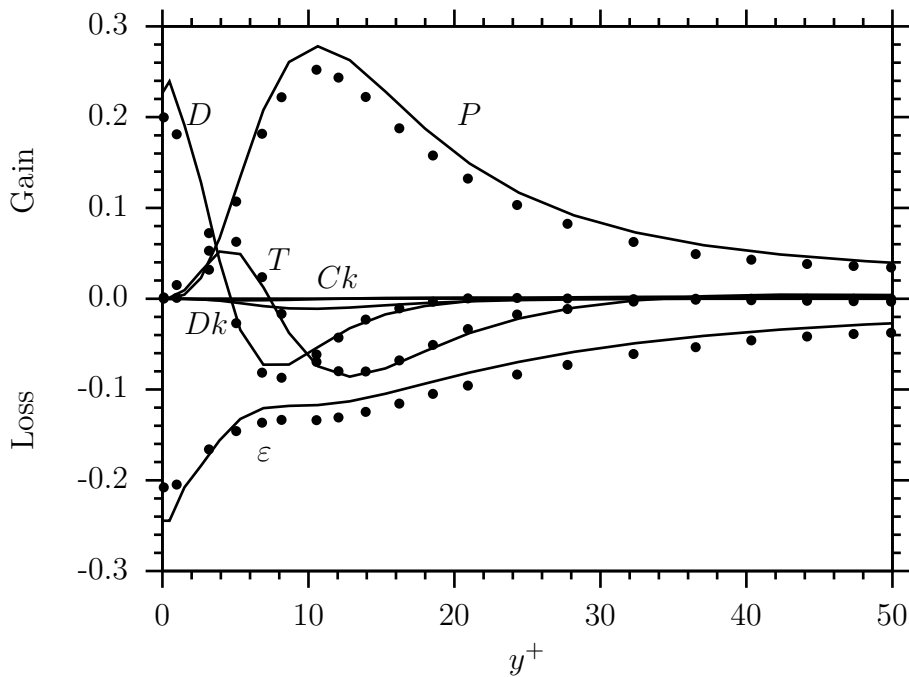


Figure 4.10: Turbulent kinetic energy budget at $Re_x = 5 \times 10^6$; \bullet : Pirozzoli et al. (2004).

4.2 DNS of a turbulent boundary layer under APG / FPG

Nozzle flow boundary layers handle various types of pressure gradient. In the divergent part of an over-expanded nozzle flow, the turbulent boundary layer is first subject to a weak favorable pressure gradient (*i.e.* the pressure is slowly decreasing) followed by a strong adverse pressure gradient due to pressure equalization with the atmosphere. In order to develop a suitable wall model for the nozzle flow simulations (see Introduction), we used the previous simulation of the supersonic/turbulent boundary layer to create a DNS of a turbulent boundary layer under an adverse and a favorable pressure gradient. The DNS will study the effect of adverse pressure gradient on a turbulent boundary layer close to separation by using an adverse pressure gradient and a favorable pressure gradient.

Numerous DNS and LES of laminar and turbulent boundary layer under APG have been done in the past and most of them are done with incompressible and subsonic boundary layers (Kitsios et al. 2015, Nagano et al. 1993, Na & Moin 1998, Abu-Ghannam & Shaw 1980, Hickel & Adams 2008). In supersonic/compressible flow, studies of TBL under weak pressure gradient are rare and most of them simulate TBL under strong APG. The case of a supersonic turbulent boundary layer under strong APG is often assimilated to the Shock Wave Boundary Layer Interaction (SWBLI). SWBLI studies have been done through experiments and numerically by many researchers (see Introduction).

Several methods have been used in the literature to enforce a pressure gradient. The farfield wall-normal boundary condition is often used to enforce a pressure gradient. Following an experiment from Marušić & Perry (1995), where the pressure gradient is adjusted by the height of a flexible test section ceiling, Inoue et al. (2013) attempted to simulate the same experiment by applying a pressure boundary condition at the top of their domain. The pressure gradient boundary condition presents some drawbacks particularly on the wall-normal velocity field. Mellor & Gibson (1966) have developed a farfield wall normal velocity BC to impose a pressure gradient. They control the streamwise velocity field by using a power law, *i.e.* $u_{\text{top BC}} \propto x^m$. The wall normal velocity is then deduced from the streamwise velocity via the boundary layer stream function solution in the far-field region. The main drawback of all of those methods is that the pressure gradient is propagating across the domain through the wall-normal direction. Due to the freestream velocity, the wave is propagating inclined from the wall and thus, a wall-normal pressure gradient exists inside the boundary layer, *i.e.* $\frac{dp}{dy} \neq 0$.

The simulation uses the same parameters as the DNS of section 4.1. The domain starts at $x_i = 4''$, *i.e.* $Re_x = 2.54 \times 10^6$ and the same perturbation model between $x = 4.5''$ to

Case	L_x	$F_{pg} \propto dp/dx$	Note
1	6"	5×10^6	Unstable flow
2	7"	10^6	Stable flow

Table 4.1: Pressure gradient specifications for each case.

$x = 5''$ is used. The inlet flow is set at Mach 2.25 and at a static temperature of 169.44K. The same laminar boundary layer profiles are used at the inlet boundary condition. The domain has been extended in the x -direction to have enough space to perform the separation/reattachment phenomena of the TBL. Two simulations have been done using different domain dimensions and different pressure gradients, table 4.1 summarizes both. The wall-normal length has been increased to avoid reflection of the separated shock on the boundary layer ($L_y = 1''$). The spanwise length is left unchanged and set to 0.175'' using periodic BC. The length of the spanwise direction will be discussed later, especially in the recirculating zone where the large structure of turbulence can be cutoff by the periodic boundary condition.

Due to the difficulty to predict the response of the pressure gradient to the force, a simulation (Case 1) has been made using boundary layer informations from the previous DNS simulation (Sec. 4.1). The amplitude of the pressure gradient is an important factor since it can lead to a separated flow and sometimes to a strong unphysical deceleration of the boundary layer. We have designed the amplitude of the adverse/favorable pressure gradient using the Clauser's parameter β from previous simulation of separated flow found in the literature using:

$$\beta = \frac{\delta^*}{\tau_w} \frac{dp}{dx}, \quad (4.2)$$

where, δ^* is the displacement thickness, τ_w the shear stress at the wall and $\frac{dp}{dx}$ the streamwise pressure gradient.

The first simulation (Case 1) led to the a strong separation of the boundary layer. Figure 4.11 shows the pattern of the separated zone. The recirculating bubble created by the separation was large enough to generate a strong separated shock upstream of the separation accentuating the separation phenomenon which led to an instability of the separation line. This instability has been observed on the slices, they showed that the separation line was constantly sliding upstream of the flow and reaching the transition zone. Despite the fact that this simulation led to an interesting flow field, we have decided to reduce the pressure gradient (Case 2) applied on the boundary layer because of the instability observed in Case 1. A comparison of the solution for both cases is presented in figure 4.12. Case 1 displays the large recirculation bubble created by the strong adverse

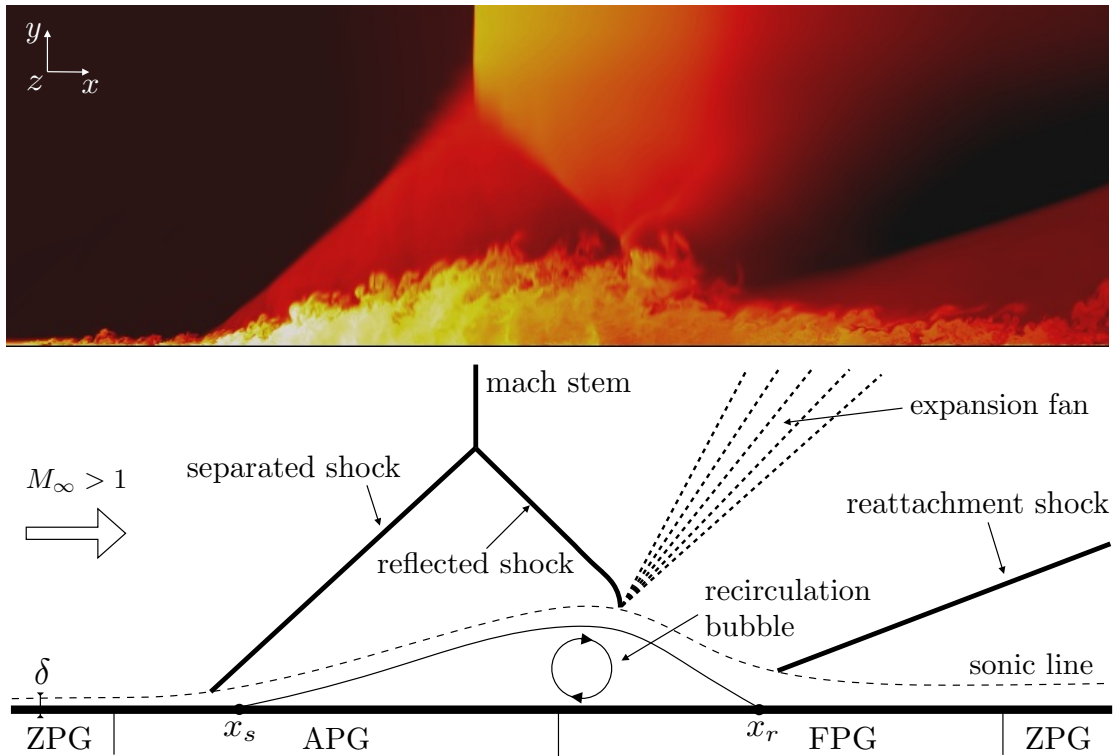


Figure 4.11: Temperature field contour (Case 1) (*top*) and associated diagram of shock pattern (*bottom*).

pressure gradient. In Case 2, the boundary layer handles a moderate pressure gradient. A weak oblique shock can be observed but does not lead to an unstable flow as in Case 1.

For our DNS, the pressure gradient is enforced by an additional force. This additional force allows us to control the pressure gradient location and amplitude more precisely than the wall-normal velocity BC, *i.e.* $dp/dy = 0$. An additional term is added to the streamwise momentum equation and to the total energy equation, *i.e.* $\rho f \propto dp/dx$.

The pressure gradient is applied only in the fully-turbulent zone. The laminar and transition zones are still computed to develop a fully-turbulent flow and can be viewed as a buffer zone similar to the one used with synthetic turbulence boundary conditions. Figure 4.13 shows the design of the pressure gradient applied along the x -direction. For Case 1, the force was applied too close to the transition ($x = 6.5''$) which increase the instability of the separation observed. For Case 2, we have decided to shift the force downstream away from the transition zone.

The streamwise length was about $6''$ in Case 1 and was increased to $7''$ to enlarge the domain of study. The pressure gradient is set as a constant F_{pg} in the favorable and adverse zone. A smooth function (tanh) has been used to connect the three phases: zero, adverse and favorable pressure gradient. The pressure gradient is decreased to a zero

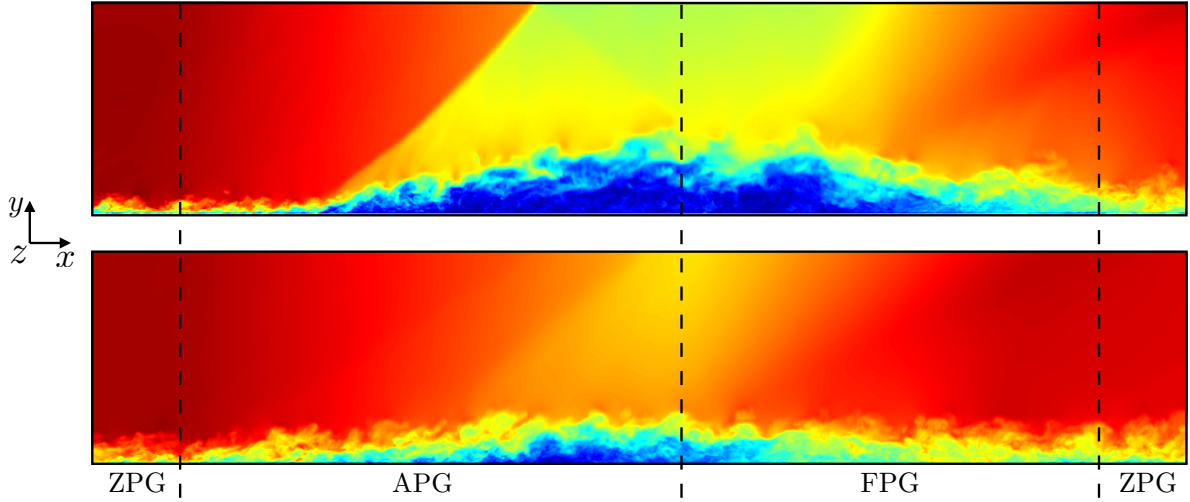


Figure 4.12: Mach number field contour in the x-y plane; *top*: strong pressure gradient (Case 1), *bottom*: moderate pressure gradient (Case 2).

pressure gradient before the outlet to avoid over-constraint boundary condition.

The additional force is supposed to mimic the pressure gradient along the streamwise direction. Applying Navier-Stokes equations in the freestream zone, one can isolate the terms that the force needs to counteract:

$$\frac{\partial \rho u u}{\partial x} = -\frac{\partial p}{\partial x} + F_{pg}. \quad (4.3)$$

In this equation, the additional force is supposed to counterbalance the pressure term and the convective term. If a constant pressure gradient is required, one could compute the additional force by removing the convective term:

$$F_{pg} = F' + \frac{\partial \rho u u}{\partial x}, \quad (4.4)$$

where F' is a constant corresponding to the target pressure gradient, *i.e.* $F' \propto \frac{d\bar{p}}{dx}$.

Due to the difficulty in computing the convective term during the simulation, especially near shocks, we have decided to use a constant F_{pg} instead of a constant pressure gradient F' . Because of that, the pressure gradient computed by the simulation will not be constant in the adverse and favorable zone.

Figure 4.14 shows the response of the pressure and velocity gradient fields to the applied force (Case 2). In the APG zone ($x/\delta_{in} = [250 : 300]$), the sum of the convective force and the pressure terms follows the amplitude imposed by the additional force F_{pg} . One can observe that the pressure gradient along the x-direction is not strictly constant in the APG zone as predicted. Due to the deceleration of the boundary layer and the creation of a weak separated shock (fig. 4.12), the actual force imposed in the FPG zone

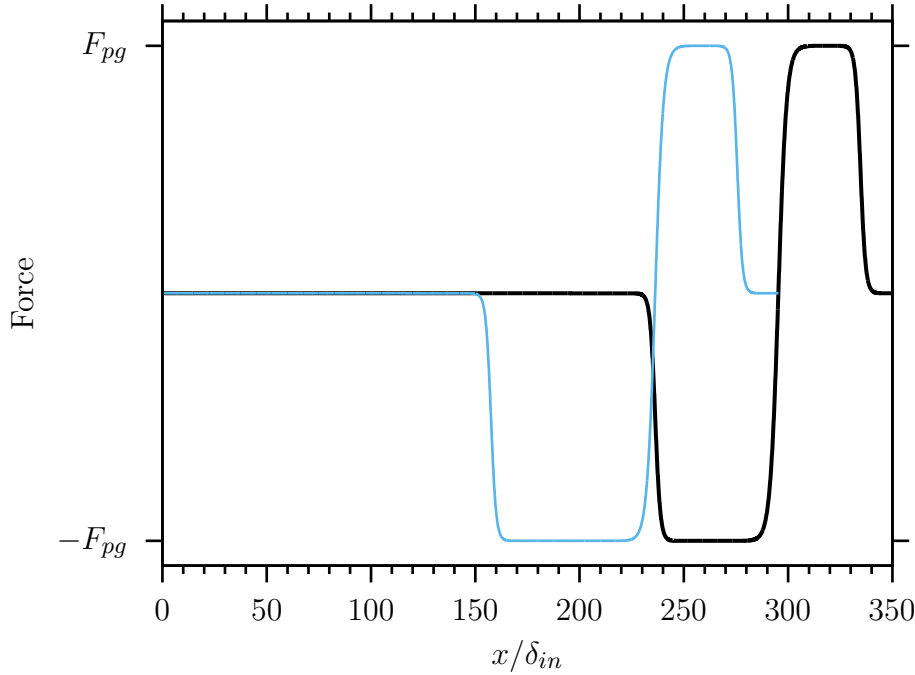


Figure 4.13: Additional force distribution along the x -direction; —: Case 1, —: Case 2

is not visible on figure 4.14 ($x/\delta_{in} \sim 320$). One can also notice the effect of the transition on the pressure field at $x/\delta_{in} \sim 140$.

Figure 4.15 shows the friction coefficient from the statistics for the two test cases. Due to the unstable property of Case 1, the statistics are not converged and will never be (the shock was moving upstream to the transition area and probably to the laminar area). This figure is still interesting because it shows the position of the separation line for Case 1 where $C_f = 0$. It also shows the strong pressure gradient applied close to the transition zone ($x/\delta_{in} \sim 175$). One can notice that the transition zone is not at the same location in both cases. Case 2 uses the corrected perturbation model discussed in section 2.3.4. For the second case, the friction coefficient is close to zero but never reaches the separation. The APG zone is located far from the transition in the fully-turbulent region. Only the second test case will be considered.

In zero-pressure gradient boundary layer, the law of the wall is divided in two regions, the inner and the outer region (sec. 3.4). The inner layer connect the viscous sublayer, the buffer region and the log-law region. The limit of the inner layer is commonly defined as 0.2δ . The log-law (eq. 4.5) at zero-pressure gradient extends generally from $y^+ \sim 30 - 50$ to $y^+ \sim 200$ Marusic et al. (2013) and the values of κ and C^+ change depending on the simulated case Örlü et al. (2010). In compressible flow, the Van Driest transformation (eq. 4.6) is often applied to the normalized velocity u^+ in order to scale the logarithmic law to the density/viscosity variation effect of the boundary layer.

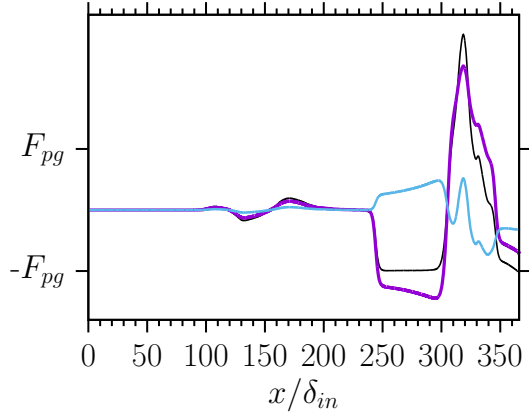


Figure 4.14: Navier-Stokes terms in the freestream zone along the x -direction (Case 2); $-$: $d\bar{p}/dx$, $-$: $d\bar{\rho}\bar{u}\bar{u}/dx$, $-$: $d\bar{p}/dx + d\bar{\rho}\bar{u}\bar{u}/dx$

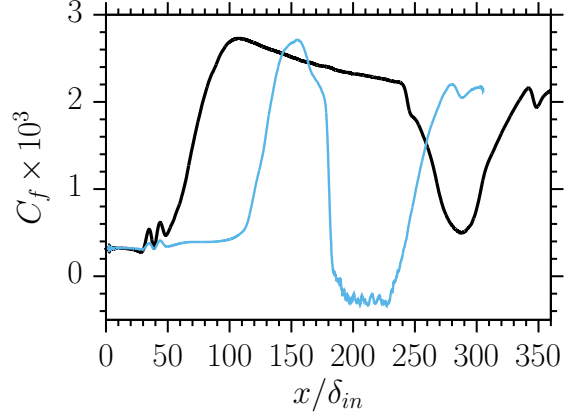


Figure 4.15: Friction coefficient along the x -direction; Line types as in figure 4.13.

$$\langle u \rangle^+ = \frac{1}{\kappa} \log y^+ + C^+, \quad (4.5)$$

$$\langle u \rangle_{VD}^+ = \int_0^{\langle u \rangle^+} (\langle \rho \rangle / \rho_w)^{1/2} d\langle u \rangle^+. \quad (4.6)$$

In adverse or favorable pressure gradient, the universality of the law of the wall does not apply and many researchers have worked on the subject to find a scaling law for the inner part of the boundary layer. The behavior of a turbulent boundary layer under adverse or favorable pressure gradient is still in debate among researchers. There are different theory in the literature concerning the law of the wall for pressure gradient boundary layer. Huang & Bradshaw (1995) proposed that the region occupied by the log-law is slowly reduced with an adverse pressure gradient but the coefficients κ and C^+ still have the same values as for a flat plate boundary layer under zero-gradient pressure. Stratford (1959) suggested the same behavior for the log-law and proposed that beyond the log-law region there is a so-called half-power law region where both regions are joined smoothly. This overlap region extends from 0.15δ to $y^+ < 300$ (Alving & Fernholz 1995). Nagib & Chauhan (2008) proposed another theory where the log-law still holds but κ and C^+ change their values. Several studies (Nagano et al. 1993, Lee & Sung 2009) have followed that path and suggested a functional dependence of the coefficients on the so-called pressure gradient parameter Δp^+ :

$$\Delta p^+ = \frac{\nu}{\rho u_\tau^3} \frac{dp}{dx}. \quad (4.7)$$

Lastly, Skote & Henningson (2002) considered that the pressure gradient causes a continuous, general breakdown of the log-law and that the previous assumptions does not

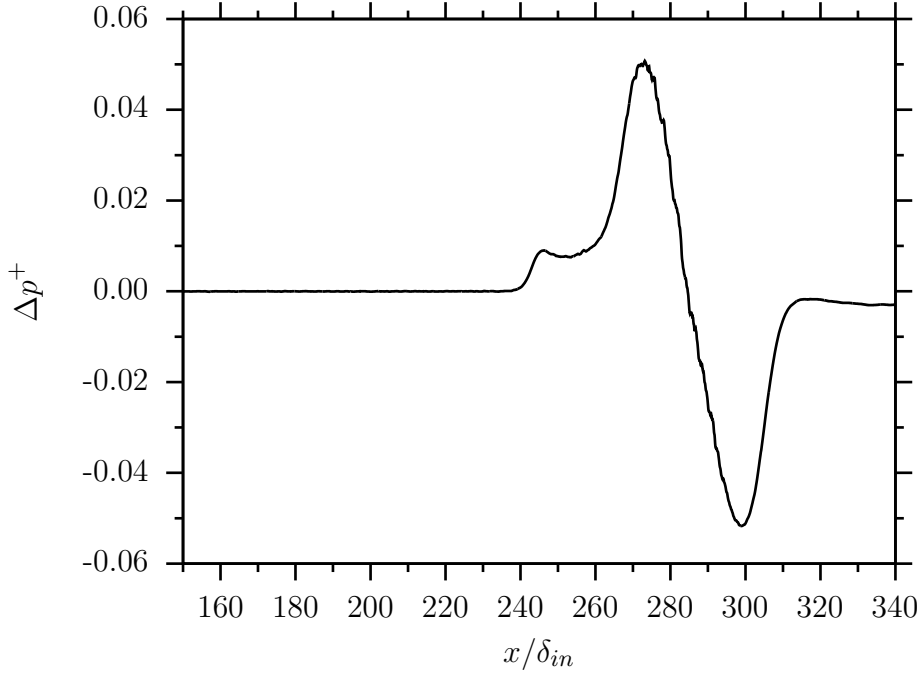


Figure 4.16: Pressure gradient parameter along the x -direction.

hold for pressure gradient boundary layer flow. Figure 4.16 shows the pressure gradient parameter Δp^+ centered in the fully-turbulent region. The pressure gradient parameter is positive in the adverse pressure gradient region ($x/\delta_{in} \sim 250$) and negative in the favorable pressure gradient region ($x/\delta_{in} \sim 320$). Figure 4.17 shows the Van Driest velocity for several x -positions ($x/\delta_{in} = 170, 250$ and 330) corresponding to different values of the pressure gradient parameter, *i.e.* $\Delta p^+ = 0, 0.0075$ and -0.0025 , respectively. One can observe that the self similar solution of the velocity profile for both the adverse and favorable pressure gradient is changing along the boundary layer. For both APG and FPG cases, the classical log-law, *i.e.* $\kappa \sim 0.41$ and $C^+ \sim 5.0$ Örlü et al. (2010), does not apply anymore.

For the adverse pressure gradient region, one could fit the log-law with different coefficients as proposed by Nagib and others (Nagib & Chauhan 2008, Nagano et al. 1993, Lee & Sung 2009). One could also confirm that the log-law zone is reduced compared to the zero-gradient region, *i.e.* $y_{\log\text{-law,APG}}^+ = [30 : 90]$ and that it extends to the half-power law region from $y^+ \sim 100$. In fact, all the theory presented above could fit the velocity profile of the adverse pressure gradient region. For the favorable pressure gradient region, a log-law can also be fitted in a region slightly shifted compared to the zero-pressure gradient region, *i.e.* $y_{\log\text{-law,FPG}}^+ = [60 : 200]$.

As in section 3.5.1, the adaptability of the log-law can be confirmed by the non-dimensional parameter $\gamma^+ = y^+(du^+/dy^+)$. We seek a region where γ^+ shows a plateau. The second coefficient C^+ can be deduced from γ^+ at a specific y^+ using the following

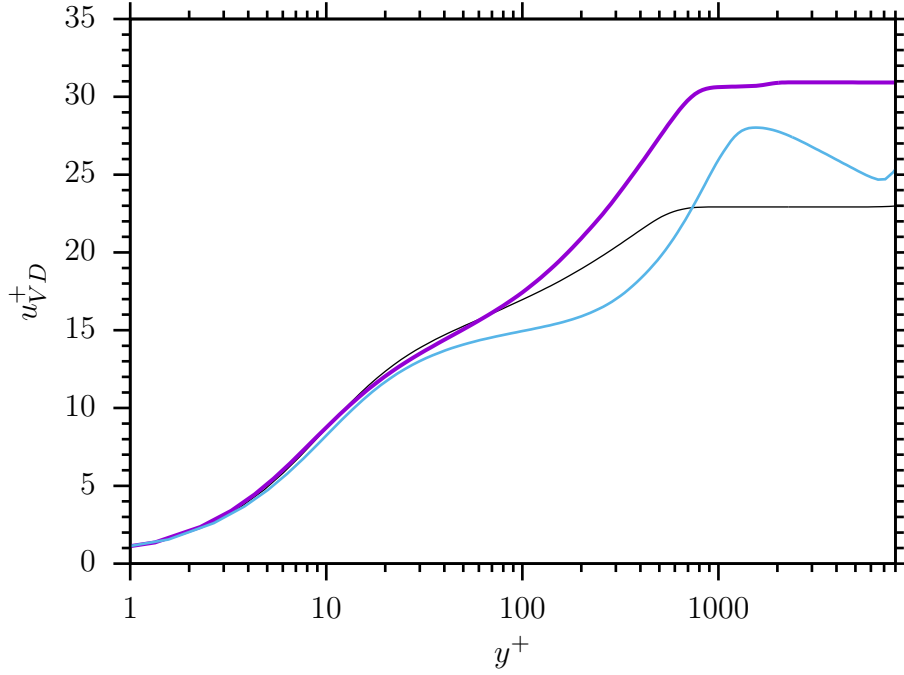


Figure 4.17: Van Driest velocity along the wall-normal direction; $-$: zero-pressure gradient $\Delta p^+ = 0$, $-$: adverse pressure gradient $\Delta p^+ = 0.0075$, $-$: favorable pressure gradient $\Delta p^+ = -0.0025$

relation:

$$C^+ = u_{VD}^+ - \gamma^+ \log y^+. \quad (4.8)$$

According to Brown & Joubert (1969), in a thin region around $y^+ \sim 100$, the velocity profile can be fitted by the log-law with coefficients depending on the pressure gradient parameter Δp^+ . Figure 4.18 shows the γ^+ parameter along the wall-normal direction for the three x -locations, *i.e.* $\Delta p^+ = 0, 0.0075$ and -0.0025 . κ coefficient can be deduced from the γ^+ parameter with $\kappa = 1/\gamma^+$ in region where the γ^+ parameter forms a plateau. Zero-pressure gradient solution gives a slightly constant $\gamma^+ \sim 2.423$ in the range $y_{\log\text{-law}}^+ = [40 - 150]$ giving $\kappa \sim 0.413$. For the APG and FPG cases, the γ^+ is not strictly constant but one can notice that the range is shifted closer to the wall ($y_{\log\text{-law},\min}^+ \sim 30$) for the adverse pressure gradient and far from the wall ($y_{\log\text{-law},\min}^+ \sim 100$) for the favorable pressure gradient.

Following Brown & Joubert (1969) assumptions where the log-law can be fitted in a thin region around $y^+ \sim 100$, the $\kappa^+ = 1/\gamma^+$ coefficient is plotted along the x -direction at $y^+ = 100$ in figure 4.19 along with the second log-law coefficient C^+ (eq. 4.8). Upstream $x/\delta_{in} = 240$, the flow is at zero-pressure gradient and both coefficients are constant and similar to the literature (Nickels 2004, Coles 1968, So et al. 1994, Örlü et al. 2010), *i.e.* $\kappa = [0.41 : 0.54]$ and $C^+ = [4 : 6.2]$. In the APG zone ($x/\delta_{in} = 250$), κ and C^+

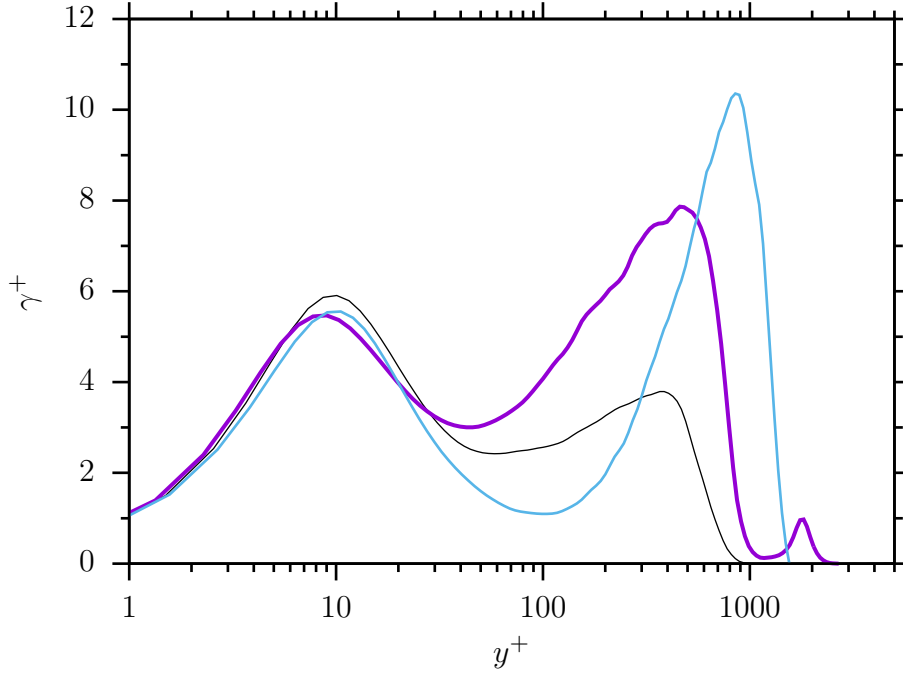


Figure 4.18: Non-dimensional parameter γ^+ along the wall-normal direction; Line types as in figure 4.17

coefficients are reduced compared to ZPG following what has been found in literature (Nagib & Chauhan 2008, Nickels 2004). On the contrary, both coefficients are increased for the FPG region ($x/\delta_{in} = 320$).

Nickels (2004) proposed a function to determine K_i and C_i from Δp^+ , where the law of the wall is expressed by $u^+ = 1/K_i \log y^+ + C_i$:

$$K_i = \frac{\kappa_0}{\sqrt{1 + \Delta p^+ y_c^+}}, \quad (4.9)$$

where $\kappa_0 = 0.39$ and y_c^+ is the thickness of the viscous sublayer computed by $\Delta p^+(y_c^+)^3 +$

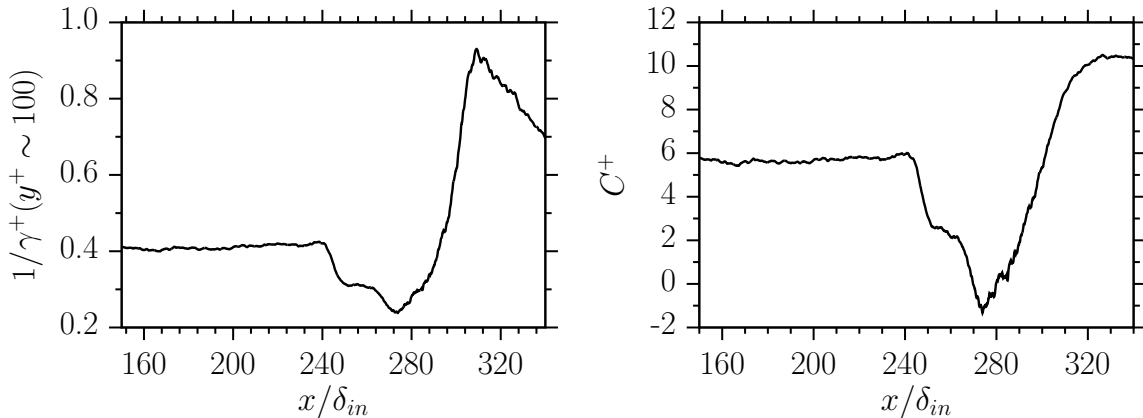


Figure 4.19: Log-law coefficient κ^+ (left) and C^+ (right) computed at $y^+ = 100$ along the x -direction.

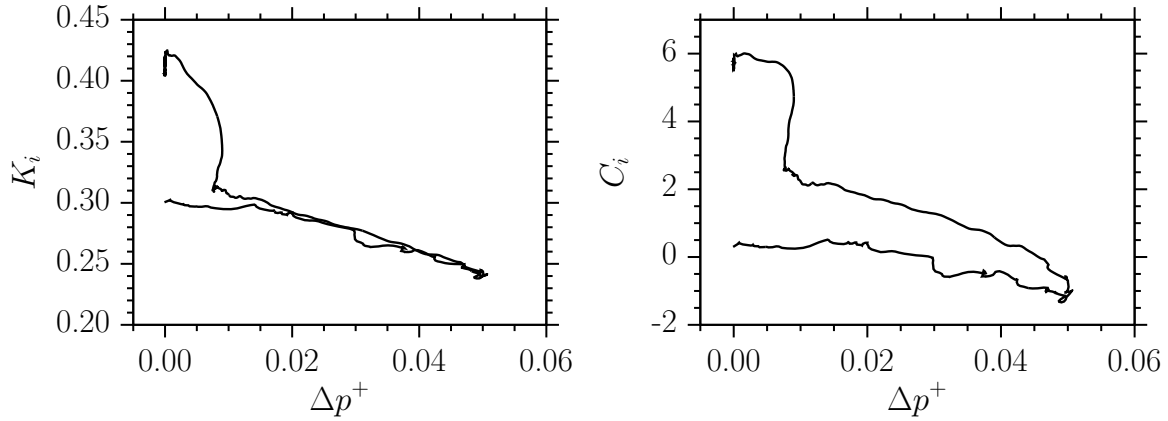


Figure 4.20: Log-law coefficients K_i (left) and C_i (right) at $y^+ = 100$ along the pressure parameter Δp^+ in the ZPG and APG region.

$(y_c^+)^2 - 12^2 = 0$ using the smallest positive root. It is worth noticing that those coefficients are computed for incompressible flow at high Reynolds number Nickels (2004).

C_i is then deduced by the following equation as proposed by Nagib & Chauhan (2008):

$$F_i C_i = 1.6 (\exp(0.1663 B_i) - 1). \quad (4.10)$$

Following Nickels (2004) assumptions, figure 4.20 shows the log-law coefficients $K_i = \kappa$ and $C_i = C^+$ as a function of Δp^+ for both ZPG and APG zones. At zero-pressure gradient, both parameters give constant values, *i.e.* $K_i \sim 0.41$ and $C_i \sim 5.6$. The change of K_i versus Δp^+ in figure 4.20 (left) shows a pronounced correlation in the region $\Delta p^+ = [0.008 : 0.05]$. This region corresponds to the zone where the force is constant (fig. 4.13). One can notice that the correlation does not change whether the pressure parameter gradient is positive or negative, *i.e.* $d\Delta p^+/dx > 0$ or $d\Delta p^+/dx < 0$.

A noticeable spreading of C_i in figure 4.20 (right) can be observed in the constant force region. Recently, Knopp et al. (2014) observed a similar sensitivity of C_i (20%) for different pressure parameters depending on the choice of $y_{\log\text{-law}}^+$. The correlation slope is changing whether the pressure parameter gradient is positive or negative.

A modified log-law has been proposed by Mcdonald (1969) for mild pressure gradient. It combines the log-law and the half-power law in the overlap region (Stratford 1959).

$$u_{mod}^+ = \frac{1}{\kappa_{mod}} \left(\log y^+ - 2 \log \frac{\sqrt{1 + \lambda \Delta p^+ y^+} + 1}{2} + 2(\sqrt{1 + \lambda \Delta p^+ y^+} - 1) \right) + C_{mod}^+ \quad (4.11)$$

where λ is a coefficient found experimentally for mild pressure gradient flow (Mcdonald 1969).

The modified non-dimensional parameter γ_{mod}^+ can be deduced from the previous

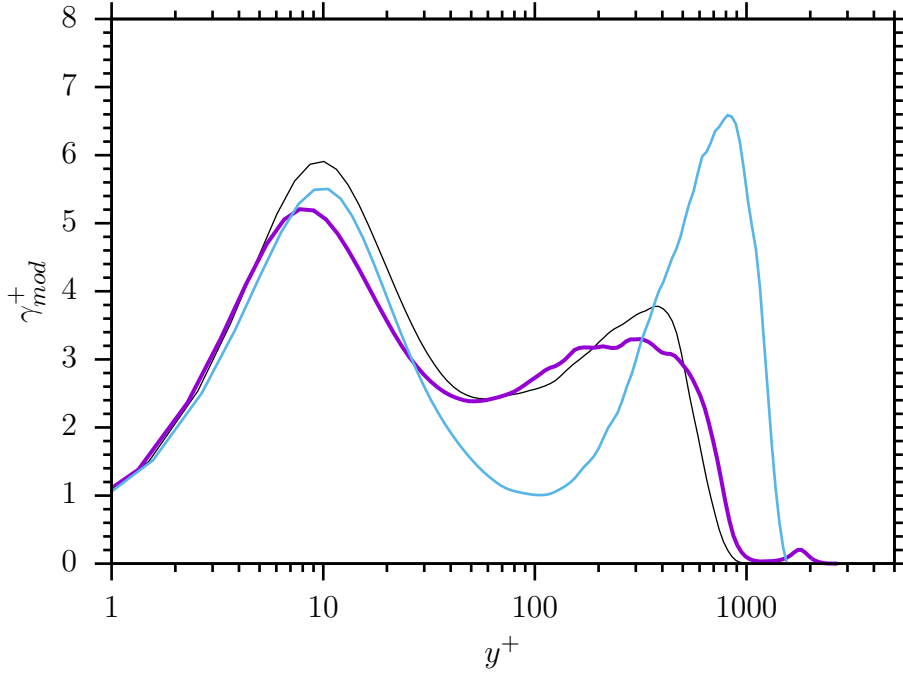


Figure 4.21: Modified non-dimensional parameter γ_{mod}^+ along the wall-normal direction; Line types as in figure 4.17

equation giving:

$$\gamma_{\text{mod}}^+ = \frac{y^+}{\sqrt{1 + \lambda \Delta p^+ y^+}} \frac{du^+}{dy^+}. \quad (4.12)$$

Figure 4.21 shows the γ_{mod}^+ parameter along the wall-normal direction for the three x -location, *i.e.* $\Delta p^+ = 0, 0.0075$ and -0.0025 with $\lambda = 1$. The adverse pressure gradient case is similar to the zero-pressure gradient one. The region $y_{\text{log-law}}^+ = [40 - 150]$ gives a slightly constant γ_{mod}^+ for both ZPG and APG. On the contrary, the modified log-law does not apply for the favorable gradient pressure region. The previous Van Driest velocity profile for ZPG and APG region is plotted along the modified log-law (eq. 4.11) in figure 4.22. It shows the good prediction of the modified log-law in the range $y_{\text{log-law}}^+ = [30 - 150]$.

The region below the log-law, *i.e.* the viscous sublayer and the buffer zone, have also different behavior whether the adverse or the favorable pressure gradient is considered.

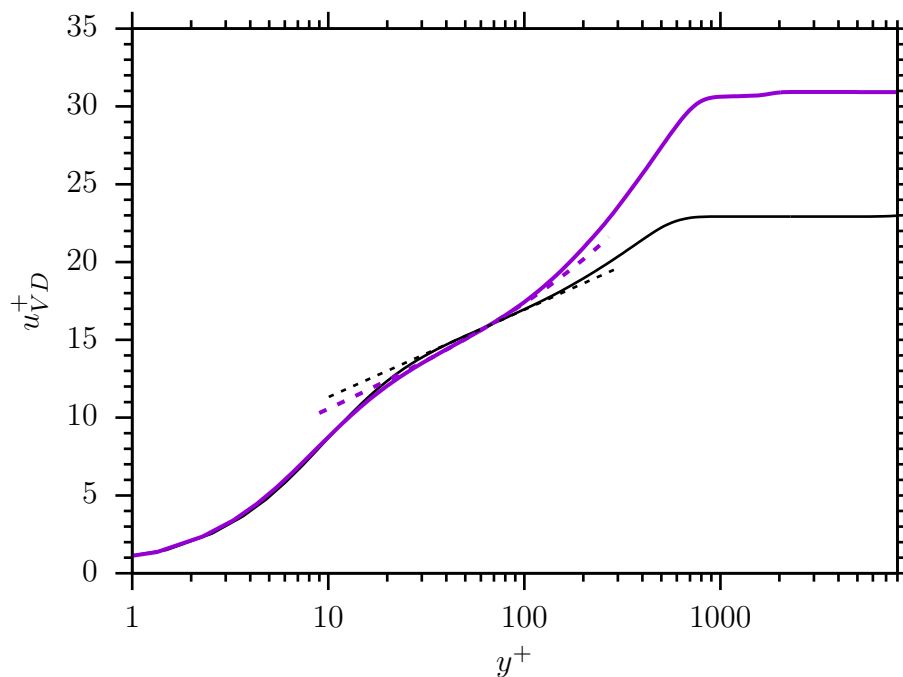


Figure 4.22: Van Driest velocity along the y -direction; Line types as in figure 4.17, --- : Modified log-law (McDonald 1969).

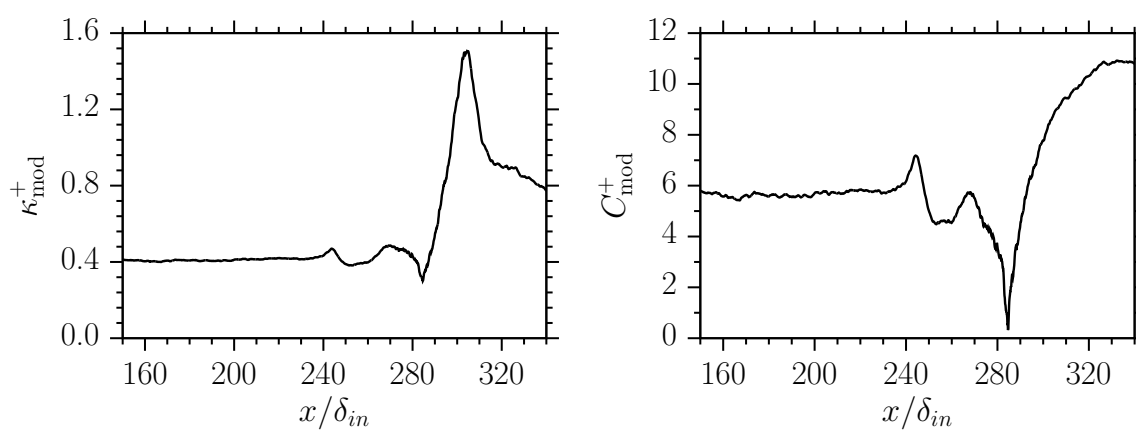


Figure 4.23: Modified log-law coefficient κ_{mod}^+ (left) and C_{mod}^+ (right) at $y^+ = 100$ along the x -direction.

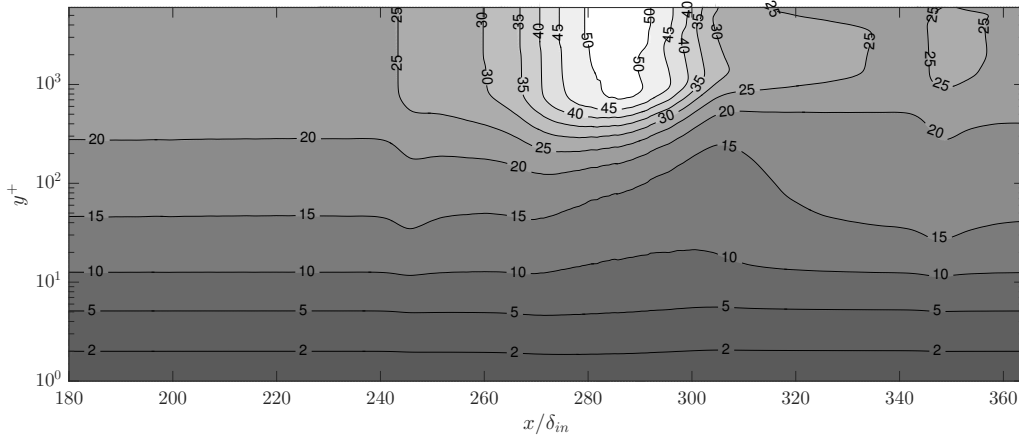


Figure 4.24: Van Driest velocity field u_{VD}^+ in x - y plane

4.3 Near wall modeling

Near-wall modeling is required in order to reduce the computational cost of turbulent boundary layer simulations. The near-wall modeling is also necessary when simulating high Reynolds number flows with complex geometry. Instead of DNS, the large-eddy simulation is used to reduce the computational resources. For wall-bounded flow, the wall-resolved LES is strongly dependent on the Reynolds number, so a very refined grid needs to be used close to the wall. At high Reynolds number, the cost of the wall-resolved LES becomes prohibitive, even with the current computational power. To overcome this limitation, it is common to use a near-wall model in order to reduce the number of points of the grid and the time step of the simulation. Various methods have been proposed in the literature (Grötzbach 1987, Schumann 1975, Spalding 1961, Cabot & Moin 2000, Piomelli & Balaras 2002). Many of those strategies are case-sensitive, which means that it has been designed for a specific case. In our case, the compressible wall-model needs to be developed in the presence of a pressure gradient.

The approach presented in this section consists in using a relatively coarse grid on the wall combined with a wall-model, supposed to mimic the dynamical effects of the turbulent eddies in the near-wall layer. Schumann (1975) was the first to develop such approach for channel flow simulations. The purpose of this method was to obtain, in both space and time, detailed turbulent velocity and pressure fields for high-Reynolds number flows. Grötzbach (1987) improved the model of Schumann by adapting its formulation to wall-bounded flow. Nonetheless, these methods made the assumption of an equilibrium boundary-layer, which is not valid for turbulent boundary layer subjected to pressure gradient.

The effects of pressure gradient on the wall stress models have been proposed by Manhart et al. (2008). Despite the fact that their model was adapted for streamwise

pressure gradient, they also neglected the Reynolds stress effects, which limits the range of validity of the model to the viscous sublayer, *i.e.* $y^+ < 5$. Duprat et al. (2011) have extended the work of Manhart et al. (2008) to extent its application up to the inertial layer, *i.e.* $y < 0.1\delta$. They proposed an analytical formulation of the streamwise velocity taking into account both streamwise pressure gradient and Reynolds stresses effects of the buffer layer. They validated their model with a periodic channel flow and with a periodic arrangement of hills subjected to both favorable and adverse pressure gradients. Their simulations yield to good results for first order statistics even when the first near-wall point was located in the logarithmic region. They were able to reproduce flow separation phenomenon even with a very coarse grid.

The methods presented above are for incompressible flows. Wang & Moin (2002) have implemented a similar method but they added the energy equation to the model in order to compute the temperature profile for compressible flow. Larsson and Kawai (Kawai & Larsson 2012, 2013) proposed a similar technique and compared the length scales, grid resolution and accuracy. These models are commonly called two-layers wall-model. Nonetheless, the model presented by Larsson and Kawai has been developed for equilibrium boundary layer only. The strategy proposed in this study is to combine the two-layers model of Larsson and Kawai and the non-equilibrium wall model developed by Duprat et al. (2011).

The averaged Navier–Stokes equations are used to develop the wall-model since the filtered velocity is equivalent to the averaged velocity closer to the wall (Piomelli & Balaras 2002). This set of equations, known as the unsteady thin-boundary-layer equations or UTBLE, can be derived from the Navier-Stokes equations:

$$\frac{\partial \bar{u}_i}{\partial t} + \frac{\partial \bar{u}_i \bar{u}_j}{\partial x_j} = -\frac{1}{\bar{\rho}} \frac{\partial \bar{p}}{\partial x_i} + \frac{\partial}{\partial y} \left[(\nu + \nu_t) \frac{\partial \bar{u}_i}{\partial y} \right], \quad (4.13)$$

$$\frac{\partial \bar{e}}{\partial t} + \frac{\partial \bar{e} \bar{u}_j}{\partial x_j} = -\frac{\bar{u}_j}{\bar{\rho}} \frac{\partial \bar{p}}{\partial x_j} + \frac{\partial}{\partial y} \left[(\nu + \nu_t) \bar{u}_j \frac{\partial \bar{u}_j}{\partial y} + C_p \left(\frac{\nu}{P_r} + \frac{\nu_t}{P_{rt}} \right) \frac{\partial \bar{T}}{\partial y} \right], \quad (4.14)$$

where \bar{u}_i , $\bar{\rho}$ and \bar{p} are the filtered parameters and ν_t the turbulent viscosity.

Wang & Moin (2002) neglected the left-hand side terms, the advection terms, in the vicinity of the wall. They showed that neglecting the pressure gradient term is not adapted for non-equilibrium flow. In fact, the inclusion of the pressure term allows for a significant improvement of the model predictions. Duprat et al. (2011) proposed to reduce the TBLE to the terms of the right-hand side. Under these assumptions, the simplified velocity streamwise momentum can be computed with:

$$\frac{\partial \bar{u}}{\partial y} = \frac{\frac{\partial \bar{p}}{\partial x} y + \tau_w}{(\mu + \mu_t)}, \quad (4.15)$$

where the wall-shear stress τ_w and the turbulent viscosity μ_t are the unknown variables of the equation, P_r is the Prandtl number and P_{rt} the turbulent Prandtl number.

Similarly, the temperature equation using adiabatic boundary conditions can be computed as:

$$\frac{\partial \bar{T}}{\partial y} = \frac{(\mu + \mu_t) \bar{u} \frac{\partial \bar{u}}{\partial y} + \frac{\partial \bar{p}}{\partial x} y \bar{u}}{C_p \left(\frac{\mu}{P_r} + \frac{\mu_t}{P_{rt}} \right)}. \quad (4.16)$$

This simplified model, also called STBLE, has two unknown variables. To close the system, one of the variables needs to be predicted. Nituch et al. (1978) and Balaras et al. (1996) have proposed a definition of the turbulent viscosity using an ad-hoc damped mixing-length limited to the linear and inertial region. The pressure gradient effect on the eddy viscosity is modeled by a non-dimensional parameter α that quantifies the preponderant effect between shear stress and streamwise pressure gradient. The turbulent viscosity is defined by:

$$\mu_t = \mu \kappa y^* [\alpha + y^* (1 - \alpha)^{3/2}]^\beta \left(1 - \exp \left(\frac{-y^*}{(1 + A \alpha^3)} \right) \right)^2, \quad (4.17)$$

where κ is the Von Karman constant, $\alpha = \frac{u_\tau^2}{u_{\tau,p}^2}$ the non-dimensional parameter and y^* the non-dimensional length. The constant A and β are determined through *a priori* tests.

The non-dimensional variables have been proposed by Manhart et al. (2008) as a scaling for boundary layer subjected to pressure gradient. The scaling takes into account the wall shear stress and the streamwise pressure gradient. The non-dimensional velocity u^* and length scale y^* are defined by:

$$u^* = \frac{\bar{u}}{u_{\tau,p}}, \quad (4.18)$$

$$y^* = \frac{\bar{\rho} y u_{\tau,p}}{\bar{\mu}}, \quad (4.19)$$

where $u_{\tau,p} = \sqrt{(u_\tau^2 + u_p^2)}$ is the combined velocity with $u_\tau = \sqrt{(\tau_w/\bar{\rho})}$ the friction velocity and $u_p = \left| \bar{\mu}/\bar{\rho}^2 \partial \bar{p}/\partial x \right|^{1/3}$ the pressure gradient based velocity as proposed by Simpson (1983).

Equations 4.15 and 4.16 are ordinary differential equations that are solved algebraically every time step. The STBLE model uses its own grid of length y_{wm} . The 2 coupled ODES uses the filtered variables from the LES as a boundary condition, while

the LES uses the predicted wall-shear stress $\tau_{w_{\text{wm}}}$ and wall heat diffusion $\dot{q}_{w_{\text{wm}}}$. The wall-model is characterized by an “input-output” process that takes information from the LES; this becomes the upper boundary condition for the STBLE model; the STBLE is then resolved numerically to compute the wall-shear stress and the heat flux; which is injected back into the LES.

The model allows the use of a coarser grid where the first near-wall point y_1 has to lie in the inertial layer, *i.e.* $y < 0.1\delta$. Duprat et al. (2011) showed that their model was accurate until roughly 100 wall units. They estimated that the best results are found when the first near-wall cell lies in the buffer layer, *i.e.* $y_1^+ < 40$. Kawai & Larsson (2013) proposed a similar location for the first grid point, *i.e.* $y_1^+ > 50$. They also showed that almost all the STBLE model use the first off-wall LES nodes as a matching location to feed the wall model, *i.e.* $y_{\text{wm}} = y_1$. Due to the poor near-wall resolution in the LES mesh, numerical errors and subgrid modeling are expected to be large in the first grid point of the LES. In order to reduce the resulting errors, Kawai and Larsson proposed to increase the length y_{wm} , *i.e.* $y_{\text{wm}} \neq y_1$. Due to the validity range of the turbulent viscosity model (eq. 4.17), the wall-model top BC needs to lie in the inertial layer, *i.e.* $y_{\text{wm}} < 0.1\delta$.

Kawai & Larsson (2013) demonstrated, through high Reynolds number channel flow simulations, that using the second near-wall cell was enough to improve the results. Using the wall-model from the first grid point yielded to an overprediction of the Van Driest velocity.

Figure 4.25 shows a representation of the STBLE near the wall using the off-set method of Kawai and Larsson with $y_{\text{wm}}/y_1 = 3$. The model is validated through *a priori* and *a posteriori* comparisons with direct numerical simulations of the evolving boundary layer subjected to a favorable/adverse pressure gradient (sec. 4.2).

4.3.1 *A priori* test

The model is first validated by *a priori* tests using the DNS data of section 4.2. A and β coefficients from equation 4.17 have to be determined through these *a priori* tests. The DNS data along the wall-normal direction at two x -locations (ZPG and APG) are used as inputs to feed the STBLE ODEs. The wall-shear stress and the wall temperature computed by the wall-model are then compared to the resolved shear-wall stress and the resolved wall temperature. The streamwise pressure gradient, $\partial p/\partial x$, computed by the LES and injected into the STBLE, has been averaged in z -direction to avoid spurious fluctuations of the wall-modeled solution due to the turbulence of the pressure field. The

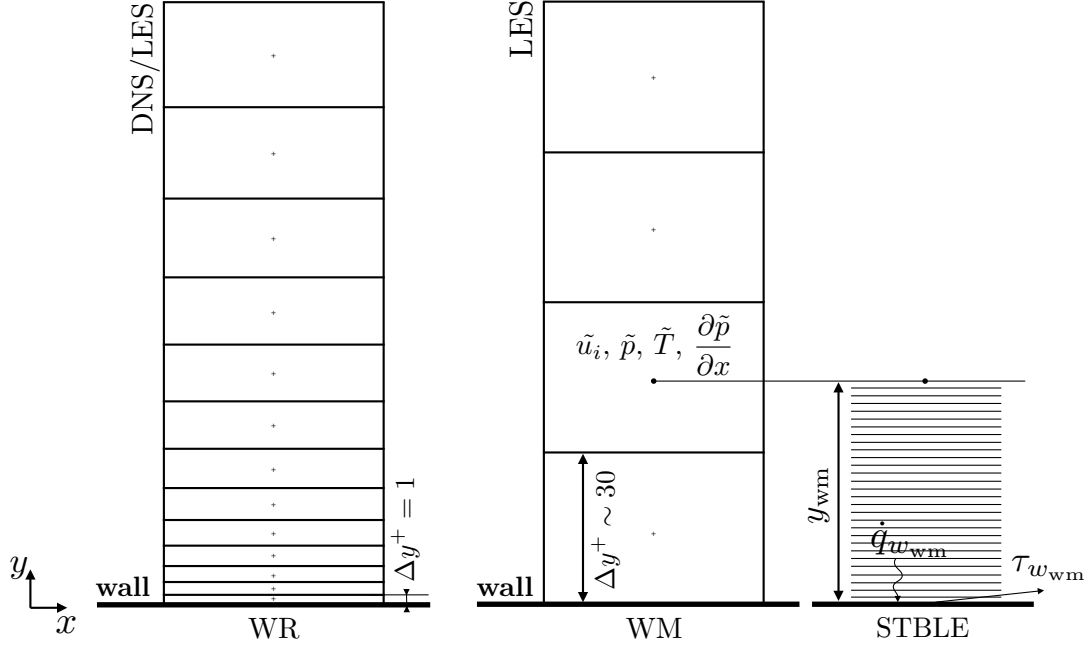


Figure 4.25: Representation of the STBLE model coupling with LES compared to DNS.

pressure gradient, injected into equations 4.15 and 4.16, is computed by:

$$\frac{\partial \bar{p}}{\partial x} = \frac{1}{L_z} \frac{\partial}{\partial x} \int_0^{L_z} p \, dz. \quad (4.20)$$

Figure 4.26 shows a wall-shear stress comparison over time for both zero- and adverse-pressure gradient. For those tests, the length in wall-units y_{wm}^+ is set to 25, or equivalently $\Delta y_{wm}^+ = 50$ for both zero and adverse pressure gradient regions. This means that the dimensional length y_{wm} is changed accordingly to the wall-shear stress to keep the wall unit length constant.

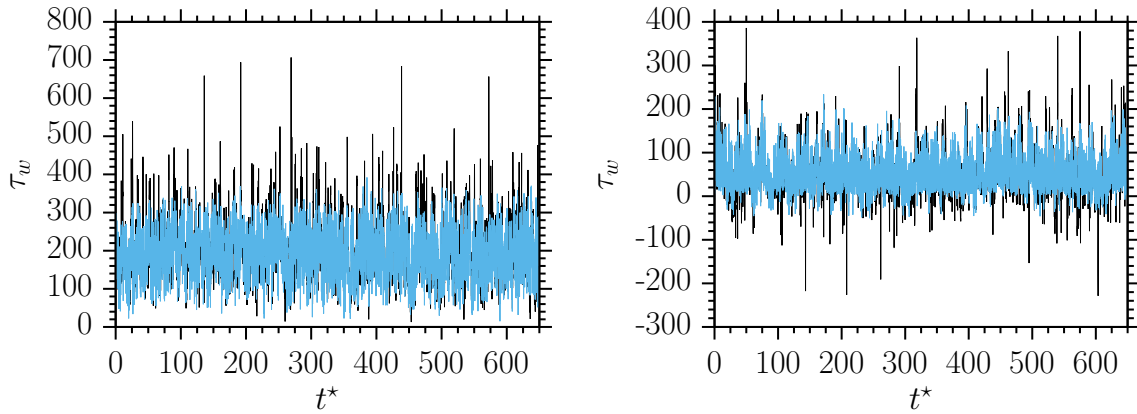
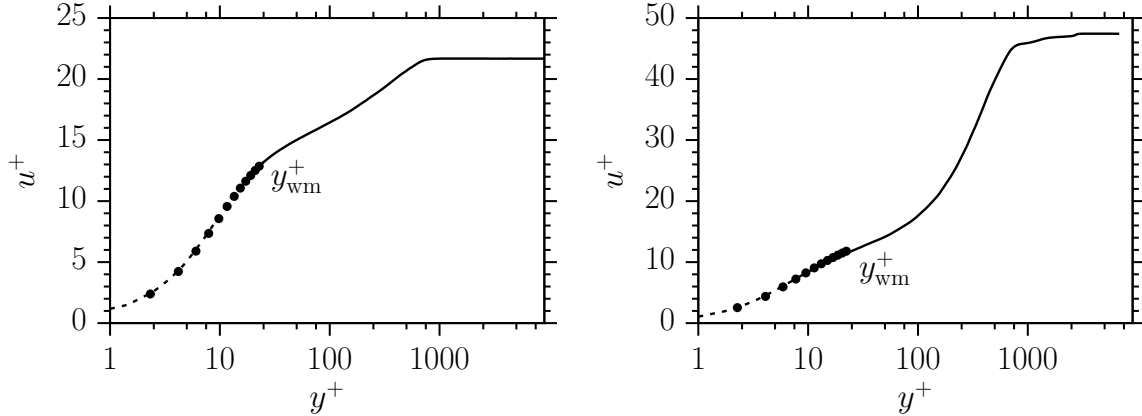


Figure 4.26: Wall-shear stress over time with zero-pressure gradient (*left*) and adverse pressure gradient (*right*); —: Wall-resolved data, —: Reconstructed data using the STBLE model.

Pressure gradient	y_{wm}	N_{wm}	L1-error	L2-error
Zero	25	50	1%	12%
Adverse	15	50	-2.5%	14%

Table 4.2: Results of the *a priori* test using the DNS of section 4.2.Figure 4.27: Van Driest velocity along the wall-normal direction with zero-pressure gradient (*left*) and adverse pressure gradient (*right*); $-$: Wall-resolved data ($--$: Subtracted data), \bullet : Reconstructed data using the STBLE model showing every 4th-grid line.

The coefficient A and β have been setup in order to reduce the L1-error on the wall-shear stress, *i.e.* $\text{L1-error} = \langle (\tau_{w_{\text{wm}}} - \tau_w) / \tau_w \rangle$. The best choice for β is found to be $\beta = 0.4$ which is lower than the previously chosen value of $\beta = 0.78$ from Duprat et al. (2011) but closer to the value used by Nituch et al. (1978) of 0.5. The damping coefficient A is fixed at 18. The values proposed in the literature are similar for the equilibrium flow, *i.e.* $\alpha = 1$. The damping function from equation 4.17 is expressed by $(1 - \exp(-y^*/(1 + A\alpha^3)))$. Without pressure gradient, Wang & Moin (2002), Cabot & Moin (2000) used $(1 - \exp(-y^*/19))$ and $(1 - \exp(-y^*/17))$, respectively. It is similar to the value $(1 - \exp(-y^*/19))$ computed in the *a priori* test. For non-equilibrium flow, Duprat et al. (2011) found a similar value of $(1 - \exp(-y^*/18))$.

The Van Driest velocity is presented in figure 4.27. The averaged profile computed by the wall-modeled simulation is similar to the DNS data profile, especially for the zero-pressure gradient case. In the APG region, the law of the wall is slightly over-predicted at y_{wm} by less than 1%. Table 4.2 shows the L1- and L2-error of the wall-shear stress prediction. The L1-error gives good results for both regions as it has been used to determine the coefficient of the wall-model. The under-prediction of the wall-shear stress RMS can be seen on figure 4.26, especially on the large fluctuation of the wall-shear stress where the model cannot handle the spurious fluctuations of the inner layer turbulence.

	L_x/δ_{in}	L_y/δ_{in}	L_z/δ_{in}	N_x	N_y	N_z
WM-LES	80	13	2.5	768	64	64
Kawai & Larsson (2013)	15	15	3	-	-	-
	Δx^+	Δy_1^+	Δz^+	Re_θ		
WM-LES	67	45	45	4260		
Kawai & Larsson (2013)	613	154	368	50×10^3		

Table 4.3: Grid requirements for the WM-LES

4.3.2 *A posteriori* test

In this section, a WM-LES is performed using a boundary layer configuration similar to the DNS of section 4.2. The grid resolution and accuracy of the wall-model in Large Eddy Simulation have been discussed by Kawai & Larsson (2012). They suggested that the inner layer of the boundary layer in free-stream flow, *i.e.* $y/\delta < 0.1$, can be modeled by an universal law. They assumed that the first near-wall grid point must be located in the log-layer, *i.e.* $y_1^+ > 40 - 50$. Using the off-set method explained above, the first point where the wall-model takes as input the instantaneous solutions from the LES should be at least $y_{wm}^+ > 50$.

The grid resolution in both streamwise and spanwise directions should be, at minimum, of the same wall unit length as the wall-normal grid spacing. As shown by Larsson and Kawai, the motion of the turbulence is cut-off by the grid-spacing at the wall, so that the LES cannot resolve turbulent eddies of size below Δy_1^+ . Kawai & Larsson (2013) have performed a WM-LES of high Reynolds number supersonic turbulent boundary layer from Souverein (2010). The momentum thickness Reynolds number of their WM-LES was about 50×10^3 . Their model is in good agreement with the DNS solutions for the total stresses and velocity profiles. The grid resolutions of the WM-LES was $\Delta x^+ = 613$, $\Delta y^+ = 153$ and $\Delta z^+ = 368$.

In our WM-LES, the momentum thickness Reynolds number is lower than the simulation of Kawai and Larsson, *i.e.* $Re_\theta \sim 4.3 \times 10^3$. Using the same grid resolution will end up with an under-resolved boundary layer due to the reduced size of the boundary layer. The first grid point in wall-unit, Δy_1^+ , is set to 45. For the streamwise and spanwise direction, the grid spacing is $\Delta x^+ = 67$ and $\Delta z^+ = 45$. The grid requirements are summarized in table 4.3. The WM-LES uses the WALE sub-grid scale model defined in section 2.1.3.

The transition phenomenon observed in section 4.2 cannot be simulated using the wall-model implemented. The inlet boundary layer is then generated by a synthetic turbulence inflow boundary condition introduced in section 2.3.3. The inlet profiles, used by the inflow boundary condition, are extracted from the DNS in the fully-turbulent zone

($x/\delta_{in} = 200$). The streamwise length L_x is similar to the previous DNS. The first part of the streamwise length is used as a buffer for the synthetic inflow boundary condition. The figures are taken at a specific x where the flow is fully turbulent, away from the synthetic inlet.

As for the DNS, the WM-LES uses an additional force to impose the pressure gradient along the streamwise direction. This force is similar to the one defined in figure 4.14. The x -direction is normalized by the incoming turbulent boundary layer thickness δ_{in} which is different from section 4.2 where the incoming boundary layer is laminar. The statistics are averaged over 200 non-dimensional time unit. The wall-model is implemented using the following algorithm,

Algorithm 3 WM-LES

- 1: **procedure** AT EACH ITERATION
 - 2: LES calculation
 - 3: The LES solutions at a specific y_{wm} is injected in the top STBLE BC
 - 4: The STBLE is solved to compute $\tau_{w_{wm}}$ and $\dot{q}_{w_{wm}}$
 - 5: $\tau_{w_{wm}}$ and $\dot{q}_{w_{wm}}$ are injected back to LES through an additional force at y_1 .
-

Duprat et al. (2011) used an additional viscosity term to impose the wall-shear stress at the wall. This corrective parameter, which can be assimilated to a viscosity, is computed using the wall-shear stress computed by the LES and the wall-shear stress predicted by the wall-modeled simulation. This method is suitable for finite volume code but can lead to spurious results with finite difference code. Other methods exist in the literature to impose a wall-shear stress (BC). The method implemented in this study is an additional force integrated along the wall-normal direction following equation 4.21. This force is added to the x -momentum equation with an additional energy source computed by the wall-modeled heat diffusion term ($\dot{q}_{w_{wm}}$). The wall boundary condition uses the regular no-slip condition with a fixed temperature computed by the wall-modeled heat diffusion term.

$$F_x = \frac{\tau_{w_{wm}} - \tau_{w_{LES}}}{y_1}. \quad (4.21)$$

Figure 4.28 shows the normalized velocity profiles where the solution of the inner layer is plotted using the previous DNS. It shows the zero-pressure gradient solutions taken at a similar Re_θ and the adverse pressure gradient profiles taken at a similar Δp^+ . The velocity has not been normalized by the Van Driest formulation, as it should be the case in compressible flow, due to integration term along the wall-normal direction which misses the information of the inner layer in the WM-LES. The grid resolution can be seen in the plot at $y_1^+ = 22$ and $y_2^+ = 68$. These two first-points are slightly underestimated

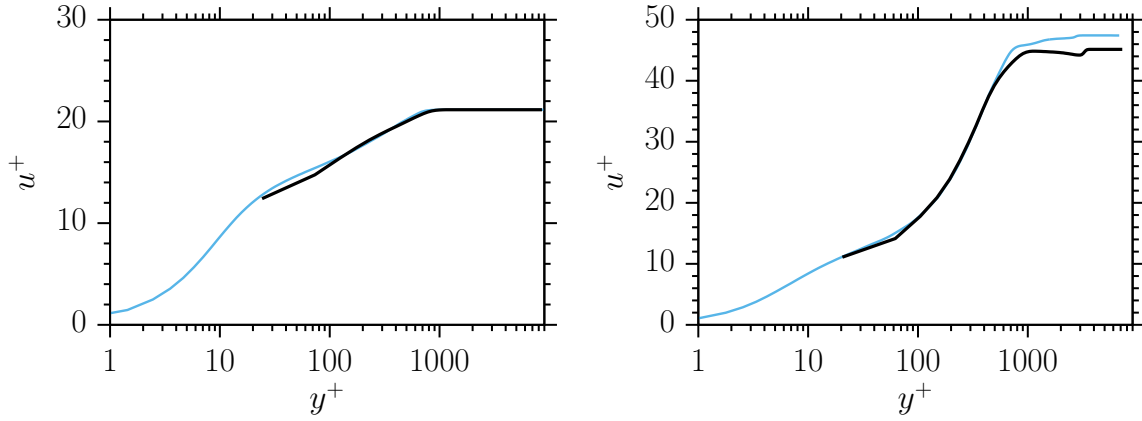


Figure 4.28: Normalized velocity along the wall-normal direction, zero-pressure gradient (*left*) and adverse pressure gradient (*right*); —: WM-LES, —: DNS.

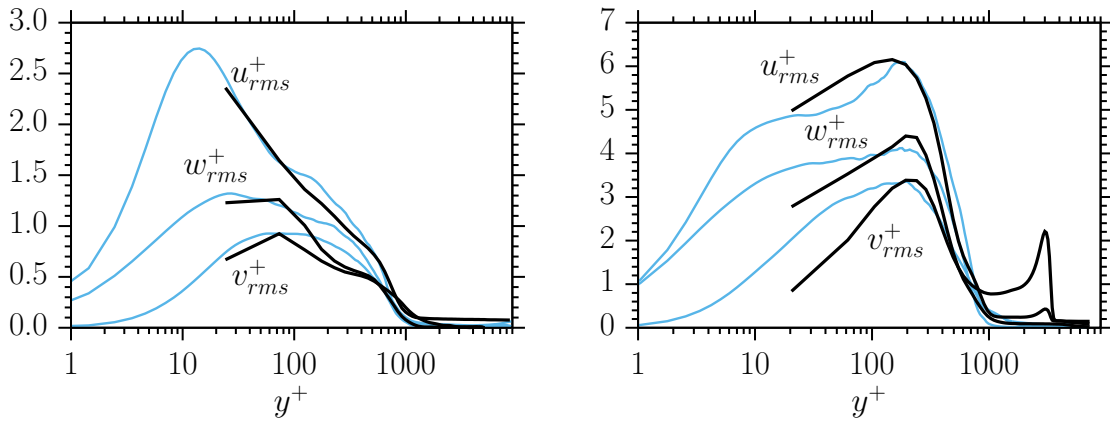


Figure 4.29: Normalized velocities RMS along the wall-normal direction, zero-pressure gradient (*left*) and adverse pressure gradient (*right*); —: WM-LES, —: DNS.

due to the unavoidable numerical and sub-grid modeling errors captured from the wall-modeled simulation. For the ZPG, the outer layer is in good agreement with the DNS. For the APG, the first part of the outer layer is well captured. The normalized velocity is underestimated outside of the boundary layer (the friction velocity u_τ is over-predicted in the APG zone). This behavior is due to the fact that we are comparing the profile at a similar Δp^+ and not at a comparable Re_θ .

Figure 4.29 shows the velocities RMS along the wall-normal direction for both ZPG and APG. The region in the range $100 < y^+ < 500$ is under predicted in all directions with a maximum difference of 6%. This behavior can be explained by the fact that we are cutting the most energetic part of the fluctuations, *i.e.* $y^+ < 50$. The upper layer is then unresolved due to the lack of energy from the buffer layer that has been removed by the grid near the wall. In the APG region, the wall-modeled boundary layer is underestimated near the wall, especially for the wall-normal and spanwise velocities. The peak of spanwise fluctuating velocity at $y^+ = 3000$ is due to the presence of a weak shock emanating from the adverse pressure gradient zone.

This section demonstrates that the wall-model implemented from Kawai & Larsson (2013) and from Duprat et al. (2011) shows a good agreement with the previous resolved DNS. The velocity fluctuations match the DNS profiles even with an adverse pressure gradient, especially in the outer layer.

5

Planar nozzle flow

The large-eddy simulation of an over-expanded planar nozzle is simulated in this section to validate the code with complex geometry and to confirm the adaptability of the wall-model for nozzle flow simulation. This flow case has been simulated before by Olson & Lele (2011) reproducing a similar experiment from Johnson & Papamoschou (2010). The results of this section highlight and explain the different phenomenon producing the shock separation unsteadiness using spectra analysis. These phenomena, such as the incoming turbulent boundary layer, the shocks pattern, the separated shear layer or the recirculation bubbles downstream of the separation, interact with each others to create complex motions of the separation line. Meanwhile, the adaptability of the wall-model to reproduce the low-frequency unsteadiness is validated by comparing wall-resolved and wall-modeled results.

5.1 Experimental setup

The experimental setup of Papamoschou & Johnson (2006) was first published in an AIAA paper. Then, Papamoschou et al. (2009) and Johnson & Papamoschou (2010) investigated the causes of the jet plume unsteadiness observed in the experiment.

The experiment uses two flexible plates forming the upper and lower walls of the diverging section of the planar nozzle. The nozzle can be shaped using two sets of actuators located at the end of each plate. The side-walls of the nozzle test section are made of large optical windows in order to create a visualization of the entire internal flowfield. The characteristics of the test section are shown in table 5.1. The test section consists of a converging-diverging nozzle connected to a high pressure tank. The incoming flow is regulated by a honeycomb section to laminarize the flow. The converging section contour is fixed while the diverging section contour can be controlled by a deflection mechanism (fig. 5.1).

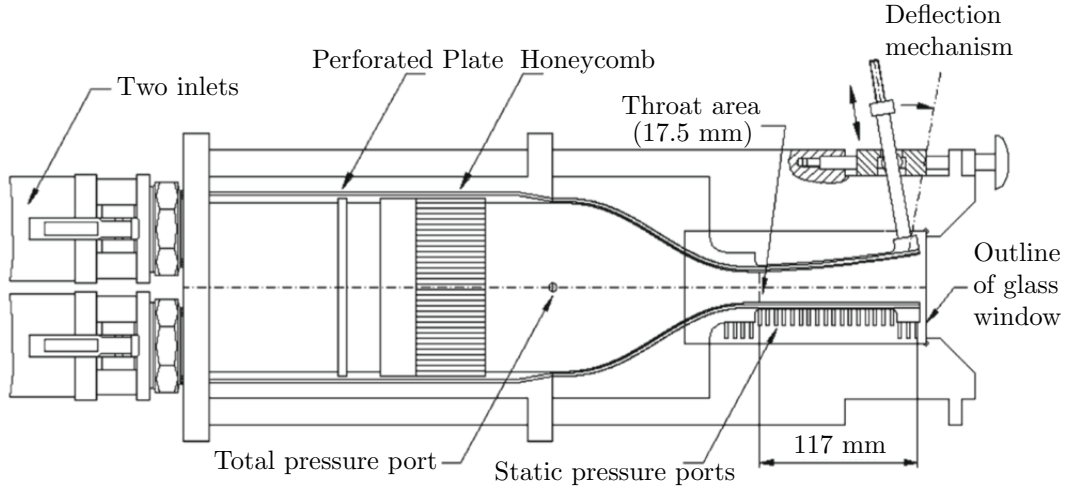


Figure 5.1: Schematic of the planar nozzle test section from Papamoschou & Johnson (2006).

H_t (mm)	L_d (mm)	NPR	ε
17.8	117	[1.45 : 1.9]	[1.4 : 1.7]

Table 5.1: The geometrical parameters of Papamoschou et al.'s planar nozzle.

The flow visualization is captured by a spark Schlieren system with a spatial resolution of 2560x1712 pixels. To capture the dynamic of the flow, they used time-resolved measurement probes. Four transducers were used on the upper wall to capture the static pressure with a frequency response of 30 kHz. A fifth probe was mounted on the lower wall. A dynamic probe was also used to measure the pressure fluctuations downstream of the shock. The number of probes along the wall is an important factor for the upcoming comparison with the simulation data since we are comparing a highly space-resolved wall pressure to only four time-resolved probes in the experiment.

The separation lines location is extracted from those four probes using a tracking procedure (Johnson & Papamoschou 2010). In the LES simulation, the wall is resolved in time and space. Thus, the tracking system will not be used in the numerical simulation.

The versatility of the test section allowed to create different test configurations. They studied four cases by changing the NPR and the nozzle area ratio ε (table 5.1). In terms of unsteadiness, the third case ended up to be the most interesting one. It showed a stronger shock amplitude combined with an asymmetric behavior of the separation line. The third case is the one used by Olson & Lele (2011) for their LES. The NPR for this case is set to 1.7 and the nozzle area ratio ε is equal to 1.6.

5.2 WR-LES simulation of Olson & Lele (2011)

To achieve a feasible computation, Olson & Lele (2011) have simulated the experiment of Johnson & Papamoschou (2010) by reducing the incoming Reynolds number by a factor of four and by increasing the throat boundary layer thickness δ_t by a factor of two. To reduce the computational cost, they have simulated only the diverging section of the experiment where the flow is considered supersonic ($M_t \sim 1$). Given the unsteady nature of the shock boundary layer interaction in the nozzle diffuser, they have used a LES code to elucidate the flow physics which govern the unsteadiness.

The incoming turbulent boundary layer has been generated by a synthetic boundary condition using the method of recycling/rescaling of Lund et al. (1998). In order to create a fully-turbulent boundary layer at the throat, the inlet is shifted upstream of the throat to create a buffer zone for the evolving boundary layer. Their simulation is advanced in time with a 4th-order Runge-Kutta scheme. All derivatives are computed using a 10th-order compact central differencing scheme combined to a high-wave number-biased artificial diffusivities to smooth out sharp discontinuity.

The computational mesh is generated by a structured mesh following the nozzle area contour defined by Papamoschou's experiment. The nozzle contour from the experiment, noted $f(x)$, can be approximated by a third-order polynomial law combined with a set of mathematical constraint used in the experiment:

$$f(x) = Ax^3 + Bx^2 + Cx + D. \quad (5.1)$$

The computational mesh is generated by mapping the structured mesh along the nozzle contour walls. The corner at the exit of the nozzle is approximated by a corner radius which has the size of the boundary layer δ . The maximal half-angle of the divergent is about 4° . Olson (2012) have performed a mesh convergence study by using three different meshes. They set up a parametric study by changing the NPR, the area ratio ε , the flange width at the exit or the incoming Reynolds number (Olson 2012).

The boundary condition in the span-wise direction ($L_z = 2H_t$) is periodic which differs from the experiment that has side walls. The outlet boundary condition uses the compressible far-field boundary condition combined to a "buffer" region near the outlet where the grid is stretched in order to smooth out gradients and to enforce the ambient condition.

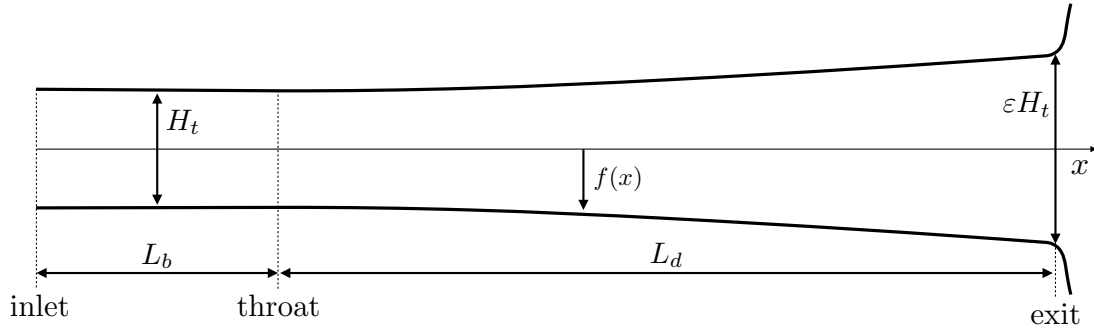


Figure 5.2: Schematic representation of the planar nozzle flow.

5.3 Wall-Resolved LES

The simulation of the wall-resolved planar nozzle follows the same parameters used by Olson & Lele (2011). The mesh is generated with the nozzle contour from equations A.2. Our wall-resolved LES is compared to the second mesh (Mesh B) of Olson & Lele (2011). They concluded that the averaged profiles of the mesh B were identical to the experimental results and that the flow was resolved in all directions.

All the subscripts used in this chapter are summarized in figure 5.2, where i is the inlet, t the throat, e the nozzle exit, a the atmospheric region, c the centerline of the nozzle, w the nozzle contour walls, d the divergent section and b the buffer section.

The exit lip, where the ambient domain (atmosphere) meets the nozzle exit, is generated by a different function than the one used by Olson (appendix A). The flange (exit wall) is defined as an infinite wall. The experiment uses finite flanges at the exit of width approximately $0.85H_t$. Olson (2012) showed that the behavior of the shock was not very sensitive to the flange width. The code is fully curvilinear, meaning that the mesh must be generated by a unique function to avoid multiple domains generation. This function must be of class C^∞ , or at least C^2 , to ensure good quality grid for the curvilinear Navier–Stokes equations. The mesh functions $(x(\xi, \eta, \zeta), y(\xi, \eta, \zeta), z(\xi, \eta, \zeta))$ are given in appendix A along with the parameters used to generate the mesh. Outside of the nozzle, the grid coarsens to form a buffer domain which models the far-field boundary condition of the experiment. The size of the outside domain is about $20H_t$. The grid quality is improved by using orthogonal cells close to the wall. Figure 5.3 illustrates a representation of the grid showing every 10th grid-line. The simulation uses the generalized curvilinear equations with the hybrid scheme activated. The hybrid scheme switches between the centered 6th-order scheme and the WCNS scheme. The 4th-order time scheme is used for time-advancement. The SGS model for the LES is the *WALE* model developed in section 2.1.3 and used for the wall-model simulation of section 4.3. Details of the solver and the numerical methods associated are given in the chapter 2.

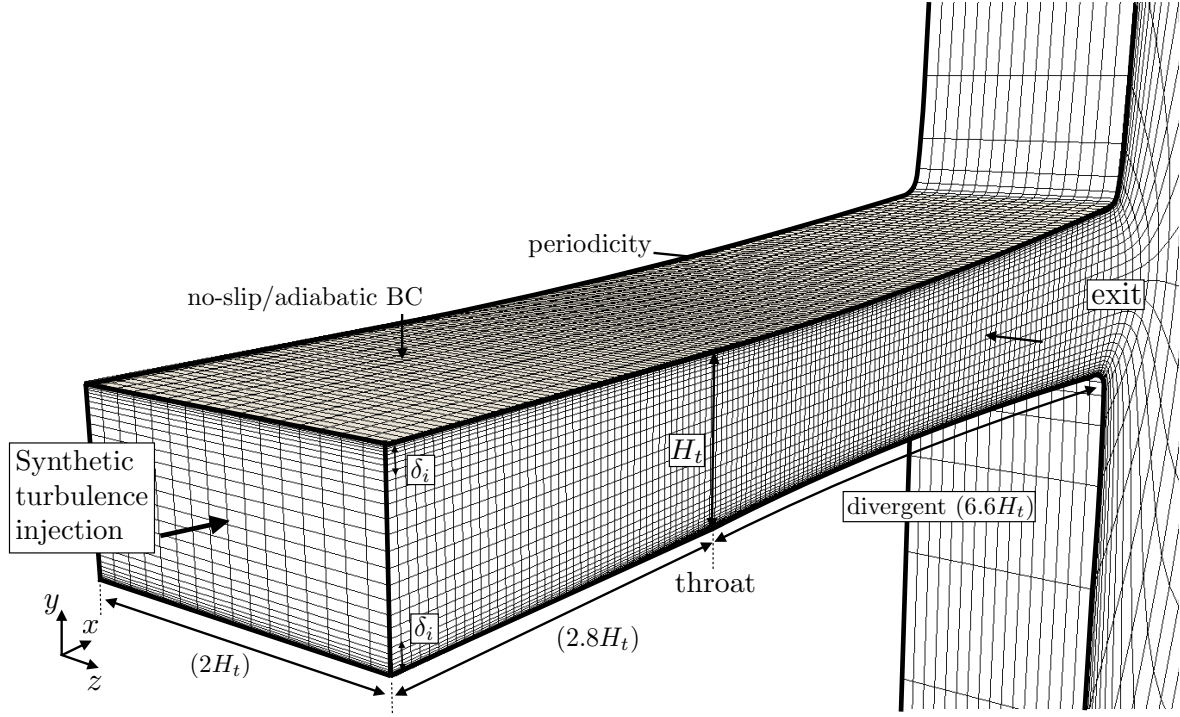


Figure 5.3: Grid representation from the Wall-Resolved case showing every 10th grid-line.

	N_ξ	N_η	N_ζ	L_z/H_t	L_b/H_t	Δx_i^+	Δy_i^+	Δz_i^+	Nb cells
WR-LES	896	256	320	2	2.8	30	[1 : 29]	20	73.4 M
Olson et al. (B)	768	256	256	2	3	30	[1 : 23]	20	50.3 M

Table 5.2: Grid parameters for the WR-LES of the planar nozzle flow.

	NPR	ε	Re	Re_θ	δ/H_t	Inlet synthetic method
WR-LES	1.7	1.6	90000	1000	0.1	Xie & Castro (2008)
Olson & Lele (2011)	1.7	1.6	90000	1100	0.11	Lund et al. (1998)

Table 5.3: Physical parameters for the WR-LES of the planar nozzle flow.

The span-wise length is two times the throat height following the setup of Olson. Periodic boundary conditions are used in the span-wise direction. The upper and lower walls are considered adiabatic with a no-slip condition on the velocity. For this wall-resolved simulation, a stretching law is used in the wall-normal direction to capture the viscous sublayer. The inlet boundary condition differs from the LES of Olson. They used the Lund method (Lund et al. 1998) to create the synthetic turbulence at the inlet. For our simulation, the method of Xie and Castro from section 2.3.3 has been used. The inlet profiles, containing the averaged variables and the Reynolds stress tensor, have been generated from the paper of Olson & Lele (2011), taken at the throat. A buffer zone, noted L_b , is added between the inlet and the throat in order to generate an accurate turbulent boundary layer. Table 5.3 shows the parameters compared to Olson & Lele (2011).

The flow is initialized by the Klein method where the flow is supersonic. In the diverging section of the nozzle, the flow variables follow the isentropic laws along the streamwise direction. To avoid a strong pressure rise at the initialization due to the internal shock, a \tanh function has been used to smooth the transition between the supersonic speed region and the atmospheric region. The results of the LES (probes, slices, time-resolved lines) have been saved after a time t_{start} in order to reach a “steady” state.

The figures presented in this section are normalized by the properties of the inlet boundary layer as $t^* = tu_{i,\infty}/\delta_i$ and $St = f\delta_i/u_{i,\infty}$. The streamwise direction x is centered at the throat for convenience. All figures have been averaged using slices extracted from the simulation during a time $t^* \sim 2000$.

5.3.1 Boundary-layer separation analysis

Figure 5.4 shows the time dependent boundary layer separation location for both upper and lower walls. It also captures the unsteady motion of the shock. The separation location x_s is computed by searching the location where the near-wall velocity becomes negative:

$$\overline{u_w(x_s(t), t)} < 0, \quad (5.2)$$

where $\overline{u_w}$ is the z -averaged streamwise velocity at the first point near the wall.

As it can be seen from figure 5.4, the separation location oscillates at a low frequency with an amplitude of 20 inlet boundary layer thicknesses. One can notice the difference of separation position between the upper and lower walls. The flow is known to be asymmetric at this given NPR. Johnson & Papamoschou (2010) have studied the asymmetric behavior of the separation as well as Olson & Lele (2011) who have observed the same behavior in their LES study. Figure 5.4 has not been compared to the experiment, nor to the WR-LES of Olson due to the different tracking systems used. The experiment uses four time-resolved probes combined with a system to track the position of the shock. Similarly, the LES of Olson uses the minimum value of pressure along the nozzle contour to find the separation location.

The asymmetric behavior of the separation line is highlighted in figure 5.5 through the ratio $x_s^{\text{top}}/x_s^{\text{bottom}}$ which shows the temporal asymmetry. The asymmetric parameter is mostly greater than one which means that the separated jet is always on the same side of the nozzle. This asymmetry, *i.e.* 4%, does not seem important but a small change in the separation locations can lead to a highly asymmetric flow downstream of the separation. For this run, the jet is oriented to the bottom of the nozzle. This behavior has been reported by Johnson and Papamoschou in their experiment. They have observed that the exhaust jet was oriented in either side during a given experiment. However, they observed that it can change from one experiment to the next suggesting that the asymmetry is sensitive to the startup condition. In our case, we have observed the same behavior by changing the initialization parameters for the Klein method (different seed). In one of our early test-case, the flow was oriented to the top wall of the nozzle (results not shown). The velocity at which the separation line oscillates, is given by:

$$u_s = \frac{d\bar{x}_s}{dt}, \quad (5.3)$$

where \bar{x}_s is the space filtered separation location at the bottom wall of the nozzle.

From figure 5.5, one can notice that the two signals are anti-correlated. This figure highlights the following patterns: When the internal shock moves downstream ($u_s > 0$), the flow is mostly symmetric. On the contrary, when the separation line moves upstream ($u_s < 0$), the flow is mostly asymmetric.

This behavior can be seen in the averaged Schlieren imaging shown in figure 5.6. When the internal shock is moving downstream, both top and bottom recirculation bubbles are of comparable sizes however when the internal shock is going upstream, a large recirculation bubble appears at the upper wall of the nozzle. The separated jet is then highly asymmetric. A detailed study of the asymmetric phenomenon will be proposed later.

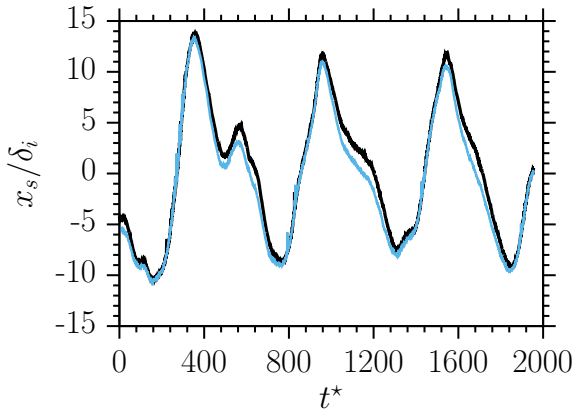


Figure 5.4: Separation location vs. time; —: Upper wall, —: Lower wall.

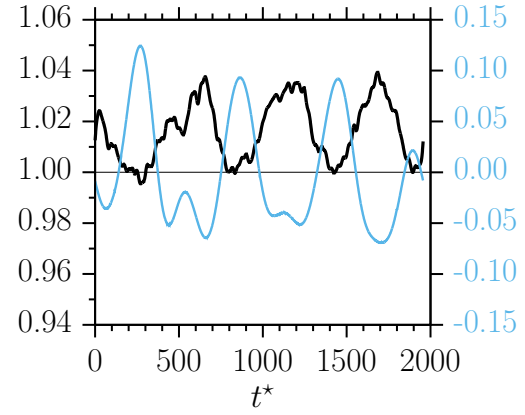


Figure 5.5: Asymmetric parameter $x_s^{\text{top}}/x_s^{\text{bottom}}$ (—) and dimensionless separation velocity speed $u_s/u_{i,\infty}$ (—) over time.

5.3.2 Comparison of profiles and boundary layer statistics

Figure 5.7 shows the longitudinal mean pressure distribution at the centerline and at the lower wall of the nozzle. The results have been compared to the LES of Olson as well as the experiment of Papamoschou and Johnsson. A conditional averaging has been operated using the separation line location x_s in the range of $x_s/\delta_i = 0$. Pressure distributions are in good agreement compared to both the experience and the simulation. The pressure peak in the nozzle centerline shown in figure 5.7-left at $x/\delta_i = 42$ is observed in both LES. This peak is the first Mach stem observable in the Schlieren imaging. The oscillations behind the Mach stem correspond to the compression and expansion waves, commonly called shock train.

At the nozzle throat, *i.e.* $x/\delta_i = 0$, the experiment does not correlate with the LES. This is expected, as the experience uses a converging section upstream of the throat, while the simulations use a channel section. The pressure distribution downstream of the throat seems to match that of the experiment indicating that the buffer zone at the throat has a minimal effect on the flow past the throat. The NPR of the LES, based on the throat pressure, is decreased by 4% compared to the experiment. Figure 5.11 shows a comparison of the normalized pressure gradient using Clauser's parameter β (equation 5.4). In the buffer layer, the flow is subjected to a favorable pressure gradient. The results indicate that the computations are accurately capturing the pressure gradient downstream of the throat compared to the experiment.

$$\beta = \frac{\delta^*}{\tau_w} \frac{dp}{dx} \quad (5.4)$$

The range of figures 5.8 and 5.9 is limited to $x/\delta_i = 20$ because of the unsteady

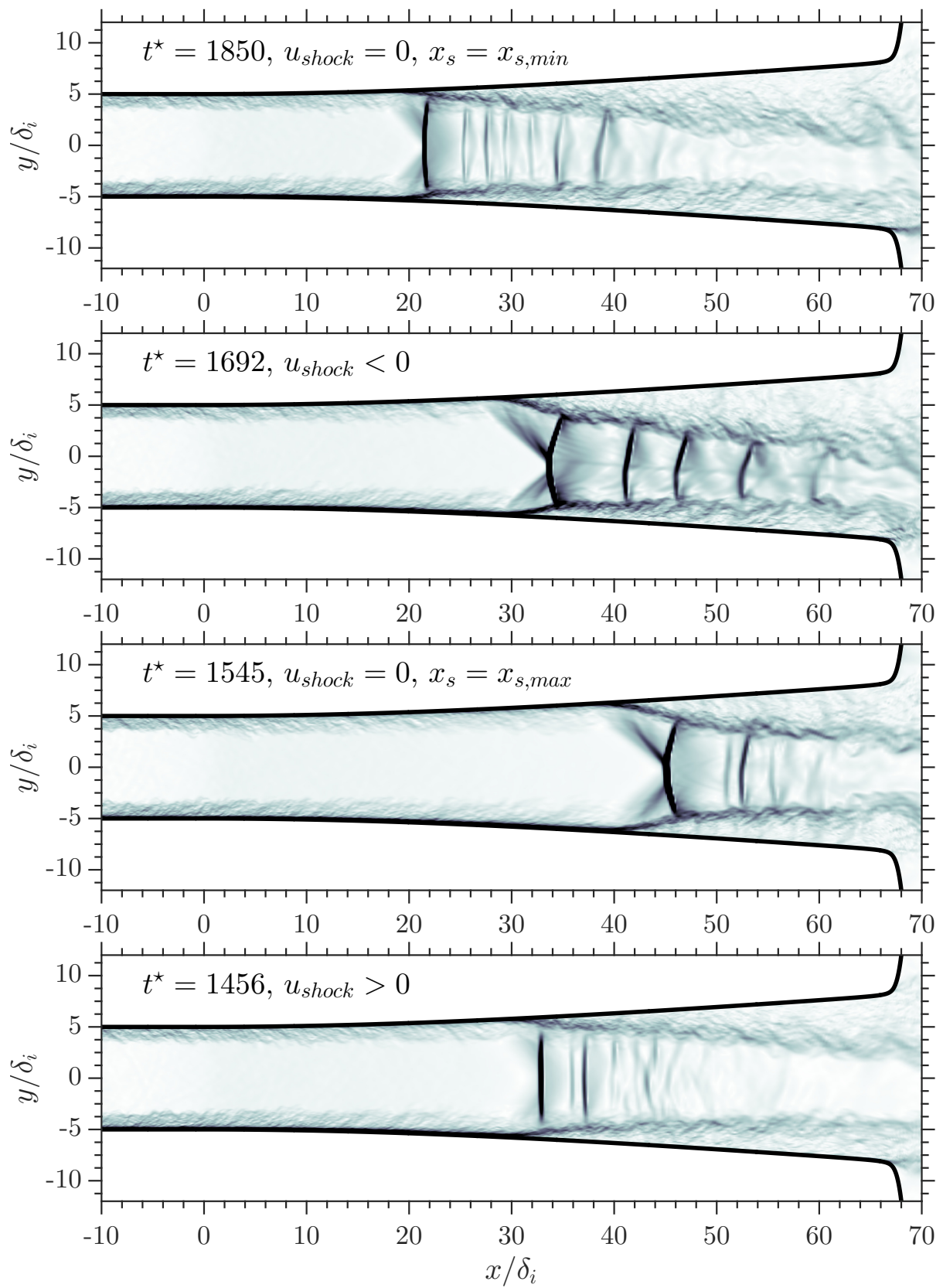


Figure 5.6: z -averaged numerical "Schlieren" imaging contour $|\nabla\rho|$ in the x - y plane at different times.

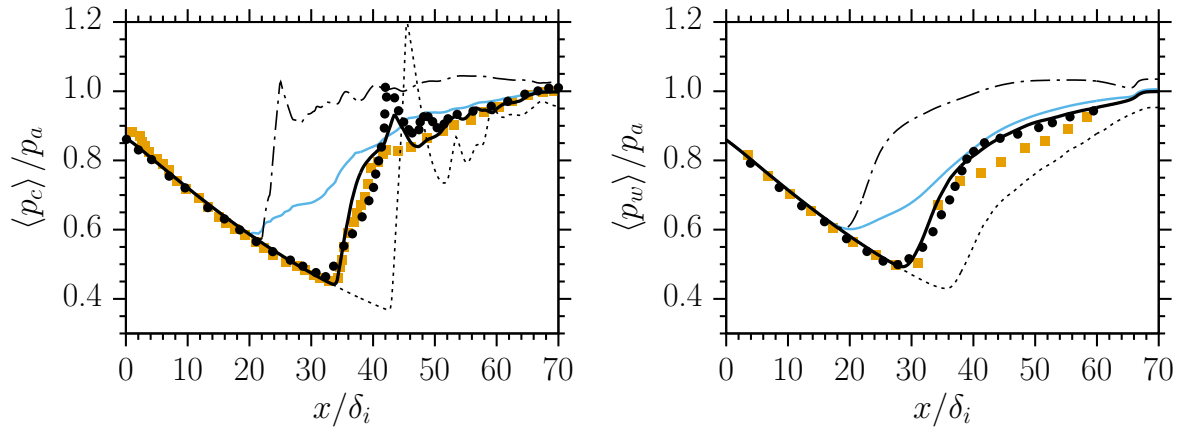


Figure 5.7: Longitudinal pressure distribution at the nozzle centerline (*left*) and pressure distribution at the lower wall (*right*); $-$: Total time average, $-$: Conditional averaging $x_s/\delta_i \sim 0$, $--$: Conditional averaging showing the maximal position $x_s/\delta_i \sim 10$, $- \cdot -$: Conditional averaging showing the minimal position $x_s/\delta_i \sim -10$, \bullet : WR-LES from Olson & Lele (2011), \blacksquare : Experimental results from Johnson & Papamoschou (2010).

fluctuations of the separation line that affect the time averaging. The first grid point in wall unit is displayed in figure 5.8. It shows a good resolution in y -direction, *i.e.* $\Delta y^+ < 1$. The different boundary layer thicknesses are shown in figure 5.9. It points out the growing effect of the boundary layer in the buffer zone due to the favorable pressure gradient. The shape factor $H = \delta^*/\theta$ captured along the x -direction is about 2.0. Downstream of the throat, the flow is following the isentropic relation and the boundary layer is subjected to a moderate favorable pressure gradient (fig. 5.11), *i.e.* $\beta \sim -0.7$. The discrepancy between the simulated data and the experiment comes from the fact that before the throat, the simulations use a buffer layer while in the experiment, the divergent region is directly connected to the throat.

Figure 5.12 shows the Van Driest velocity profiles downstream of the throat at $x/\delta_i = -10$. As explained by Olson, the boundary layer at the throat is subjected to a non-negligible pressure gradient, *i.e.* $\beta \sim -0.7$. The converged profile is thus shifted upward from the standard log-law fit. The profiles, captured at $x/\delta_i = -10$, are averaged in a mild-pressure gradient zone, *i.e.* $\beta \sim -0.2$, so that the effect of the pressure gradient on the boundary layer is moderate. The synthetic turbulence injection starts at $x/\delta_i = -28$ giving 18 boundary layer thicknesses for the flow to relax to a physical boundary layer. Xie & Castro (2008) have demonstrated that the method of synthetic injection needs at least 10 boundary layer thicknesses to reach a fully-turbulent flow. Figure 5.10 shows the structure of turbulence of the boundary layer in the buffer layer through the velocity fluctuations field. The synthetic eddy structures seem to extend to $x/\delta_i \sim 15$ giving 13 boundary layer thicknesses, in agreement with the streaky structures as observed by Xie and Castro. Past this recovery length, the velocity fluctuations exhibits more coherent

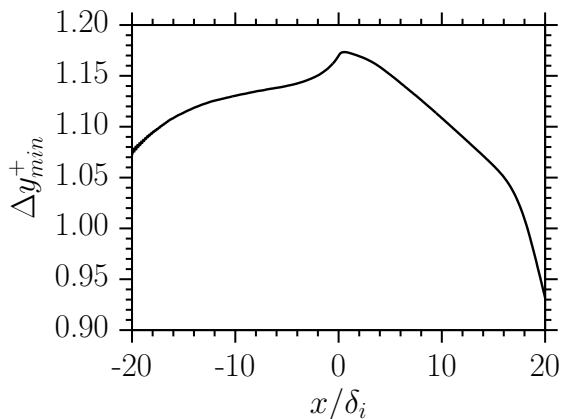


Figure 5.8: Wall-unit length Δy^+ at the first cell near the wall along the x -direction.

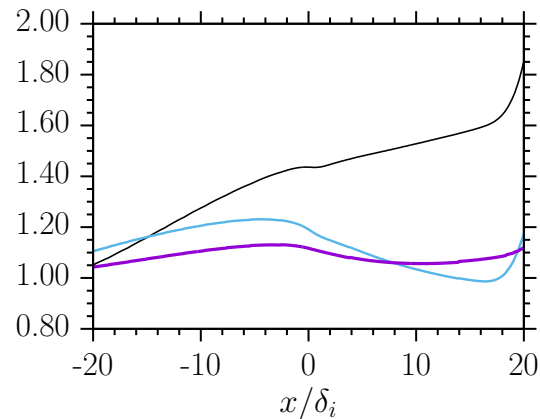


Figure 5.9: Normalized boundary layer thicknesses along the x -direction; —: boundary-layer thickness δ/δ_i (at 99%), —: momentum thickness θ/θ_i , —: displacement thickness δ^*/δ_i^* .

turbulent structures as previously observed in section 3.4. The velocity profile computed at $x/\delta_i = -10$ seems to have a better fit with the standard log-law compared to Olson’s results because of the reduced pressure gradient.

Similarly, the rms velocity profiles are displayed in figure 5.13 and compared to the LES of Olson. The outer layer of the boundary layer, *i.e.* $y^+ > 100$, has higher rms values especially in the streamwise direction. This behavior is due to the difference of x -location, *i.e.* a difference of pressure gradient, between the two profiles. The profile of Olson is plotted at the throat where the normalized pressure gradient is -0.7 ; while in the present LES, the profile is plotted at a normalized pressure gradient of -0.2 . This difference of the outer layer effect has also been observed by Spalart & Watmuff (1993). They experimented and simulated a turbulent boundary layer subjected to a pressure gradient. Figure 5.14 shows the present u_{rms}^+ profile compared to the results of Spalart. It shows the same behavior of the outer layer for moderate favorable pressure gradient. While at the throat, they showed similar behavior compared to Olson’s profile.

The present LES uses periodic boundary conditions in the spanwise direction. The aspect ratio of the grid, *i.e.* width to height at the throat, is about 3.5. The spanwise length must be sufficiently large to capture the large-scale turbulence. A two-point correlation based on pressure fluctuations along the spanwise direction is plotted at the throat and shown in figure 5.15. The decay of correlation at $z/L_z = 0.1$ demonstrates that the length in the spanwise direction does not impact the dynamics and the development of coherent structure in the flow. Similarly, the spectra of the two-point correlation is shown in figure 5.16 for two streamwise locations, at the throat and in the shear layer downstream of the separation. The range of energetic scales present in the shear layer is larger than in the boundary layer as observed by Olson & Lele (2011). The decay of the spectra for high

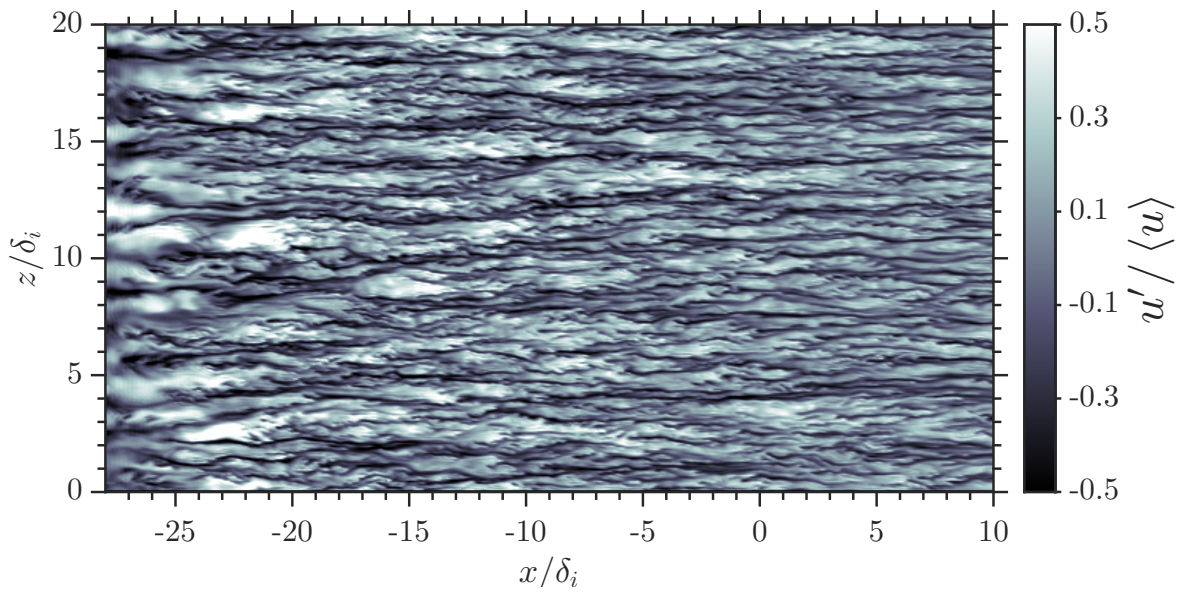


Figure 5.10: Instantaneous velocity fluctuations in the x - z plane at $y^+ \sim 20$.

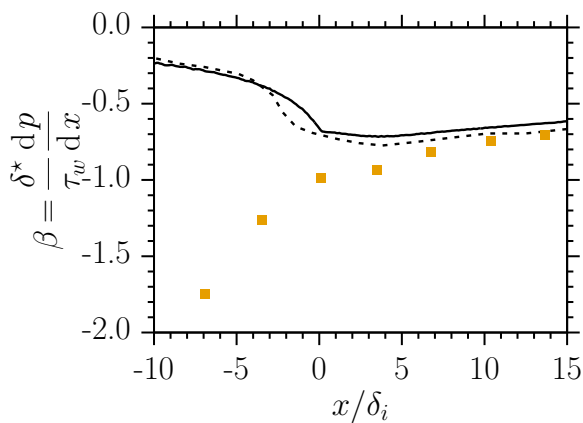


Figure 5.11: Normalized pressure gradient along the x -direction; $-$: present LES, $-$: WR-LES from Olson & Lele (2011), \blacksquare : Experimental results from Johnson & Papanoschou (2010).

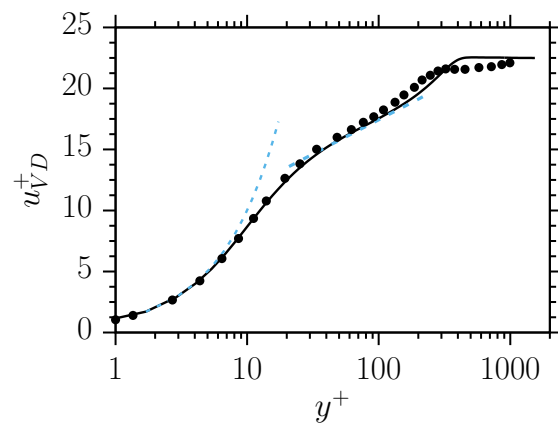


Figure 5.12: Van Driest velocity along the wall-normal direction at $x/\delta_i = -10$; $--$: $u^+ = y^+$ and the log-law with $\kappa = 0.41$ and $C^+ = 6.2$, $-$: present LES, \bullet : WR-LES from Olson & Lele (2011).

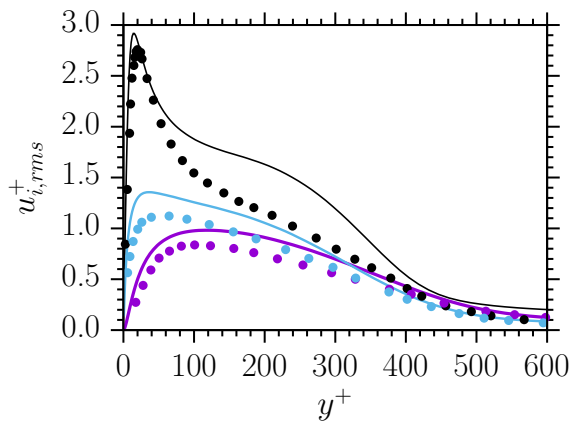


Figure 5.13: Normalized rms velocities along the wall-normal direction at $x/\delta_i = -10$; $-$: u_{rms}^+ , $-$: v_{rms}^+ , $-$: w_{rms}^+ , \bullet : WR-LES from Olson & Lele (2011).

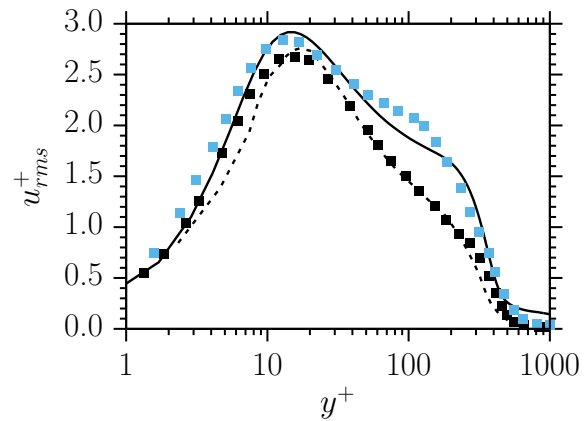


Figure 5.14: Normalized rms x -velocity u_{rms}^+ along the wall-normal direction at $x/\delta_i = -10$; $-$: Present DNS, $--$: WR-LES from Olson & Lele (2011), DNS from Spalart & Watmuff (1993) at \blacksquare : throat, \blacksquare : FPG.

wave numbers indicates the good quality of the grid resolution for both locations.

Figure 5.17 shows the pressure force on the structure discretized into x - and y -directions. The forces are computed as follow:

$$\vec{F} = \int_S (p_w - p_a) \cdot \vec{n} ds, \quad (5.5)$$

where p_w is the wall pressure, p_a the ambient pressure, ds the local surface element where the force apply, \vec{n}_i the normal vector to the surface and S the total surface of the nozzle including the upper and lower wall.

The y - and z -direction forces are commonly called side-loads. One can observe that the x -force fluctuates at a low frequency while the side-loads, *i.e.* y -force, has a broad range of fluctuations. The two forces are anti-correlated. When the shock reaches its downstream position, the streamwise force is maximum. As explained before, at this position, the flow is mostly symmetric. The symmetry of the flow reduces the side loads (fig. 5.17). When the shock is located at its upstream position, the streamwise force is minimal, the flow is highly asymmetric and the side loads are maximum.

The direction of the resulting force, noted α_F , defined in equation 5.6, is shown in figure 5.18 along with the separation location. The direction of the force applied on the nozzle is null when the shock is located farther downstream of the throat. On the contrary, when the separation is at its minimal position upstream of the nozzle, the force is highly asymmetric with an angle of about 50° . It is interesting to note that this force is oriented in the opposite way compared to the exhaust plume. In fact, the asymmetry of the flow, observable in figure 5.6 at $t^* = 1692$, creates a low-pressure area along the

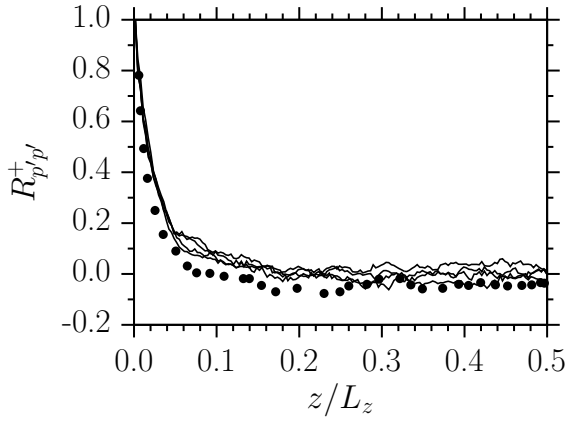


Figure 5.15: Two-point correlations function of wall pressure fluctuations along the span-wise direction at $x/\delta_i = 0$; —: Results at different x -location in the pre-shock boundary layer zone, •: WR-LES from Olson & Lele (2011).

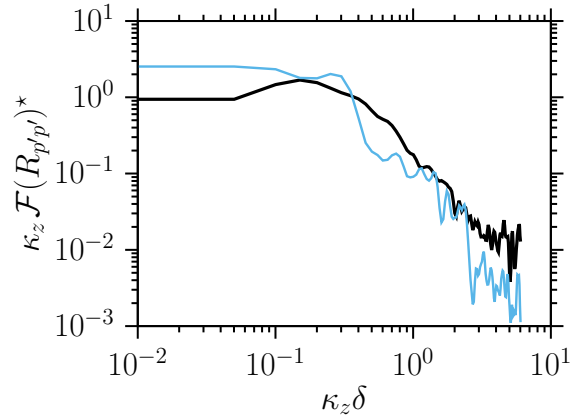


Figure 5.16: Pre-multiplied power spectral density of the two-point pressure fluctuations correlation function; —: at the throat, —: in the separated shear layer.

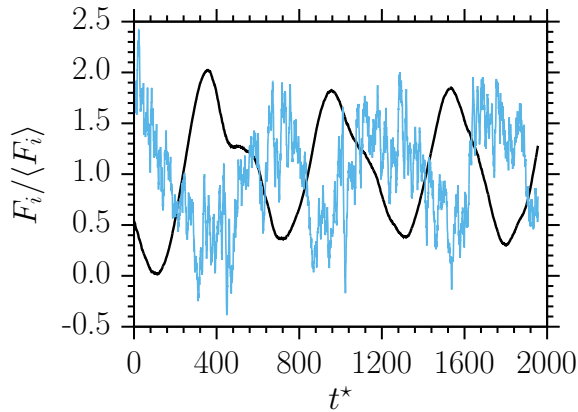


Figure 5.17: Normalized pressure forces over time; —: x -direction (F_x), —: y -direction (F_y).

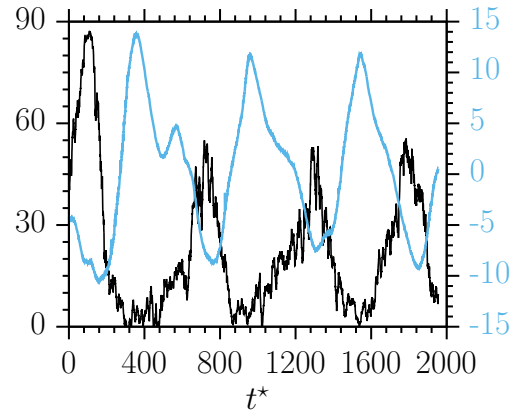


Figure 5.18: Angle of the resultant pressure force \vec{F} on the nozzle wall in degrees (—) and lower-wall separation location x_s/δ_i (—).

lower wall where the mixing layer is attached to the wall. At the top of the nozzle, a large recirculation area can be seen where the pressure is of the same order than the atmospheric pressure. While the exhaust plume is oriented to the bottom, the side-loads are opposed to it and oriented to the top.

$$\alpha_F = \tan^{-1} \left(\frac{F_y}{F_x} \right) \quad (5.6)$$

5.3.3 Shock-wave patterns

The numerical Schlieren picture (fig. 5.6) shows interesting shock-wave patterns. The classical shock pattern expected in divergent nozzles exhibits a lambda shock-wave structure (sec. 1). This pattern is close to the solution at $t^* = 1545$ which consists of an incident shock, IS, a reflected shock, RS and a Mach stem, MS (fig. 5.19). In this configuration, the separation of the boundary layer, due to the high adverse pressure gradient, creates an incident shock impinging the Mach stem at the triple point TP. The reflected shock, emanating from the triple point, realigns the incident flow to the original direction. The Mach stem is strong shock which creates a subsonic flow behind it.

The slip line that delimits the shear layer and the recirculation zone can be seen as a fictive wall, as proposed by many authors (Östlund 2002, Damgaard et al. 2004). The slip line then redefines the “effective” geometry of the nozzle by displacing the “effective” wall. The effective nozzle geometry is shorter and has a lower expansion ratio. Hunter (2004) showed that the change of effective geometry due to the slip line is acting as a natural “adjustment mechanism”. The area reduction coming from the effective geometry is acting as a confinement on the flow, which reaccelerates and produces multiple shocks. The succession of shocks is called a shock train and has been observed in many nozzle flows (Waltrup & Billig 1973, Matsuo et al. 1999, Weiss et al. 2010). At a given NPR, the over-expansion created by the effective geometry improves the thrust efficiency.

As discussed in section 1.3, the free interaction theory developed by Chapman can predict the pressure distribution in the separation zone. The deflection angle of the separated boundary layer θ_s corresponds to the deviation of the displacement thickness δ^* at the separation. This angle can be calculated by the Chapman theory and used afterwards to compute the incident shock angle θ_i (fig. 5.19) using the oblique shock-wave theory. The coupled system between the incident shock angle and the separation angle is complex, unsteady and highly sensitive to any change in the flow. Figure 5.19 shows a diagram of the separation area.

Due to the unsteadiness of the shock separation, the shock moves along the x -direction at a specific speed observed in figure 5.5. The speed of the shock is high enough to be taken into account by the Chapman theory. The diagram in figure 5.19 is similar to the SWBLI theory and shows the free interaction length L_I . The actual Mach number for the free interaction theory can be calculated by the relative speed of the shock:

$$M_I = M - M_{shock}, \quad (5.7)$$

where M_I is the relative Mach number of the shock, M the Mach number in the inviscid flow and M_{shock} the Mach number of the shock.

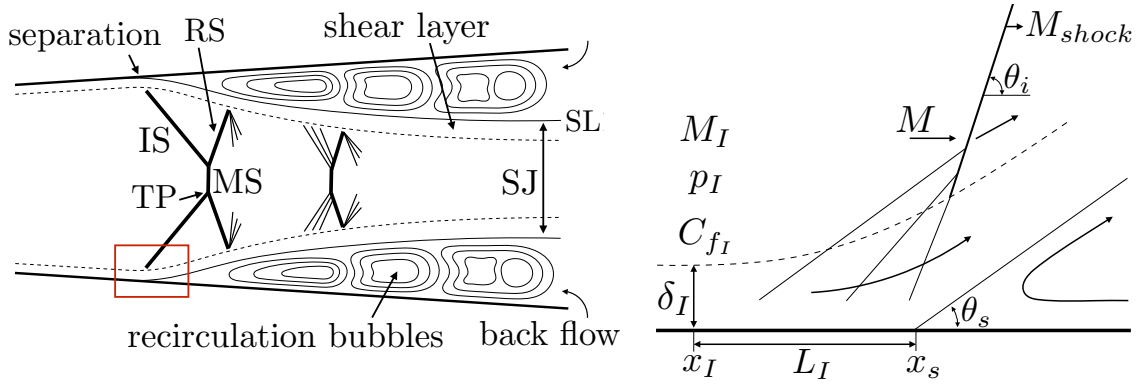


Figure 5.19: Representation of the lambda shock pattern (*left*) and the separation area (*right*); *MS*: Mach stem, *IS*: incident shock or separated shock, *RS*: reflected shock, *TP*: triple point, *SL*: slip line, *SJ*: supersonic jet, *s*: separation location, *I*: interaction location.

When the velocity of the shock is positive, *i.e.* the shock is moving downstream, the relative velocity of the interaction is reduced. This reduction of speed decreases the interaction length L_I and the adverse pressure gradient across the boundary layer. Thus, the deflection of the boundary layer becomes milder and the angle of deflection opens the effective area of the nozzle to the atmosphere. Because of the angle reduction and the relatively slow M_I , the incident shock vanishes for compression waves. The Mach stem expands across the wall-normal direction, delimited by the separated boundary layer. The modified shock pattern, when the shock is moving downstream, is shown in figure 5.6 at $t^* = 1456$ and in the diagram in figure 5.20.

5.3.4 Asymmetry of the separation line

As observed in figure 5.5, the separation is asymmetric as it moves upstream. The asymmetry phenomenon has been studied both experimentally and numerically (Johnson & Papamoschou 2010, Verma & Manisankar 2014, Hunter 2004). Johnson & Papamoschou (2010) observed the asymmetric flow separation for $NPR < 2.0$ and attributed the flow asymmetry to the ‘‘Coanda effect’’ (Wille & Fernholz 1965), whereby a jet surrounded by or adjacent to a solid surface attaches to that surface. Hunter (2004) observed similar asymmetric behavior in planar nozzle for $NPR < 1.8$ and attributed the reason to the natural tendency of an over-expanded nozzle flow to detach and reach a more efficient thermodynamic balance. They said that the effect was not a result of stronger shock-wave boundary layer interactions. Verma & Manisankar (2014) observed experimentally the asymmetric nature of the flow for $NPR < 2.0$. By changing the state of the upstream boundary layer (laminar, transitional and turbulent), they suggested that the boundary layer can trigger a flow asymmetry. They also confirmed the idea of Papamoschou

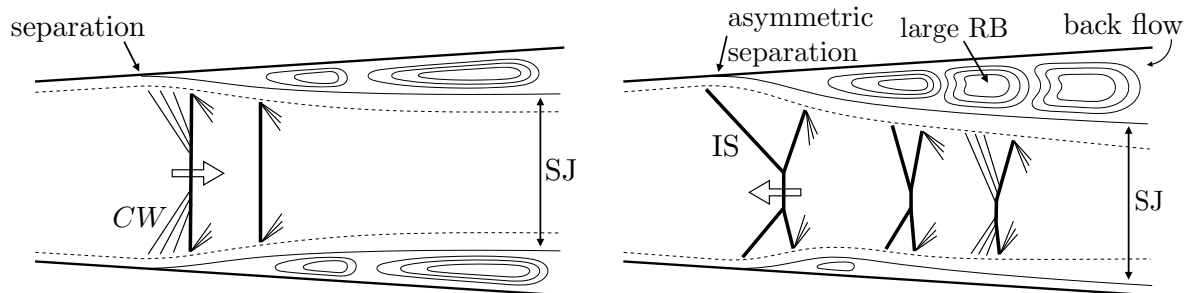


Figure 5.20: Representation of the shock pattern at $t^* = 1456$ when the shock is moving downstream (*left*) and at $t^* = 1692$ when the shock is moving upstream (*right*); Subscript as in figure 5.19, *CW*: compression waves, *RB*: recirculation bubbles.

who stipulate that the proximity of the separated shear layer to the nozzle walls plays a dominant role in initiating the asymmetry of the flow.

The flow asymmetry can be observed at $t^* = 1692$ in figure 5.6. The diagram associated with the instantaneous solution is shown in figure 5.20. A reattachment of the flow is observed at the lower wall after the first shock. This shock pattern is similar to the Restricted Shock Separation observed in Thrust Optimised Contour nozzle flow (Shimizu et al. 2006, Frey & Hagemann 2000). However, the restricted shock separation (RSS) is due to the internal shock originating just downstream of the throat which creates an inverse Mach reflection at the central portion further downstream of the throat. The restricted shock pattern is known to be mildly symmetric in TOC nozzle. On the contrary, when the flow separates from the wall, creating a large recirculation zone downstream of the separation, the shock pattern is commonly called Free Shock Separation (FSS). The transition between FSS and RSS is known to be highly unsteady, generating a sudden change in the side-loads level (Nave & Coffey 1973, Nguyen et al. 2003, Martelli et al. 2010). The FSS and RSS shock patterns are characterized in section 1.

In the present simulation, the flow seems to exhibit a FSS-like pattern at the upper wall and a RSS-like pattern at the lower wall. When the flow is symmetric, *i.e.* $u_s > 0$, the lower wall RSS pattern changes to FSS pattern. The transition between FSS and RSS is complex and presents a hysteresis cycle (Martelli et al. 2010, Frey & Hagemann 1998) (sec. 1). The theory of Papamoschou on the origin of the asymmetry is plausible in this simulation. The proximity of the separated shear layer to the nozzle walls can force the shear layer to reattach to the wall using the “Coanda effect”. The reattachment at both walls at the same time is not possible because the flow would be under-expanded at the exit which is not physically balanced. The choice of the side is still undefined but is known to be sensitive to the startup condition, *i.e.* the incoming boundary layer state (Johnson & Papamoschou 2010, Verma & Manisankar 2014).

When the shock is moving downstream, the flow does not reattach to any wall due to

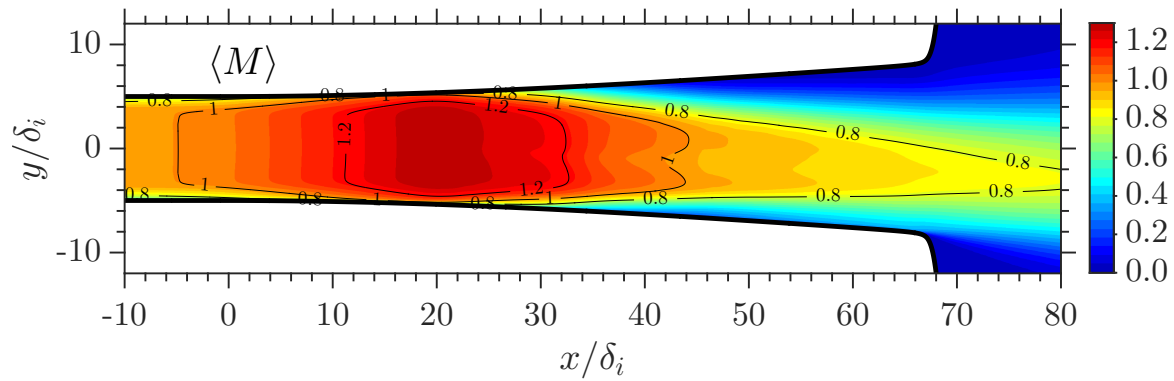


Figure 5.21: Mean Mach number $\langle M \rangle$ contour in the x - y plane.

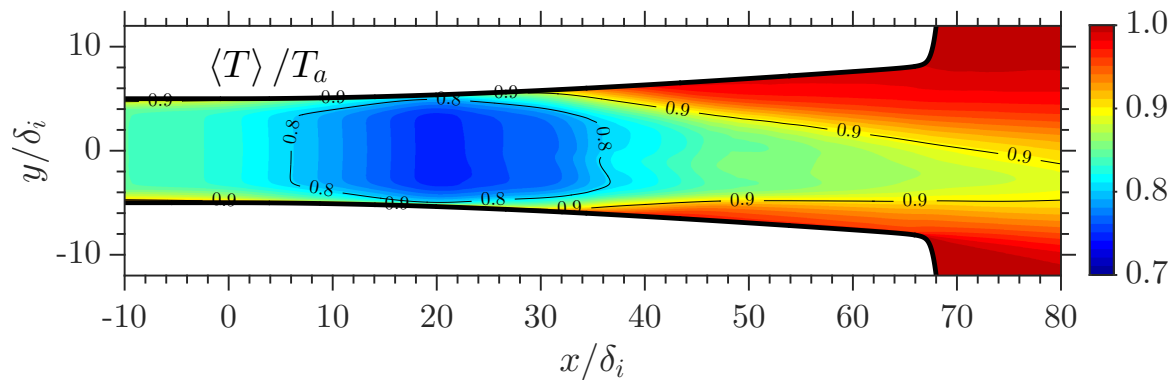


Figure 5.22: Mean temperature $\langle T \rangle / T_a$ contour in the x - y plane.

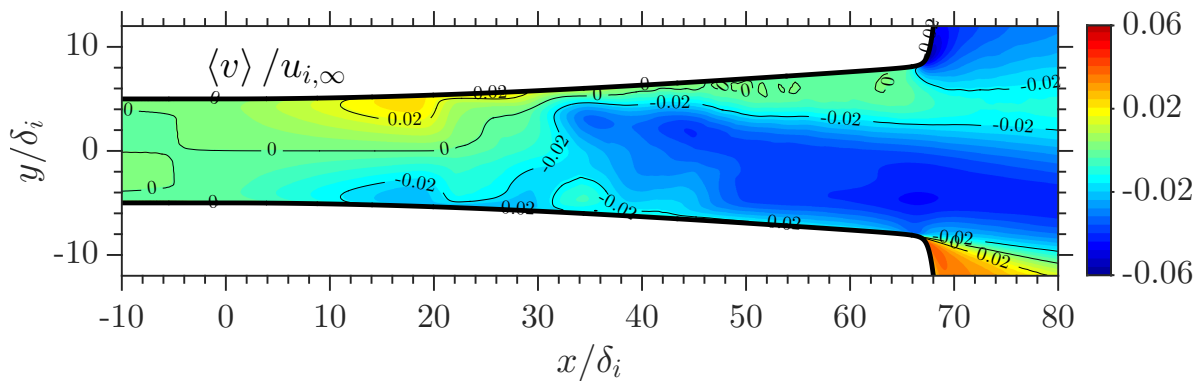


Figure 5.23: Mean wall-normal velocity $\langle v \rangle / u_{i,\infty}$ contour in the x - y plane.

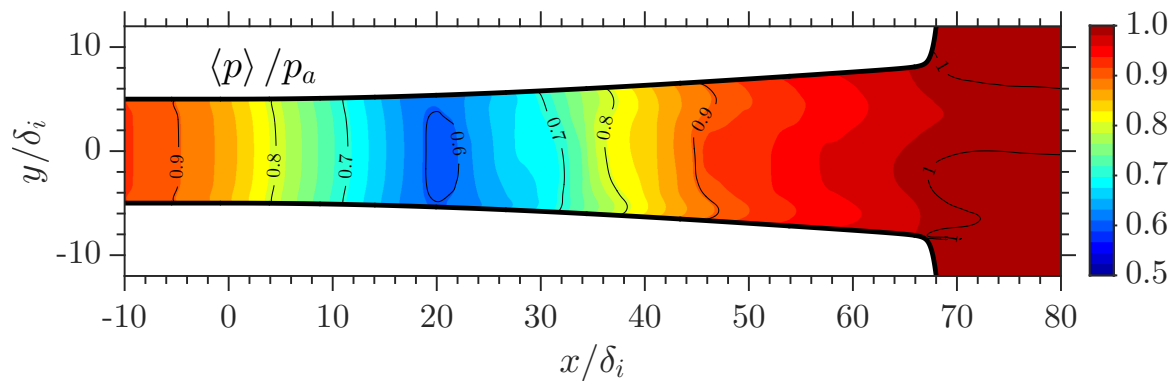


Figure 5.24: Mean pressure $\langle p \rangle / p_a$ contour in the x - y plane.

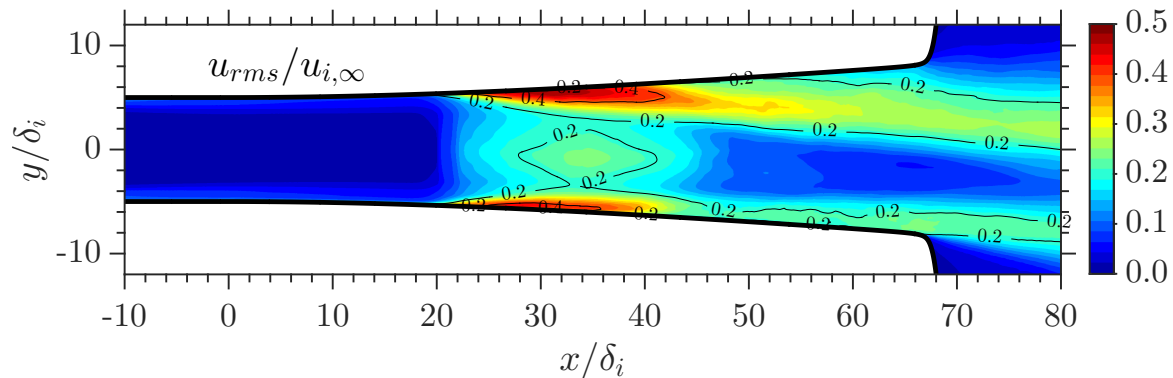


Figure 5.25: Rms velocity $u_{rms}/u_{i,\infty}$ contour in the x - y plane.

the suction effect happening along the wall in the recirculating flow. Figure 5.26 shows the instantaneous velocity fluctuations close to the wall when the shock is moving downstream for both upper and lower walls. Velocity fluctuations are positive in the recirculating flow, meaning that the flow and the shock are sucked up by the low ambient pressure. This mild positive velocity developing along the separated flow prevents the mixing layer to reattach to the wall. On the contrary, when the flow is moving upstream, *i.e.* the flow is asymmetric, the velocity fluctuations are highly negative due to a backflow coming from the atmosphere (fig. 5.27). One can notice that the backflow is more distinctive on the upper wall of the nozzle where the large recirculation bubbles take place. This “breathing” process explains the difference observed in the shock pattern whether the shock is moving downstream or upstream.

This section was dedicated to explain the different shock patterns observed in the simulation and the presence of the asymmetry within the nozzle. The data created with the WR-LES does not cover a sufficiently long time sample to capture the low frequency oscillations. As observed in figure 5.4, the number of periods simulated by the wall-resolved computation is on the order of 3 which is not enough to create converged spectra for unsteady analysis. The mechanism of the very low frequency shock motion will be explained in the next section (sec. 5.4) using time-resolved data from the wall-modeled simulation.

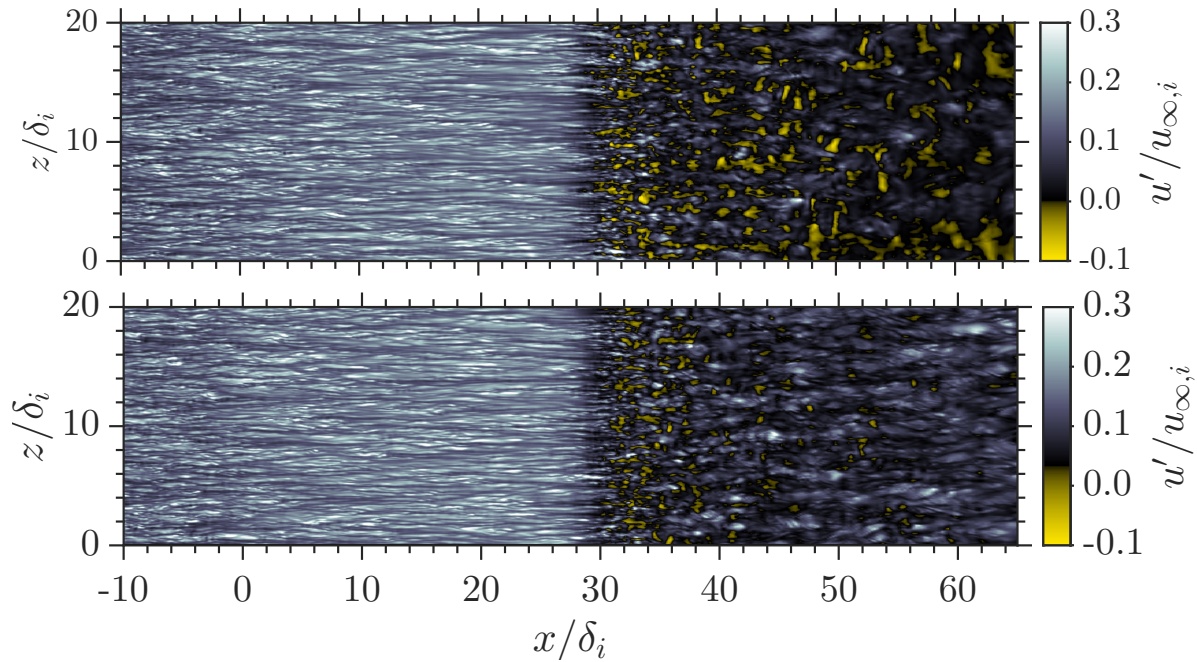


Figure 5.26: Instantaneous velocity fluctuations contour for the upper wall (*top*) and the lower wall (*bottom*) in the x - z plane at $y^+ \sim 5$ when the shock is moving downstream, *i.e.* $u_s > 0$ ($t^* = 1456$).

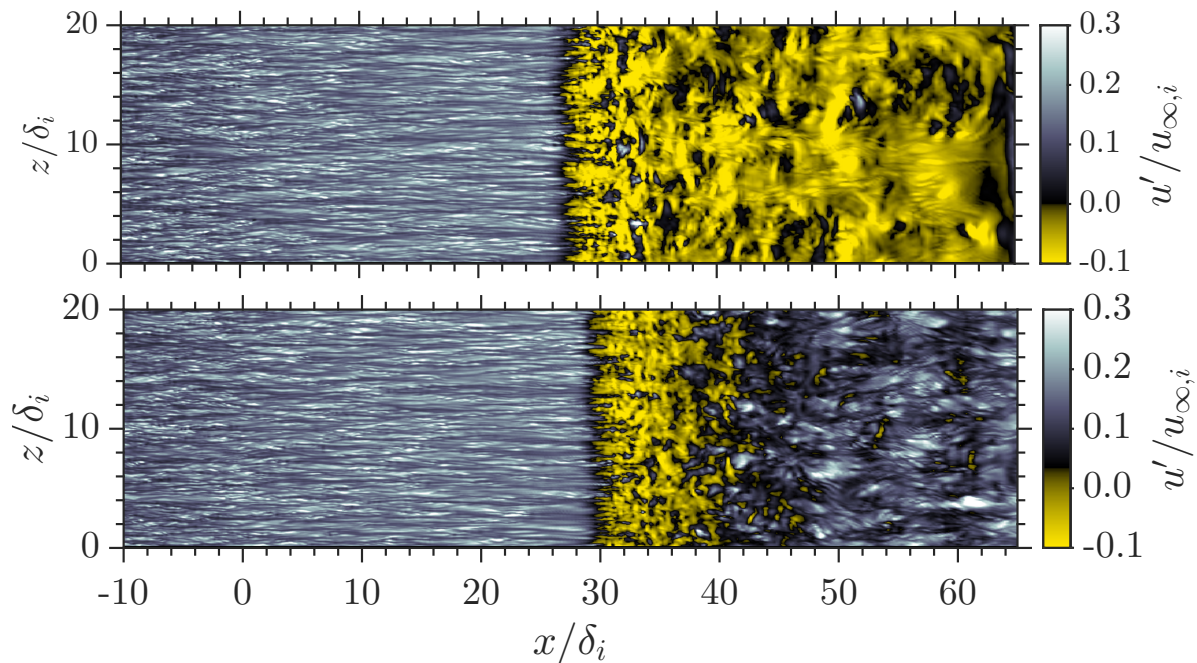


Figure 5.27: Instantaneous velocity fluctuations contour for the upper (*top*) and lower walls (*bottom*) in the x - z plane at $y^+ \sim 5$ when the shock is moving upstream, *i.e.* $u_s < 0$ ($t^* = 1692$).

5.4 Wall-Modeled LES

In the wall-modeled LES strategy, the computational mesh is generated by mapping the same wall function as the wall-resolved LES (eq. A.2). The domain lengths are similar to the wall-resolved case. However, the mesh size is reduced accordingly to the grid resolution of the wall-model requirements discussed by Kawai & Larsson (2012). The wall-modeled grid is two times coarser in both streamwise and spanwise directions compared to the wall-resolved case. The spacing in the wall-normal direction is constant with the first cell near-wall localized at 45 wall unit. Similarly to the wall-resolved simulation, the grid is orthogonal close to the wall which allows us to use the wall-model in the same way as the flat-plate simulations from section 4.3.2. Table 5.4 shows the grid resolution and the differences with the wall-resolved simulation.

	N_ξ	N_η	N_ζ	L_z/H_t	L_b/H_t	Δx_i^+	Δy_i^+	Δz_i^+	Nb cells
WR-LES	896	256	320	2	2.8	30	[1 : 29]	20	73.4 M
WM-LES	672	128	160	2	2.8	60	45	40	13.7 M

Table 5.4: Grid parameters for the WM-LES of the planar nozzle flow.

The nozzle walls are considered as adiabatic with a no-slip boundary condition. The wall-model is activated on the first near-wall cells through an additional force as discussed in section 4.3.2. The inlet boundary condition uses the method of Xie and Castro to continuously feed the simulation with synthetic turbulence similarly to the WR-LES. The buffer length is kept the same as in the wall-resolved case. The turbulent inflow takes approximately 10 boundary layer thicknesses to reach equilibrium as studied in section 5.3.2. The inlet is at 28 boundary layer thicknesses upstream of the throat allowing sufficient length for the boundary layer to develop coherent turbulent structures. The numerical methods are similar to those applied in the wall-resolved simulation except for the spatial discretization scheme. The WCNS is used to discretize the convective terms instead of the hybrid scheme. The additional force is known to create spurious fluctuations close to the wall where the centered scheme could become unstable. The flow is started using the last solution of the wall-resolved simulation to avoid the starting phase of the nozzle. The WR-grid solution is interpolated on the WM-grid using bi-linear interpolations.

The grid convergence is not a necessary step in the wall-modeled case since the grid resolution is already small compared to Kawai & Larsson (2012) grids. The first near-wall cell is at 45 in wall units where the wall-model is known to be usable up to 150 (Kawai & Larsson 2012), especially for high Reynolds number. In this case, the incoming Reynolds number $Re_\theta \sim 1100$ at the inlet is quite small compared to Larsson and Kawai simulations

$Re_\theta \sim 50000$. The number of points within the boundary layer is about 15-20 at the inlet which is already low compared to previous WM-LES simulations.

In the recirculated zone, where the wall-model cannot be applied because of the low Reynolds number flow and the recirculated flow, the wall model is turned off. Disabling the wall-model is done using a shock sensor along each wall. At the separation, the flow is subjected to a high pressure gradient along the streamwise direction that can be used as a criteria to turn off the wall-model. The shock sensor detects the peak of pressure gradient at the upper and lower wall, separately. To avoid detecting spurious pressure oscillations caused by the incoming turbulence, the pressure gradient is averaged in the spanwise direction. Figure 5.28 shows a representation of the shock sensor. The formulation of the shock locator is as follows:

$$x_{\text{loc}} = \max \left(\frac{\overline{dp_w(\xi)}}{d\xi} \right), \quad (5.8)$$

where the maximum is found along the body fitted direction ξ between the throat and the nozzle exit, p_w is the pressure at first near-wall cell and $\overline{(\cdot)}$ is the spatial averaging in the z -direction.

As explained in section 4.3.2, the wall-model requires information from the LES computations to compute the appropriate wall-shear stress to be used in the LES. The model needs the velocity close to the wall as an input parameter. In the nozzle flow and especially in the diverging section, the cells are not parallel to the y -direction. The grid for the near-wall cells has been generated so that the cells are always orthogonal to the wall. The wall-normal direction is not the Cartesian y -direction but the η -direction, normal to the wall (fig. 5.28). The curvilinear equations use Cartesian velocity but some of the terms use the so-called contra-variant velocity which are aligned with the grid. The simplified thin boundary-layer equations (STBLE) model uses the parallel velocity to the wall, noted u_{\parallel} , as an input to solve the ODEs. Strong curved walls are not adapted for the wall-model developed by Larsson and Kawai since STBLE are derived from the Cartesian coordinates. In this case, the curvature of the wall is not an issue because of the weak slope of the divergent (low half-angle). The effect of curvature in divergent nozzle becomes large when the ratio δ/R' of the boundary layer thickness to the radius of curvature is higher than 0.01 (Neves et al. 1994). For the present LES, the ratio δ/R' is close to zero due to the large radius of curvature of the divergent section.

The computational time for the wall-modeled simulation is 40 times shorter than the wall-resolved simulation. This computational cost reduction is due to the combination of the grid reduction and the time-step relaxation using the wall-model developed. This reduction in computational time makes the capture of the very low-frequency unsteadiness possible.

Case	$\langle p_i/p_a \rangle$	NPR	$\langle x_s/\delta_i \rangle$	$\langle St_1 \rangle$
Exp.	0.898	1.7	30	—
Olson et al.	0.86	1.63	28	0.0021
WR-LES	0.86	1.63	29	0.0019
WM-LES	0.83	1.57	31	0.0019

Table 5.5: Results of the planar WM-LES compared to WR-LES.

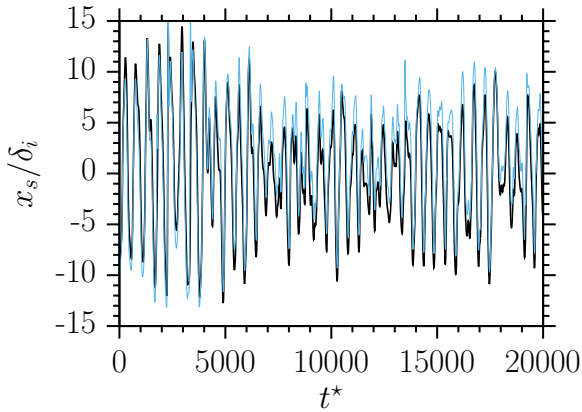
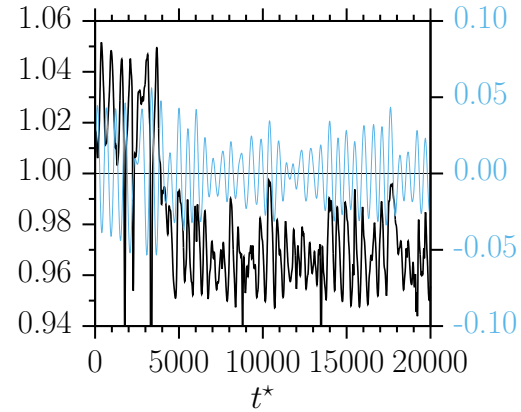


Figure 5.29: Separation location over time; —: Upper wall, —: Lower wall.

Figure 5.30: Asymmetry parameter $x_s^{\text{top}}/x_s^{\text{bottom}}$ (—) and shock speed $u_s/u_{i,\infty}$ (—) over time.

resolved simulation. The average shock location is well predicted by the wall-model. The pressure at the throat is slightly smaller in the wall-modeled case. The actual NPR of the simulation is then reduced by 3% (tab. 5.5). The decay of pressure at the throat is due to a stronger pressure gradient in the buffer section as observed in figure 5.32. Wall-modeled Clauser's pressure gradient β is 30% higher compared to the wall-resolved. This high normalized pressure gradient is due to the under-resolved wall-shear stress, τ_w , computed by the wall-model. Despite the decay of the NPR, the pressure distribution is in good agreement with the experimental data as well as the wall-resolved simulations.

Figure 5.33 shows the normalized streamwise velocity along the wall-normal direction at $x/\delta_i = -10$. The first near-wall cells are located at $y^+ \sim 20$, *i.e.* $\Delta y^+ \sim 40$. The results are in good agreement with the wall-resolved case, especially in the outer layer of the boundary layer and in the log-law region. The first near-wall point seems to be slightly under-resolved probably due to the unavoidable numerical and sub-grid modeling errors emanating from the wall-model as explained in section 4.3.2.

5.4.2 Side-loads generation

The normalized forces in both x - and y -direction are plotted in figure 5.34 for the overall time sample. Table 5.6 summarizes the averaged and RMS forces for WR- and WM-LES

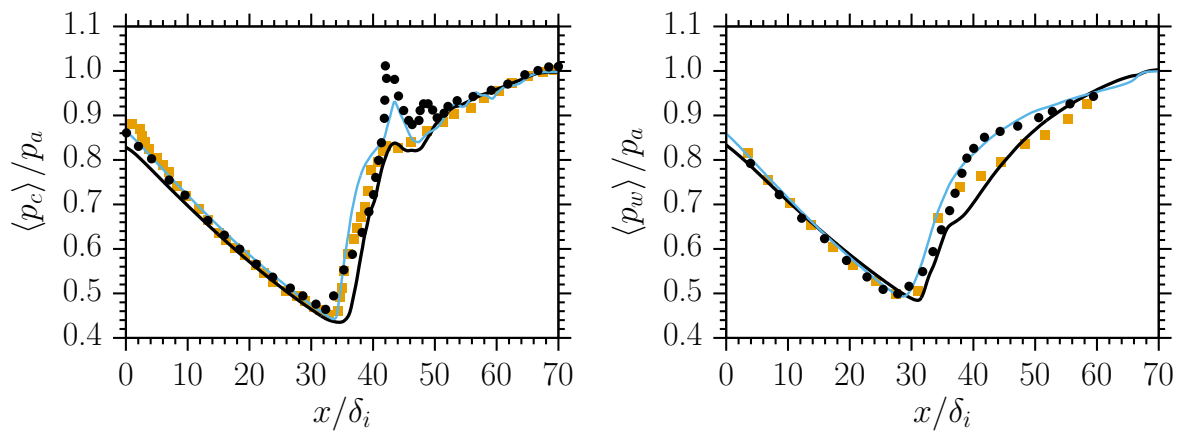


Figure 5.31: Pressure distribution at the center of the nozzle (*left*) and pressure distribution at the lower wall (*right*) along the x -direction; —: WM-LES (conditional averaging at $x_s/\delta_i \sim 0$), - - : WR-LES (conditional averaging at $x_s/\delta_i \sim 0$), •: WR-LES from Olson & Lele (2011), ■: Experimental results from Johnson & Papamoschou (2010).

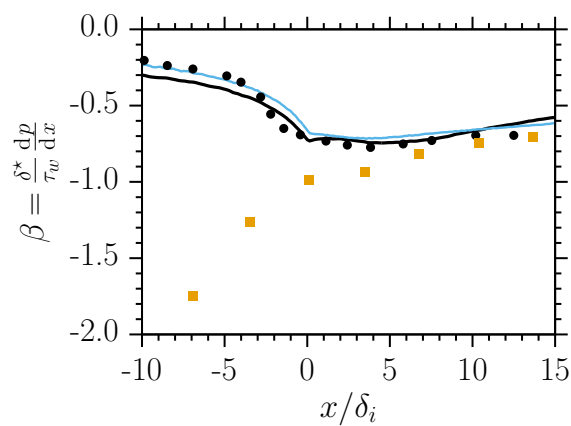


Figure 5.32: Normalized pressure gradient along the x -direction; —: WM-LES, - - : WR-LES, •: WR-LES from Olson & Lele (2011), ■: Experimental results from Johnson & Papamoschou (2010).

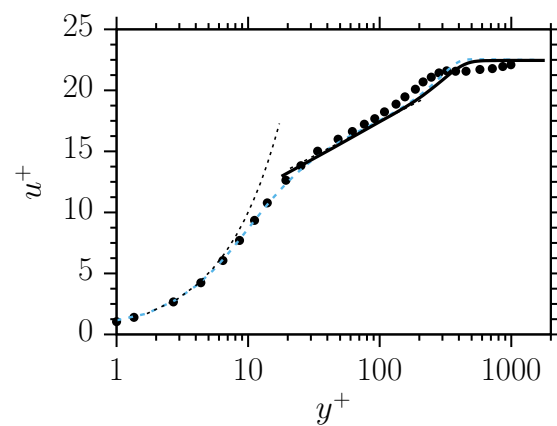


Figure 5.33: Van Driest velocity along the wall-normal direction at $x/\delta_i = -10$; —: WM-LES, - - : WR-LES, - · - : $u^+ = y^+$ and the log-law with $\kappa = 0.41$ and $C^+ = 6.2$, •: WR-LES from Olson & Lele (2011).

Case	$\langle F_x \rangle / F_{isen}$	$\langle F_y \rangle / F_{isen}$	$F_{x,rms} / F_{isen}$	$F_{y,rms} / F_{isen}$
WR-LES	0.71	0.22	0.26	0.11
WM-LES	0.8	-0.24	0.26	0.13

Table 5.6: Averaged/rms forces of the planar WM-LES compared to WR-LES scaled by the isentropic normal force.

simulations. As for the previous figure, the averaged forces have been averaged from $t^* = 6000$ to avoid the change of side that could lead to an under-predicted force value. The change of side is clearly observable on the side-loads (F_y). As explained in section 5.3.4, when the shock is oriented towards the lower wall, the side-loads are in the opposite direction oriented towards the upper wall due to the low pressure developing along the attached mixing layer. As observed in the previous simulation, the force in y -direction is noisier than the streamwise force due to the slight slope of the divergent.

The same forces are compared to the wall-resolved simulation in figure 5.35 using the same time sample of 2000 time units. The results show a good agreement of the data, especially on the streamwise force where the wall-modeled simulation seems to capture the same magnitude and frequency compared to the WR-LES.

Autospectra of the forces are also shown in figure 5.36. The WR-LES spectra lacks of low frequency resolution at $St_{min} \sim 10^{-3}$. Capturing more low frequencies is expected to improve the Fourier analysis and the quality of spectra. The wall-modeled simulation go up to $St_{min} \sim 10^{-5}$ allowing to capture lower frequencies compared to the wall-resolved case. The second peak of energy in the streamwise force, at $St = 4 \times 10^{-3}$, is hardly defined in the wall-resolved computation compared to the wall-modeled solutions.

The most energetic peak in the streamwise force signal is defined as the main tone, noted St_1 , of the separation line fluctuations. This tone has been captured at a similar frequency in both the experiments and the WR-LES of Olson. The wall-modeled simulation seems to capture correctly the main tone compared to the WR-LES (tab. 5.5). This low frequency is observed in the side-loads (F_y) but seems to be less energetic compared to the streamwise force. On the contrary, high frequency phenomena are less energetic in the streamwise force than in the side-loads. Two high frequency peaks can be observed in both spectra, at $St \sim 4 \times 10^{-2}$ and $St \sim 0.15$. As explained in section 1, those two peaks could originate from the recirculated zone and from the turbulent mixing layer turbulence, respectively. It seems that the side-loads are highly sensitive to the high frequency oscillations while the streamwise force is more sensitive to the main tone of the separation line.

The autospectra of forces show some information about the different frequencies captured by the simulation but miss the boundary layer time scales, up to $St = 0.5$. The

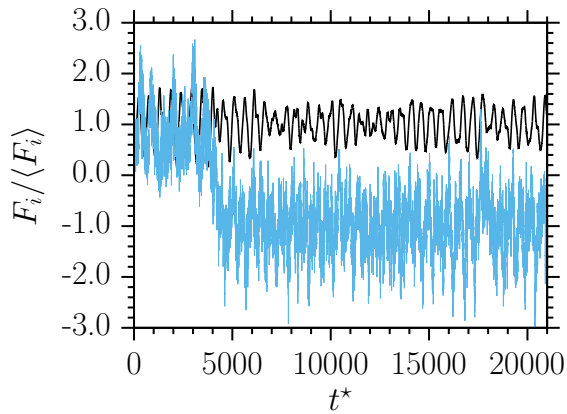


Figure 5.34: Normalized forces for the WM-LES; $-$: x -direction (F_x), $-$: y -direction (F_y).

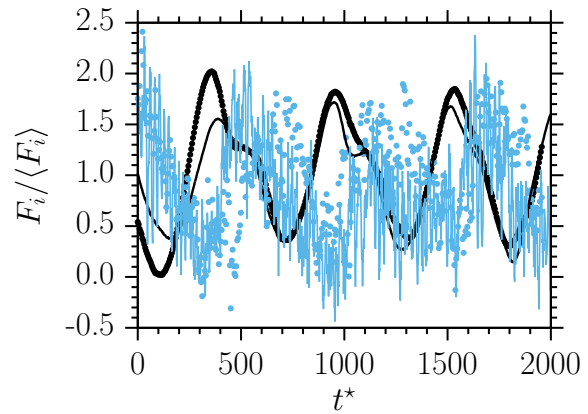


Figure 5.35: Comparison of forces between WM-LES ($-$) and WR-LES (\bullet); Line colors as in figure 5.34.

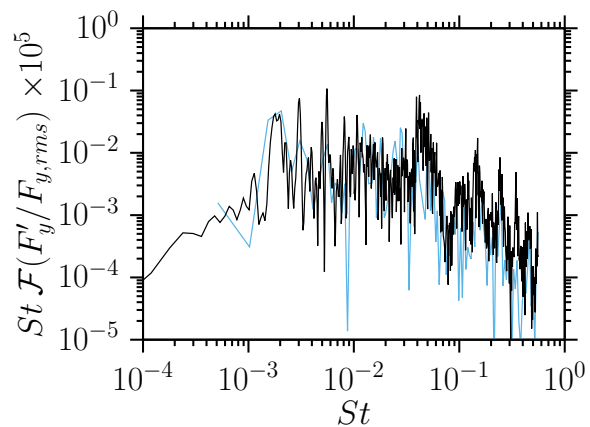
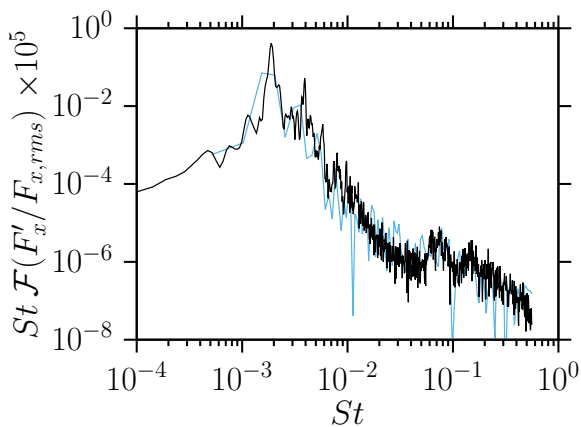


Figure 5.36: Pre-multiplied spectra of the normalized fluctuating forces in x -direction (left) and y -direction (right); $-$: WM-LES, $-$: WR-LES.

integration of the force along the surface has also reduced some of the energy contained at higher frequencies scale. For a proper frequency analysis, a time-resolved line at the wall has been saved during the simulations to analyze precisely the different frequencies along the wall. Figures 5.37 and 5.38 show the normalized pre-multiplied spectra of the fluctuating pressure field along the wall for two streamwise locations, at the throat and at the exit of the nozzle. The normalized spectra are computed by integrating the pre-multiplied spectra along the frequency range, so the normalized pre-multiplied spectra integration is equal to one,

$$St\mathcal{F}(\phi)^* = \frac{St\mathcal{F}(\phi)}{\int_{St} St\mathcal{F}(\phi) dSt} \quad (5.9)$$

The spectra of the incoming boundary layer shows a peak of energy at $St = 1$ as expected by the definition of the Strouhal number. Some energy can be observed in the lower frequency range. The main tone of the separation line is also captured within the boundary layer. Physically, the subsonic part of the boundary layer is known to carry some of the downstream acoustic waves. This upstream propagation of the acoustic waves is highly sensitive to the low frequencies downstream of the throat. On the contrary, the high frequencies are damped by the turbulent energy of the boundary layer.

Figure 5.38 shows the spectra at the exit of the nozzle for the upper and lower walls. The main tone captured in the force spectra is clearly observable for both walls. One can notice that the upper wall has more energy at $St = 0.1$ than the lower wall. Conversely, the upper wall has less energy at $St = 5 \times 10^{-2}$ compared to the lower wall. As observed before, the flow is mostly asymmetric and oriented to the upper wall. The later is highly sensitive to the fluctuations of the attached mixing layer while the lower wall is more receptive to the fluctuations of the recirculation zone. Thus, the $St = 0.1$ frequencies from the upper wall would originate from the mixing layer confirming some work on mixing layer downstream of a shock (Touber & Sandham 2009). While the $St = 5 \times 10^{-2}$ frequency from the lower wall could be created by the recirculation zone. Figure 5.39 shows the same spectra at the bottom wall along the streamwise direction. The main tone is captured between $x/\delta_i = 22$ and the exit of the nozzle and illustrates the feedback phenomenon between the shock and the exit of the nozzle that drives the low frequency phenomenon.

Figure 5.40 was obtained from the high-spatial/high-temporal resolution pressure field at the wall. A reference point is chosen at two streamwise locations, inside the incoming boundary layer centered at $x/\delta_i = 0$ (fig. 5.40) and inside the separated region at $x/\delta_i = 52$

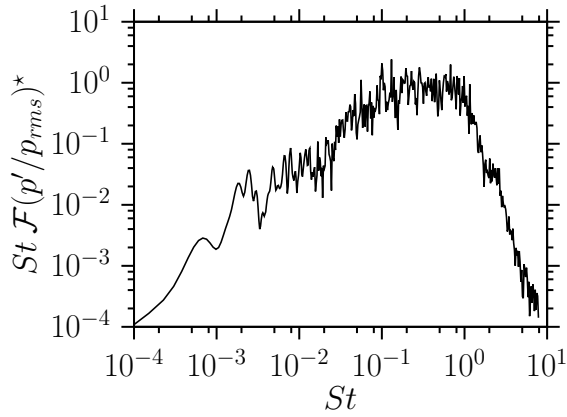


Figure 5.37: Normalized pre-multiplied spectra of the pressure fluctuations at the wall in the incoming boundary layer, *i.e.* $x/\delta_i = 0$.

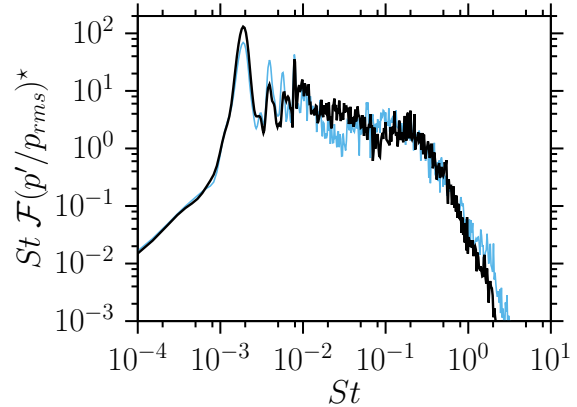


Figure 5.38: Normalized pre-multiplied spectra of the pressure fluctuations at the exit of the nozzle, *i.e.* $x/\delta_i \sim 66$; —: lower wall, —: upper wall.

(fig. 5.41). The two-point correlations function in space and time is computed by,

$$R_{p'p'} = \frac{\langle R_{\varphi(x_0, t_0), \varphi(\Delta x, \Delta t)} \rangle}{\langle R_{\varphi(x_0, t_0), \varphi(x_0, t_0)} \rangle} \quad (5.10)$$

where $\varphi = p'/p_{rms}$ and x_0 is the centered location according to each figure.

The boundary layer correlation function shows a strong time correlation of the pressure waves along the positive speed of sound c_w which is relevant knowing that the boundary layer turbulence waves propagate along the wall, where the no-slip condition applies. Looking more closely at the positive wave region, a mild ridge corresponding to positive waves propagating at the velocity of the inviscid flow $u_\infty + c_w$ seems to emerge. This ridge is related to the acoustic wave traveling outside of the boundary layer confined between the upper and lower walls.

Conversely, in the separation region (fig. 5.41), the subsonic acoustic waves $u_\infty - c_w$ seem to be strongly correlated in time for the upper wall where the shock is periodically attached to the wall due to the asymmetry. This behavior validates the assumption made by many (Bogar et al. 1983, Johnson & Papamoschou 2010, Olson & Lele 2013) on the two way coupling between the shock and the nozzle exit that leads to the unsteady oscillation of the shock. For the lower wall, where the large recirculation bubbles apply, a ridge can be observed along the convection speed of the mixing layer u_2 corresponding to some propagating low-frequency waves inside the mixing layer. These waves are related to the development of coherent structures in the shear-layer at the bubble interface.

Figure 5.42 shows numerical Schlieren pictures of the wall-modeled simulation for different times. The results have to be compared with the wall-resolved simulation (fig.

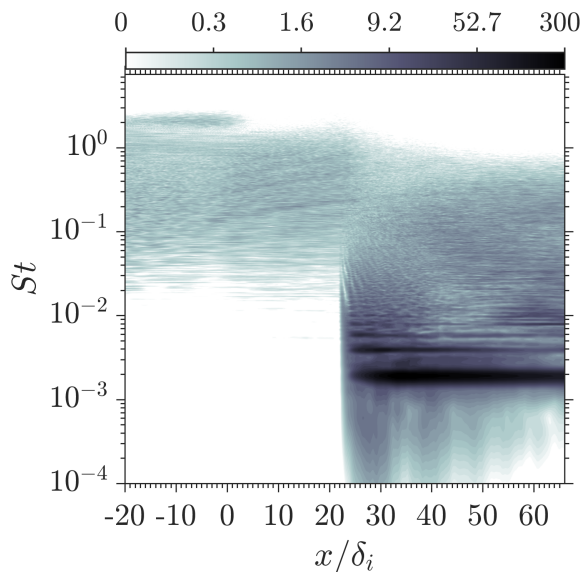


Figure 5.39: Normalized pre-multiplied spectra of the pressure fluctuations $St \mathcal{F}(p'/p_{rms})^*$ at the lower wall along the x -direction.

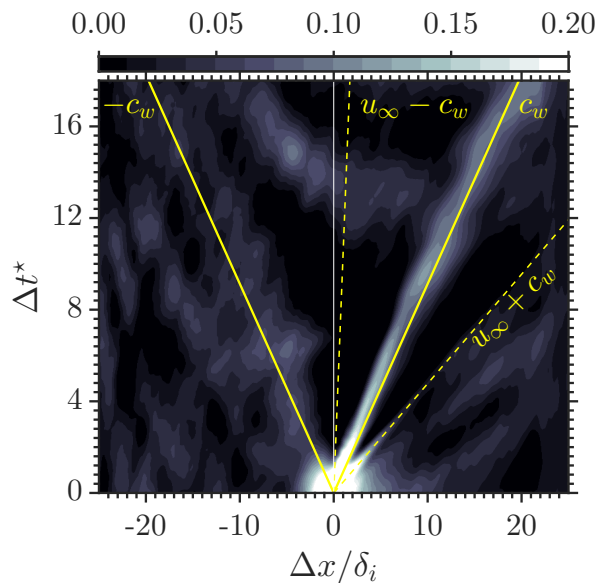


Figure 5.40: Space-time correlation of the normalized pressure field in the boundary layer centered at $x/\delta_i = 0$.

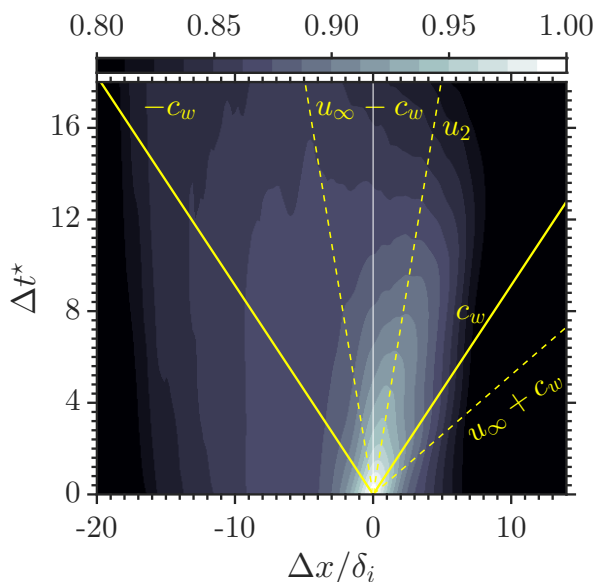
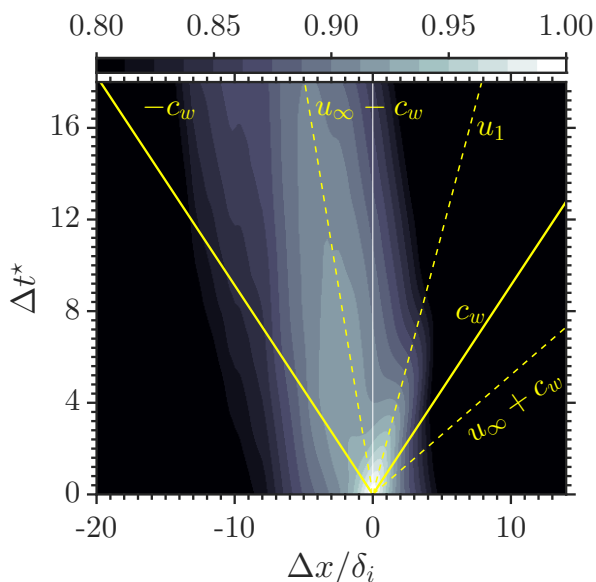


Figure 5.41: Space-time correlation of the normalized pressure field in the separated zone at the upper (*left*) and lower wall (*right*).

5.6). Patterns of shock seem to be equivalent to the wall-resolved case except for the case when the shock is moving downstream. At $t^* = 14940$, the separated shock is stronger than in the wall-resolved case resulting in a pronounced “lambda” shock pattern where the wall-resolved calculation gives compression waves and a large Mach stem (fig. 5.6 at $t^* = 1850$). The compression waves observed in the wall-modeled case does not coalesce within the viscous sublayer because of the low resolution close to the wall $\Delta y^+ \sim 45$. As explained by Chapman et al. (1958) in the free-interaction theory, the separation length L_s reduces linearly with the displacement thickness δ^* which is the case in the present WM-LES due to the unresolved part of the boundary layer. In fact, separation occurs when the viscous sublayer cannot sustain the strong adverse pressure gradient imposed by the inviscid flow. Removing the viscous sublayer of the incoming boundary layer results in stronger compression waves that collapse rapidly into a strong separated shock which forms a lambda shock pattern. Despite the change in shock patterns, the amplitude, the frequency and the asymmetric aspect of the separation are well captured by the wall-modeled simulation.

5.4.3 Low-frequency unsteadiness

The mechanism of low frequency unsteadiness in over-expanded nozzle flow has been discussed by many researchers (Bogar et al. 1983, Wong 2006). Sajben & Kroutil (1980) and Zaman et al. (2002) observed in their experiments that the oscillation of the separation line was consistent with the transonic resonance of the nozzle, *i.e.* the frequency is inversely proportional to the length between the mean separation location $\langle x_s \rangle$ and the exit of the nozzle x_e . They observed two stages of resonance for a specific range of ‘jet Mach number’, noted M_j , defined by:

$$M_j = \sqrt{\frac{2}{\gamma - 1} \left(\text{NPR}^{\frac{\gamma-1}{\gamma}} - 1 \right)}. \quad (5.11)$$

Those resonant tones occur for small opening angle in planar and cylindrical nozzles. The mechanism proposed by Zaman is similar to that involved in longitudinal acoustic resonance. The shock becomes the “source” of perturbation and can be seen as a wave antinode while a node occurs near the nozzle exit. As for a resonant tube, where one side is open to the atmosphere, the fundamental pressure wave corresponds to the case where one-quarter wavelength is fitted within the distance from the foot of the shock $\langle x_s \rangle$ to the nozzle exit x_e . The resonance depends also on the characteristics of the incoming boundary layer prior to the separation as observed in the experiment of Papamoschou by tripping the incoming boundary layer. Thus, resonant tones happen; when the length between the separation and the shock is similar to a quarter wavelength at the speed of

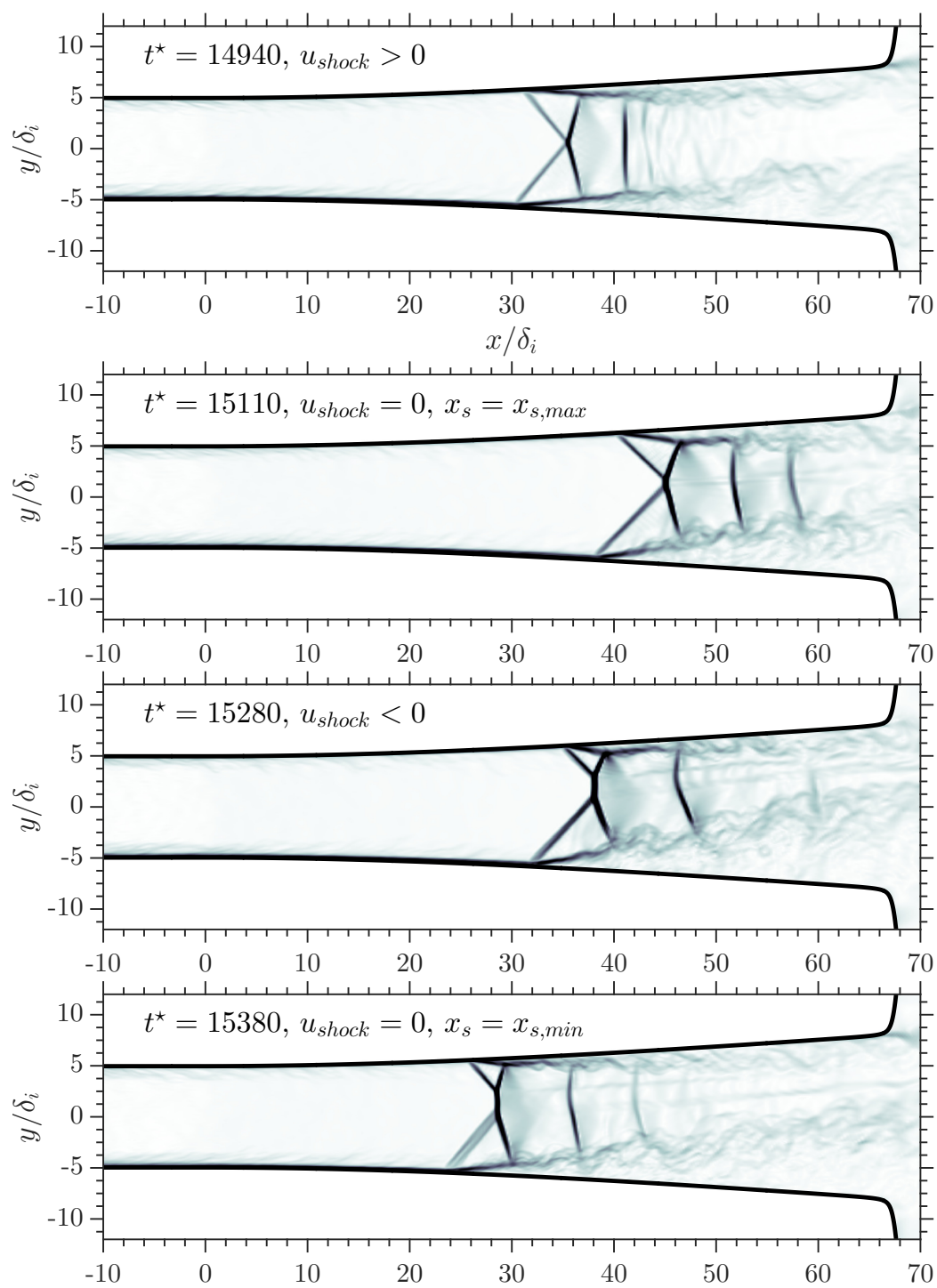


Figure 5.42: z -averaged numerical "Schlieren" pictures contour $|\nabla\rho|$ in the x - y plane at different times.

sound; for small opening angle in either planar or cylindrical flow; for transonic jet Mach number; for smooth nozzle walls. Zaman proposed the following correlation to compute the resonant tone:

$$f_r = \frac{c_0^2 - u_e^2}{4c_0 L_{s,e}}, \quad (5.12)$$

where $L_{s,e}$ is the length between the averaged separation location and the exit of the nozzle, c_0 the speed of sound within the separated boundary layer and u_e the velocity at the exit.

Despite the good prediction of Zaman's correlation, the lack of experimental measurements inside the nozzle prevents us to conclude that the proposed acoustic resonance drives the unsteadiness. In the present planar nozzle, the jet Mach number M_j is equal to 0.76 and the maximum half-angle of the nozzle is about 4° which fits the transonic tone requirements proposed by Zaman et al. (2002). The large-scale transonic resonance has been captured in the experiment of Papamoschou & Johnson (2006) and the LES of Olson & Lele (2013). The resonance phenomenon is known to create odd harmonics within their spectra. Some of the harmonic have been captured by the LES as observed in figure 5.38. Olson & Lele (2013) concluded that the unsteady mechanism was due to a transonic resonant tone between the shock location and the exit of the nozzle. They found a two way coupling between the shock and the shear layer combined with a time lag leads to the unsteady oscillation of the shock. The mechanism proposed by Olson & Lele (2013) for the unsteady shock motion exhibits similar frequencies and length scales as the present LES.

Figure 5.43 highlights the correlation between the effective exit area A_e^* , computed using the cross-section slices localized at the exit, and the velocity separation shock u_s computed by equation 5.3. It shows a time lag of approximately one-quarter wavelength reinforcing the prediction of Olson & Lele (2013) about the resonant tone.

Similarly, figure 5.44 shows the anticorrelation between the exit pressure p_e and the separation location x_s . When the shock is located at its downstream position, the pressure is minimal because of the increased effective area. Conversely, when the shock is at its upstream position, the pressure is maximum considering the small effective area. On these extreme positions, the total pressure is thermodynamically unstable forcing the flow to correct the shock position, increasing the unsteadiness of the shock. A small delay can be observed between the shock location and the exit pressure due to the time of acoustic waves to propagate upstream to the shock. In the paper of Olson & Lele (2013), "this temporal phase shift", *i.e.* the lag between the shock position signal and the effective area signal, "is the amount of time it takes for pressure waves from the confined exit area to propagate upstream to the shock". In the present LES, we have observed that the

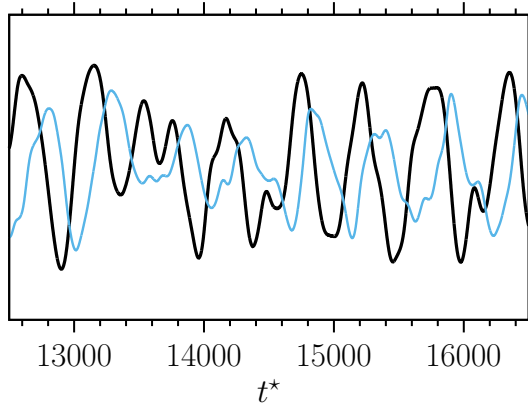


Figure 5.43: Highlight of the delay phenomenon between the effective exit area A_e^* (—) and the separation location x_s (—).

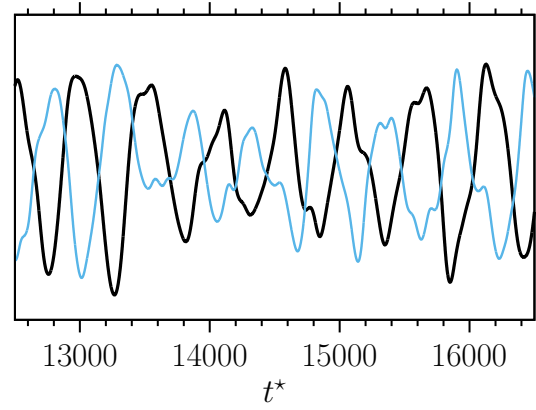


Figure 5.44: Highlight of the anti-correlation between the exit pressure p_e (—) and the separation location x_s (—).

lag between the shock position signal and the effective area signal was about one-quarter wavelength, *i.e.* $\Delta t_{\text{lag}}^* \sim 150$, confirming the resonance phenomenon observed by Zaman et al. (2002). This lag is not due to the time for pressure waves from the confined exit area to propagate upstream to the shock, *i.e.* $\Delta t_{\text{lag}}^* \sim 40$, but to constant change of effective area downstream of the shock. However, the time lag due to acoustic wave propagation increases the unsteadiness and the resonant effect of the shock separation.

The proposed mechanism for the low frequency oscillation is given below by summarizing the observations from sections 5.3.3, 5.3.4 and 5.4.3 and to the feedback mechanism of Olson & Lele (2013). Figure 5.45 shows the shock wave motion over one resonant tone period St_1 at different times.

(1) The separation shock moves downstream at $u_s = \max(u_s)$. Due to the high effective pressure at the exit coming from the change of effective geometry / effective area (sec. 5.3.3), the flow is sucked up by the atmosphere $p_e > p_a$. A positive velocity flow is developing along the wall preventing the ‘‘Coanda effect’’ to happen and forcing the symmetric behavior of the separation lines. The relative speed of the incident shocks, M_I , is reduced because of the suction effect caused by the ambient pressure. The incident shocks vanish for compression waves removing the ‘lambda’ shock pattern for one large internal Mach stem (fig. 5.6).

(2) At one-quarter wavelength, the exit pressure is lower than that of the ambient pressure creating a slight back flow from the exit. This reversal flow starts to increase the deflection angle of the mixing layer and changes the effective geometry of the nozzle. The effective area starts to reduce with one quarter delay compared to the position of the shock (fig 5.43). Due to the inertia of the flow, the shock is still moving towards the exit while the back flow intensifies. At this point, the flow is mildly symmetric and a back flow occurs on both sides of the nozzle.

(3) The shock is at its maximal position with no velocity. The exit pressure is minimal (fig. 5.44) increasing the back flow from the ambient pressure and the reattachment to one side. At this time step, the mixing layer reattaches to one of the walls (upper or lower depending on the initial condition). The effective area is decreased compared to (2) and the flow is thermodynamically unbalanced forcing the shock wave position to adapt to those new parameters.

(4) The shock moves upstream at $u_s = \min(u_s)$. The lower mixing layer is completely attached to the wall and the large recirculation bubbles emerge along the upper wall. The back flow acts only on the upper side opened to the ambient pressure. The effective geometry of the nozzle downstream of the shock behaves as a convergent nozzle where the subsonic flow accelerates to supersonic speed to form a series of shocks, commonly called “shock train”.

(5) After five quarters wavelength, the shock is still moving upstream but the exit pressure becomes higher than the atmosphere suppressing the back flow on the upper wall. As for the one quarter wavelength time step, the effective geometry of the nozzle starts to increase which unbalanced the total pressure at the exit.

(6) The shock is at its minimum position with no velocity. The suction effect from the ambient pressure forces the mixing layer to move closer to the walls, increasing the effective area. As for (3), the flow is thermodynamically unbalanced forcing the shock wave position to move downstream. The acoustic lag due to the time it takes for pressure waves to acoustically propagate from the back pressure up to the shock is maximal at this position, increasing the unsteady motion of the shock.

(7) Cycle repeats to (1)

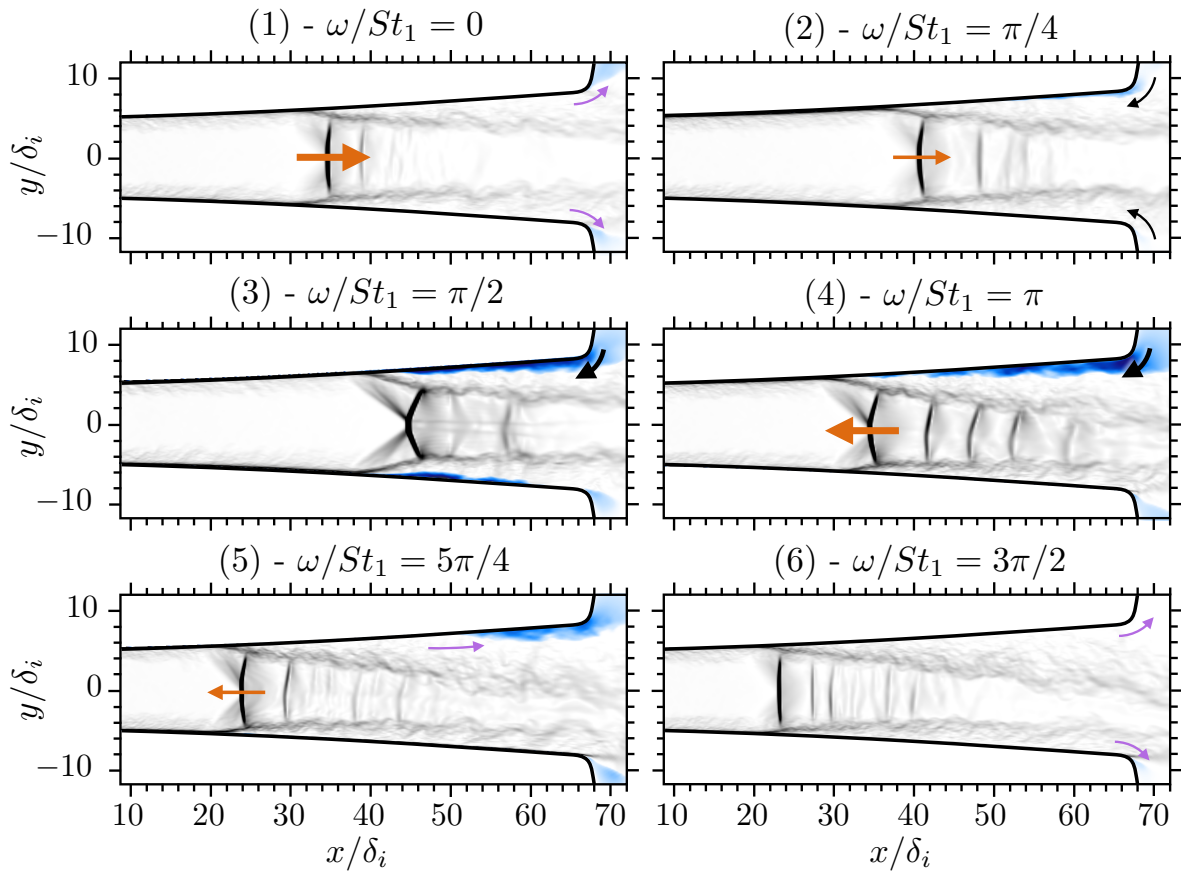


Figure 5.45: Shock excursion over one resonant tone period St_1 for different time step using the WR-LES; z -averaged Schlieren pictures are shown in grayscale, blue regions highlight negative x -velocity, orange arrows represent the velocity of the shock, black arrows the backflow and purple arrows the suction effect from the ambient pressure.

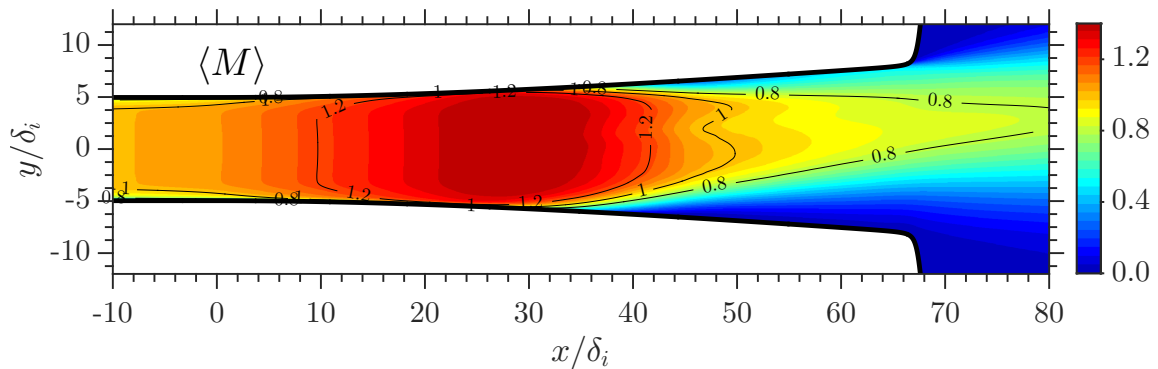


Figure 5.46: Averaged Mach number $\langle M \rangle$ contour in the x - y plane.

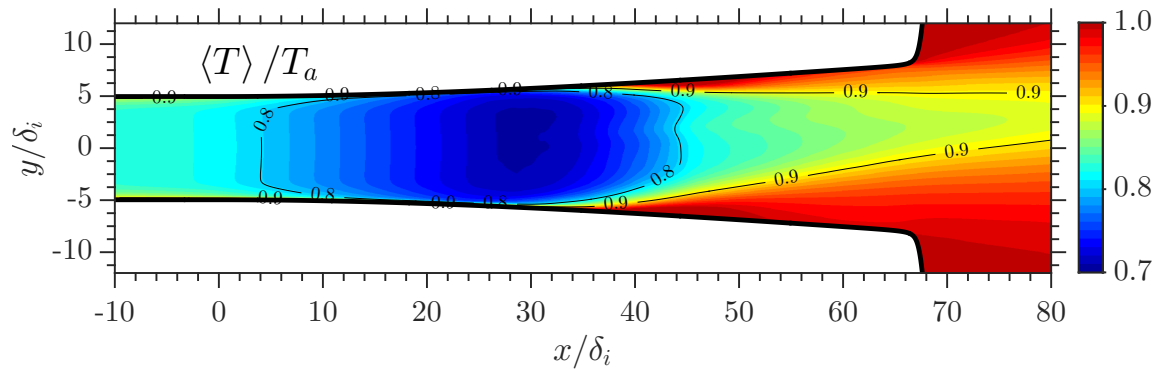


Figure 5.47: Averaged temperature $\langle T \rangle / T_a$ contour in the x - y plane.

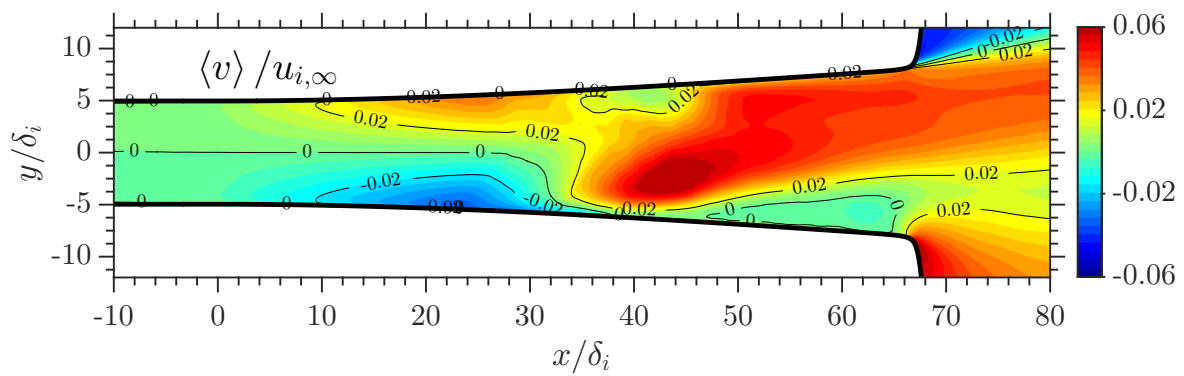


Figure 5.48: Averaged wall-normal velocity $\langle v \rangle / u_{i,\infty}$ contour in the x - y plane.

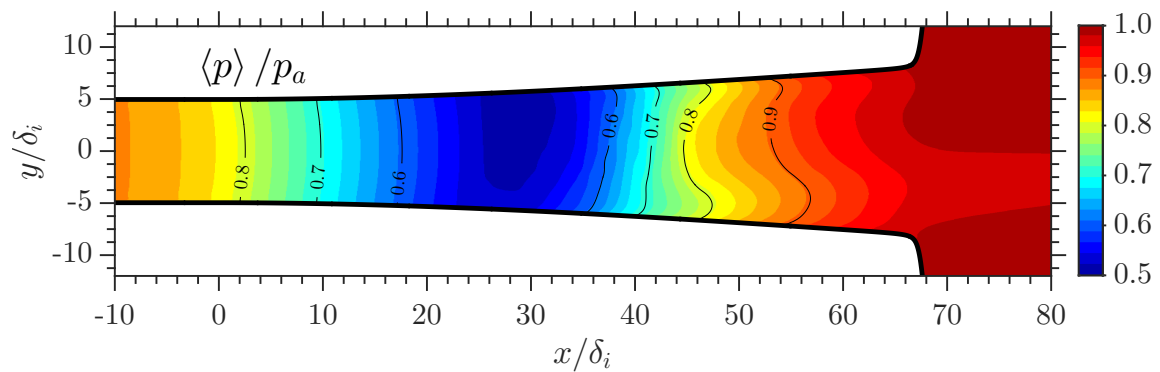


Figure 5.49: Averaged pressure $\langle p \rangle / p_a$ contour in the x - y plane.

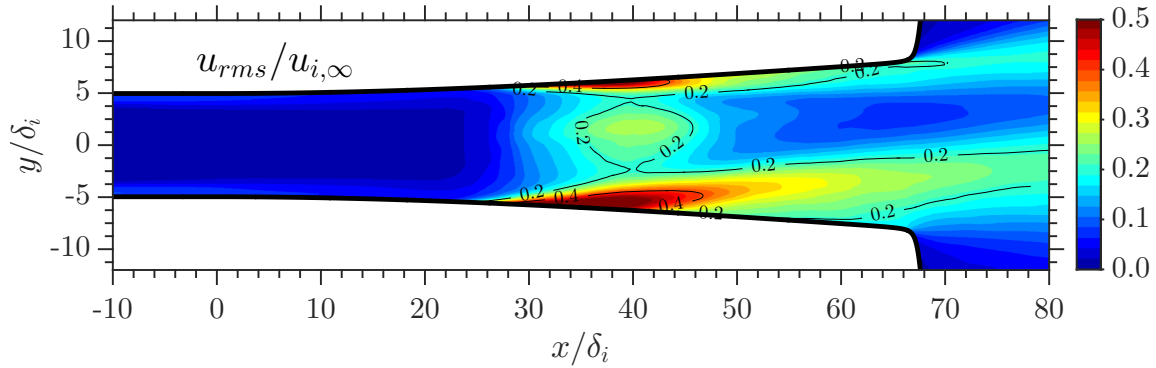


Figure 5.50: Rms velocity $u_{rms}/u_{i,\infty}$ contour in the x - y plane.

5.5 Summary

The LES data show a quite good agreement with the experimental results and the previous LES of Olson & Lele (2011). The wall-modeled simulation indicates that the flow physics are being captured despite the modeled viscous sublayer. The unsteady motion of the shock is accurately represented by the LES. The low-frequency shock oscillations phenomena have been captured using the wall-model developed in section 4.3.2.

The study on side-loads shows that they contain some energy at higher frequencies than the transonic resonant tone. They originate from the instability of the mixing layer and from the recirculation bubbles downstream of the separation. It is clear from the flow cycle presented in the previous section that the angle of deflection of the separated shear layer, which gives the effective geometry of the nozzle downstream of the shock, is coupled to the shock wave position with a phase shift of about a quarter wavelength. This phase shift between these two motions, *i.e.* moving upstream or downstream, causes the cycle to constantly over compensate its total pressure to match the exit pressure, giving the unsteady motion captured by the present LES. This cycle acts as a resonant tone but it is more complex than the classical resonant tone observed in the acoustic tube. It is a complex combination of acoustic lags, shock patterns, thermodynamic balancing and phase shift between the shock location and the effective geometry.

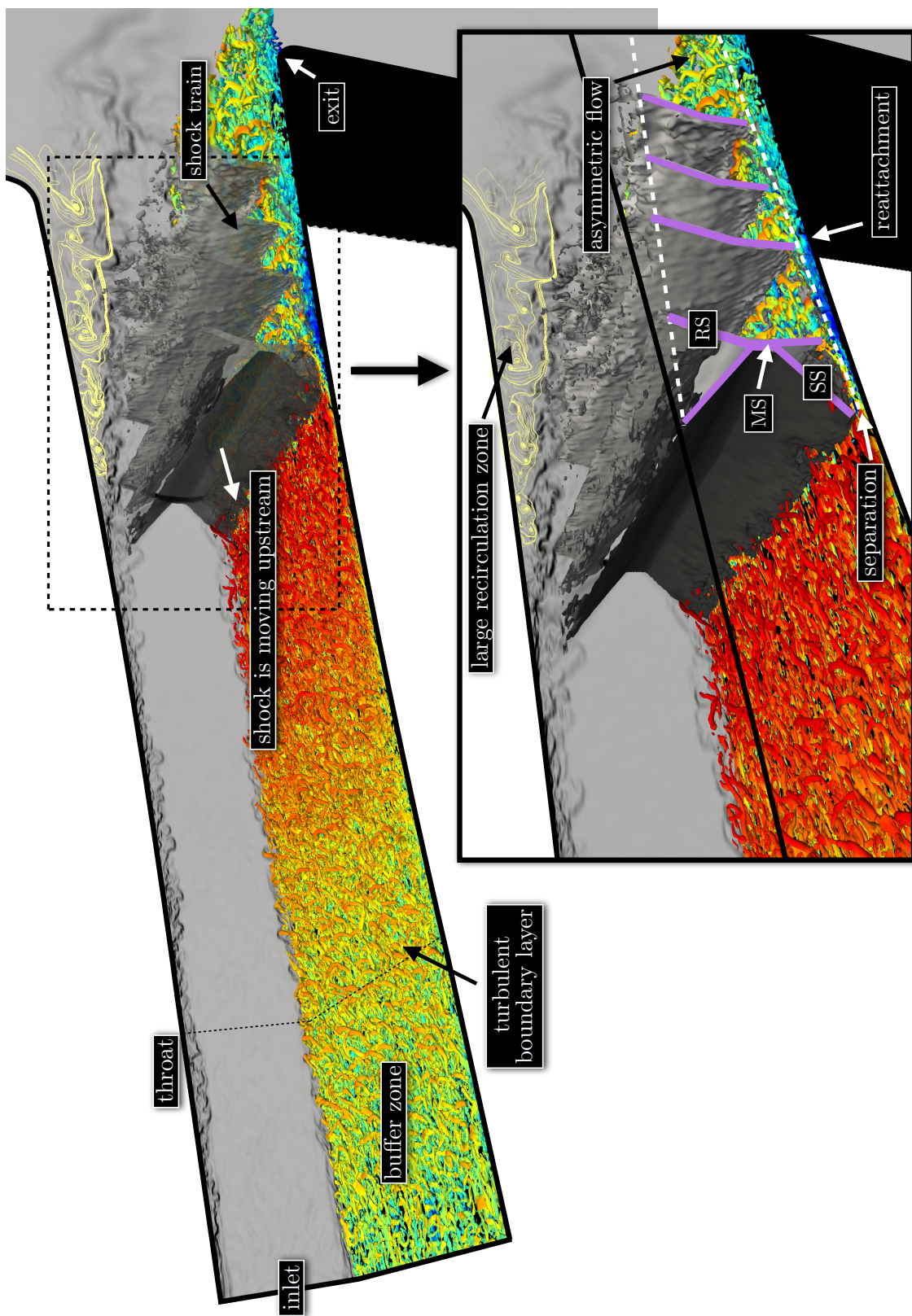


Figure 5.51: Planar WR-LES: The separated shock is moving upstream towards the throat, MS: Mach stem, SS: separated shock, RS: reflected shock; grayscale surface: Schlieren imaging in the x - y plane, grayscale volume: iso-volume of $\nabla ||u||$, jet color: iso-contour of Q criterion colored by the velocity field (blue: slow, red: fast).

6

Cylindrical nozzle flow

In this chapter, Large Eddy Simulation of an over-expanded cylindrical nozzle flow is performed to study the complex interaction between the turbulent boundary layer, the internal shock wave and the separated mixing layer. The results of both wall-modeled and wall-resolved LES aim to explain the separation unsteadiness by using spectra analysis. Similarly to the previous chapter, the mechanism driving the shock wave instability was identified and explained which led to a better understanding of the unsteady shock wave motion.

6.1 Simulation setup

The same high-order schemes, LES model and wall-model, from section 5, are used in this LES. The domain decomposition method, presented in section 2.4, is applied to a grid that contains two overlapping meshes. Figure 6.1 shows the wall-resolved grid representation with the two overlapping grids. The internal grid, Ω_1 , uses constant spacing in both y and z directions while the external grid Ω_2 is stretched in the radial direction to ensure WR-LES grid resolution close to the wall. As presented in the [Domain decomposition method](#) section, the overlapping limit between the two grid is set to $R_{\Omega_1} = 0.6R(x)$. The buffer layer between the inlet and the throat is approximately $28\delta_i$ (δ_i : the inlet BL thickness), allowing sufficient extent for the boundary layer to develop. The outside domain is similar to the planar nozzle flow of length $20H_t$. For convenience, all figures presented in this chapter will use the classical wall-normal notation y equivalent to the radius coordinates $y = R - r$. The angular/spanwise direction θ will be represented by the z -direction, unless otherwise specified.

The incoming boundary layer characteristics are similar to the planar case. The Reynolds number, based on the throat diameter D_t , is about 90000. The boundary condition at the inlet, δ_i , is kept the same as for the planar case, using the method of Xie

and Castro (sec. 2.3.3). The method has been adapted for the cylindrical coordinates r - θ . The outlet boundary condition uses a buffer area to damp the acoustic waves combined with far-field boundary conditions. Both wall-resolved and wall-modeled simulations are conducted using the same boundary layer parameters compared to the planar flow.

As explained in section 3.5.1, the effect of the spanwise curvature on the turbulent boundary layer has a marked influence on the velocity profiles. The characteristic surface-curvature parameter δ/R (R : the radius of the pipe) is often used to compare and classify the effects of curvature on a growing boundary layer. In the fully-developed pipe flow from section 3.5, the δ/R parameter was equal to unity and the effect of the curvature was strong enough to affect the first-order statistics. Several experimental and computational investigations have been carried out in the past on flat plate boundary layer, but much less effort was devoted to boundary layer in circular geometries. Numerically, some DNS and LES have been done with circular walls (Unger & Friedrich 1993, Eggels et al. 1994, Xu 2003, Wu & Moin 2008) focusing mainly on the fully-developed flows. Transverse curvature effects on growing boundary layer in pipe flows becomes important when the characteristic surface-curvature parameter is in the range [0.25:1]. Surface-curvature between 0 and 0.05 are known to have a weak effect on the boundary layer, so that the classical law of the wall can apply. For a characteristic surface-curvature parameter around 0.05, the inner region of the boundary layer is not highly influenced by the external flow and the log-law can be used with different coefficients, *i.e.* κ and C^+ .

The ratio δ/R' , where R' is the curvature of the wall, is close to zero due to the high radius of curvature of the divergent section. Thus, the wall-model developed in section 4 can be used for the present configuration as long as the transverse curvature compared to the boundary layer thickness is low enough, *i.e.* $\delta/R' < 0.25$. In the present study, the characteristic surface-curvature parameter is about 0.05. In the wall-model, the coefficients A and β have to be re-computed to fit the cylindrical law of the wall. Those two parameters are computed using *a-priori* test on the WR-LES, similarly to section 4.3.1.

The comparison between the planar and the cylindrical nozzle simulations is not relevant due to differences in geometry. Even though, the incoming boundary layer is kept the same, the nozzle area ratio ε and the mass flow rate are different. Two options for configuration are available; (*i*) the nozzle shape is kept the same ($\varepsilon = 1.6$) but the pressure gradient across the boundary layer is changed; (*ii*) the pressure gradient follows the planar nozzle flow but the structure of the nozzle is changed (reduced divergent angle).

We have decided to keep the structure of the nozzle similar to the planar nozzle flow while the pressure gradient is modified. The second option was irrelevant since the divergent section of the nozzle would have looked like a pipe flow and not to a nozzle

($\varepsilon_{\text{option 2}} = 1.26$).

To capture the shock separation at the same location as in the planar nozzle flow, the NPR is adjusted according to the isentropic relation and set to 2.0, so that the isentropic profiles between the planar and the cylindrical nozzles are the same. To perform a proper comparison with the planar nozzle flow, the incoming boundary layer pressure is kept constant, while the atmospheric pressure is changed to fit the present NPR.

The grid configurations for both WR- and WM-LES is shown in table A.1 and in the appendix A. The wall-unit grid spacing is similar to the planar case. The angular spacing in wall-unit $R\Delta\theta^+ = 20$ is setup to match the value of the planar nozzle flow. From the literature (Unger & Friedrich 1993, Eggels et al. 1993, Rudman & Blackburn 1999, Xu 2003), the angular spacing in LES of pipe flow should be in the range of 15-40. The number of points of the internal grid Ω_1 is set as an odd integer, so that to have the centerline aligned with the grid. The wall-normal r -direction is stretched in the wall-resolved case to match the resolution near the wall, *i.e.* $\Delta y^+ < 1$.

As for the planar case, the WR- and WM-LES are initialized using the Klein method (sec. 2.3.2). The results are averaged using slices extracted from the simulation during a dimensionless time $t^* \sim 4000$ for the wall-resolved simulation and $t^* \sim 18000$ for the wall-modeled simulation.

	N_ξ	$N_\eta^{\Omega_1}$	$N_\zeta^{\Omega_1}$	$N_\eta^{\Omega_2}$	$N_\zeta^{\Omega_2}$	L_b/H_t	Δx_i^+	Δy_i^+	$R\Delta\theta_i^+$	Nb cells
WR-LES	896	99	99	72	512	2.8	36	[1 : 30]	20	41 M
WM-LES	672	81	81	26	256	2.8	60	45	40	8.8 M

Table 6.1: Grid parameters of the cylindrical nozzle flows.

6.2 Incoming boundary layer

The DNS of the [Turbulent channel flow at \$Re_\tau = 220\$](#) and the [DNS of a turbulent pipe flow at \$Re_\tau = 220\$](#) have identified the similarities and differences between channel and pipe flow with fully-developed boundary layer. As observed by many (Eggels et al. 1994, Eckhardt et al. 2007, Wu & Moin 2008, Marusic et al. 2013), the effect of the transverse curvature of the wall in a pipe flow is not negligible and differences are clearly noticeable, even on the first-order statistics. The overlap layer where the universal log-law applies is slightly different in the case of a fully-developed pipe flow, compared to the channel flow, especially with the constants κ and C^+ . This overlapping region could be predicted by the power-law in fully-developed pipe flow as proposed by Barenblatt et al. (1997), Zagarola & Smits (1998) and McKeon et al. (2004).

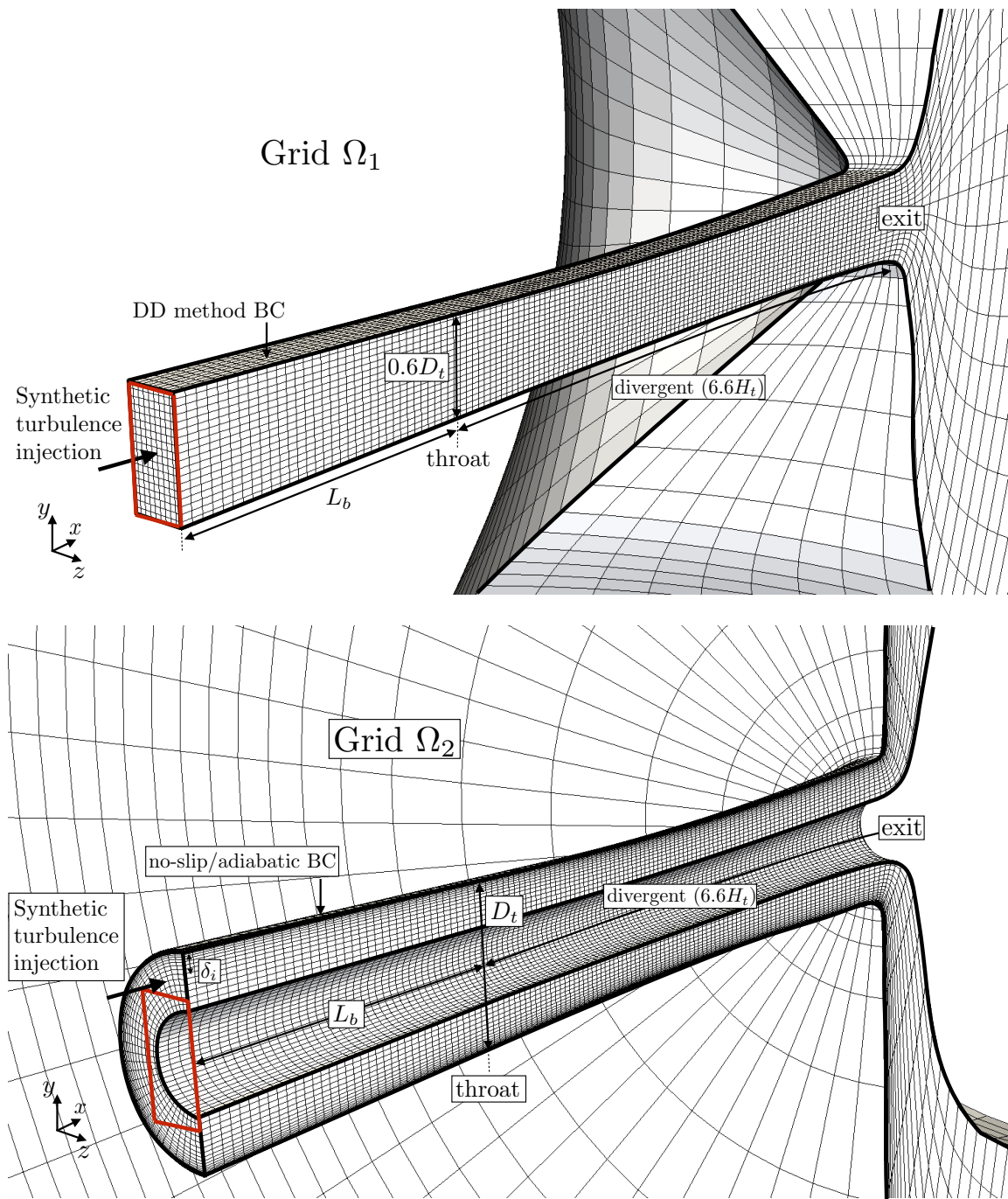


Figure 6.1: Grid representation from the Wall-Resolved case showing every 10th grid-line from half of the domain in z -direction or θ -direction. *Top*: Internal mesh Ω_1 (cartesian coordinates), *Bottom*: External mesh Ω_2 (cylindrical coordinates)

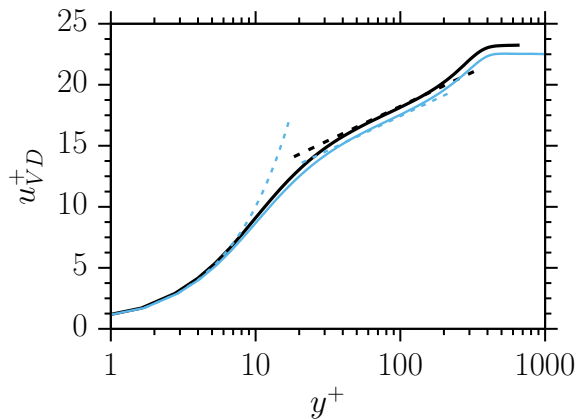


Figure 6.2: Van Driest velocity profiles along the wall-normal direction at $x/\delta_i = -10$; —: cylindrical WR-LES, - - : planar WR-LES, . . : $u^+ = y^+$ and the log-law.

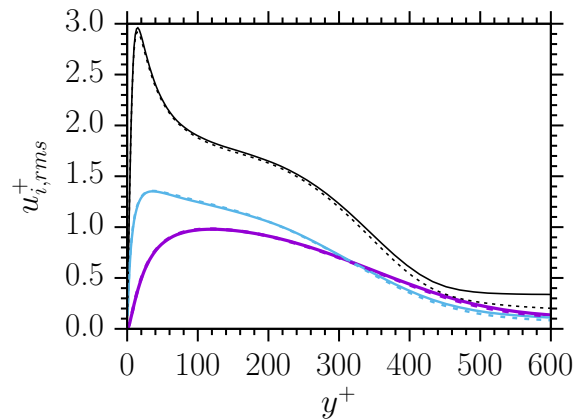


Figure 6.3: WR-LES: Normalized Reynolds stress along the wall-normal direction at $x/\delta_i = -10$; —: R_{11}^+ , - - : R_{22}^+ , —: R_{33}^+ , . . : planar WR-LES.

In the present LES, the incoming boundary layer is not fully-developed across the section. The incoming boundary layer thickness is about 5% of the radius at the throat. The effect of curvature at this specific boundary layer thickness is mild compared to fully-developed flow. Figure 6.2 shows the Van Driest velocity profiles downstream of the inlet at $x/\delta_i = -10$ for the wall-resolved simulation. The present results appear to contradict with the latter hypothesis. The velocity in the overlap region and in the outer layer is shifted upward compared to the planar flow but the slope of the log-law seems to follow the planar case. It confirms the conclusions on the pipe flow where the coefficient κ of the log-law is constant and the coefficient C is affected by the transverse curvature effects.

Conversely, figures 6.3, 6.4 and 6.5 show the second-order statistics along the wall-normal direction where all of the solutions pretty much coincide between the cylindrical and the planar flow. For fully-developed pipe flow, the effect of transverse curvature can be important on the wall-normal Reynolds stress and on the wall-normal RMS fluctuations (Ghosh et al. 2010). We have observed similar behavior in our simulation of the DNS of a turbulent pipe flow at $Re_\tau = 220$. In the present wall-resolved simulation, the wall-normal Reynolds stress is similar to the planar nozzle flow. Second-order statistics do not seem to be influenced by the wall curvature.

Figure 6.6 shows the wall turbulent structures at $y^+ \sim 20$. The streaks observed in the previous chapter are again captured by the wall-resolved LES. The effect of the synthetic boundary condition is captured from the inlet to $x/\delta_i \sim -15$ corresponding to the length of the coherent structure observed by Xie & Castro (2008) of about 10-15 δ . From the throat, the turbulent structures seem to be affected by the favorable pressure gradient present in the divergent section of the nozzle.

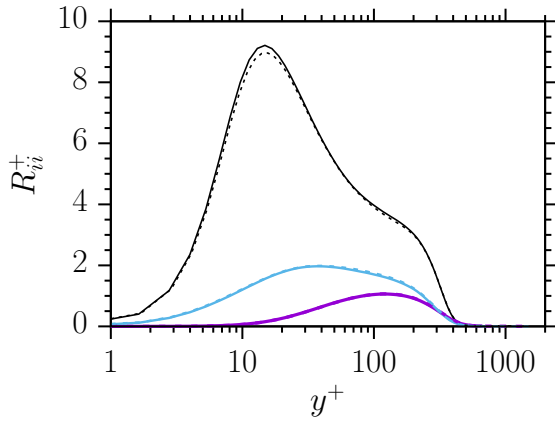


Figure 6.4: WR-LES: Normalized velocity RMS along the wall-normal direction at $x/\delta_i = -10$; $-$: u_{rms}^+ , $-$: v_{rms}^+ , $-$: w_{rms}^+ , $--$: planar WR-LES.

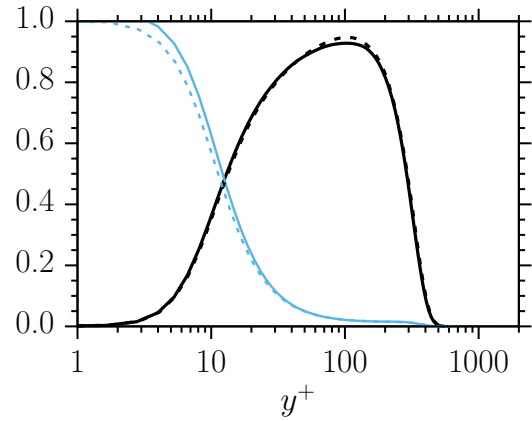


Figure 6.5: WR-LES: Normalized shear stress, turbulent ($-$) and viscous ($-$) terms, along the wall-normal direction at $x/\delta_i = -10$; $--$: planar WR-LES.

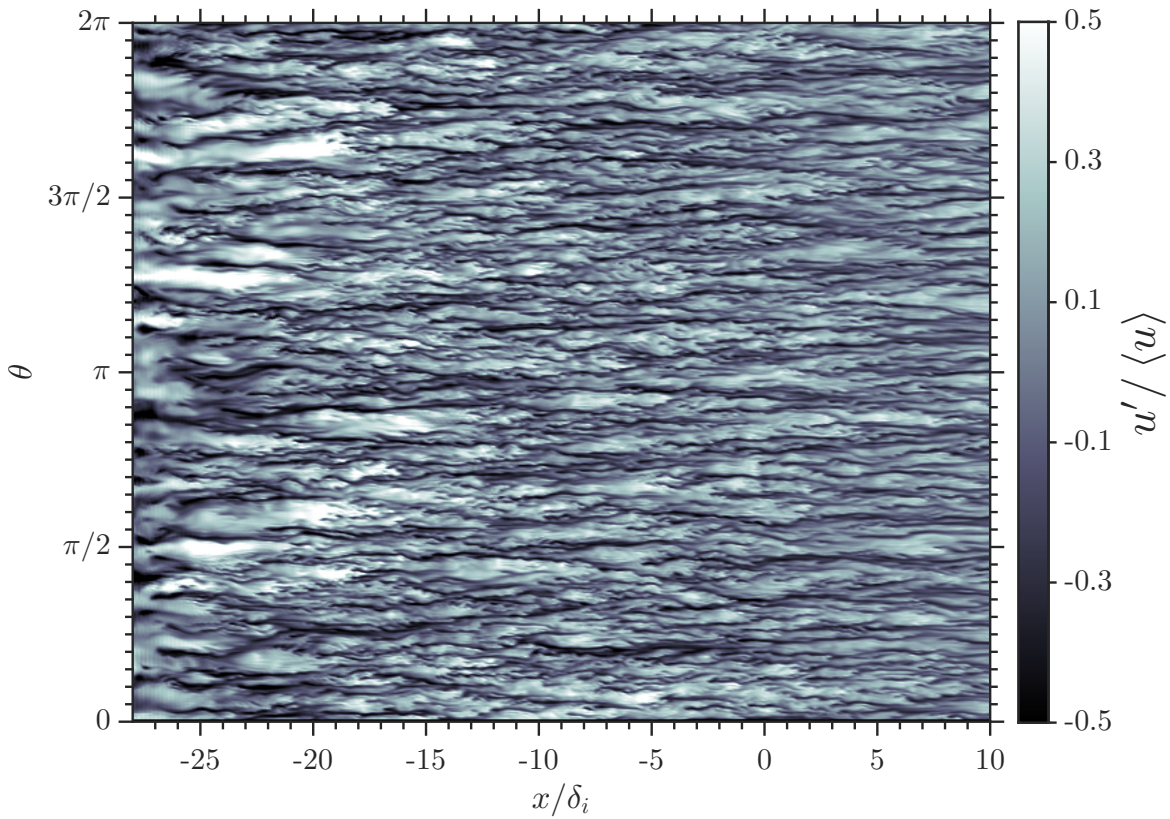


Figure 6.6: WR-LES: Instantaneous velocity fluctuations in x - θ plane at $y^+ \sim 20$.

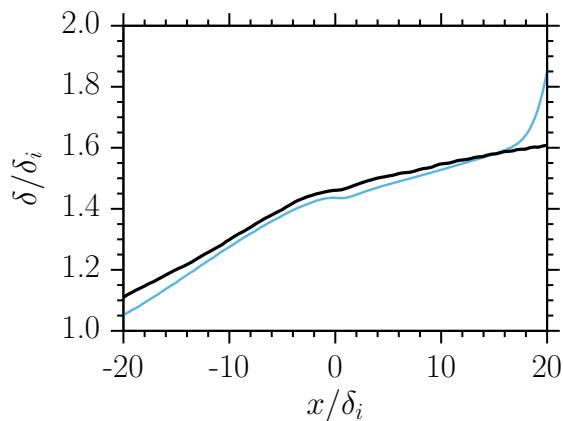


Figure 6.7: WR-LES: Boundary layer thickness along the x -direction; —: planar WR-LES, - -: cylindrical WR-LES.

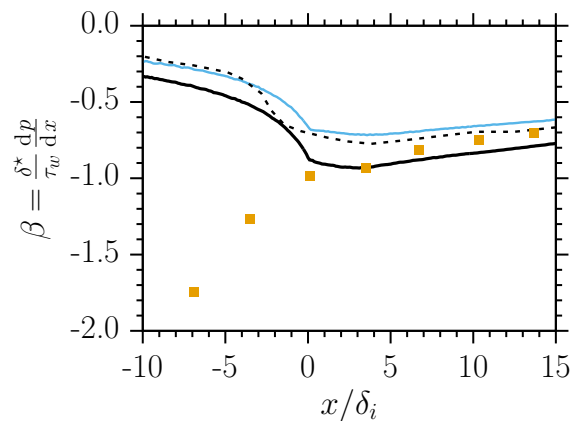


Figure 6.8: WR-LES: Normalized pressure gradient along the x -direction; —: planar WR-LES, - -: planar WR-LES from Olson & Lele (2011), —: cylindrical WR-LES, ■: planar experimental results from Johnson & Papamoschou (2010).

6.3 Some statistics

Figure 6.9 shows the grid resolution near the wall in wall-unit. The first grid spacing along the nozzle wall of the wall-resolved case satisfy the condition of $\Delta y_{min}^+ < \sim 1$. Figure 6.10 shows the wall pressure distribution for the wall-resolved and the wall-modeled simulation. The concordance between the two solutions shows that the wall-modeled simulation is able to properly capture the pressure gradient effect. One can also notice a small difference in the separated region where the wall-resolved computation is smooth while the wall-modeled distribution is sharp. This behavior is due to the strong compression waves in the wall-modeled simulation applying in the interaction zone upstream of the separation point. As explained in section 5.4, the coarse grid of the wall-modeled case reduces the length of interaction and increases the strength of the compression waves. This results in a sharper shock with a more pronounced λ -shape pattern as observed in figure 6.27 and 6.33. The shock strength is imposed by the upstream boundary layer and the flow deviation from the separation.

Figure 6.8 shows the Clauser's parameter β along the x -direction. The pressure gradient is increased by 40-80% compared to the planar case. The buffer section, upstream of the throat, is subjected to a stronger pressure gradient due to the reduced cross section of the nozzle compared to the planar case which does not use side walls. Clauser's parameter is about 0.35 at $x/\delta_i = -10$, while the planar case was about 0.2. The profiles from figure 6.8 handles a more pronounced pressure gradient compared to the planar solution which could explain the gap observed in the log-law (fig. 6.2).

Figure 6.11 shows the rms wall pressure distribution for the WM-LES. The p_{rms} is

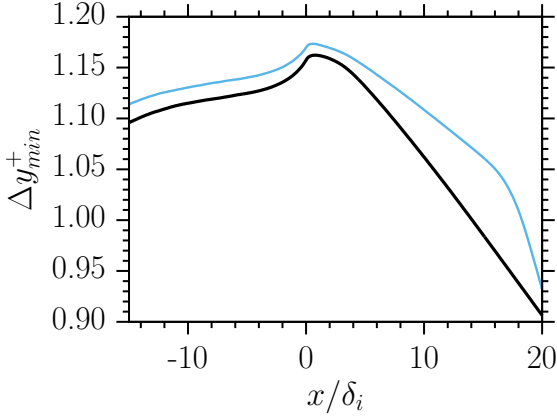


Figure 6.9: WR-LES: Wall-unit length Δy_{min}^+ at the first near-wall cell along the x -direction; —: planar WR-LES, - -: cylindrical WR-LES.

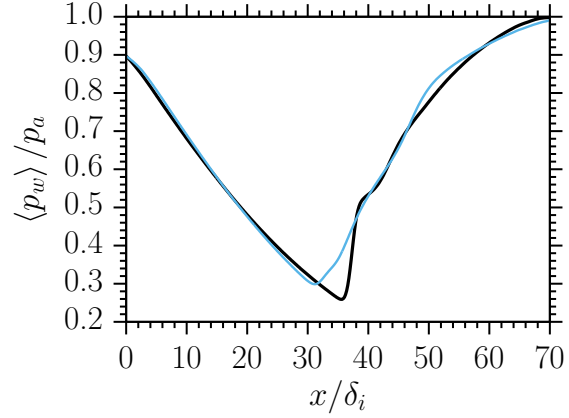


Figure 6.10: Normalized wall pressure along the x -direction; —: WM-LES, - -: WR-LES.

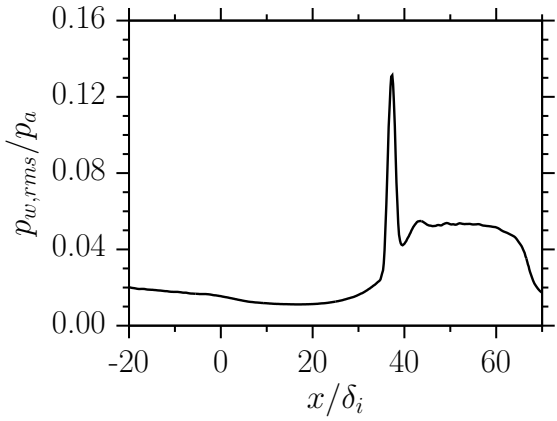


Figure 6.11: WM-LES: Normalized pressure RMS at the wall along the x -direction.

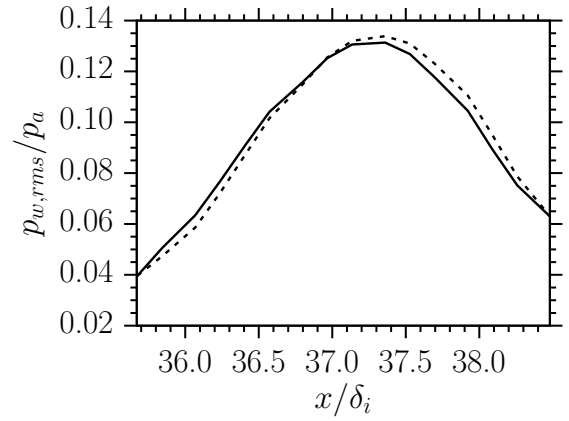


Figure 6.12: Normalized pressure RMS centered in the separation area; —: present WM-LES, - -: theoretical function.

slightly reducing along the boundary layer upstream of the separation. At the separation, *i.e.* $x/\delta_i = 37.1$, the p_{rms} is intermittent in the interaction zone, as explained by Kistler (1964). The pressure oscillates back and forth between the mean pressure at the start of the interaction (p_I) and the mean pressure at the plateau (p_p). Using the intermittent factor ε_i (eq. 1.6), the p_{rms} can be predicted by equation 1.7 from Kistler (1964). Kistler's function is plotted along with the present WM-LES computation (fig. 6.12), the result indicates that the theoretical function is accurately capturing the fluctuations of the pressure field within the interaction length.

Figure 6.13 shows the separation location for both wall-resolved and wall-modeled simulations. The separation location is computed similarly to the planar case (eq. 5.2), except for the velocity that is averaged in θ -direction instead of the z -direction. The amplitude of the separation line is moderate compared to the planar nozzle. In the cylindrical nozzle flow, the amplitudes of the separation line are about two boundary

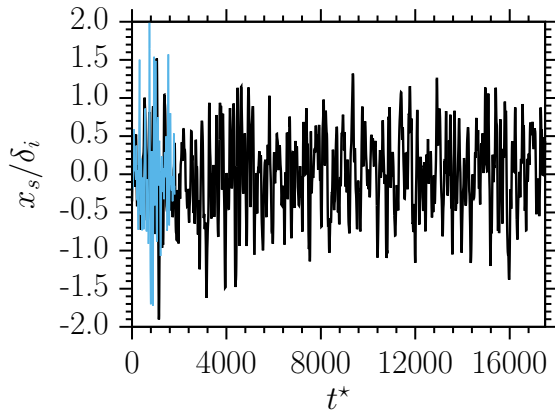


Figure 6.13: Separation location over time; —: WM-LES, —: WR-LES.

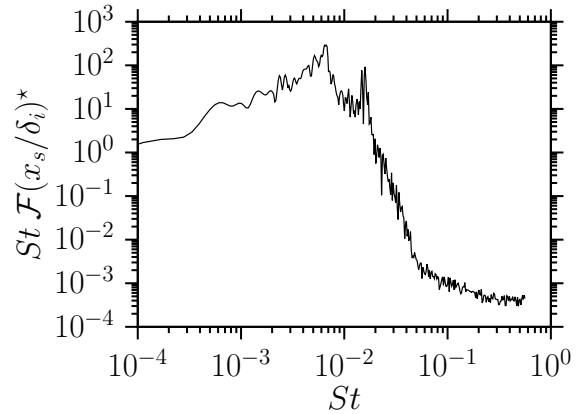


Figure 6.14: Normalized pre-multiplied spectrum of the separation location from the time-resolved WM-LES.

layer thickness order of magnitude where the planar one had 20. This is expected because of the strong adverse pressure gradient developing upstream of the separation that acts on the boundary layer. Figure 6.14 shows the normalized spectrum of the separation location. The normalization of the next spectra is similar to section 5 following equation 5.9. Three peaks of energy can be extracted from this spectrum. The tone at $St = 0.0067$ is the most energetic one and can be assimilated to the resonant tone illustrated in [Planar nozzle flow](#). Equation 5.12 from Zaman et al. (2002) can be used for the present cylindrical nozzle as it fits the requirements proposed by Zaman (mild opening angle of divergent, low Reynolds number, subsonic Mach jet). The predicted Strouhal number of resonance can be computed by:

$$St = \frac{1 - M_e^2}{M_e} \frac{\delta}{4L_{x,e}}, \quad (6.1)$$

where M_e is the averaged Mach number at the nozzle exit and $L_{x,e}$ the length between the mean separation location and the nozzle exit.

The computed Strouhal number of resonance is about 0.007 which is close to the peak of energy observed in figure 6.14. The two way coupling between the separation and the nozzle exit seems to fit one-quarter wavelength as observed in the planar nozzle flow.

A second peak of energy can be observed around Strouhal number of 0.015. We will see later in this chapter that the second peak is due to the recirculation bubbles developing in the separated zone upstream of the nozzle exit. Above $St = 0.015$, the spectrum collapses and no energy can be extracted from the high frequency range. This is expected as the separation location is spatially averaged (in θ -direction) which removes the high frequency oscillations from the mixing layer or from the boundary layer. For proper time-resolved spectra, the time-resolved pressure field will be used later in this chapter.

6.4 Side-loads analysis

The streamwise force (F_x) and side-loads (F_y, F_z) are computed using equation 5.5. The forces are integrated along the azimuthal direction θ from the inlet x_i to the exit of the nozzle x_e . Table 6.2 shows averaged and RMS forces in each directions. The averaged y - and z -direction forces are close to zero, which means that the exhaust plume is, in average, mostly symmetric. The side-loads, *i.e.* y -direction and z -direction forces, can be combined to form the normed vector ($F_{\vec{n}}$) and the angle (Θ_F) between F_y and F_z using:

$$F_{\vec{n}} = \sqrt{F_y^2 + F_z^2}, \quad (6.2)$$

$$\Theta_F = \left(\tan^{-1} \frac{F_z}{F_y} \right). \quad (6.3)$$

Figure 6.15 shows the streamwise force and the norm of the side-loads as function time. One can notice that the fluctuations of the streamwise force are weak compared to the side-loads. The mild opening angle of the divergent and the small fluctuations of the separation line result in a weak rms of the streamwise force. Figure 6.16 shows a typical polar plot of the side-loads. One can notice the isotropic and chaotic behavior of the fluctuating side-loads. The two side-loads vectors follow a two-dimensional Gaussian distribution. Those two vectors are uncorrelated, Gaussian distributed with equal variance, and zero mean which fits the Rayleigh distribution:

$$f(x; \sigma) = \frac{x}{\sigma^2} \exp\left(-x^2/(2\sigma^2)\right). \quad (6.4)$$

The computed side-loads probability density function, in figure 6.19, is compared with experimental results and URANS computations from Deck & Nguyen (2004). The present LES seems to indicate that the distribution of the side-loads amplitude follows a Rayleigh distribution as proposed by many authors (Dumnov et al. 1996, Terhardt et al. 2001, Sé et al. 2002, Deck & Nguyen 2004). The scale parameter $\sigma \sim 0.8862$ fits reasonably the prediction of the Rayleigh distribution function ($< 0.1\%$) where the URANS computations of Deck & Nguyen (2004) was about 2%. These correlations demonstrate that the vectors of side-loads are not correlated. Thus, the side-loads do not have any twirling movement and the angle of the force is acting chaotically on the structure of the nozzle. It has also been confirmed, from the averaged vorticity field at the exit, that the exhaust plume does not swirl or twirl around the centerline.

Figure 6.17 and 6.18 show the normalized spectrum of the streamwise force and the side-loads, respectively. As observed in the planar case, the streamwise force is sensitive to the low-frequency oscillations of the separation line while the side-loads seems to be

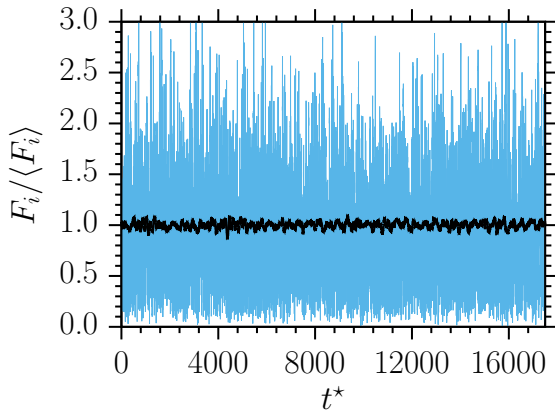


Figure 6.15: WM-LES: Forces over time; $-$: streamwise direction F_x , $-$: wall-normal direction $F_{\vec{n}}$.

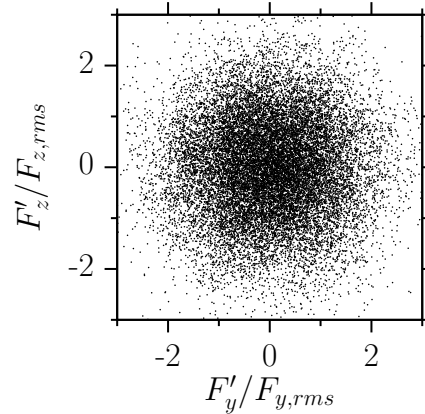


Figure 6.16: WM-LES: Polar plot of the side-loads over time.

Case	$\langle F_x \rangle / F_{isen}$	$\langle F_{\vec{n}} \rangle / F_{isen}$	$F_{x,rms} / F_{isen}$	$F_{y,rms}$	$F_{z,rms} / F_{isen}$
WR-LES	0.44	0.78	0.008	0.59	0.59
WM-LES	0.5	0.84	0.014	0.67	0.67

Table 6.2: Averaged/rms forces of the cylindrical WM-LES compared to WR-LES scaled by the isentropic normal force.

receptive to the higher frequency ranges. The same peaks of energy observed in figure 6.14 are captured in the streamwise force spectrum. The main tone computed by the spectrum is about $St = 0.0067$, similarly to the previous analysis of the separation location. The second peak at $St = 0.016$ is also captured within the streamwise force. Another peak of energy is observed in the high frequency range at $St = 0.1$. As observed in the planar nozzle and according to literature (Dupont et al. 2006, Toubert & Sandham 2009), the fluctuations of about a tenth of the Strouhal number originate from the mixing layer downstream of the separation.

A mild peak of energy is also noticeable in the low-frequency range at 0.002. This tone originates from the outlet boundary condition reflecting some of the acoustic waves created by the separation unsteadiness. The length between the exit of the nozzle and the outlet boundary condition is about $200\delta_i$. Using the averaged speed of sound in the ambient region, one can compute the time/frequency of a wave to propagate and reflect to the outlet which ends up to a tone of about 0.002. Despite the use of a far-field boundary condition and a sponge layer close to the outlet boundary condition, a part of the acoustic waves created by the separation are reflected by the outlet condition creating this mild peak of energy in the spectrum. This issue has been corrected by implementing the NSCBC or non-reflecting BC (see appendix B).

The side-loads spectrum is plotted in figure 6.18. Similarly to the planar nozzle

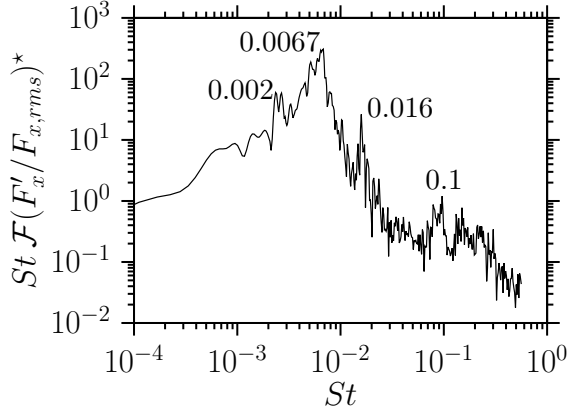


Figure 6.17: WM-LES: Normalized pre-multiplied spectrum of the streamwise force $F_x/F_{x,rms}$.

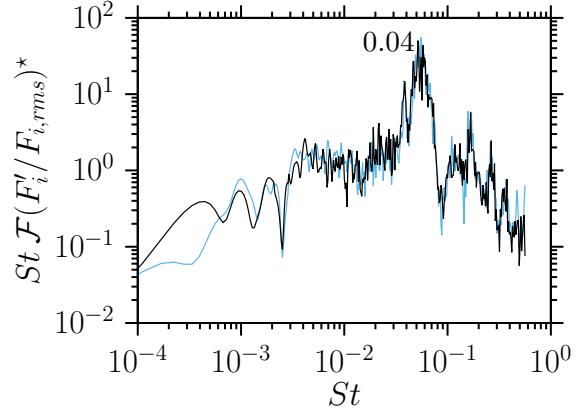


Figure 6.18: WM-LES: Normalized pre-multiplied spectra of the side-loads; $-: F_y/F_{y,rms}$, $-: F_z/F_{z,rms}$.

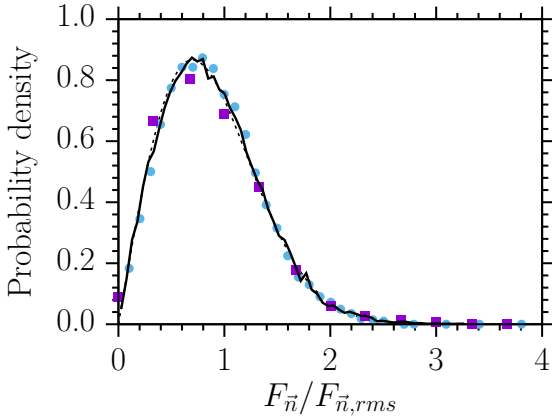


Figure 6.19: Probability Density Function of the side-loads $F_{\bar{n}_i}$; $-$: current WM-LES, $--$: Rayleigh distribution, \bullet : experiment from Deck & Nguyen (2004), \blacksquare : URANS from Deck & Nguyen (2004).

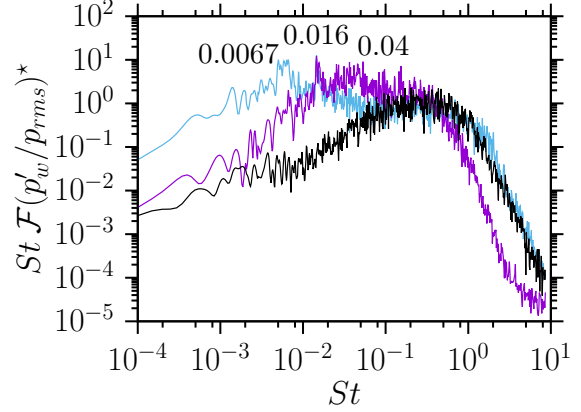


Figure 6.20: WM-LES: Normalized pre-multiplied spectra of the pressure field at the wall; $-$: in the incoming boundary layer $x/\delta_i = 0$, $-$: at the separation $x/\delta_i \sim 37.1$, $-$: at the exit $x/\delta_i = 66$.

flow, the side-loads are affected by the high frequency range oscillations arising from the separated flow downstream of the shock. The two side-loads signal have similar spectrum along the frequency range of study. The main peak of energy is around $St = 0.04$ or $St_D \sim 1$ using the Strouhal number based on the nozzle exit conditions, *i.e.* $St_D = \varepsilon D / (\delta M_e) St$. From previous studies (Tanna 1977, Bodony & Lele 2008, Bühler et al. 2014), the nozzle lip is known to generate trailing-edge noises at $St_D = 1$. This noise affects the exit pressure field which propagates acoustic waves upstream through the subsonic recirculation area. Changing the lip curvature or reducing the flange width could lead to a shifted range of frequencies as observed by Ponton & Seiner (1992).

Based on the side-loads spectra, one can characterize and identify the origin of energy peaks. As for the planar flow, a time-resolved line has been captured along the circular wall and will be used for the next figures. The time-resolved line captures a large range

of frequencies from Strouhal number 10^{-4} to 10. Figure 6.20 shows the spectra of the normalized pressure field at the wall for different x -location. One can notice from the spectrum at the throat that the energy is centered around $St = 1$, following the definition of the Strouhal number based on the boundary layer characteristics. At the separation location, the peak of energy is captured at $St = 0.0067$ similar to the peak observed in the separation spectrum (fig. 6.14). The resonant tone is also captured at the nozzle exit along with the recirculation bubble effect $St = 0.016$ and with the trailing-edge noise at $St = 0.04$.

Figure 6.22 shows the frequency analysis at the wall along the x -direction. The main tone is captured at the separation location and in a region around $x/\delta_i \sim 45$. The latter is due to the reflected shock impinging the separated flow and the wall, creating acoustic waves of a frequency similar to the main tone. The second peak of frequency, *i.e.* $St = 0.016$, is captured in two specific locations, for $x/\delta_i = [40 : 45]$ and $x/\delta_i = [54 : 66]$, *i.e.* the recirculating regions; the separated bubble downstream of separation and the second recirculation bubbles upstream of the exit. The large streamwise vortices formed in those regions are similar to the superstructures observed by many authors (Dupont et al. 2006, Toubert & Sandham 2009, Piponniau et al. 2009). They can have a length of up to 30δ and could be a source of very low-frequency unsteadiness as observed in the present LES.

Figure 6.21 shows the frequency analysis using z -slice at the axis of the cylinder. For each point in the x - y plane, the Strouhal number associated with the maximum energy from the normalized pressure field spectrum is displayed using iso-contours values of the different phenomena captured above. A color is associated to each phenomenon with,

- $St = 0.0067$, the resonant tone predicted by Zaman et al. (2002) is captured at the separation, in the λ -shock and in the second shock train at $x/\delta_i \sim 50$. It is interesting to notice that the second shock oscillates at the same resonant tone compared to the first λ -shock.
- $St = 0.016$, the subsonic flow downstream of the separation, at $x/\delta_i \sim 60$, is trapped between the mixing layer and the wall producing small unsteady eddies oscillating at this specific frequency. This phenomenon is strongly impacting the lateral forces (side-loads).
- $St = 0.04$, the trailing-edge noises from the lip is captured at the nozzle exit and in most of the atmosphere, as explained by Bühler et al. (2014). The frequency at which noises are captured is similar to the vortex shedding phenomenon taking place outside of a nozzle jet plume.

St	Phenomenon	Effect on x_s	Effect on F_x	Effect on $F_{\bar{n}}$
0.0067	Resonant tone	Strong	Strong	<i>Weak</i>
0.016	Recirculation bubbles	Mild	Mild	<i>Weak</i>
0.04	Trailing-edge noises	-	<i>Weak</i>	Strong
0.1	Mixing layer unsteadiness	-	<i>Weak</i>	Mild
1	Boundary layer turbulence	-	-	-

Table 6.3: Effects of different nozzle unsteadiness.

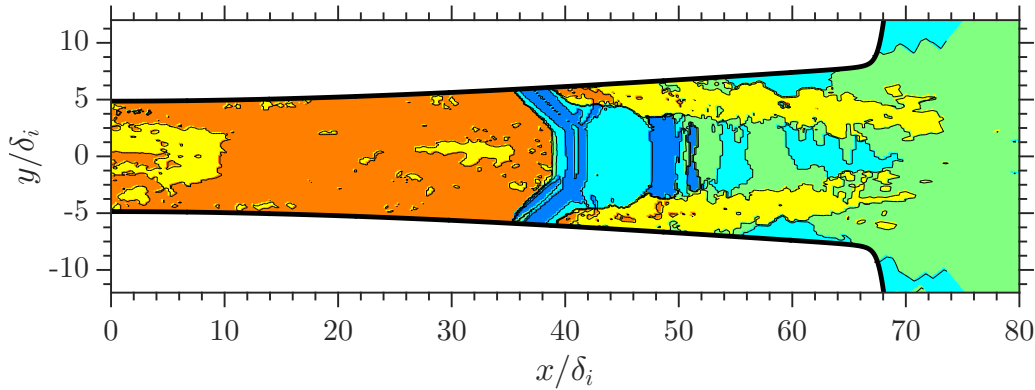


Figure 6.21: WM-LES: Frequency analysis in the x - y plane showing the Strouhal number associated with the maximal energy extracted from the normalized pressure field spectra $\mathcal{F}(p'/p_{rms})$; **boundary-layer turbulence** ($St \sim 1$), **mixing layer unsteadiness** ($St \sim 0.1$), **trailing-edge noises** ($St \sim 0.04$), **recirculation bubbles** ($St \sim 0.016$), **resonant tone** ($St \sim 0.0067$).

- $St = 0.1$, the mixing layer developing from the separation to the exit is observed at this frequency as explained in section 6.4. The large 2-dimensional Kelvin-Helmholtz vortices impact the exit conditions, modifying the effective exit area and the position of the separation shock.
- $St = 1$, upstream of the separation, the pressure fluctuations are dominant in the range of turbulent boundary layer frequencies. The position of the shock is slightly correlated with the upstream condition. However, the asymmetry of the separation is strongly influenced by the incoming boundary layer turbulence, particularly observed in the planar flow (sec. 5).

6.5 Summary

Accordingly to the results, the wall-modeled LES matched with the wall-resolved simulation. The feedback mechanism proposed by Olson & Lele (2011) is validated from the spectra analysis. The wall-modeled simulation has reduced the computational time by a factor of 40 compared to WR-LES. This allowed us to perform a better spectra

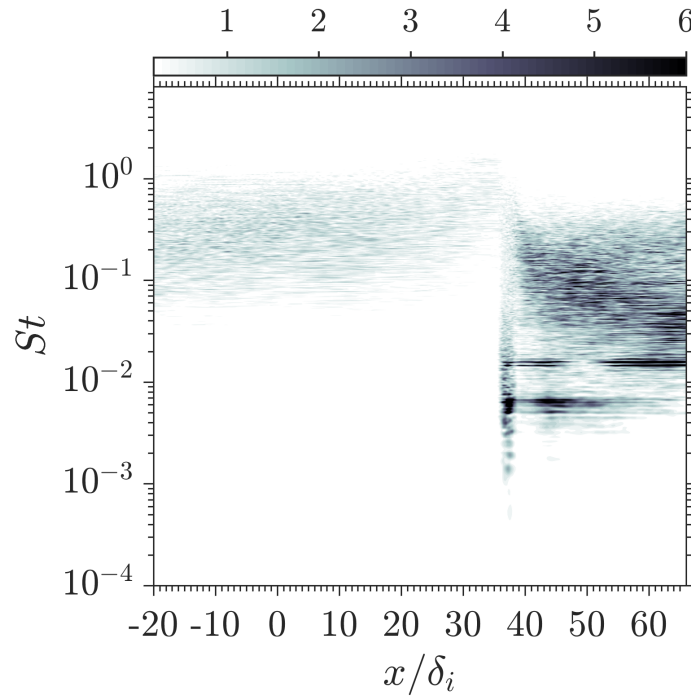


Figure 6.22: WM-LES: Normalized pressure fluctuations spectra $St\mathcal{F}(p'_w/p_{rms})^*$ along x -direction.

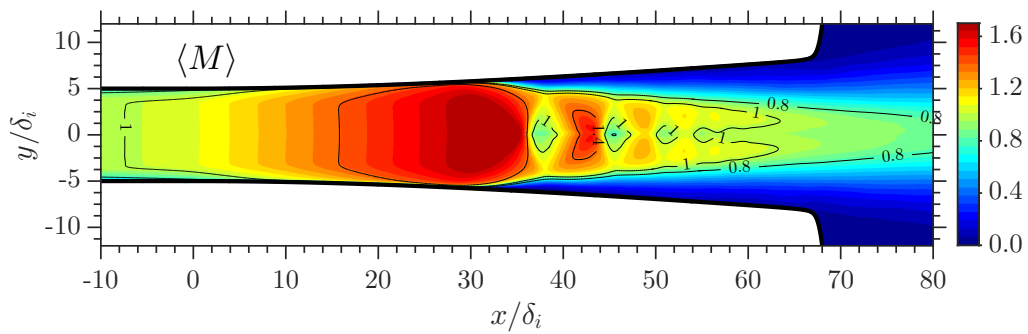


Figure 6.23: WR-LES: Averaged Mach number $\langle M \rangle$ contour in the x - y plane.

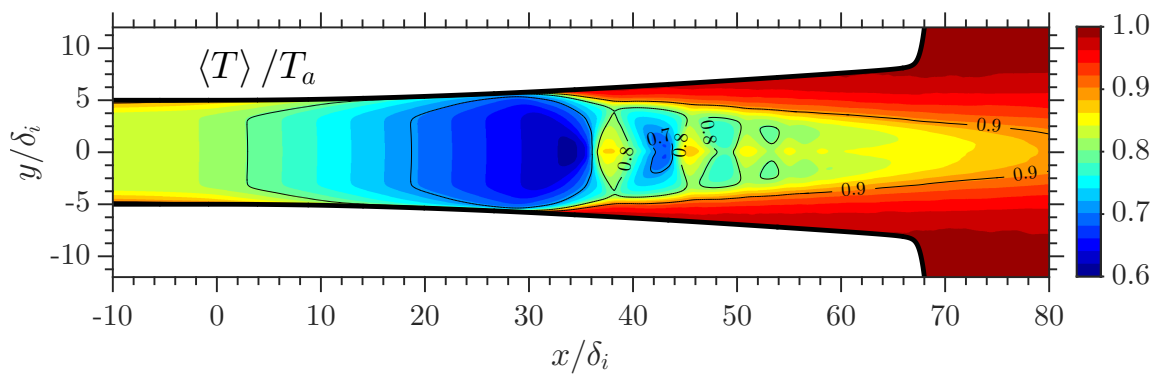


Figure 6.24: WR-LES: Averaged temperature $\langle T \rangle / T_a$ contour in the x - y plane.

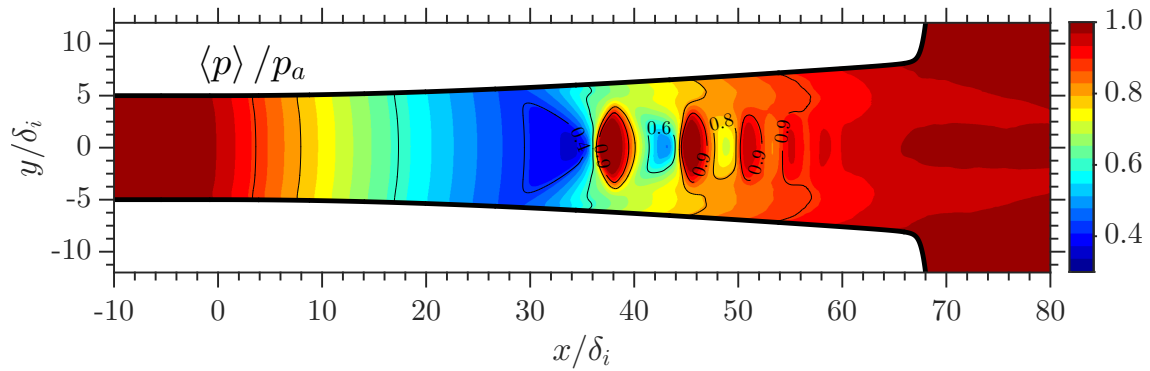


Figure 6.25: WR-LES: Averaged pressure $\langle p \rangle / p_a$ contour in the $x-y$ plane.

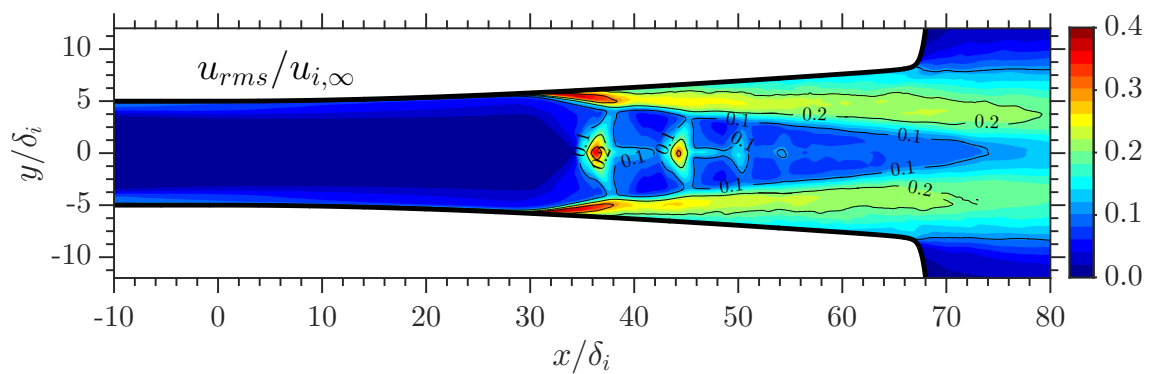


Figure 6.26: WR-LES: RMS velocity $u_{rms} / u_{i,\infty}$ contour in the $x-y$ plane.

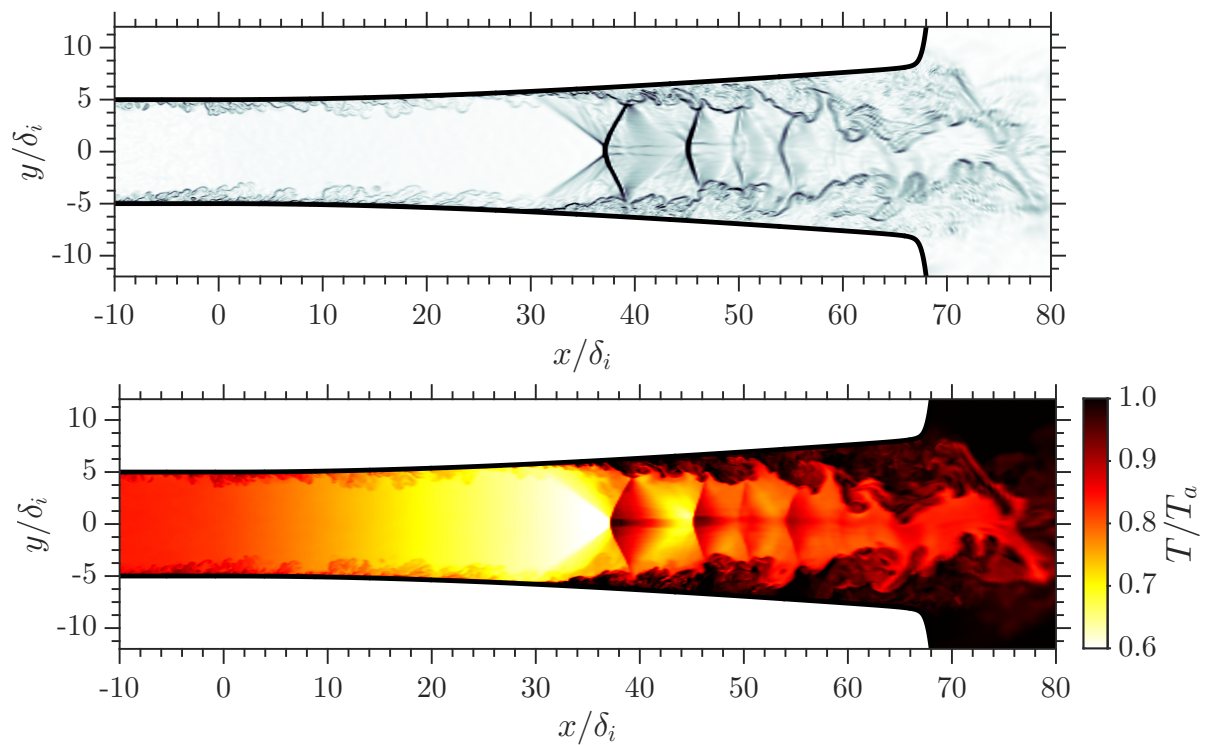


Figure 6.27: WR-LES: Instantaneous density gradient contour $\nabla \rho$ (top) and temperature field (bottom) in the $x-y$ plane at $t^* = 1025$.

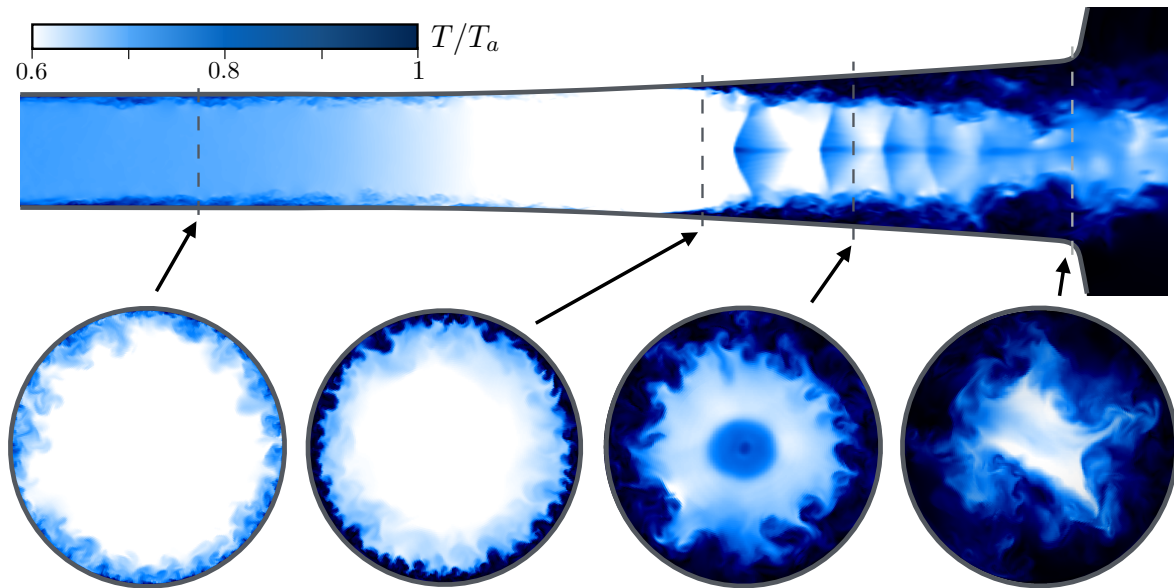


Figure 6.28: WR-LES: Instantaneous temperature contour T in the $x-y$ plane (top) and in the $\theta-r$ plane (bottom) for different x -position: in the upstream boundary layer, at the separation, downstream of separation and at the exit (from left to right).

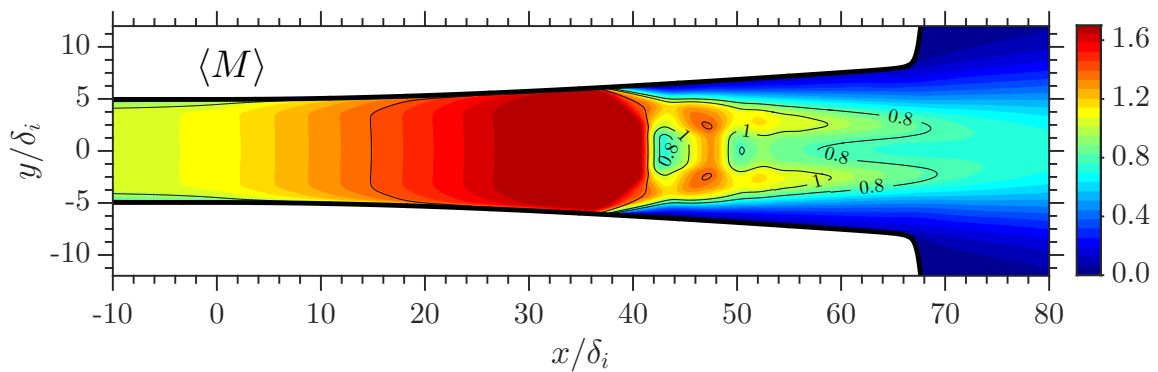


Figure 6.29: WM-LES: Averaged Mach number $\langle M \rangle$ contour in the $x-y$ plane.

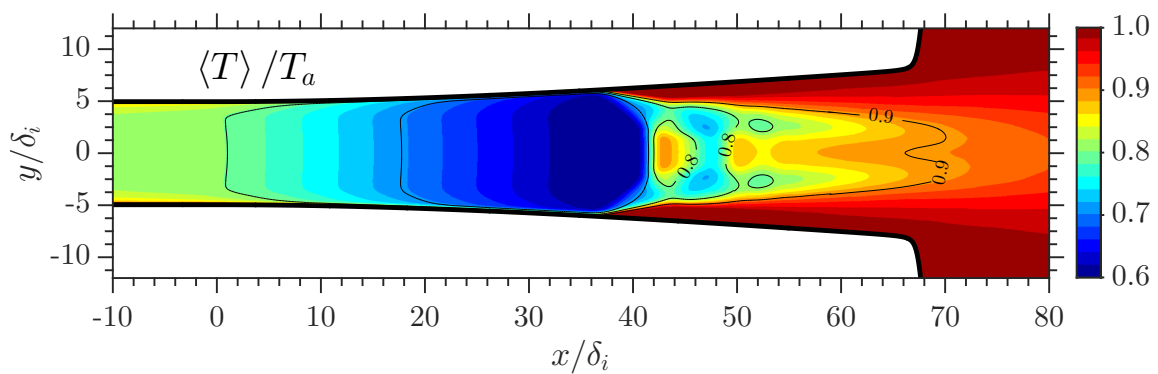


Figure 6.30: WM-LES: Averaged temperature $\langle T \rangle / T_a$ contour in the $x-y$ plane.

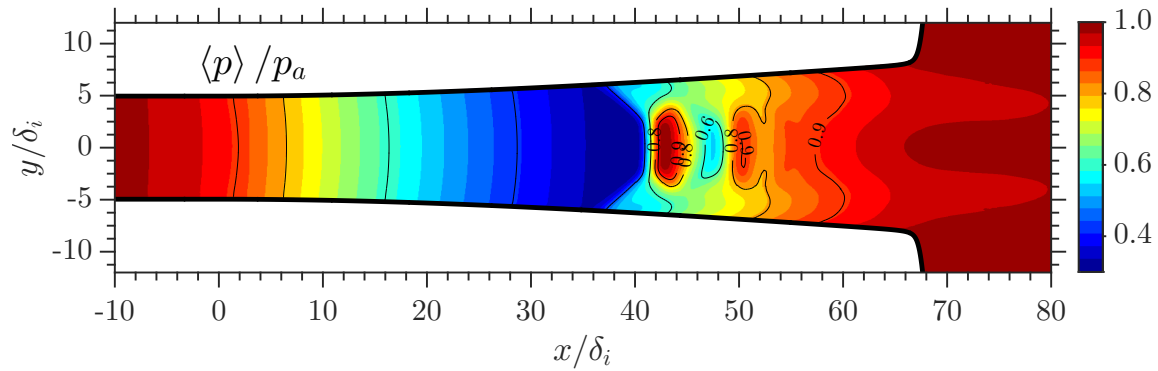


Figure 6.31: WM-LES: Averaged pressure $\langle p \rangle / p_a$ contour in the $x-y$ plane.

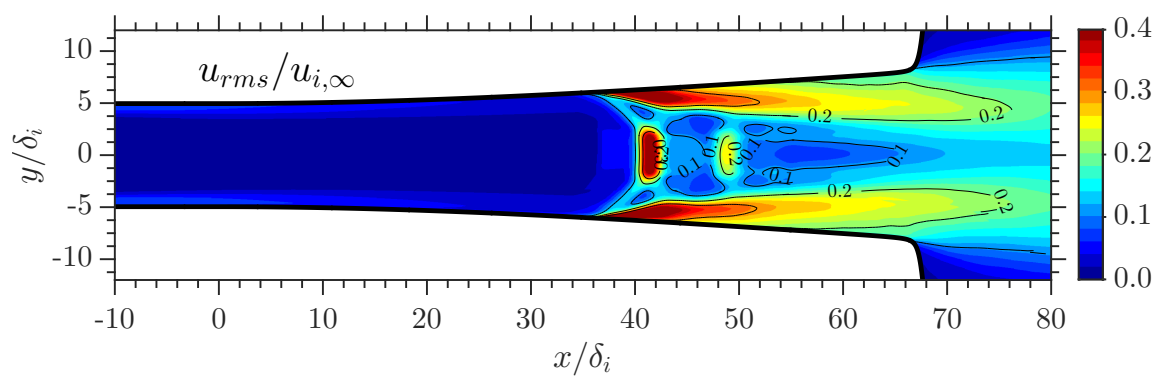


Figure 6.32: WM-LES: RMS velocity $u_{rms}/u_{i,\infty}$ contour in the $x-y$ plane.

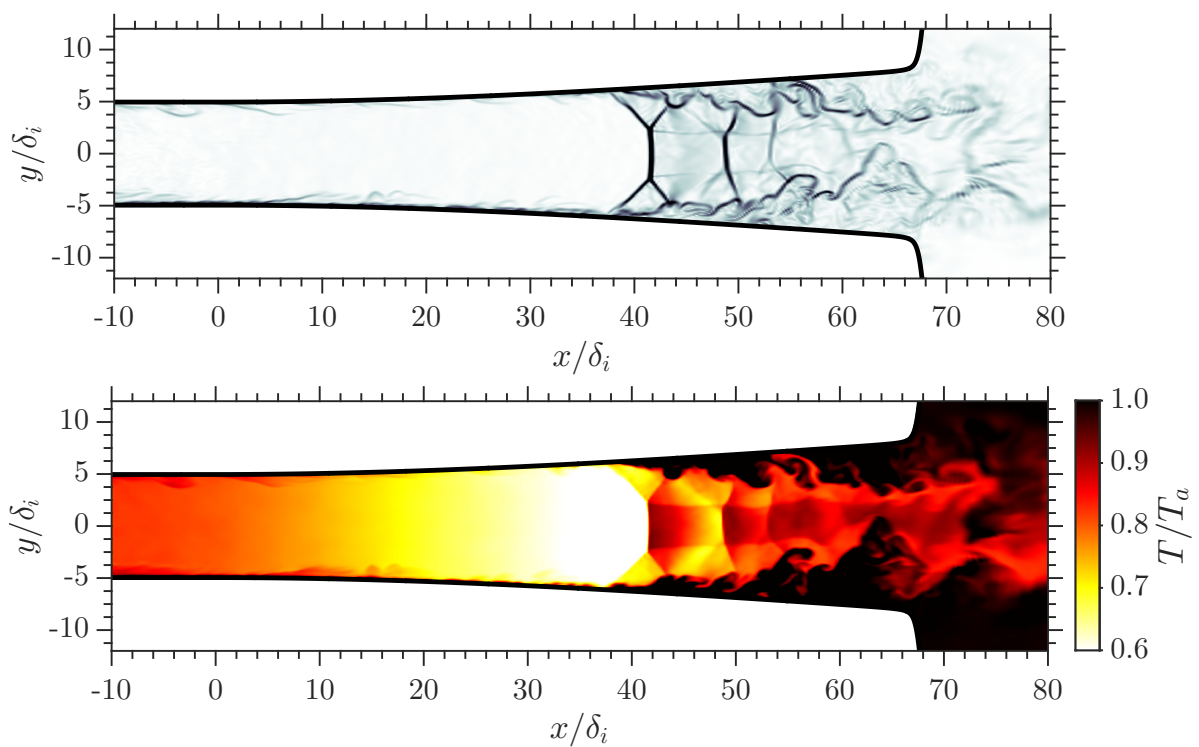


Figure 6.33: WM-LES: Instantaneous density gradient contour $\nabla \rho$ (top) and temperature field (bottom) in the $x-y$ plane at $t^* = 8190$.

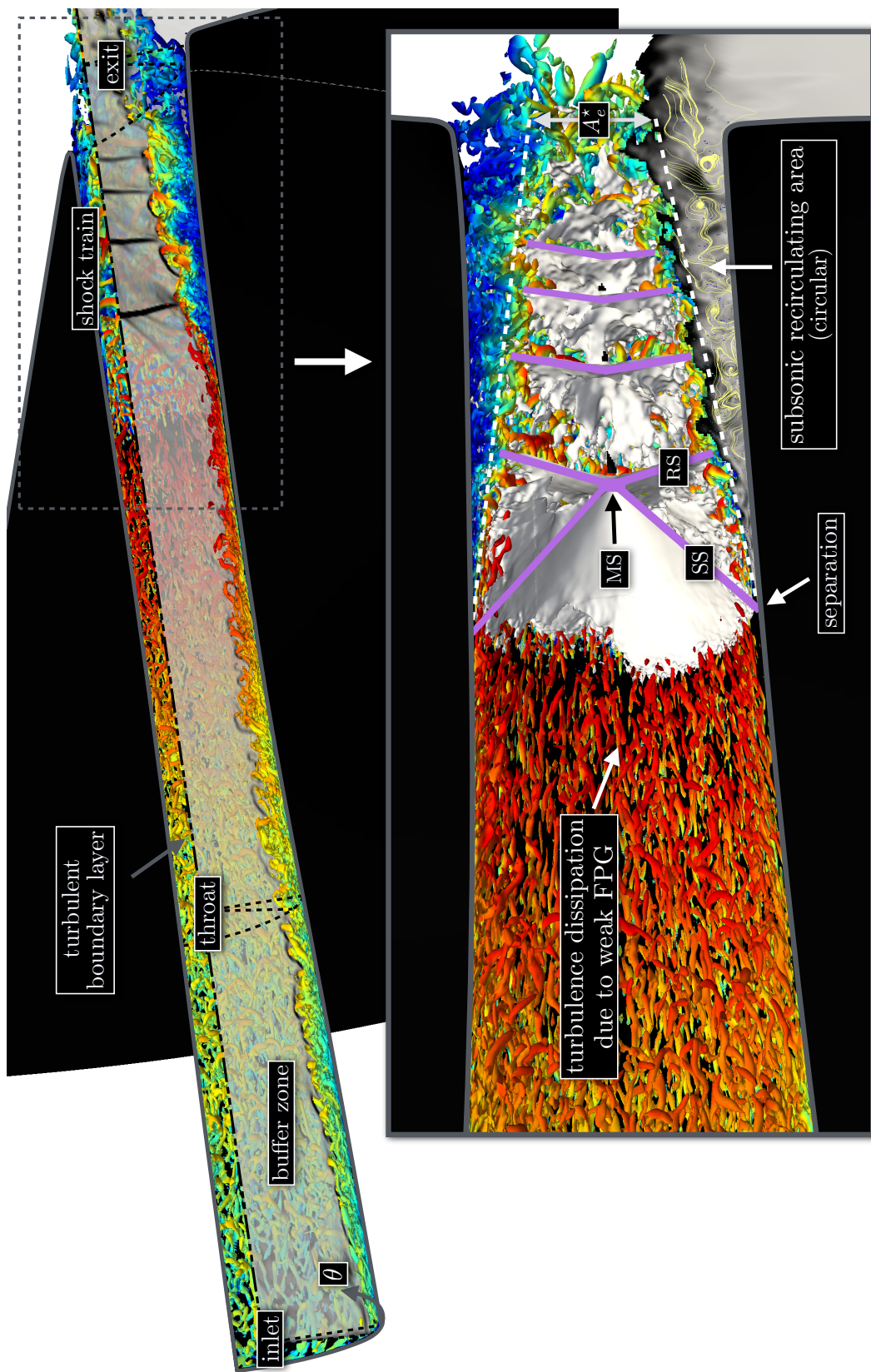


Figure 6.34: Cylindrical WR-LES: iso-contour of Q criterion colored by the velocity field (blue: slow, red: fast); MS: Mach stem, SS: separated shock, RS: reflected shock, A_e^* : effective exit area; grayscale surface: Schlieren imaging at $\theta = 0$, white volume: iso-volume of $\nabla||u||$.

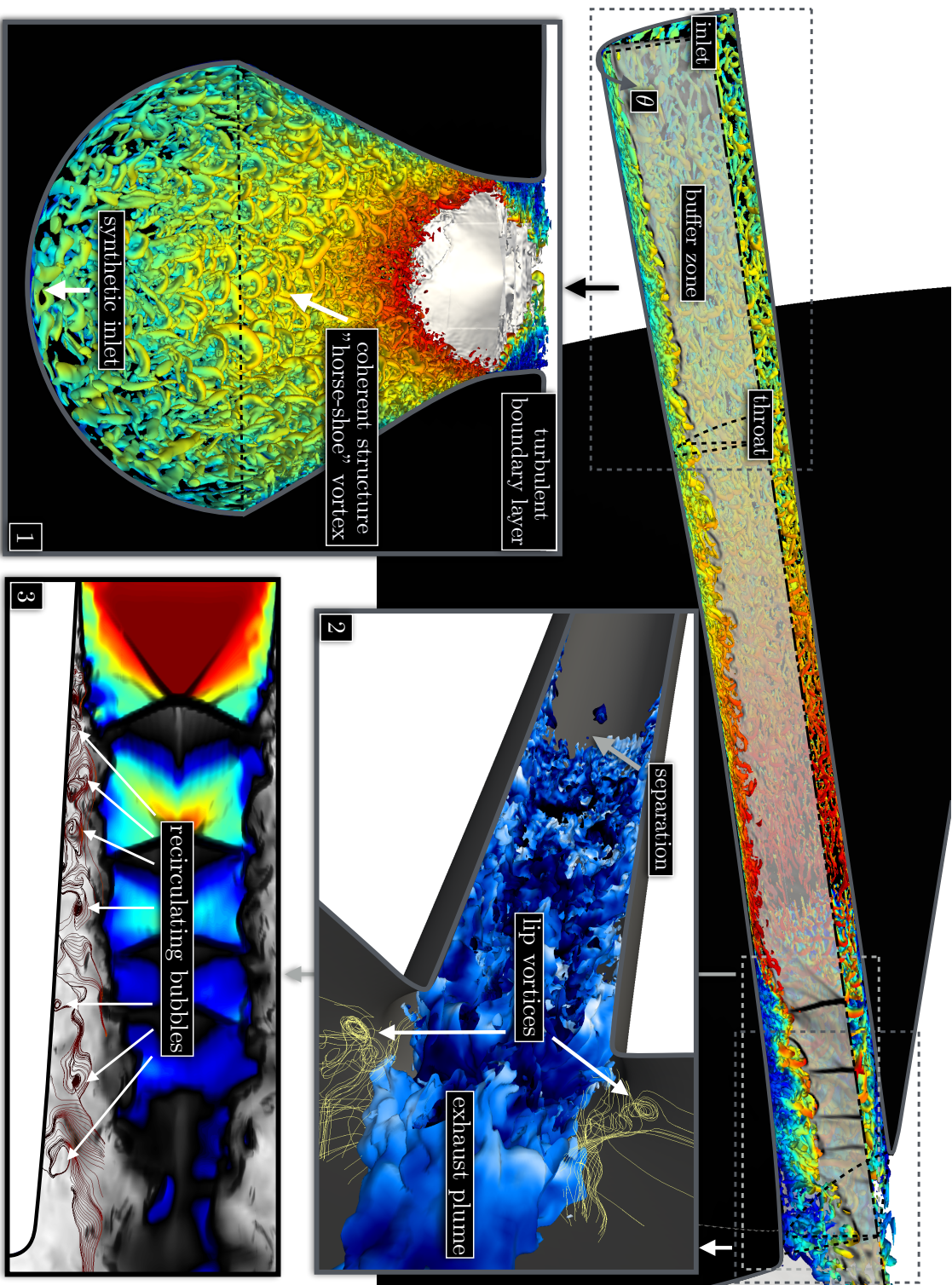


Figure 6.35: Cylindrical WR-LES: 3D representation of the different phenomenon observed in cylindrical nozzle flow; legend as in figure 6.34, box 2: iso-contour of temperature $T/T_\infty \sim 0.9$ colored by velocity (blue/black) and streamline near the nozzle lip (yellow), box 3: jet color represents the supersonic field while b/w color represents the subsonic part.

analysis than the WR-LES. The cycle of low-frequency oscillations has been explained using the database created by the WM-LES. The different perturbations and their frequency ranges have been captured and explained from the spectra analysis, *i.e.* incoming boundary layer, the shear layer turbulence, the recirculation bubbles, the lip-vortex and the transonic tone.

7

Conclusion

The objective of the present thesis was to understand and explain the separation phenomenon occurring in over-expanded supersonic nozzles. Experiments offer limited data needed for a better understanding of the flow physics inside the nozzle due to difficulties to measure the relevant quantities. However, the numerical simulations offer the possibility to capture the phenomena with full detail.

To the best of the author's knowledge, few Large Eddy Simulations have been conducted on separated cylindrical nozzles flow so far. The existence of low-frequency shock motions in over-expanded nozzle has been observed experimentally by Sajben & Kroutil (1980) or Zaman et al. (2002). For planar nozzle flows, both experimental and numerical studies are available but the cost of computation of the high fidelity calculation prevented Olson & Lele (2013) to perform a time-resolved study. Olson & Lele (2013) concluded that additional simulations of full axial over-expanded nozzles would be required to determine if similar physics exist in circular nozzle flow. The present thesis focuses on both planar and cylindrical nozzle flows based on a similar nozzle profile used by Papamoschou & Johnson (2006). To perform a time-resolved study, time integration of the order of $10^4 \delta / u_\infty$ was used. The development of a wall-model capability to the code allowed us to create a database for a reasonable computational cost.

A complete code has been written from scratch to solve the full compressible Navier-Stokes equations in a generalized curvilinear form. The code combines a new LES model, temporal/spatial high-order schemes, a wall-model and the domain decomposition method to perform cylindrical simulations. It is highly parallelizable and can be run on massively parallel supercomputers with a good scalability. A portion of these computations was performed on the TGCC Curie-CEA accessed from the European PRACE resources and the French GENCI resources. High-fidelity calculations of the compressible nozzle flow were performed and as a result a large database, for both planar and cylindrical nozzle flows is created. Rigorous analysis of this database has demonstrated the

mechanism that drives the separation unsteadiness in transonic nozzles.

In both planar and cylindrical nozzle flows, the length between the separation and the exit appears to lead the frequency of the unsteadiness. Similarly to resonators, the length between the separation and the exit is exactly a quarter wavelength of the resonant frequency. The feedback mechanism between the separation and the nozzle exit acts as a two-way coupling system. The compression shock affect the boundary layer which separates from the wall at a specific angle; the flow reaccelerates due to the change of the effective geometry following the slip line; the effective area at the exit is changed modifying the thermodynamic stability of the system; the altered exit flow conditions moves the shock upstream. The time lag of the wave propagation between the separation and the nozzle exit acts as a hysteresis phenomenon on the system which starts the low-frequency phenomenon. The relative speed of the separated shock changes the shock patterns, whether the separation line is moving upstream or downstream of the nozzle.

For the planar nozzle case, the amplitudes of the separation line were increased compared to the cylindrical nozzle flow considering the modified pressure gradient used. A large asymmetry was observed when the shock moves upstream towards the throat. On the contrary, in the cylindrical nozzle case, the exhaust plume was almost symmetric. The wall-model did not impact the amplitude nor the frequency of the separation line. However, the shock patterns have been modified due to the low resolution near wall. The frequency study on the WM-LES database allowed us to characterize the effects of the different phenomena occurring during the separation. Effects of the incoming boundary layer on the separation line are mild, confirming previous work where the separation unsteadiness are basically driven by the downstream flow perturbations.

For small half-angle divergent nozzle, the side-loads are strongly correlated to the separation line unsteadiness. However, the results showed that for both planar and cylindrical the main tone of side-loads is in the frequency range of the recirculation bubbles as well as of the lip vortices.

There is significant potential for additional research extracted from the LES database. Further studies could be done on the impact of the unsteady separation on the side-loads generated by more realistic nozzle geometries. Parametric studies should be conducted to understand the sensitivity of the shock unsteadiness: to upstream conditions of the turbulent boundary layer, *i.e.* boundary layer thickness or incoming Reynolds number; or to downstream conditions, *i.e.* ambient pressure or NPR. As point out by Olson & Lele (2013), computations can become extremely costly if the turbulent boundary layer thickness is small compared to the radius of the nozzle itself, especially in the angular direction.

Appendix A

Nozzle flow grid

The computational mesh for both planar and cylindrical nozzle flows is generated through a single function for each direction $x(\xi, \eta, \zeta)$, $y(\xi, \eta, \zeta)$ and $z(\xi, \eta, \zeta)$. The use of a single function for the whole domain ensures the metrics to be of class C^2 . A function of class C^2 avoids discontinuity of the second derivative of the metrics which are used in the viscous terms (sec. [Governing equations and numerical methods](#)).

This single function is supposed to generate the grid for the buffer layer, the divergent of the nozzle and the ambient domain. The first near-wall cells are supposed to be orthogonal to the wall and the atmospheric/ambient region is stretched along the ξ -direction.

The following system of equations shows the function and the constraints used to create the nozzle contour f . This is the solution to the Cantalever beam problem.

$$f(x) = Ax^3 + Bx^2 + Cx + D \quad (\text{A.1})$$

$$\left\{ \begin{array}{l} f(0) = H_t/2 \\ f(L_d) = \varepsilon H_t/2 \\ \frac{df(0)}{dx} = 0 \\ \frac{d^2f(L_d)}{dx^2} = 0 \end{array} \right. \quad (\text{A.2})$$

By solving this system of equations, one can find the five coefficients to generate the nozzle contour function,

$$A = -\frac{(\varepsilon - 1)H_t}{4L_d^3} \quad (\text{A.3})$$

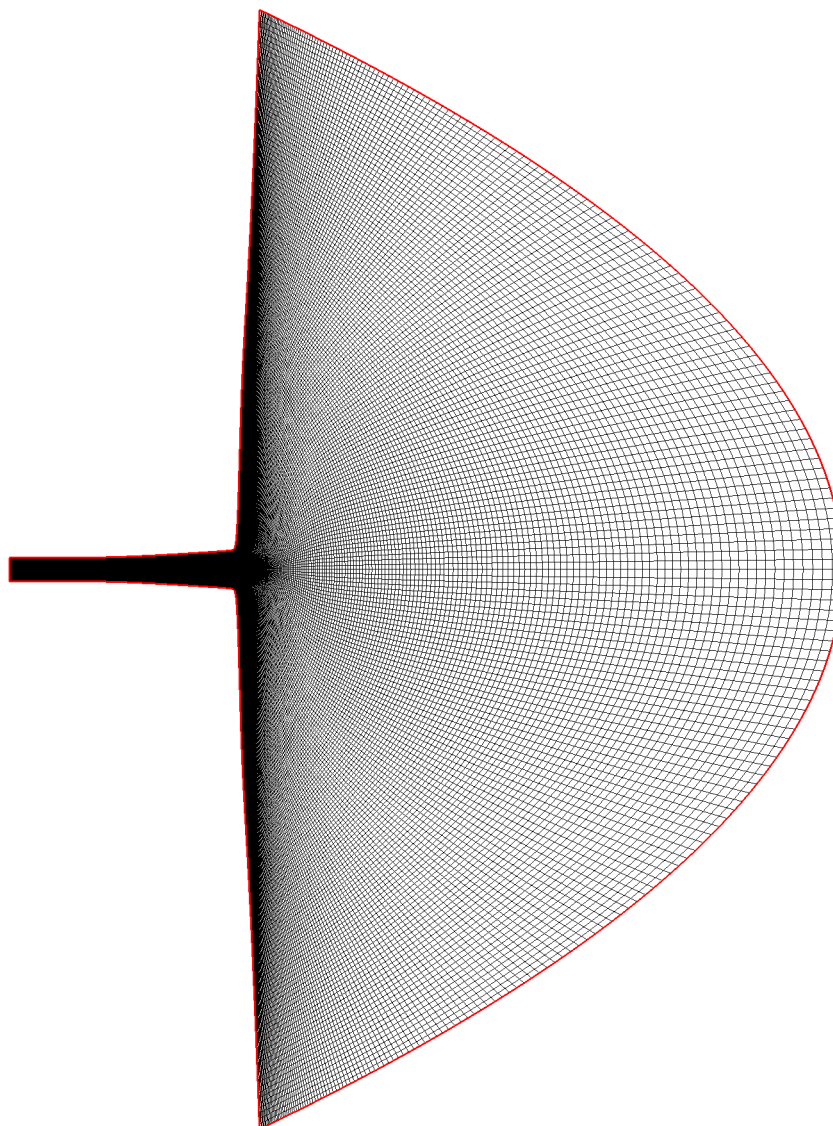


Figure A.1: 2D grid representation of the planar nozzle flow with the ambient domain.

$$B = \frac{3}{2} \frac{(\epsilon - 1) H_t}{2L_d^2} \quad (\text{A.4})$$

$$C = 0 \quad (\text{A.5})$$

$$D = H_t/2 \quad (\text{A.6})$$

A.1 Planar nozzle

The following equations are used to generate the grid shown in figures [A.1](#) and [A.2](#). The grid uses classical Cartesian coordinates in the buffer region, between the inlet and the

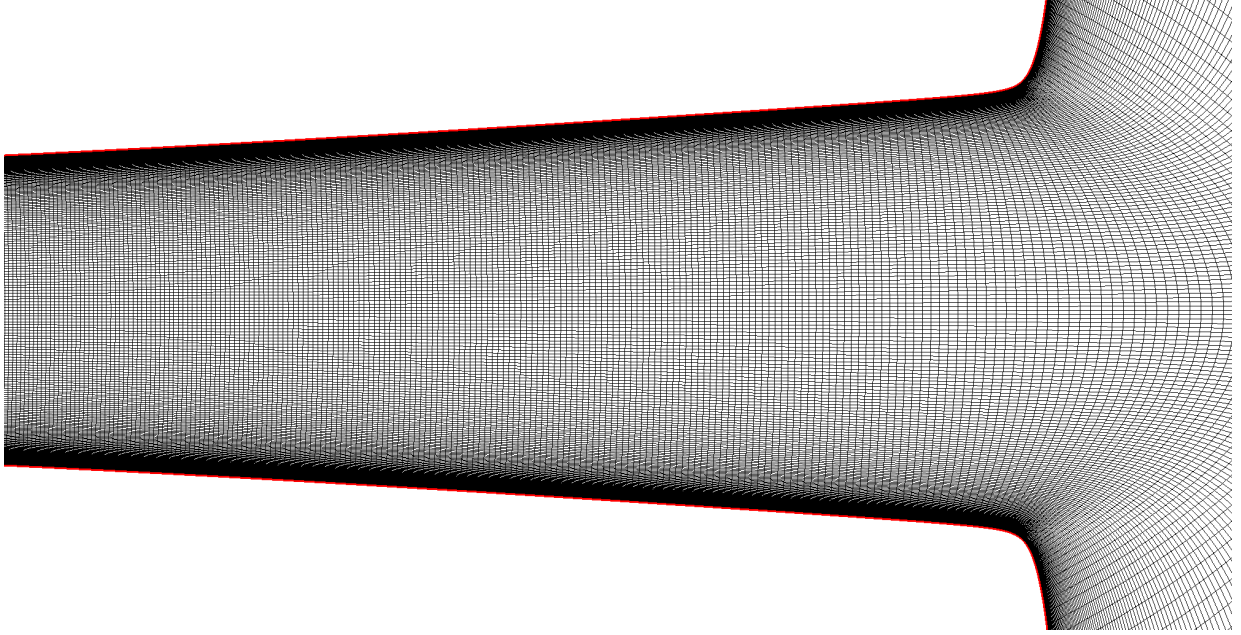


Figure A.2: Grid representation of the planar nozzle flow in the x - y direction showing the exit of the nozzle.

throat of length L_b . From the throat to the outlet, the grid uses the following,

$$x = f_{str,x} f_y + L_b \quad (\text{A.7})$$

$$y = f_{str,y} f_x \quad (\text{A.8})$$

$$z = f_z Lz \quad (\text{A.9})$$

where,

$$f_x = f_1 f_{x,1} + f_2 f_{x,2} \quad (\text{A.10})$$

$$f_y = (1 - C_2 (1 - f_{str,y}^2)) \quad (\text{A.11})$$

$$f_z = \frac{\zeta}{N_z} \quad (\text{A.12})$$

$$f_1 = A \left(\frac{\xi - n_b}{n_d} L_d \right)^3 + B \left(\frac{\xi - n_b}{n_d} L_d \right)^2 + D \quad (\text{A.13})$$

$$f_2 = \left(\varepsilon \frac{H_t}{2} + C_1 \frac{(\xi - n_b - n_d + n_{\text{shift}})}{n_a} \right)^4 \quad (\text{A.14})$$

$$f_{x,1} = \frac{1}{2} \left[1 - \tanh \left(r_v \left(\frac{\xi - n_b - n_{\text{shift, str}}}{n_d} - 1 \right) \right) \right] \quad (\text{A.15})$$

$$f_{x,2} = \frac{1}{2} \left[1 + \tanh \left(r_v \left(\frac{\xi - n_b - n_{\text{shift,str}}}{n_d} - 1 \right) \right) \right] \quad (\text{A.16})$$

$$f_{str,x} = \frac{\left(1 + \frac{\tanh \left(r_{v,x} \left(\frac{\xi - n_b}{n_d} - 1 \right) \right)}{\tanh \left(r_{v,x} \right)} \right)}{\left(1 + \frac{\tanh \left(r_{v,x} \left(\frac{1}{n_d} - 1 \right) \right)}{\tanh \left(r_{v,x} \right)} \right)} \left(\frac{L_b}{n_b} \right) \quad (\text{A.17})$$

$$f_{str,y} = \frac{\tanh \left(r_{v,y} \left(\frac{2\eta}{N_y} - 1 \right) \right)}{\tanh r_{v,y}} \quad (\text{A.18})$$

$$C_2 = \left[C_{21} f_{x,1} \frac{df_1}{d\xi} + C_{22} f_{x,2} \left(\frac{df_2}{d\xi} + \frac{df_1}{d\xi} \Big|_{x_e} \right) \right] \quad (\text{A.19})$$

	N_ξ	N_η	N_ζ	H_t	ε	L_b/H_t	L_d/H_t	L_z/H_t	C_1
WR-LES	896	256	320	0.0178	1.6	50/17.8	117/17.8	2	$20 H_t$
WM-LES	672	128	160	0.0178	1.6	50/17.8	117/17.8	2	$9 H_t$

Table A.1: Grid parameters of the planar nozzle.

	n_b	n_d	n_a	$n_{\text{shift,str}}$	n_{shift}	r_v	$r_{v,x}$	$r_{v,y}$	C_{21}	C_{22}
WR-LES	300	506	90	20	15	$60n_d/n_x$	0.725	2.3	$2/R_t$	$0.016/R_t$
WM-LES	200	372	100	30	80	$50n_d/n_x$	0.445	—	$2/R_t$	$0.034/R_t$

Table A.2: Grid parameters of the planar nozzle.

For the wall-modeled grid, the wall-normal direction is regularly spaced following,

$$f_{str,y} = \left(\frac{2\eta}{N_y} - 1 \right) \quad (\text{A.20})$$

A.2 Cylindrical nozzle

The grid distribution for the cylindrical nozzle follows the same parameters as for the planar nozzle flow (Tab. A.1 and A.2). Figures A.3, A.4, A.5 and A.6 depict different views of the cylindrical grid using the domain decomposition method developed in section 2.4. The external cylindrical grid uses the following set of equation,

$$y = [R_o + (f_x - R_o) f_{str,y}] \cos \left(2\pi \frac{\zeta - 0.5}{N_\zeta} \right) \quad (\text{A.21})$$

$$z = [R_o + (f_x - R_o) f_{str,y}] \sin \left(2\pi \frac{\zeta - 0.5}{N_\zeta} \right) \quad (\text{A.22})$$

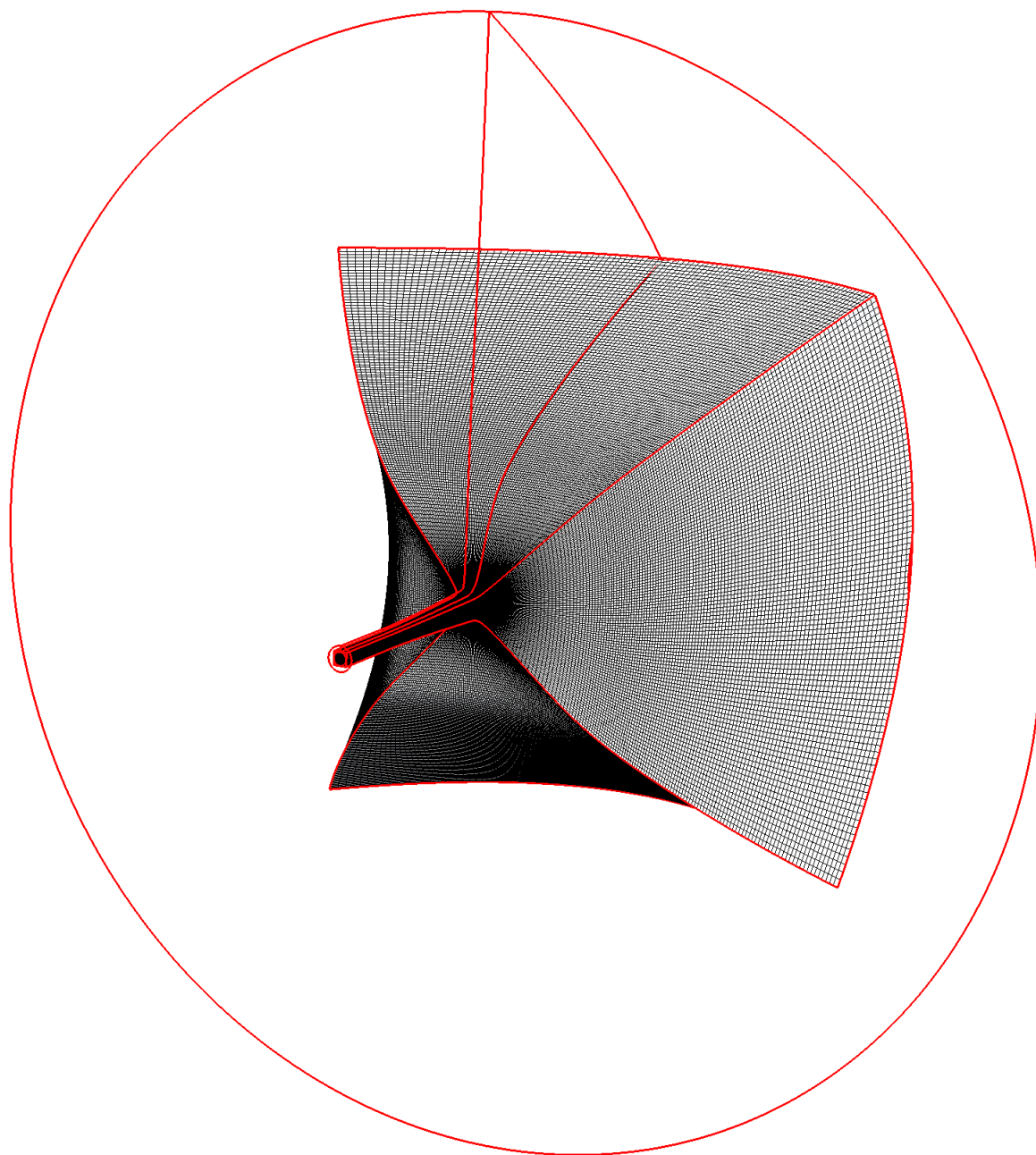


Figure A.3: Grid representation of the cylindrical nozzle showing the internal mesh Ω_1 and the contour of the external mesh Ω_2 .

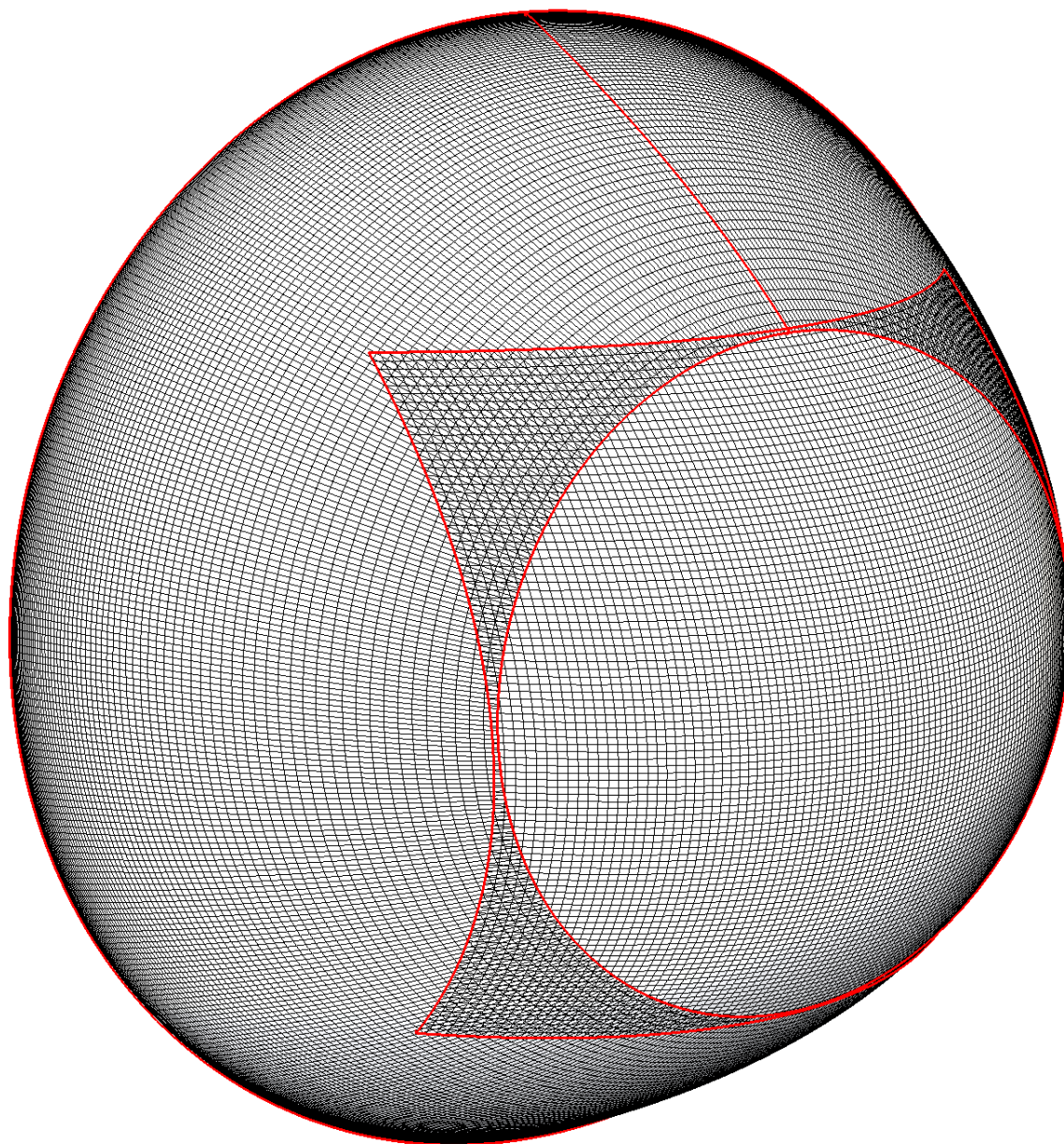


Figure A.4: Grid representation of the planar cylindrical showing both internal Ω_1 and external Ω_2 meshes; View of the ambient domain.

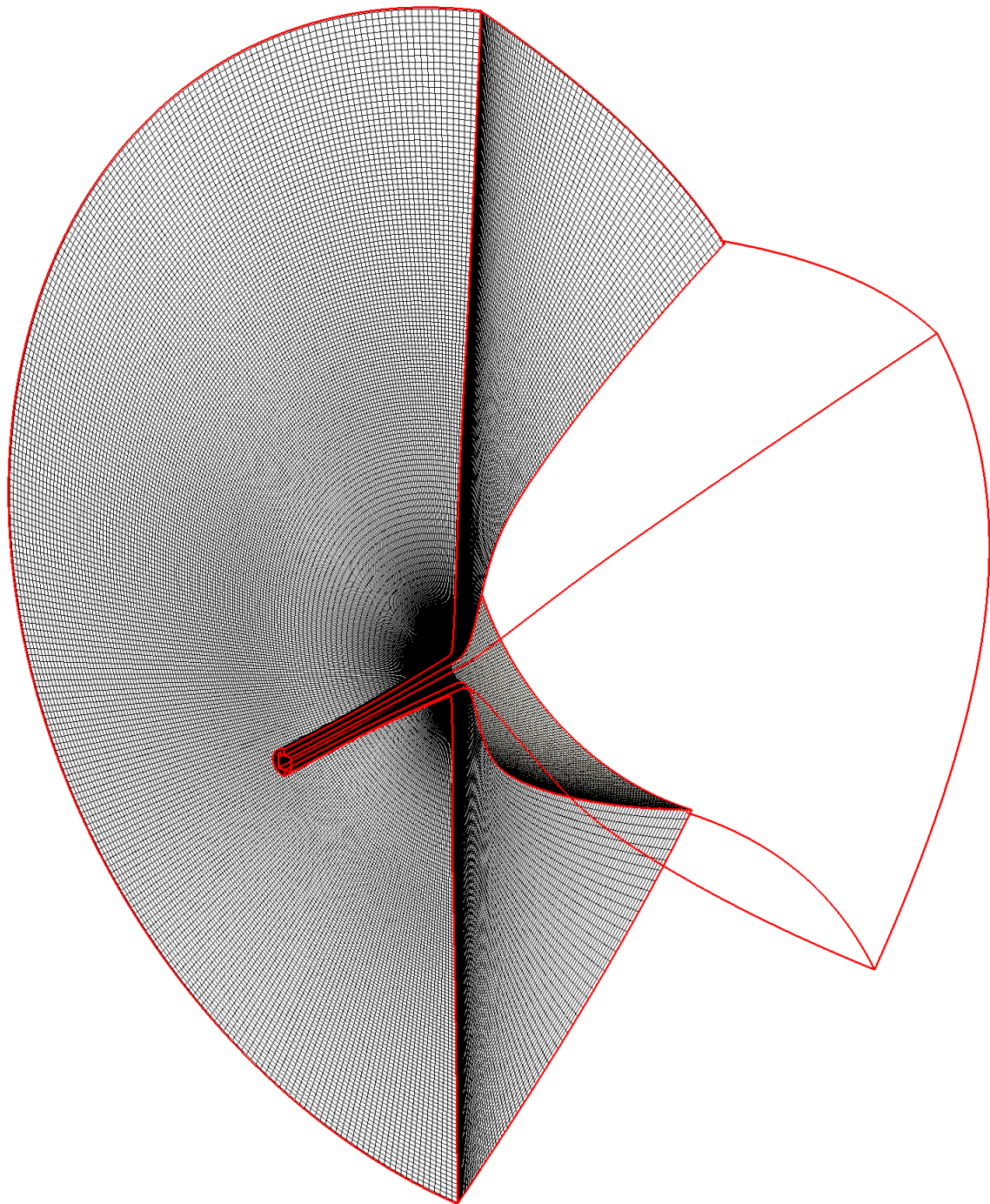


Figure A.5: Grid representation of the cylindrical nozzle showing half-domain of the external mesh Ω_2 and the contour of the internal mesh Ω_1 .

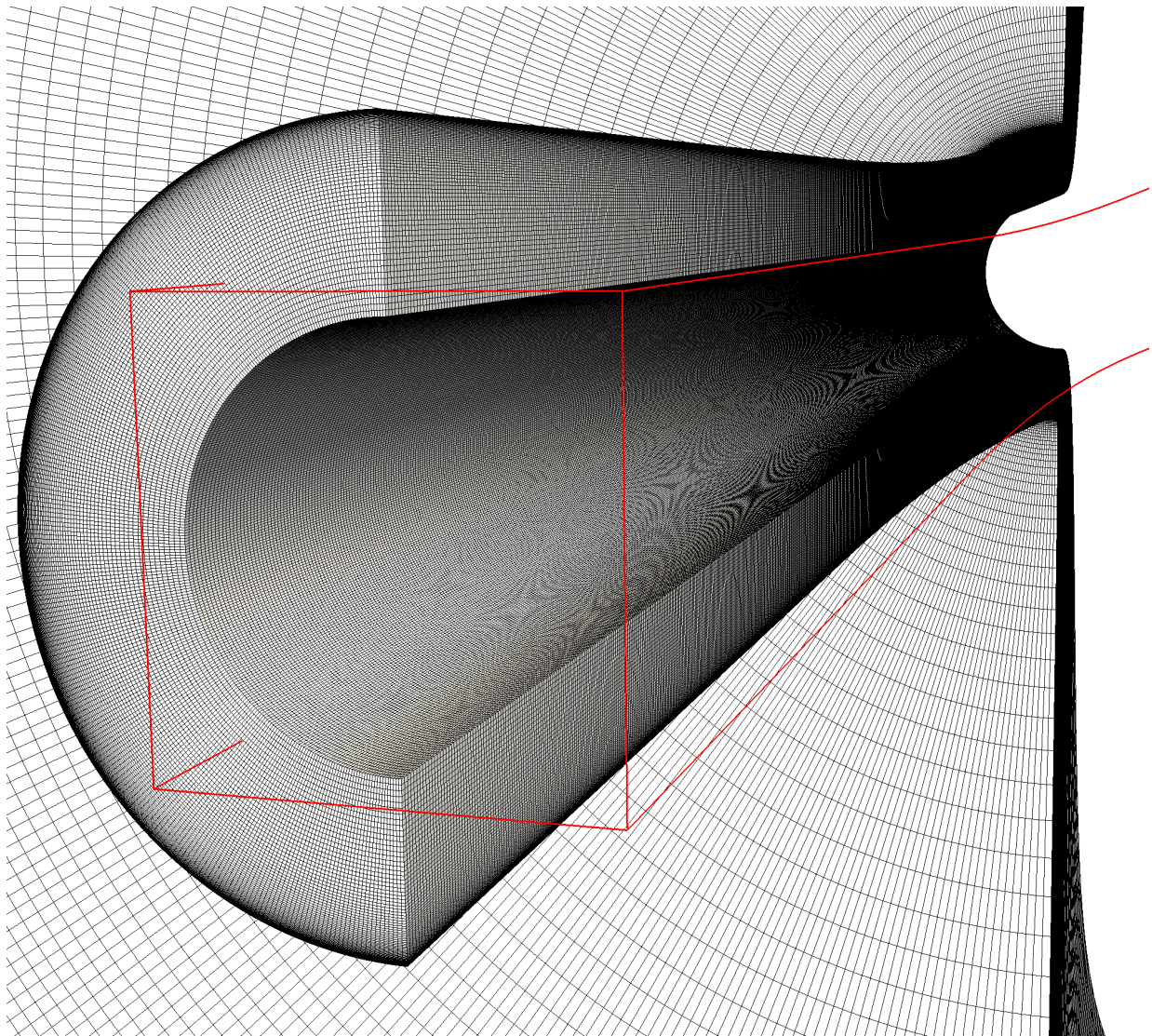


Figure A.6: Grid representation of the cylindrical nozzle showing half-domain of the external mesh Ω_2 and the contour of the internal mesh Ω_1 ; View from the inlet.

where $r_{v,y} = 2.2$ for the wall-resolved simulation only,

$$f_{str,y} = \frac{\tanh\left(r_{v,y}\frac{\eta}{N_y}\right)}{\tanh r_{v,y}} \quad (\text{A.23})$$

and for the wall-modeled simulation,

$$f_{str,y} = \frac{\eta}{N_y} \quad (\text{A.24})$$

Appendix B

NSCBC outflow

To remove the reflected waves captured in both planar and cylindrical nozzle flow simulations, emanating from the reflecting outlet BC, the Navier-Stokes Characteristic Boundary Conditions (NSCBC) have been developed. The NSCBC follows the method developed by Poinsot & Lele (1992), its modifications for three-dimensional flows by Lodato et al. (2008) and for curvilinear grids by Landmann et al. (2010).

B.1 NSCBC method

For non-reflecting boundary condition, the streamwise waves, $\mathcal{L}_{\xi,i}$, need to be set accordingly to table B.1. For a subsonic outlet, without any recirculating flow, the perfectly non-reflecting boundary condition for the $\mathcal{L}_{\xi,i}$ associated waves are $\mathcal{L}_{\xi,1} = 0$, which corresponds to the ingoing/unknown waves $u - c$. In the case of a perfectly non-reflecting BC, the ingoing wave, $u - c$, is purely removed. Poinsot & Lele (1992) and various authors (Rudy & Strikwerda 1980, Hagstrom & Hariharan 1988, Keller & Givoli 1989) recognized that the perfectly non-reflecting BC can lead to an ill-posedness problem where the static pressure p_∞ is not known by the flow. Thus, the outlet pressure could drift and lead to wrong calculations. Some authors have proposed to develop a partially non-reflecting boundary condition which became the roots of the NSCBC methods. Poinsot & Lele (1992) proposed a formulation based on the static pressure p_∞ to obtain the amplitude of the ingoing wave $\mathcal{L}_{\xi,1}$:

$$\mathcal{L}_{\xi,1} = K(p - p_\infty) \tag{B.1}$$

where K is a constant calculated by $K = \sigma(1 - M^2)c/L$ with M the maximal mach number at the outlet, c the speed of sound, L a characteristic length and σ a constant.

ξ -boundary	State	Inflow	Outflow
min	Subsonic	$\mathcal{L}_{\xi,2}-\mathcal{L}_{\xi,5}$	$\mathcal{L}_{\xi,5}$
	Supersonic	$\mathcal{L}_{\xi,1}-\mathcal{L}_{\xi,5}$	-
max	Subsonic	$\mathcal{L}_{\xi,1}-\mathcal{L}_{\xi,4}$	$\mathcal{L}_{\xi,1}$
	Supersonic	$\mathcal{L}_{\xi,1}-\mathcal{L}_{\xi,5}$	-

Table B.1: Wave amplitude treatment for various non-reflecting boundary conditions. Wave subscript 1 corresponds to $u - c$ wave, 2-4 to u and 5 to $u + c$.

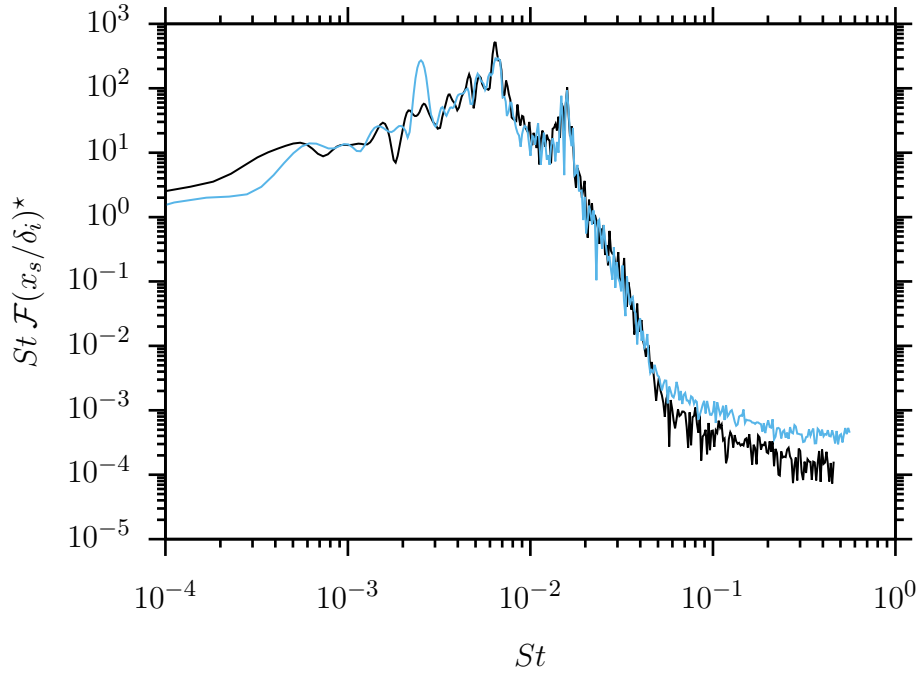


Figure B.1: WM-LES: Normalized pre-multiplied spectrum of the non-filtered separation location from the time-resolved WM-LES; —: original data, —: with NSCBC.

B.2 WM-LES of the cylindrical nozzle flow with NSCBC

The simulation of the wall-modeled cylindrical nozzle flow has been restarted using the NSCBC formulation at the outlet boundary condition. Probes and slices have been gathered for a similar time of computation compared to the results of chapter 6. Figure B.1 shows the spectrum of the separation location signal with and without NSCBC. The resonant tone and recirculation bubbles phenomenon are captured at the same Strouhal number using the NSCBC. However, the low-frequency tone ($St \sim 0.002$) observed in the previous simulation, assimilated to the reflection of the outlet BCs, is removed by the NSCBC boundary condition. This study confirm the good implementation of the NSCBC with curvilinear grid. It also confirms that removing the outlet reflection issue does not modify the main tone of the unsteadiness, nor the the frequency range of the phenomena captured in chapter 5 and 6.

Appendix C

Conference paper

A. PIQUET, A. GEORGES-PICOT, A. HADJADJ, Unsteadiness of supersonic flows in over-expanded nozzles, *30th Int. Symp. Shock Waves (ISSW31)*, Tel-Aviv, Israel, **2015**.

Unsteadiness of Supersonic Flows in Over-Expanded Nozzles

A. Piquet, A. Georges-Picot, A. Hadjadj and E. Toubert

Abstract The present paper presents numerical simulations of the separation phenomenon in an over-expanded convergent-divergent nozzle. The origin of flow separation in over-expanded supersonic nozzles would be investigated to define whether the phenomenon is due to the incoming boundary layer (upstream of the separation) or the excitation of the ambient pressure (downstream of the nozzle exit). The energy of the recirculation flow behind the Mach disk could lead to large unsteadiness of the shock at the separation line. Coupling this effect to an adverse gradient pressure along the nozzle wall and to the interaction of the shock with the boundary layer, lead to complex flow structures.

1 Introduction

Optimization of nozzle by increasing expansion ratios and reducing the size of divergent has becoming a real challenge due to the presence of flow separation and coupled complex shock structures inside the nozzle, which lead to significant mechanical and thermal loads. The knowledge of separation phenomenon in supersonic nozzle is important to predict the side loads and the stability of the exhaust plume. Both experimental and numerical studies have shown several shock patterns induced flow separation, which leads to specific pressure distribution along the nozzle structure and side-loads generation. A comprehensive review of nozzle flow separation is given by Hadjadj and Onofri [1]. Papamoschou and Johnson [2], among others, have investigated the stability of the separation phenomenon in experimental planar nozzle. Nevertheless, studies of the origin of shock-induced flow for canonical nozzle are not abundant in the literature. These effects are reflected in the lateral loads subjected by the pressure field within the nozzle. These lateral loads are vital in the mechanical stability of the nozzle. The low-frequency oscillations of the recirculation bubble and the geometrical asymmetry of the separation line can be a source of lateral loads on the structure.

A nozzle is a device designed to transform a potential energy (high pressure, high temperature) to a kinetic energy in order to have the maximum force at the exhaust. When the nozzle is choked (sonic condition at the throat), the flow regime depends only on the ratio between the ambient pressure p_a and the static exit pressure $p_{e,vac}$ (where *vac* refers to the vacuum state). In practice, there are three nozzle operating regimes depending on the pressure ratio: the adapted ($p_e/p_a = 1$), the under-expanded ($p_e/p_a < 1$) and the over-expanded regime ($p_e/p_a > 1$). In the present paper, the over-expanded regime will be simulated and studied. The over-expanded regime is often characterized by the appearance of a shock wave at the exit lip of the divergent. The boundary layer faces an adverse pressure gradient (APG) which leads to its thickening. If the pressure ratio between the exit and the atmosphere is very important ($p_e/p_a \gg 1$), the regime is called highly over-expanded. It exists a threshold value of this ratio for which the boundary layer can no longer counteract the adverse pressure gradient effect and finally separate from the walls. The prediction of the separation line based on pressure ratio is an known issue and considered as the main reason for the generation of lateral loads. Depending on the nozzle profile and the flow conditions, several shock structures can appear in the supersonic

A. Piquet, A. Georges-Picot and A. Hadjadj
CORIA – UMR 6614 CNRS – INSA Rouen and Normandie Université, Avenue de l'Université, 76801 Saint-Étienne-du-Rouvray, France,
e-mail: arthur.piquet@coria.fr

E. Toubert
Department of Mechanical Engineering, Imperial College London, South Kensington Campus, London SW7 2AZ, UK

jet. Regular reflections are characterized by the direct impact of the incident shock on the axis of the nozzle which then, generate a reflected oblique shock (IR: Internal reflection). Mach reflections are characterized by the formation of a Mach disk. This strong shock (subsonic downstream of the shock), often perpendicular to the jet axis, may have a slightly concave or convex profile depending on the geometry of the nozzle or on the local flow conditions. The point of interaction, or Triple Point (TP), between the incident shock and the Mach disk, forms a reflected shock, IR, and a Slip Line (SL), which divides the subsonic region downstream of the Mach disk from the supersonic jet. Mach reflections can be either direct or reverse. A direct reflection is when the angle between the slip line, from the triple point, and the main flow is positive and an inverse reflection otherwise. Finally, the interaction of the internal shock with the Mach disk can lead to shock structure shaped as a hat or more commonly called cap-shock pattern [3]. This structure corresponds to the sequence of an inverse Mach reflection and direct Mach reflection, formed by the shock from the triple point and by the shock resulting from the boundary layer separation. The main parameters that influence the topology of shock structures are the geometry of the nozzle and the NPR. Theoretical studies conducted by Ben-Dor [4, 5] on shock interference phenomena have shown a hysteresis effect in the transition between these two types of reflection (direct and inverse). Similarly, the transition between a Mach reflection and cap-shock pattern in shock structure is characterized by a hysteresis phenomenon [6].

Many studies have been conducted on the over-expanded nozzles to better understand the influence of different parameters and operating conditions on the flow properties ???. A detailed study of jet separation phenomena and lateral loads was conducted by Jan stlund [7]. The authors summarize exhaustively the results of numerical and experimental work obtained on supersonic nozzles. Two phenomena were particularly studied. The first is related to the transition from free detachment or Free Shock Separation (FSS) to Restricted Shock Separation (RSS). This transition is at the origin of strong lateral forces. It occurs mainly in the Thrust Optimized Contour nozzles (TOC or TOP) and is characterized by an hysteresis cycle during the pressure increase of the vacuum chamber [8]. The second phenomenon is related to the end-effect regime [9, 10]. This occurs when, in a typical RSS flow, the recirculation bubble trapped by the separation-reattachment reached the exit lip. The jet suddenly opens to the atmosphere and causes a rapid increase in pressure downstream of the separation shock. This cyclic phenomenon causes significant fluctuations of the separation line. The low frequency oscillations phenomenon can be dangerous to the engine integrity especially if they coincide with the normal modes of the mechanical structure. If the origin of these phenomena is still poorly understood in the case of separated flows, the literature on the subject gives two main assumptions: (i) low frequency oscillations are the result of disturbances from the upstream [11, 12], (ii) it is a result of the downstream recirculation bubble [13] coupled to the separation shock. This can be assimilated to a mass-spring system with a low-pass filter [14]. The second hypothesis is the one that holds the attention of the scientific community.

2 Results and discussion

In this present paper, a Large Eddy Simulation (LES) is used to simulate the nozzle flow separation in a Thrust Optimized Contour (TOC) nozzle. High-order WENO scheme based 3D numerical flow solver equipped with direct-forcing immersed boundary method (IBM) is used for this purpose. An LES wall-model, which account for Adverse Pressure Gradient (APG) have been developed to overcome the low-resolution of the very thin incoming boundary layer [15]. It takes into account a large number of phenomenon occurring during the separation. The desired Nozzle Pressure Ratio (NPR) of the simulation is achieved by a temporal increase of the inlet pressure. This transitional phase initializes the simulation to avoid any discontinuity of pressure in the computational domain. Walls are set as adiabatic. Mesh dimensions are $N_x = 1024$, $N_y = 512$ and $N_z = 512$, giving 268 million cells. The Immersed Boundary Method with bi-linear interpolation has been used to reconstruct the surface of the nozzle from a STL file. The boundary conditions for the outflow are similar to a far-field boundary condition with $p_a = 1bar$.

Two simulations, at NPR of 25 and 37.9, have been performed. As the transition between the RSS regime and FSS regime is happening for a NPR around 24 in a TOC nozzle, these simulations will be characterized by a Restricted Shock Separation pattern (Figure 1). Moreover, figure 2 shows that the numerical and the experimental wall pressure agree well. Thus, the wall model can correct with good accuracy the position of the separation line. The RSS pattern does not present any asymmetrical behavior, as explained by Nguyen *et al.*[16], either in quasi-stationarity or in transient state, except for the End-Effect phenomenon which occurs at high NPR when the separation line reached the exit lip of the nozzle. The stability of this flow pattern can be explained by the structure of complex shock that characterizes it. In fact, the RSS pattern of the supersonic jet on the wall results in a lambda shock structure at the wall which is

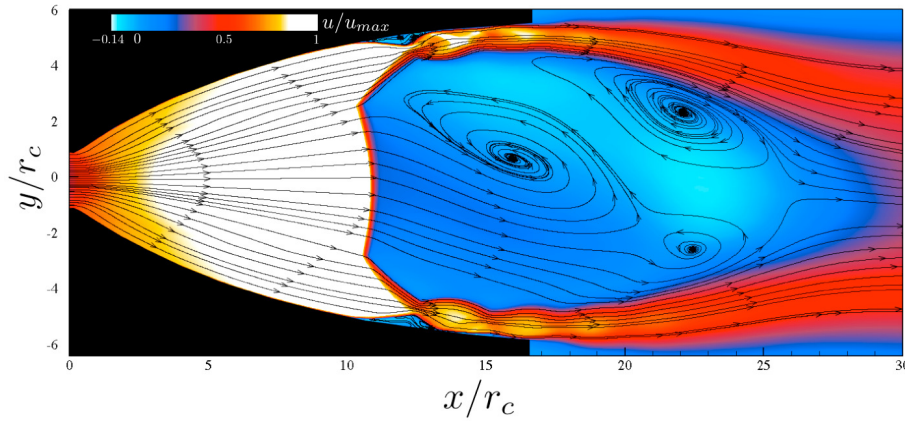


Fig. 1: Averaged normalized x-velocity contour and streamlines (*white*), TOC nozzle, $NPR = 37.9$

less sensitive to external fluctuations. Moreover, as the supersonic jet is attached to the wall, the subsonic downstream flow can influence the separation line through the main recirculation zone. However, this zone is confined within a supersonic torus, which itself based on the wall. Thus, the whole structure of the flow is very stable due to the pressure applied from the recirculation bubble on the supersonic jet. Only the pressure applied from the recirculation bubble directly on the shock structure can influence the position of the separation. However, as this pressure is mainly exerted uniformly on the Mach disk (the direction of the force is parallel to the stream), oscillations of the position of the separation line can be seen, but the asymmetries, for their part, remain very low.

Figure 3 represents the iso-contour of the Q criterion, which can be defined as a representation of coherent structure and vortices within the flow. Although the separation line is perfectly symmetrical, we can notice that the first reattachment line is not. This asymmetry may be explained by the slight asymmetry of the eddies in the recirculation zone behind the Mach disk.

We focused the study on the large scale structures characterized by lower frequency ranges which involve high energy, enough to influence the flow. The visualization of the averaged x-velocity fields for the two simulations (Figure 2, center) highlights the main structures of the flow: a supersonic jet (circular), which relies on the wall of the nozzle, a recirculation bubble framed by the supersonic jet, a Mach disk and at least two small vortices trapped between the supersonic jet and the wall. The RSS pattern, due to its complex structure, is naturally more robust to the fluctuations of the environment than the FSS. The influence of these fluctuations is felt mainly at the exit of the nozzle between the supersonic jet and the shock structure. Indeed, when the supersonic jet is ejected into the atmosphere, it slightly curl up on itself under the effect of the ambient pressure which is greater than the pressure of the recirculation zone. As for the FSS pattern, the closing of the supersonic jet near the wall influences the recirculation zone, which can lead to a instable phenomenon of recirculation bubble. In the case of a RSS pattern, the recirculation bubble is only powered by the main jet and is isolated from the environment by the supersonic jet. This recirculation is composed of one or two large-scale structures (Figure 2, center). These structures appear to be the main sources of flow asymmetry in the case of a FSS pattern.

The vortex located just behind the Mach disk (Figure 1) has an asymmetric behavior in relation to the axis of the nozzle, which directly influences the second structure, shaped as a torus. This asymmetric behavior results from the convex shape of the Mach disk which is not fixed in time. Therefore, the structure is mainly positioned eccentrically toward the Triple Point (TP), represented by the interaction of the Mach disk with the Internal Shock (IS). Unlike the torus (second recirculation bubble), easily identifiable by the two recirculating structures, the shape of this structure is not obvious. 3D representation of an iso-pressure value (Figure 4) allows us to see that the structure do not look like a circular bubble as one might expect, but rather as a cylindrical structure supported by the supersonic jet. The flow at the downstream of the Mach disk is channeled through the structure, and then evacuated at its edges by the supersonic jet.

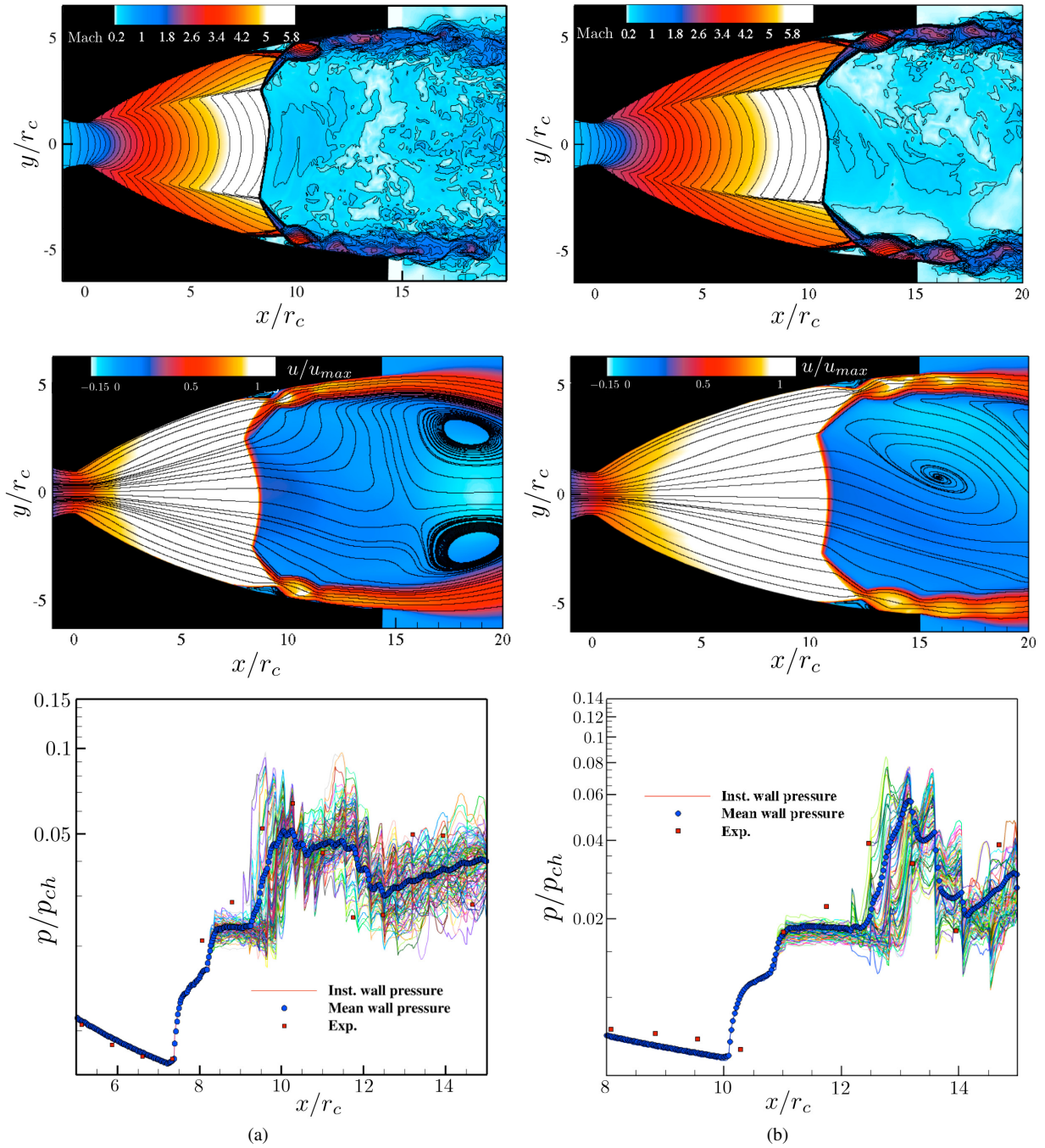


Fig. 2: Top: instantaneous Mach number contour; Center: Averaged normalized x-velocity contour, bottom: wall pressure distributions; Left column: $NPR = 25$ and Right column: $NPR = 37.9$ in a TOC nozzle

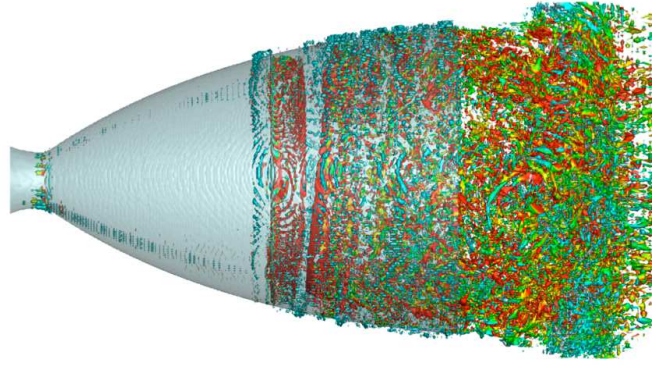


Fig. 3: Turbulent structures at $NPR = 25$; $iso-Q = 10^{-3} \times Q_{max}$, ($Q_{max} = 10^{11} s^{-2}$) with $Q = \frac{1}{2} (\Omega_{ij} \Omega_{ij} - S_{ij} S_{ij})$.

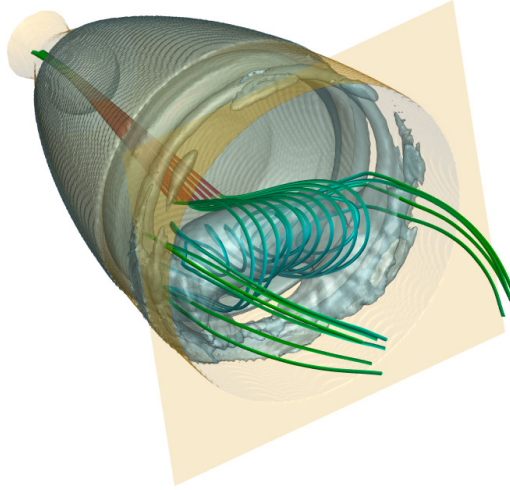


Fig. 4: Recirculation bubble visualization and the streamline downstream of the Mach disk, $iso-P = 82,000$ Pa

3 Summary

In the present paper, Large Eddy Simulations (LES) have been carried out to investigate the flow separation and the complex shock wave / boundary layer interactions associated with shock-induced unsteady flows in a Thrust Optimized Contour (TOC) nozzle. Different nozzle flow regimes have been investigated by varying the Nozzle Pressure Ratio (NPR) between RSS/FSS pattern. The computational results have been compared with the experimental data for validation. It has been shown that the flapping of the jet associated with the nozzle-lip vortex highly influences the low-frequency flow oscillations. This study has highlighted many interesting physical phenomena, in addition to the improved simulated results which show good consistency with the experimental one. Three major points can be underlined from all of these simulations:

- The condition to impose the wall-model is independent of the angular position (azimuth) in the nozzle. The direct consequence of this imposition is a perfectly symmetrical separation line which do not happens in experiments. Furthermore, this condition is said as static and does not react to the downstream conditions of the flow (atmospherical perturbation).

- Despite the fact that the separation line is perfectly axisymmetric, the downstream flow is not. It can be concluded that the downstream flow drives significantly the separation line.
- The turbulent structures in the flow are relatively small in size, but of high magnitude in term of fluctuation. Our results have significant differences in term of structures (very large scales) compared to a URANS code.

Acknowledgments

The first author is supported financially by the DGA (Direction Générale de l'Armement) from the French Ministry of Defense in collaboration with the DSTL, UK. The authors wish to thank the European PRACE project which allocated computer core-hours as part of the 9th PRACE project call under grant agreement no. RI-211528 and FP7-261557. The simulations have been achieved using the TGCC Curie Fat Node cluster of CEA in France.

References

1. A. Hadjadj and M. Onofri. Nozzle flow separation. *Shock Waves*, 19(3):163–169, 2009.
2. A. D. Johnson and D. Papamoschou. Instability of shock-induced nozzle flow separation. *Physics of Fluids (1994-present)*, 22(1):016102, 2010.
3. M. Frey and G. Hagemann. Flow separation and side-loads in rocket nozzles. *AIAA 99*, 2815, 1999.
4. G. Ben-Dor, M. Ivanov, El. Vasilev, and T. Elperin. Hysteresis processes in the regular reflection \leftrightarrow mach reflection transition in steady flows. *Progress in Aerospace Sciences*, 38(4):347–387, 2002.
5. A. Chpoun, D. Passerel, H. Li, and G. Ben-Dor. Reconsideration of oblique shock wave reflections in steady flows. part 1. experimental investigation. *Journal of Fluid Mechanics*, 301:19–35, 1995.
6. M Frey and G Hagemann. Status of flow separation prediction in rocket nozzles. *AIAA paper*, 3619:1998, 1998.
7. J. Östlund. Flow processes in rocket engine nozzles with focus on flow separation and side-loads. 2002.
8. C. Pilinski. *Etude numérique du décollement en tuyères supersoniques*. PhD thesis, INSA de Rouen, 2002.
9. S. Afaque. *Contribution to the numerical simulation of turbulent shock-induced separated flows : application to supersonic over-expanded nozzle flow*. PhD thesis, Ecole Nationale Supérieure de Mécanique et d'Aérothéchnique, 2010.
10. S. Deck. Delayed detached eddy simulation of the end-effect regime and side-loads in an overexpanded nozzle flow. *Shock waves*, 19(3):239–249, 2009.
11. DS. Dolling and CT. Or. Unsteadiness of the shock wave structure in attached and separated compression ramp flows. *Experiments in Fluids*, 3(1):24–32, 1985.
12. SJ. Beresh, NT. Clemens, and DS. Dolling. Relationship between upstream turbulent boundary-layer velocity fluctuations and separation shock unsteadiness. *AIAA Journal*, 40(12):2412–2422, 2002.
13. P. Dupont, C. Haddad, and JF. Debiève. Space and time organization in a shock-induced separated boundary layer. *Journal of Fluid Mechanics*, 559:255–277, 2006.
14. R. Schwane, L. Torngren, and H. Wong. Validation of unsteady turbulent flow predictions for over-expanded rocket nozzle. In *Computational Fluid Dynamics 2002*, pages 707–712. Springer, 2003.
15. A. Georges-Picot. *Développement de modèle physiques et numériques pour la simulation aux grandes échelles des écoulements dans les tuyères supersoniques*. PhD thesis, Institut National des Sciences Appliquées de Rouen, 2014.
16. A. T. Nguyen, H. Deniau, S. Girard, and T. A. De Roquefort. Unsteadiness of flow separation and end-effects regime in a thrust-optimized contour rocket nozzle. *Flow, Turbulence and Combustion*, 71(1-4):161–181, 2003.

Appendix D

Article

A. PIQUET, O. ROUSSELO, A. HADJADJ, A comparative study of Brinkman penalization and direct- forcing immersed boundary methods for compressible viscous flow. *Computers & Fluids*, 136:272-284, **2016**.



A comparative study of Brinkman penalization and direct-forcing immersed boundary methods for compressible viscous flows



A. Piquet^{a,b}, O. Roussel^{a,c}, A. Hadjadj^{a,*}

^aINSA and University of Normandy, Avenue de l'Université, 76801 Saint-Étienne-du-Rouvray, France

^bDepartment of Mechanical Engineering, Imperial College London, UK

^cDepartment of Physics, Umea University, 90187 Umea, Sweden

ARTICLE INFO

Article history:

Received 21 November 2015

Revised 11 May 2016

Accepted 1 June 2016

Available online 9 June 2016

Keywords:

Brinkmann penalization

Direct-forcing

Immersed boundary method

Shock waves

Supersonic channel flow

ABSTRACT

This paper deals with the comparison between two methods to treat immersed boundary conditions: on the one hand, the Brinkman penalization method (BPM); on the other hand, the direct-forcing method (DFM). The penalty method treats the solid as a porous medium with a very low permeability. It provides a simple and efficient approach for solving the Navier–Stokes equations in complex geometries with fixed boundaries or in the presence of moving objects. A new approach for the penalty-operator integration is proposed, based on a Strang splitting between the penalization terms and the convection-diffusion terms. Doing so, the penalization term can be computed exactly. The momentum term can then be computed first and then introduced into the continuity equation in an implicit manner. The direct-forcing method however uses ghost-cells to reconstruct the values inside the solid boundaries by projection of the image points from the interface. This method is comparatively hard to implement in 3D cases and for moving boundaries. In the present paper, the performance of both methods is assessed through a variety of test problems. The application concerns the unsteady transonic and supersonic fluid flows. Examples include a normal shock reflection off a solid wall, transonic shock/boundary layer in a viscous shock tube, supersonic shock/cylinder interaction, and supersonic turbulent channel flow. The obtained results are validated against either analytical or reference solutions. The numerical comparison shows that, with sufficient mesh resolution, the BPM and the DFM methods yield qualitatively similar results. In all considered cases, the BPM is found to be a suitable and a possibly competitive method for viscous-IBM in terms of predictive performance, accuracy and computational cost. However, despite its simplicity, the method suffers from a lack of regularity in the very near-wall pressure fluctuations, especially for the turbulent case. This is attributed to the fact that the method requires no specific pressure condition at the fluid/solid interface.

© 2016 Elsevier Ltd. All rights reserved.

1. Introduction

Numerical simulations of viscous flows around solid obstacles or within boundaries of arbitrary shape are of crucial interest in many engineering applications. Up to now, two main approaches have been followed to deal with complex geometries: body-fitted grid methods and immersed boundary methods. Body-fitted methods rely on structured or unstructured grids that are generated to fit with complex boundaries. Therefore, to obtain accurate solutions for complex geometries, it is required to refine the mesh near the boundary-layer region. Nevertheless, to build a body-fitted grid, an expensive grid generation process has to be followed. Moreover,

even with simple geometries, it is still difficult to generate a mesh of good quality. Finally, for a given numerical scheme, the order of accuracy on structured or unstructured grids is always lower than on Cartesian grids. An alternative approach is to perform simulations on non-body conformal Cartesian grids and to impose immersed boundary conditions on the fluid. The main advantages of this approach are its easy implementation and the possibility to treat moving boundaries in a simpler manner.

Since Peskin's pioneering work [31], various immersed boundary techniques have been developed, mostly for incompressible flows. They can be decomposed into two categories: the methods that introduce fictitious terms in the governing equations and those which locally modify the structure of the background grid. In the first category, Peskin [31] modeled immersed boundaries as elastic media that exert localized forces on the fluids and hence modify the momentum equation. Various extensions to rigid body

* Corresponding author.

E-mail address: hadjadj@coria.fr (A. Hadjadj).

problems have been proposed (Goldstein et al [16], Saiki and Birn- gen [34]). However, these methods used explicit-time stepping for such problems, which are in fact stiff. Hence the computational time step is small, which gives severe restrictions to the method. Furthermore, there is no mathematical proof of convergence for these methods. In contrast to this approach, the volume penal- ization technique, proposed by Arquis and Caltagirone [3], mod- els the solid body as a porous medium with very small perme- ability. A rigorous error estimation was proposed by Angot et al [2]. Angot [1] also proved that the solution of the penalized in- compressible Navier–Stokes equations strongly converges towards the exact solution as the penalization parameter approaches zero. Several authors successfully applied this method to incompressible flows with fixed (Kevlahan and Ghidaglia [21]) as well as moving obstacles (Kadoch et al [20]). Liu and Vasilyev [24] applied the Brinkman penalization method to the compressible flow regime and Boiron et al [5] extended this approach to large Mach number flows. However, in these two papers, only isothermal walls have been considered. Another formulation of the volume penalization, which differs from the original idea of Angot and Caltagirone [3], is proposed by Brown-Dymkoski et al [6] that takes into account adiabatic walls and mixed boundary conditions.

In the second category, the direct-forcing immersed bound- ary method consists in using ghost cells and directly impose the boundary conditions on the immersed boundaries. This method has been introduced for incompressible flows by Mohd-Yousof [29]. The term of direct-forcing and the extension of the method to three-dimensional flows was proposed by Fadlun et al [12]. The bilinear interpolation (trilinear in 3D) of ghost points was intro- duced by Majumdar et al [27]. The method has then been suc- cessfully applied to turbulent flows [18], particulate flows [39], and fluid–structure interactions [35]. The extension to high-speed flows in the configuration of shock/obstacle interactions has been per- formed by Chaudhuri et al [8,10]. A general review of immersed boundary methods can be found in Mittal and Iaccarino [28].

The objective of the present paper is to compare the Brinkman penalization method, which is the most promising method of the first category, with the direct-forcing immersed boundary method, which is, to the best of our knowledge, the most efficient method of the second category. Generally, comparing different IBM algo- rithms is not straightforward as they differ in strategy, approach, computational complexity, and prediction ability. Moreover, such methods are strongly influenced by different selected param- eters and test cases, and one wish to answer the following ques- tions: Which approach is better? and do one of them have advan- tages over the other? To our best knowledge, no such comprehen- sive comparison of IBM methods applied to transonic / supersonic regimes is available in the literature so far. In the present paper, several test cases are performed to examine the behavior of fluid solid interaction, including shock wave propagation and reflection off a wall, shock/cylinder interaction and shock-free turbulence.

The paper is organized as follows: in Section 2, the numerical approach, including the governing equations, the penalized equa- tions and the direct-forcing immersed boundary method, are pre- sented. The obtained results are discussed in Section 3. Finally, conclusions and perspectives are drawn in Section 4.

2. Numerical method

2.1. Governing equations

Let $\Omega \in R^2$ be the computational domain containing N fixed regular obstacles ω_n , $n \in \{1, \dots, N\}$, and let us set

$$\Omega_s = \bigcup_{n=1}^N \omega_n \text{ and } \Omega_f = \Omega \setminus \bar{\Omega}_s. \quad (1)$$

Here, $\bar{\Omega}_s$ denotes the closed region occupied by the solid bodies and Ω_f denotes the fluid domain.

For the fluid domain, we consider the compressible Navier– Stokes equations, together with appropriate boundary conditions on the solid bodies $\partial\omega_n$ and on the boundary of the computational domain $\partial\Omega$. The system of equations reads

$$\partial_t \mathbf{Q} + \nabla \cdot \mathbf{F}_I = \nabla \cdot \mathbf{F}_V \quad (2)$$

where \mathbf{Q} denotes the vector of conservative variables

$$\mathbf{Q} = [\rho, \rho \mathbf{v}, \rho E]^T, \quad (3)$$

\mathbf{F}_I denotes the inviscid flux tensor

$$\mathbf{F}_I = [\rho \mathbf{v}, \rho \mathbf{v} \otimes \mathbf{v} + p \mathbf{I}, (\rho E + p) \mathbf{v}]^T, \quad (4)$$

and \mathbf{F}_V the viscous flux tensor

$$\mathbf{F}_V = [\mathbf{0}, \tau, \tau \mathbf{v} + \lambda \nabla T]^T. \quad (5)$$

Here ρ , $\mathbf{v} = [u, v, w]^T$, p , T and E denote the density, velocity, pressure, temperature and total energy per unit of mass of the fluid, respectively. λ is the thermal conductivity, \mathbf{I} the identity ma- trix and

$$\tau = \mu \left[\nabla \otimes \mathbf{v} + (\nabla \otimes \mathbf{v})^T - \frac{2}{3} (\nabla \cdot \mathbf{v}) \mathbf{I} \right] \quad (6)$$

where μ denotes the dynamic viscosity of the fluid, which follows Sutherland’s law

$$\mu(T) = \mu_{ref} \left(\frac{T}{T_{ref}} \right)^{\frac{3}{2}} \frac{T_{ref} + T_s}{T + T_s} \quad (7)$$

with μ_{ref} and T_{ref} are the reference viscosity and temperature, re- spectively, and T_s is the Sutherland temperature. The system is closed by the equation of state for a calorically ideal gas

$$p = (\gamma - 1) \rho \left(E - \frac{\mathbf{v}^2}{2} \right) \quad (8)$$

with the isentropic exponent $\gamma = 1.4$ for air.

On the surface of each solid obstacle, the fluid velocity satisfies the no-slip condition

$$\mathbf{v}|_{\partial\omega_n} = \mathbf{v}_n. \quad (9)$$

We also consider that the wall temperature on each obstacle is fixed and, hence we impose Dirichlet boundary conditions for the temperature, i.e.

$$T|_{\partial\omega_n} = T_n. \quad (10)$$

It is worth noticing that the Neumann (or adiabatic) boundary condition can be easily implemented in the Direct-forcing method by applying the zero-gradient temperature condition at the wall $\partial T / \partial \vec{n} = 0$, i.e. Section 2.3.2. However, its implementation for the penalization method has lacked generality, especially for compressible flows. Recently, Brown-Dymkoski et al. [6] have proposed a Characteristic-Based Volume Penalization (CBVP) method that can address this question. However, in this paper, we will just focus on the isothermal condition for the sake of simplicity.

2.2. Space and time discretization

Space discretization is made through high-order finite differ- ences. The inviscid fluxes are discretized using a fifth-order WENO scheme [19,25]. The principle relies on a convex combination of low-order polynomial reconstructions that yield a high-order res- olution in smooth regions and keep the essentially non-oscillatory property near the discontinuities. Upwinding is made using a Roe scheme [33].

For sake of clarity, we present here the WENO scheme for a one dimensional scalar equation, considering the quantity φ . Extension

to higher dimensions is straightforward and extension to the Euler and Navier-Stokes equations is made considering the characteristic variables for the reconstruction instead of the conservative ones. For the fifth-order WENO scheme, let us consider three third-order polynomial reconstructions on three different stencils

$$\begin{aligned}\varphi_{i+\frac{1}{2}}^{(1)} &= \frac{1}{3}\varphi_i + \frac{5}{6}\varphi_{i+1} - \frac{1}{6}\varphi_{i+2} \\ \varphi_{i+\frac{1}{2}}^{(2)} &= -\frac{1}{6}\varphi_{i-1} + \frac{5}{6}\varphi_i + \frac{1}{3}\varphi_{i+1} \\ \varphi_{i+\frac{1}{2}}^{(3)} &= \frac{1}{3}\varphi_{i-2} - \frac{7}{6}\varphi_{i-1} + \frac{11}{6}\varphi_i\end{aligned}\quad (11)$$

The fifth-order WENO reconstruction corresponds to

$$\varphi_{i+\frac{1}{2}} = w_1\varphi_{i+\frac{1}{2}}^{(1)} + w_2\varphi_{i+\frac{1}{2}}^{(2)} + w_3\varphi_{i+\frac{1}{2}}^{(3)} \quad (12)$$

where the weights w_j , $j \in \{1, 2, 3\}$, are

$$w_j = \frac{\alpha_j}{\alpha_1 + \alpha_2 + \alpha_3}, \quad \text{with } \alpha_j = \frac{\gamma_j}{(\beta_j + \epsilon)^2} \quad (13)$$

The term ϵ is set to 10^{-6} to avoid divisions by zero and the coefficients β_j , $j \in \{1, 2, 3\}$, are the *smoothness indicators* of the function φ , defined by

$$\begin{aligned}\beta_1 &= \frac{13}{12}(\varphi_i - 2\varphi_{i+1} + \varphi_{i+2})^2 + \frac{1}{4}(3\varphi_i - 4\varphi_{i+1} + \varphi_{i+2})^2 \\ \beta_2 &= \frac{13}{12}(\varphi_{i-1} - 2\varphi_i + \varphi_{i+1})^2 + \frac{1}{4}(\varphi_{i-1} - \varphi_{i+1})^2 \\ \beta_3 &= \frac{13}{12}(\varphi_{i-2} - 2\varphi_{i-1} + \varphi_i)^2 + \frac{1}{4}(\varphi_{i-2} - 4\varphi_{i-1} + 3\varphi_i)^2\end{aligned}\quad (14)$$

The coefficients γ_j , $j \in \{1, 2, 3\}$, are the *linear weights* of the scheme. They are the coefficients of the fifth-order scheme when the smoothness indicators are all equal to 1.

$$\gamma_1 = \frac{3}{10}, \quad \gamma_2 = \frac{3}{5}, \quad \gamma_3 = \frac{1}{10}. \quad (15)$$

In Section 3.4, the supersonic turbulent channel flow does not contain any discontinuity or shock. Thus, the generalized conservation split-centered scheme of Pirozzoli et al. [32] are used to gain in terms of computational efficiency and accuracy.

Pirozzoli et al. [32] proposed an approximation of the convective derivatives in the compressible Navier–Stokes equations of the form,

$$\frac{\partial \rho u_k \varphi}{\partial x_k} \Big|_{x=x_i} \approx \frac{1}{\Delta x} (\hat{f}_{i+1/2} - \hat{f}_{i-1/2}) \quad (16)$$

where $\hat{f}_{i+1/2}$ denotes the numerical flux.

This equation can be expanded into a more generalized form by splitting the derivative into several other terms in order to stabilize the centered convective scheme.

$$\begin{aligned}\frac{\partial \rho u \varphi}{\partial x} &= \kappa_1 \frac{\partial \rho u \varphi}{\partial x} + \kappa_2 \left(u \frac{\partial \rho \varphi}{\partial x} + \rho \frac{\partial u \varphi}{\partial x} + \varphi \frac{\partial \rho u}{\partial x} \right) \\ &+ (1 - \kappa_1 - 2\kappa_2) \left(\rho u \frac{\partial \varphi}{\partial x} + \rho \varphi \frac{\partial u}{\partial x} + u \varphi \frac{\partial \rho}{\partial x} \right)\end{aligned}\quad (17)$$

One possible semi-discrete conservative approximation can be obtained for $\kappa_1 = \kappa_2 = 1/4$ [32]. Using the previous form of the convective derivative, the numerical flux \hat{f} can be expressed by the following equation

$$\hat{f}_{i+1/2} = 2 \sum_{l=1}^L a_l \sum_{m=0}^{l-1} (\widetilde{\rho, u, \varphi})_{j-m, l} \quad (18)$$

where the two-point, three-variable discrete averaging operator is defined as

$$(\widetilde{f, g, h})_{j, l} = \frac{1}{8} (f_j + f_{j+l})(g_j + g_{j+l})(h_j + h_{j+l}) \quad (19)$$

The fourth order split-centered scheme is expressed by the following constant, $L = 2$, $a_1 = 8/12$ and $a_2 = -1/12$.

Viscous fluxes use a classical fourth order centered scheme. The formulas for the first space derivatives for a component φ in the direction x are [17]

$$(\partial_x \varphi)_i = \frac{\varphi_{i-2} - 8\varphi_{i-1} + 8\varphi_{i+1} - \varphi_{i+2}}{12\Delta x} + O(\Delta x^4) \quad (20)$$

where Δx denotes the space step in the x -direction. We apply the same formula for the other directions.

Time integration is made using a classical explicit third-order TVD Runge–Kutta scheme. Eq. (2) can be written in the form

$$\partial_t \mathbf{Q} = D(\mathbf{Q}) \quad (21)$$

where D denotes the divergence operator. The time integration writes

$$\begin{aligned}\mathbf{Q}^* &= \mathbf{Q}^n + \Delta t D(\mathbf{Q}^n) \\ \mathbf{Q}^{**} &= \frac{1}{4}[3\mathbf{Q}^n + \mathbf{Q}^* + \Delta t D(\mathbf{Q}^*)] \\ \mathbf{Q}^{n+1} &= \frac{1}{3}[\mathbf{Q}^n + 2\mathbf{Q}^{**} + 2\Delta t D(\mathbf{Q}^{**})]\end{aligned}\quad (22)$$

where Δt denotes the time step.

2.3. Immersed boundary methods

2.3.1. Brinkman penalization method

The principle of the Brinkman penalization consists in considering the solid as a porous medium with a very low permeability and the fluid as a medium with an infinite permeability. Denoting by \mathbf{Q}_η the penalized vector of the conservative quantities, by $\mathbf{F}_{l, \eta}$ the penalized tensor of the inviscid fluxes and by $\mathbf{F}_{v, \eta}$ the penalized tensor of the viscous fluxes, Eq. (2) becomes

$$\partial_t \mathbf{Q}_\eta + \mathbf{A} \nabla \cdot \mathbf{F}_{l, \eta} + \mathbf{P}_\eta = \nabla \cdot \mathbf{F}_{v, \eta} \quad (23)$$

where

$$\mathbf{A} = \begin{bmatrix} 1 + \left(\frac{1}{\phi} - 1\right)\chi_{\Omega_s} & \mathbf{0}^T & 0 \\ \mathbf{0} & \mathbf{I} & \mathbf{0} \\ 0 & \mathbf{0}^T & 1 \end{bmatrix}, \quad \mathbf{P}_\eta = \frac{\chi_{\Omega_s}}{\eta} \begin{bmatrix} 0 \\ \rho_\eta \mathbf{v}_\eta - (\rho \mathbf{v})_{\Omega_s} \\ \rho_\eta E_\eta - (\rho E)_{\Omega_s} \end{bmatrix}, \quad (24)$$

and

$$\chi_{\Omega_s} = \begin{cases} 1 & \text{if } x \in \Omega_s \\ 0 & \text{elsewhere} \end{cases} \quad (25)$$

where ϕ is the porosity and η is the permeability.

Angot et al. [2] showed that, using *a-priori* estimation on the penalized velocity in the incompressible limit, the penalized velocity \mathbf{v}_η converges towards the velocity in the fluid \mathbf{v}_f when $\eta \rightarrow 0$ with an order of convergence of $O(\eta^{3/4})$. The error $\mathbf{v}_\eta - \mathbf{v}_f$ verifies an equation of Darcy inside the solid, which justifies an interpretation as a porous solid. Numerically, an order of convergence of $O(\eta)$ is observed.

On the other hand, and according to Kolomenskiy et al. [22,23], the penalization method is evaluated using a second-order finite-difference scheme applied to the penalized Poisson equation in 2D. The performed numerical simulations yield a second-order convergence towards the solution of the Poisson equation, given that the penalization parameter η is sufficiently small. Due to the regularity of the exact solution of the penalized equation and the $O(\eta)$ behavior of the penalization error, the authors anticipate that for higher-order numerical methods, a second-order convergence will also be obtained.

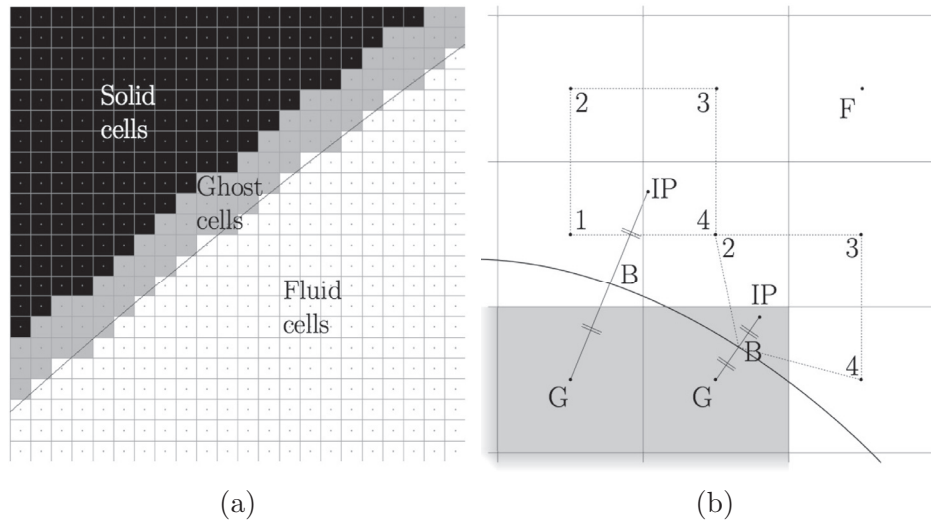


Fig. 1. Direct-forcing method: (a) Black, grey and white represent solid, ghost and fluid cells, respectively; (b) Bi-linear interpolation for IBM highlighting the specific case for a near-wall ghost cell

The numerical scheme is based on a Strang splitting of the penalization terms (**P**) on the one hand, and the convection and diffusion terms (**C**) on the other hand.

$$\mathbf{Q}^{n+1} = \mathbf{P}(\Delta t/2) \mathbf{C}(\Delta t) \mathbf{P}(\Delta t/2) \mathbf{Q}^n \quad (26)$$

Penalization terms are computed exactly for the momentum and energy equations. Denoting by q one of the conservative quantities of the momentum or energy equation, we solve, in the solid part,

$$d_t q = -\frac{1}{\eta} (q - q_{\Omega_s}) \quad (27)$$

which, between t^n and $t^{n+1} = t^n + \Delta t$, has the exact solution

$$q^{n+1} = q_{\Omega_s} \left(1 - e^{-\frac{\Delta t}{\eta}}\right) + q^n e^{-\frac{\Delta t}{\eta}} \quad (28)$$

For the continuity equation, when ϕ is different from 1, i.e. when the equation is penalized, the penalization term is treated using a semi-implicit operator. First, the momentum equation is computed and then the obtained value is used to advance the momentum term at time $n + 1$ in the continuity equation.

2.3.2. Direct-forcing method

The direct-forcing immersed boundary method uses a Cartesian grid which contains both fluid and solid cells. The latter are then split into ghost and pure solid cells. The number of ghost cell depends on the scheme used for the space discretization. The direct-forcing immersed boundary method is applied only on the ghost cells. Fig. 1a shows a sketch of the mask distribution.

For each ghost point, the corresponding image points are created in the fluid from the surface of the object. Since the image points is in the fluid, multi-dimensional interpolations are necessary, i.e. cell data to point data. The bi-linear method is used to interpolate the value in the fluid. In [30], a 2D interpolation method is proposed, which is here presented in the 3D case. This method precisely reconstructs the missing information by linearly interpolating variables from the neighbor cells. For the points located near the wall and surrounded by one or more ghost points, a simple bi-linear interpolation is not possible and will cause an ill-posed problem. Nam and Lien [30] proposed an interpolation between the fluid points and the interface. Fig. 1b shows the interpolation method for both cases: full surrounded image point and near-wall image point.

For the 3D bi-linear interpolation method, the generic flow variable φ can be calculated with

$$\varphi(x, y, z) = C_1xyz + C_2xy + C_3xz + C_4yz + C_5x + C_6y + C_7z + C_8 \quad (29)$$

The eight weighting coefficients, noted C_i , are evaluated from the eight surrounding points by solving the following algebraic system:

$$\begin{bmatrix} C_1 \\ \vdots \\ C_8 \end{bmatrix} = \begin{bmatrix} x_1y_1z_1 & x_1y_1 & x_1z_1 & y_1z_1 & x_1 & y_1 & z_1 & 1 \\ \vdots & \vdots \\ x_8y_8z_8 & x_8y_8 & x_8z_8 & y_8z_8 & x_8 & y_8 & z_8 & 1 \end{bmatrix}^{-1} \begin{bmatrix} \varphi_1 \\ \vdots \\ \varphi_8 \end{bmatrix} \quad (30)$$

The 8×8 Vandermonde matrix M_V is inverted for each ghost cell of the grid at the beginning of the simulation. For the case where one of the surrounded point lies on the ghost cells, we directly impose the value of the wall using the coordinates of the boundary point (see Fig. 1b). Eq. (31) shows the Vandermonde matrix M_V when a point, or more, (noted B) lies on a ghost cell.

$$\begin{bmatrix} C_1 \\ \vdots \\ C_B \\ \vdots \\ C_8 \end{bmatrix} = \begin{bmatrix} x_1y_1z_1 & x_1y_1 & x_1z_1 & y_1z_1 & x_1 & y_1 & z_1 & 1 \\ \vdots & \vdots \\ x_By_Bz_B & x_By_B & x_Bz_B & y_Bz_B & x_B & y_B & z_B & 1 \\ \vdots & \vdots \\ x_8y_8z_8 & x_8y_8 & x_8z_8 & y_8z_8 & x_8 & y_8 & z_8 & 1 \end{bmatrix}^{-1} \begin{bmatrix} \varphi_1 \\ \vdots \\ 0 \\ \vdots \\ \varphi_8 \end{bmatrix} \quad (31)$$

For the isothermal case, u, v, w and T are imposed by the previous method and p is such that its gradient normal to the wall is zero. The gradient condition can be expressed as follows using the wall-normal vector $\vec{n} = \{n_x, n_y, n_z\}$:

$$\begin{aligned} \frac{\partial \varphi(x, y, z)}{\partial \vec{n}} &= C_1(y_B z_B n_x + x_B z_B n_y + x_B y_B n_z) + C_2(y_B n_x + x_B n_y) \\ &+ C_3(z_B n_x + x_B n_z) + C_4(y_B n_y + z_B n_z) \\ &+ C_5 n_x + C_6 n_y + C_7 n_z = 0 \end{aligned} \quad (32)$$

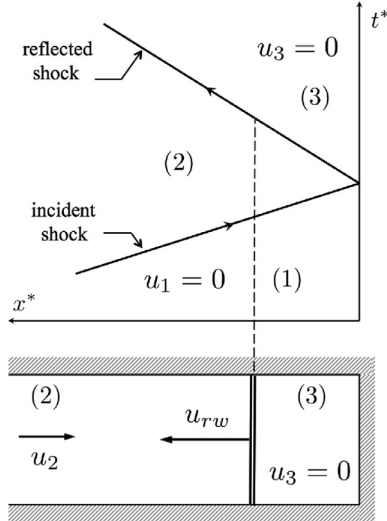


Fig. 2. Shock wave reflection from the end wall of a shock tube. Inviscid case.

As a result, the corresponding Vandermonde matrix M_V becomes

$$M_V = \begin{bmatrix} x_1 y_1 z_1 & x_1 y_1 & x_1 z_1 & y_1 z_1 & x_1 & y_1 & z_1 & 1 \\ \vdots & \vdots \\ \begin{pmatrix} y_B z_B n_x \\ +x_B z_B n_y \\ +x_B y_B n_z \end{pmatrix} & \begin{pmatrix} y_B n_x \\ +x_B n_y \end{pmatrix} & \begin{pmatrix} z_B n_x \\ +x_B n_z \end{pmatrix} & \begin{pmatrix} y_B n_y \\ +z_B n_z \end{pmatrix} & n_x & n_y & n_z & 0 \\ \vdots & \vdots \\ x_8 y_8 z_8 & x_8 y_8 & x_8 z_8 & y_8 z_8 & x_8 & y_8 & z_8 & 1 \end{bmatrix}$$

Nam and Lien [30] proposed a method for adiabatic walls and used conservative variables. In the present case, non-conserved variables have been used to apply the isothermal condition. Once the flow variables at the image point (φ_i) are interpolated, the isothermal/no-slip wall boundary conditions, from Eq. (33), will determine the values of the primitive variables (T, p, u, v, w) at the ghost cells. For the case where wall informations are needed, we simply impose the following parameters $\tilde{\mathbf{v}} = \tilde{\mathbf{0}}, T = T_w, \frac{\partial p}{\partial \mathbf{n}} = \tilde{\mathbf{0}}$. For moving boundaries, the condition on the velocity is set to $u_g = 2u_w - u_i$.

$$u_g = -u_i, \quad v_g = -v_i, \quad w_g = -w_i, \quad T_g = 2T_w - T_i, \quad p_g = p_i \quad (33)$$

According to Chaudhuri et al. [9], the direct-forcing method, using a fifth-order WENO scheme, is found to converge towards a second-order of accuracy near the boundaries.

3. Results and discussions

3.1. Shock wave reflection from a solid wall

In the first example, we consider an incident shock wave traveling at a Mach number, M_s , in a closed shock tube. The latter is assumed to have isothermal walls with free slip conditions (see Fig. 2). The quiescent gas ahead of the shock is at ambient conditions (state 1), whereas the shocked gas (state 2) is defined according to the Rankine-Hugoniot relations:

$$\begin{aligned} \frac{p_2}{p_1} &= 1 + \frac{2\gamma}{\gamma+1}(M_s^2 - 1) \\ \frac{T_2}{T_1} &= \left(1 + \frac{\gamma-1}{2}M_s^2\right) \left(\frac{2\gamma}{\gamma-1}M_s^2 - 1\right) \frac{2(\gamma-1)}{M_s^2(\gamma+1)^2} \end{aligned} \quad (34)$$

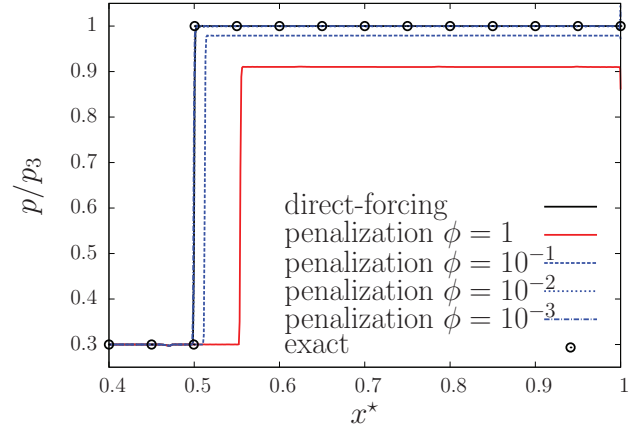


Fig. 3. Pressure of the reflected shock for both direct-forcing and penalization methods at t^* .

where p, T, M_s denote the pressure, temperature, and incident shock Mach number, respectively. The latter is defined as

$$M_s = \frac{u_s}{a_1} \quad (35)$$

with a_1 the sound speed in the quiescent gas and u_s the velocity of the incident shock. After reflection, the gas in the state (3) is at rest ($M_3 = 0$) and the reflected shock follows the jump relations from [4,15],

$$\begin{aligned} \frac{p_3}{p_2} &= \frac{-2(\gamma-1) + M_s^2(3\gamma-1)}{2 + M_s^2(\gamma-1)} \\ \frac{T_3}{T_2} &= \frac{p_3}{p_2} \frac{\alpha + \frac{p_3}{p_2}}{1 + \alpha \frac{p_3}{p_2}} \end{aligned} \quad (36)$$

The velocity of the reflected shock u_{rw} is given by [15]:

$$u_{rw} = \frac{1}{M_s^2} \left(1 + \frac{2(M_s^2 - 1)}{\alpha}\right) a_1 \quad (37)$$

where $\alpha = (\gamma+1)/(\gamma-1)$ and γ is the isentropic exponent.

The computational domain has a unit length of l and the incident shock is initially located at a normalized distance $x^* = x/l = 0.5$. In Fig. 3, we plot the pressure at a dimensionless arrival time $t^* = \frac{1}{2} \left(\frac{1}{u_s} + \frac{1}{u_{rw}}\right)$, i.e. when the reflected shock off the wall reaches the initial position of the incident shock. The obtained results, in terms of shock intensity and arrival time, show an excellent agreement between the direct-forcing method and the exact solution. However, for the Brinkman penalization, the solution seems to be penalty-parameter ϕ dependent. To clarify this point, several computations are performed with different values of ϕ . For $\phi = 1$, i.e. without penalizing the continuity equation, a weak-shock solution (reduced shock speed and lower pressure plateau profile) is obtained in contrast with the theoretical prediction. However, when ϕ is decreased, the results are substantially improved, with almost excellent collapses between numerical and exact solutions for $\phi = 10^{-2}$ and lower. Note that no difference is observed between the solutions at $\phi = 10^{-2}$ and $\phi = 10^{-3}$, the latter being recommended in [24]. Furthermore, the pressure and temperature jumps across the reflected shock, the shock velocity and the Mach number at state 3, presented in Table 1, confirm the same trends.

We also tested the effect of the shock Mach number by varying M_s from weak (transsonic regime) to very strong shock waves (supersonic regime). The same tendency is observed in terms of pressure jump across the reflected shock, p_3/p_2 (see Table 2). Based on

Table 1
Exact and computed flow conditions across the reflected shock for $M_s = 2$.

	Exact	Direct-forcing	Penalization			
			$\phi = 1$	$\phi = 10^{-1}$	$\phi = 10^{-2}$	$\phi = 10^{-3}$
$\frac{p_3}{p_2}$	3.333	3.333	3.033	3.264	3.332	3.333
		(0.0%)	(-8.9%)	(-2.0%)	(-0.03%)	(0.0%)
$\frac{T_3}{T_2}$	1.481	1.481	1.4273	1.457	1.481	1.481
		(0.0%)	(-3.64%)	(-0.82%)	(0.0%)	(0.0%)
M_3	0	$6.0 \cdot 10^{-6}$	$7.1 \cdot 10^{-2}$	$1.5 \cdot 10^{-2}$	$2.0 \cdot 10^{-4}$	$5.0 \cdot 10^{-5}$
$\frac{u_{rw}}{a_1}$	1	0.993	0.929	0.958	0.972	0.988

Table 2
Pressure ratios across the reflected shock, p_3/p_2 , compared to their exact values for different M_s .

M_s	Exact	Direct-forcing	Penalization
			$\phi = 10^{-2}$
1.2	1.478	1.478	1.477
		(0.0%)	(-0.08%)
2.0	3.332	3.333	3.332
		(+0.03%)	(-0.01%)
5.0	6.6	6.599	6.596
		(-0.02%)	(-0.06%)

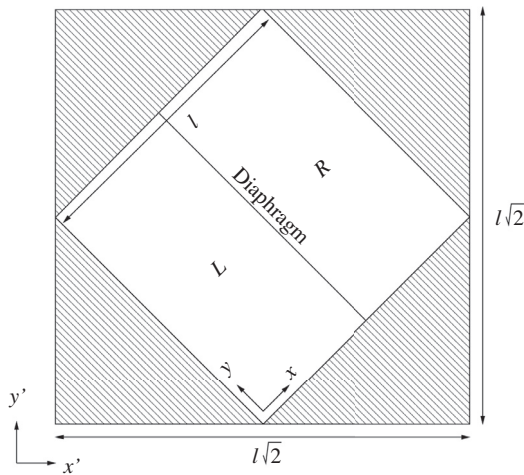


Fig. 4. Schematic representation of an inclined 2D shock tube. L and R refer to left and right states, respectively.

the above observations, the parameter ϕ will be set to 10^{-2} in the following cases, unless stated otherwise.

3.2. Inclined viscous shock tube

In the second example, we consider a two-dimensional viscous shock tube where the domain is inclined by an angle of 45° to assess the performance of the immersed boundary methods on non-aligned grid (see Fig. 4). The computational domain is a closed box of $[0, l\sqrt{2}] \times [0, l\sqrt{2}]$ with isothermal and no-slip boundary conditions. l is the length of the shock tube and is taken as a unit. At initial time, dimensionless variables are used in both sides of the shock tube with $(p_L, p_R) = (100, 1)$, $(u_L, u_R) = (0, 0)$, $(\rho_L, \rho_R) = (120, 1.2)$, $T_w = 1$ (for dimensionless wall temperature) and $p = \rho/\gamma$. The nominal Reynolds number is set to $Re = 200$, and the dynamic viscosity follows Sutherland’s law [11]. The reference solution is computed on a twice finer grid (512×512) using a regular (non-inclined) domain with fixed boundary conditions.

Fig. 5 shows the density contours for the reference solution together with the direct-forcing as well as the penalization solutions. The two IBM solutions are counter-rotated by an angle of -45° to allow direct comparison with the reference solution. Basically, one can find similar flow features for the three cases. A typical lambda-shape like bifurcated shock wave pattern is observed as a consequence of the stagnation pressure drop due to the presence of the boundary layer. When superposing the three computations on a single graph (see Fig. 6), we observe that the direct-forcing computation is well synchronized with the reference and the penalization solutions.

Further qualitative comparison are done on density and pressure distributions at a normalized distance, $y/l = 0.05$. The result is plotted in Fig. 7. The difference between the two solutions remain acceptable, since the main flow features are almost retrieved.

3.3. 2D supersonic shock/cylinder interaction

The third example concerns a moving shock at $M_s = 2.81$ interacting with a circular cylinder. Various studies [7,40–42] have shown that the shock/cylinder interaction, in particular the unsteady wake flow behind it, contains many interesting flow features with very complex shock structures. The flow conditions are fixed so that the nominal Reynolds is equal to 3000. The cylinder is kept at a constant temperature. The flow characteristics consist of unsteady evolution of multiple Mach stems, triple points, reflected (attenuated and accelerated) shocks, slip-lines and vortices. Instantaneous numerical Schlieren pictures showing the flow structures around the cylinder are depicted in Fig. 8. One can clearly see that the essential flow characteristics are reproduced by both methods with very high fidelity.

The results also exhibit two weak flow discontinuities at both top and bottom sides of the cylinder. It appears that this discontinuity is more enhanced for the penalization method. This is probably due to the difficulty of the method to properly reconstruct the pressure field at fluid/solid interface. Nevertheless, these small disturbances are not seen to drastically affect the overall quality of the solution. The computed trajectories of the two triple points are depicted in Fig. 9. The comparisons against experimental data [7,14] appear quite satisfactory for both methods.

3.4. 3D supersonic turbulent channel flow at $Re_\tau = 220$

In the last example, we consider a supersonic turbulent flow between two parallel planes of infinite width. The computational domain and the main flow parameters are taken similar to Foysi et al. [13]. Periodic boundary conditions are used in both streamwise (x) and spanwise (z) directions. The length of the computational domain has been set up as in Foysi et al. [13] and Taieb et al. [37,38]. To ensure that both stream- and spanwise lengths are sufficiently wide, the distributions of the two-point autocorrelations functions along x and z directions have been analyzed. The results

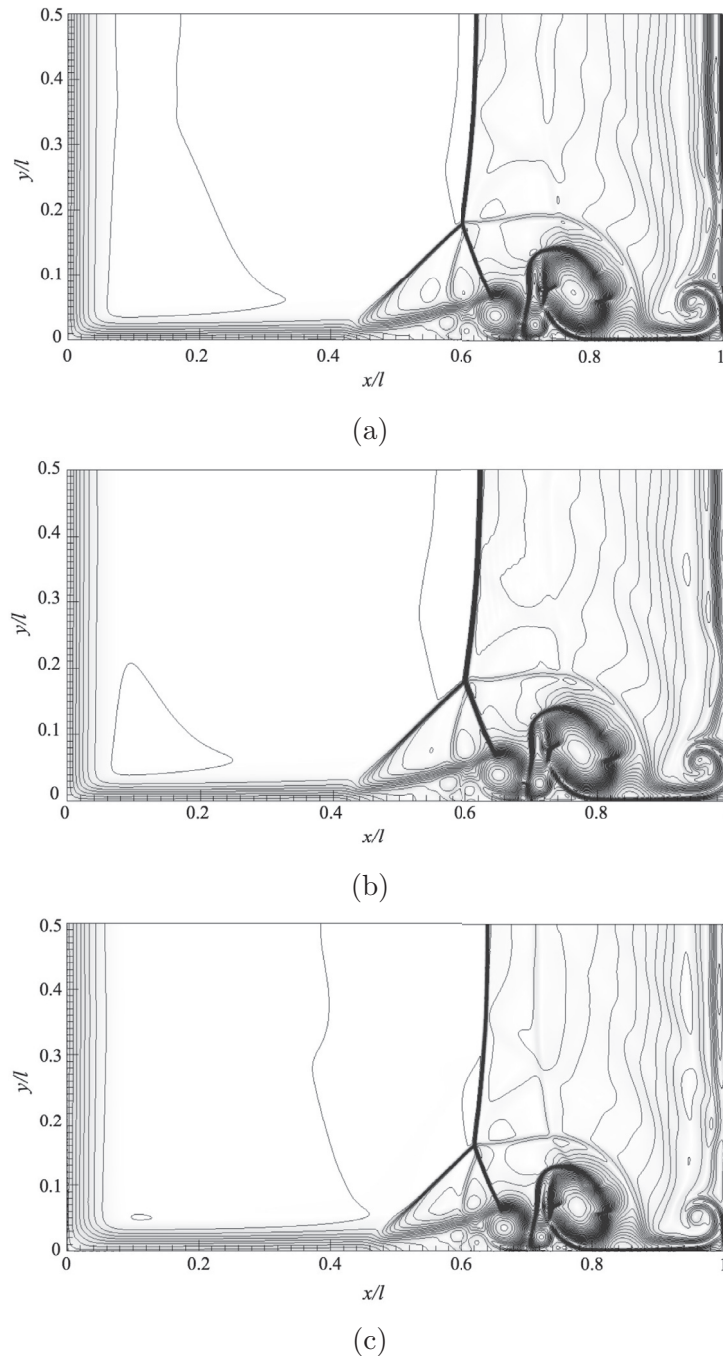


Fig. 5. 2D shock/boundary layer interaction: iso-contours of density for the reference (a), direct-forcing (b) and penalization with $\phi = 0.01$ (c). Only the bottom-half of the computed domain is shown.

[13,37,38] show that the flow variables are sufficiently decorrelated over distances $L_x/2$ and $L_z/2$, thus ensuring that the extents of the computational domain are sufficient in order to not inhibit turbulence dynamics.

Fig. 10 presents the computational domain and Table 3 summarizes the main flow properties. The mesh contains around 3.68 million cells. Since this case contains no shock, centered fourth-order schemes are used for both convective and diffusive terms. The mesh spacing is constant in both x - and z -directions and is stretched in the wall-normal (y) direction so that $\Delta y_w^+ = 1$. For both methods, the number of point in the y -direction is extended to 156 in order to create ghost points inside the computational domain. The Reynolds number, based on the friction velocity, is set

to $Re_\tau = u_\tau h/\nu_w = 220$ (h being half the height of the channel and the subscript w refers to wall quantities). To ensure a balance between the pressure drop and the shear-wall stress, a forcing term is added to the momentum equation and its equivalent, in terms of work, to the energy equation. This term is defined as

$$\rho f = \frac{\tau_w}{h} = \frac{(Re_\tau \mu_w)^2}{\rho_w h^3} \quad (38)$$

The walls are considered as isothermal with a fixed temperature of 500 K. As initial conditions, Klein method [26] is used to generate a statistically-correlated turbulent field. Turbulent statistics are averaged over approximately 10τ , where $\tau = t u_b/L_x$ is a dimensionless time unit and u_b is the bulk velocity (see Table 3).

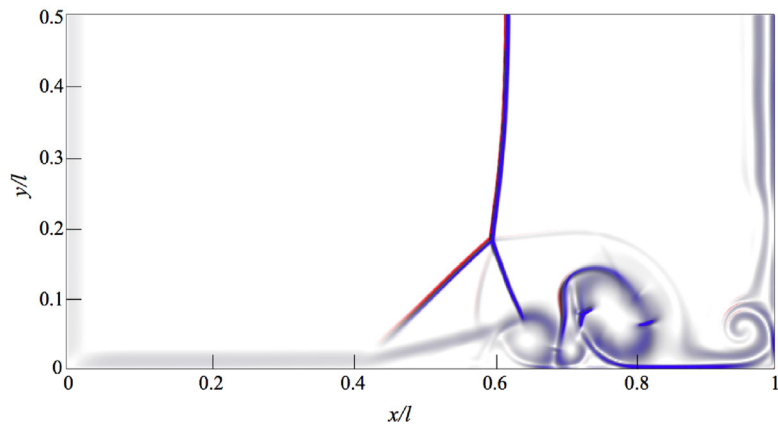


Fig. 6. 2D shock/boundary layer interaction: shock positions for the reference computation (black), direct-forcing (blue) and penalization with $\phi = 0.01$ (red) methods on the bottom-half of the walls. (For interpretation of the references to color in this figure legend, the reader is referred to the web version of this article.)

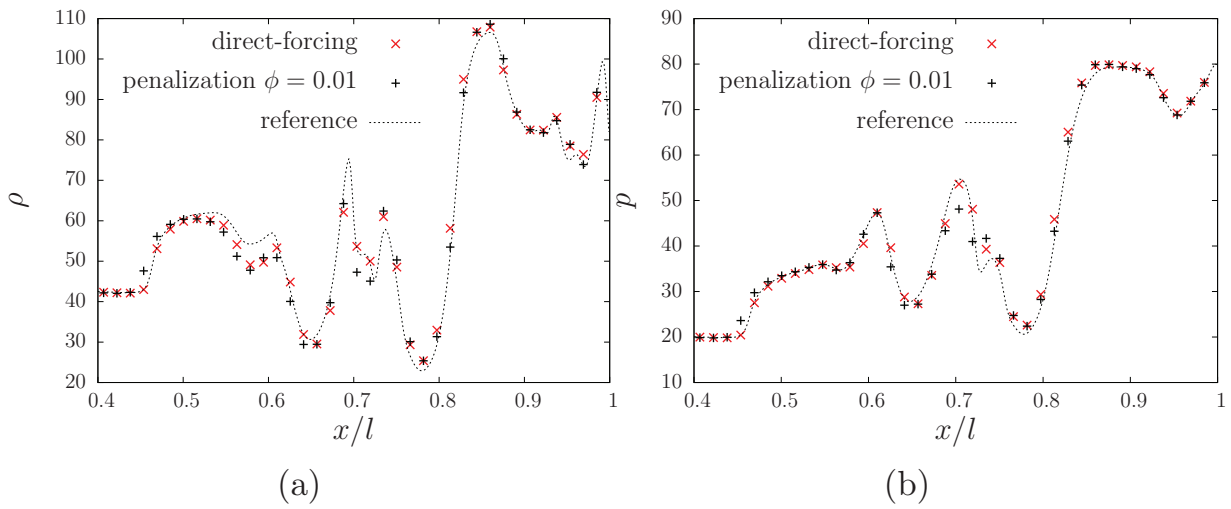


Fig. 7. Shock/boundary layer interaction in a 2D viscous shock tube: density (a) and pressure (b) profiles at $y/l = 0.05$.

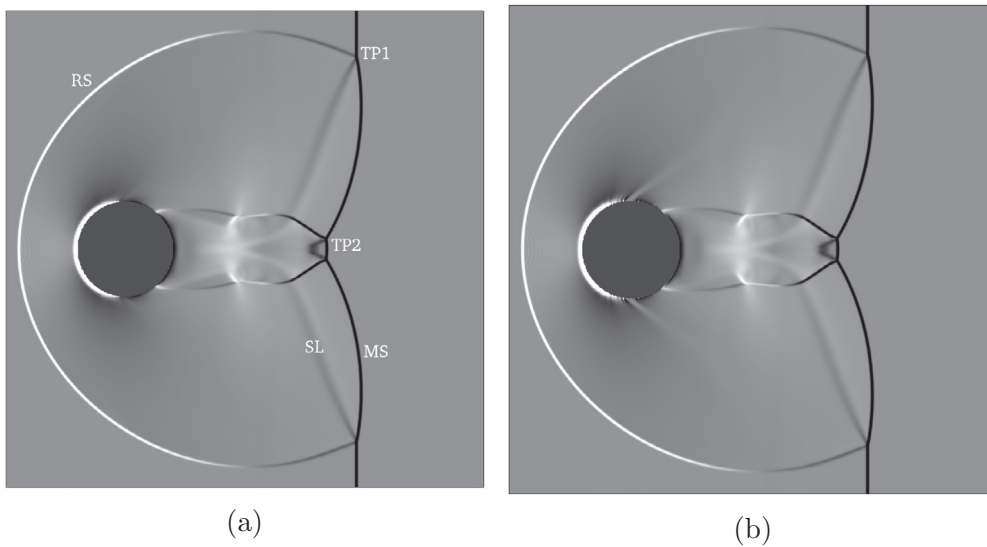


Fig. 8. 2D shock/cylinder interaction: Numerical Schlieren pictures for direct-forcing (a) and penalization method with $\phi = 0.01$ (b). RS: Reflected shock, IS: incident shock, SL: slip line, MS: Mach stem and TP1/TP2: triple points.

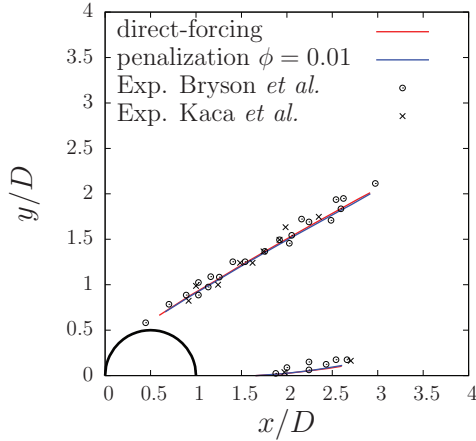


Fig. 9. 2D shock/cylinder interaction: Comparison of triple points trajectories with experiments from Bryson et al. [7] and Kaca et al. [14].

Table 3

Computational domain, grid size and flow properties with $Re_b = u_b h / \nu_w$ and $u_\tau = \sqrt{\tau_w / \rho_w}$.

L_x	L_y	L_z	N_x	N_y	N_z	h (mm)
$4\pi h$	$2h$	$4/3\pi h$	192	150	128	6.84
L_x^+	L_y^+	L_z^+	Δx^+	Δy_{min}^+	Δy_{max}^+	Δz^+
2765	440	922	14.4	0.8	5.0	7.2
Re_b	Re_τ	u_τ (m/s)	M	u_b (m/s)	T_w (K)	
3000	220	35	1.5	680	500	

Table 4

Turbulent channel flow: relative errors of direct-forcing and penalization methods on the friction Reynolds number ($Re_\tau = 220$) and the dissipation of the turbulent kinetic energy at the wall.

Method	Re_τ	relative error	ε_w^+	relative error
direct-forcing	221.65	+0.7%	0.161	0.0%
penalization $\phi = 0.01$	201.78	-8.28%	0.156	-3.27%

Table 4 shows the computed friction Reynolds number and the turbulent dissipation at the wall for both methods. The direct-forcing method gives a result with less than 1% difference, while the penalization method gives more than 8%. This departure is tied to the one on the wall friction τ_w , due to the fact that the penalization method, which considers the solid as mildly porous, transfers a small amount of momentum and energy through the wall. This effect is highlighted in Fig. 13 where the velocity gradient near the wall is computed differently for the direct-forcing and the penalization methods. We can also observe that the velocity at the

wall is not strictly null for the penalization method, due to the porosity aspect imposed by the method.

Fig. 11 shows the instantaneous iso-contours of the Q-criterion for the penalization method with $\phi = 0.01$. The Q-criterion is by definition the second invariant of the velocity-gradient tensor

$$Q = \frac{1}{2} (\Omega_{i,j} \Omega_{i,j} - S_{i,j} S_{i,j}), \quad (39)$$

where $S_{i,j}$ and $\Omega_{i,j}$ denotes the symmetric and antisymmetric parts of the velocity-gradient tensor, respectively.

In Fig. 11, we observe the coherent structures of the turbulent flow, colored by the streamwise vorticity (blue for the clockwise vortices, red for the counter-clockwise vortices). The instantaneous iso-Mach contours are projected on the sides of the figure. The picture obtained by the penalization method is quasi-identical (figure not shown).

The first-order statistics are shown in Fig. 12. The direct-forcing and the penalization methods are slightly different in terms of mean quantities: Mach number, temperature and density. The no-slip condition for the velocity at the wall, which is imposed by the direct-forcing, is not enforced by the penalization method. The velocity profile for the penalization slightly shifts from the direct-forcing method. The same issue occurs for the near-wall temperature field.

Fig. 14a compares direct-forcing and penalization methods for the van Driest normalized velocity. The latter is defined as

$$u_{VD}^+ = \int_0^{u^+} \frac{\langle \rho \rangle}{\langle \rho_w \rangle} du^+ \quad (40)$$

with $u^+ = \langle u \rangle / u_\tau$.

For both wall laws, in the viscous sublayer and in the log-law region, the reference solution and the direct-forcing method match quite well. The normalized constant C for the log-law is set to 6.9. It has been shown in [36] that, for supersonic fully-developed flows, the constant can vary significantly depending on the geometry (pipe, channel or boundary layer) or on the thermal wall condition. For the penalization method, the velocity profile is slightly above the reference computation. This can be explained by the disparity already noticed on the normalization factor τ_w .

Using the present body-forcing method, the Favre-averaging and the τ_w normalization, the momentum equation can be rewritten as

$$1 - \frac{y^+}{Re_\tau} = \frac{\langle \mu \rangle}{\langle \mu_w \rangle} \frac{\partial \langle u^+ \rangle}{\partial y^+} + \left\langle \frac{\mu'}{\mu_w} \frac{\partial u'^+}{\partial y^+} \right\rangle - \frac{\langle \rho \rangle \{ u'' v'' \}}{\tau_w} \quad (41)$$

where $\langle \rangle$ denotes the Reynolds averaging (in time and in $x - z$ directions) and $\{ \}$ is the Favre-averaging $\{ \varphi \} = \langle \rho \varphi \rangle / \langle \rho \rangle$. The prime

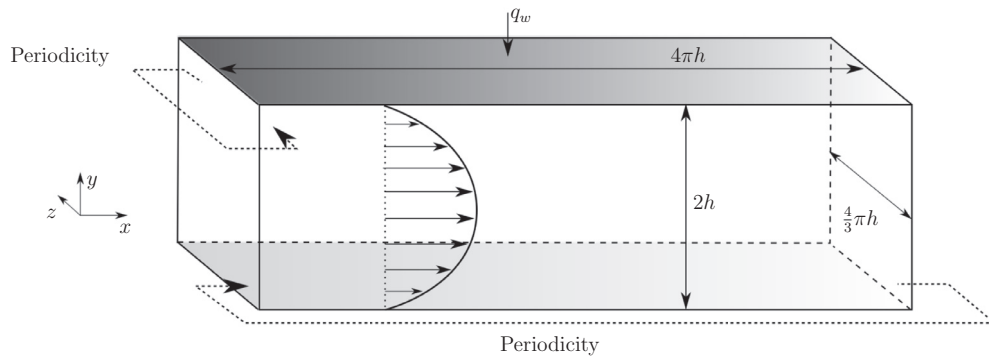


Fig. 10. Schematic representation of the supersonic turbulent channel flow domain.

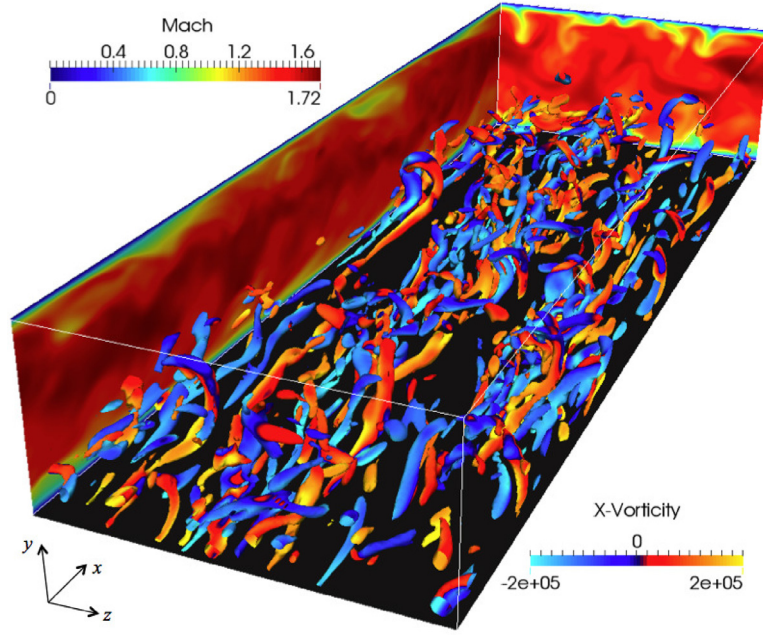


Fig. 11. Turbulent channel flow: Three-dimensional flow visualization of instantaneous iso-contour of the Q-criteria colored by the streamwise-vorticity component for penalization methods. (For interpretation of the references to color in this figure legend, the reader is referred to the web version of this article.)

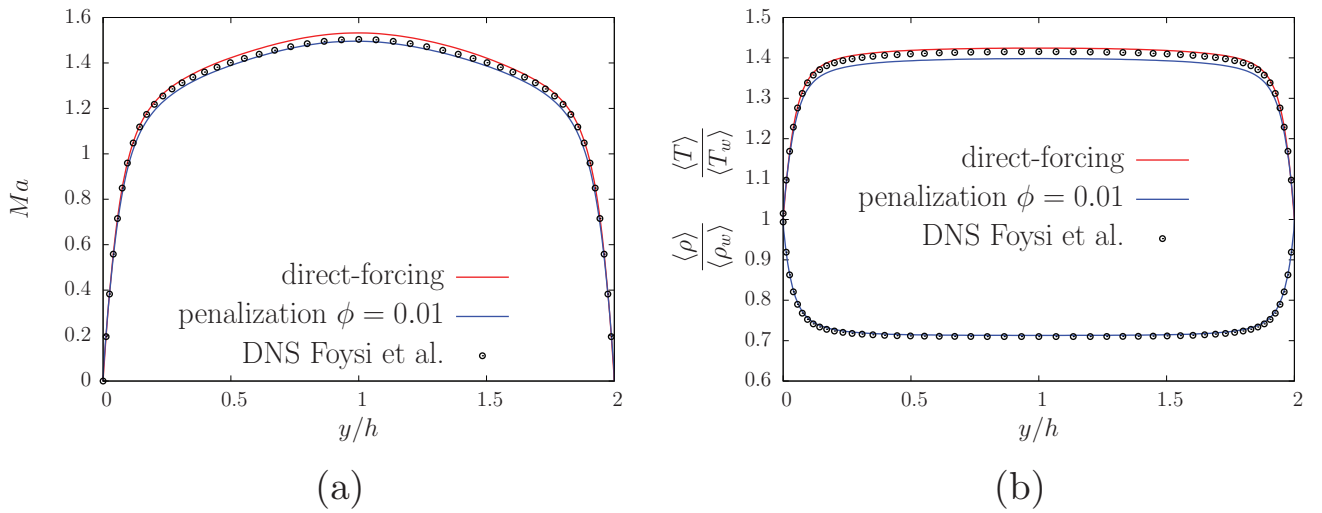


Fig. 12. Turbulent channel flow: Mach number (a) and density/temperature (b) plot for the reference DNS computation [13] and both direct-forcing and penalization methods.

(\prime) and the double prime ($\prime\prime$) represent the turbulent fluctuations with respect to Reynolds $\varphi' = \varphi - \langle \varphi \rangle$ and Favre-averages $\varphi'' = \varphi - \{\varphi\}$, respectively.

Fig. 14b shows a comparison between direct-forcing and penalization methods regarding the budget of the turbulent kinetic energy (41). The pressure-dilatation term is omitted from the budget since it is negligible for the considered range of Mach number. The contribution from the wall-shear stress is slightly overestimated in the case of the penalization method, which is again a consequence of the normalization by the wall shear stress (τ_w).

The normalized turbulent stress tensor is shown in Fig. 15 with $R_{ij}^+ = \langle \rho \rangle \{u_i'' u_j''\} / (\rho_w u_\tau^2)$. The results of both direct-forcing and penalization methods show an overestimation of the near-wall turbulence. It can be noted that the spanwise (R_{33}^+) term exhibits more difference than the other terms. Nevertheless, the discrepancy between both methods and the reference DNS is acceptable.

The turbulent kinetic energy equation, $k = 1/2 \{u_i'' u_i''\}$, is obtained by multiplying the momentum equation by the fluctuation velocity as :

$$\begin{aligned} \frac{\partial \langle \rho \rangle k}{\partial t} = & \underbrace{-\langle \rho \rangle \{u_i'' u_j''\} \frac{\partial \{u_i\}}{\partial x_j}}_{P_k} - \underbrace{\left\langle \tau_{ij}' \frac{\partial u_i''}{\partial x_j} \right\rangle}_{\varepsilon} + \underbrace{\left\langle p' \frac{\partial u_j''}{\partial x_j} \right\rangle}_{C_{k1}} \\ & + \underbrace{\left\langle u_i'' \right\rangle \frac{\partial \langle \tau_{ij} \rangle}{\partial x_j}}_{C_{k2}} - \underbrace{\left\langle u_j'' \right\rangle \frac{\partial \langle p \rangle}{\partial x_j}}_{C_{k3}} - \underbrace{\frac{\partial \langle \rho \rangle \{u_j\} k}{\partial x_j}}_{D_k} - \underbrace{\frac{\partial \langle \rho \rangle \{u_j'' u_i'' u_i''\} / 2}{\partial x_j}}_{D_t} \\ & - \underbrace{\frac{\partial \langle p' u_j'' \rangle}{\partial x_j}}_{D_{p'}} + \underbrace{\frac{\partial \langle \tau_{ij}' u_i'' \rangle}{\partial x_j}}_{D_{\tau'}} \end{aligned} \quad (42)$$

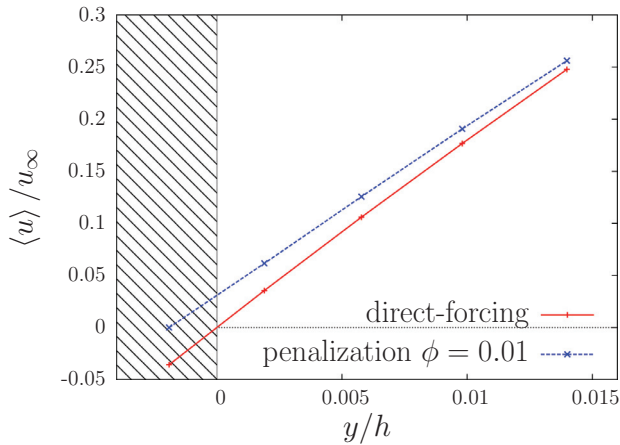
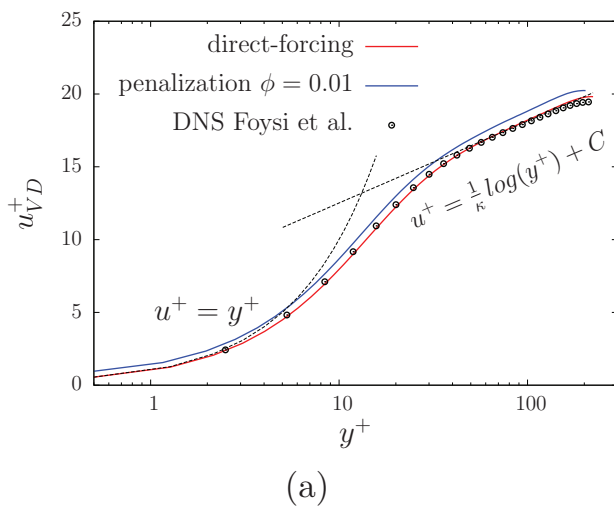


Fig. 13. Turbulent channel flow: Normalized x -velocity profile very close to the wall. The nodes represent the cell centered location. The left hatched vertical box represents the solid part and the rest is the fluid.

The different contributions are: (P_k): Production of k ; (ε): Dissipation of k ; (C_{k1}): Pressure fluctuation strain; (C_{k2}): Viscous compressibility effect; (C_{k3}): Pressure compressibility effect; (D_k): Diffusion of k ; (D_t): Turbulent diffusion; ($D_{p'}$): Pressure fluctuation diffusion and ($D_{\tau'}$): Viscous fluctuation diffusion.

The dominant terms of the turbulent kinetic-energy equation are plotted in Fig. 16a. As a result of the wall friction underestimation, the normalized terms for the penalization method are slightly overestimated. On the other hand, as shown in Table 4, the turbulent dissipation at the wall is a bit lower in the case of the penalization method. The absorption of the wall, or the porosity of the penalization method, is a direct consequence of the insufficient dissipation at the wall.

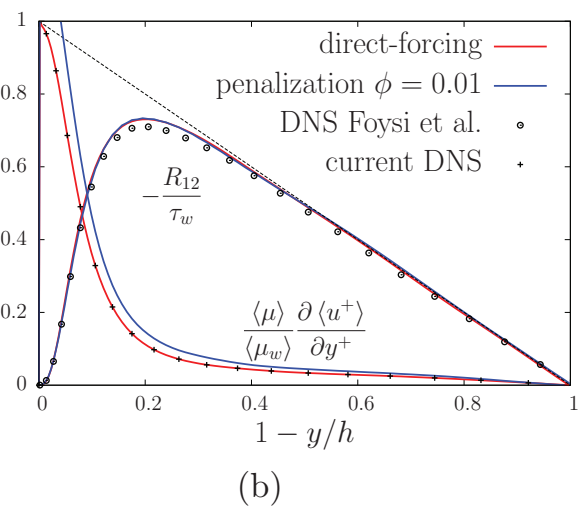
The normalized *r.m.s.* pressure, $p_{rms}/\langle p \rangle = \sqrt{\langle p' p' \rangle} / \langle p \rangle$, for the penalization method shows a wiggling effect when approaching the wall. This effect is attenuated away from it (see Fig. 16b). We assume that this behavior might be the result of the non-explicit prescription of the boundary condition (BC), since the penalization method does not require BCs at the interface. This will not necessarily enforce a zero-gradient pressure at the wall, unlike the direct-forcing method.



(a)

4. Conclusion and perspectives

In the present paper, we compare two popular methods for immersed boundary conditions: (i) the direct-forcing (DFM) and (ii) the Brinkman penalization (BPM) methods. Although the two methods are derived to handle solid-fluid problems in Cartesian grids, they are conceptually different in their philosophy and algorithm construction. The DFM uses ghost-cells at the solid boundary to reconstruct the values inside the solid, while the BPM treats the solid as a porous medium with a very low permeability. This approach relies on replacing the often difficult to implement Dirichlet fluid boundary conditions, with a simpler to integrate source terms in the Navier-Stokes equations. An efficient algorithm for source terms integration is proposed, based on a Strang splitting between the penalization terms and the convection-diffusion terms. Doing so, the penalization term can be evaluated exactly. The momentum term can then be computed first and then introduced into the continuity equation in an implicit manner. The comparison is performed over several test-cases of compressible viscous flows, including one-dimensional shock reflexion off a solid wall, two-dimensional viscous shock tube, as well as shock/cylinder interaction and three-dimensional supersonic turbulent channel flow. For all considered cases, an excellent agreement is observed between the two methods and the reference solutions. In particular, the BPM is found to be a suitable and a possibly competitive method for viscous-IBM in terms of predictive performance, accuracy and computational cost. However, despite its simplicity, the method suffers from a lack of regularity in the very near-wall *r.m.s.* pressure field, especially for the turbulent case. This behavior might be attributed to the fact that the method requires no specific pressure condition at the fluid/solid interface. Ongoing research will focus on the use of IBM for moving objects. For this purpose, the direct-forcing method seems to be much more complex to implement compared to the penalization method. In particular, the Vandermonde matrix has to be recomputed at every time step requiring thereby more CPU time for the DFM. It will also be interesting to extend the newly proposed characteristic based volume penalization method [6] to viscous flows including shock and turbulence. This method not only extends the Brinkman penalization to other kinds of boundary conditions like Neumann or Robin, but also proposes another philosophy of penalization, which seems promising for Dirichlet boundary conditions, *i.e.* isothermal walls.



(b)

Fig. 14. Turbulent channel flow: van-Driest-normalized velocity plot (a) with $\kappa = 0.41$ and $C = 6.9$; Reynolds and wall-shear stress plot (b), see Eq. (41), for the reference DNS computation [13] and both direct-forcing and penalization methods.

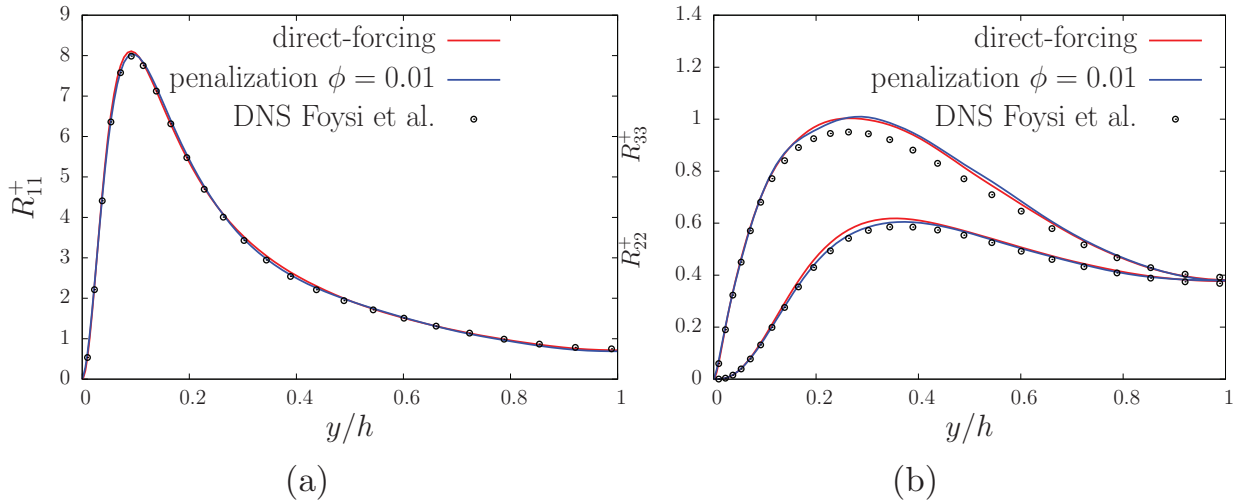


Fig. 15. Turbulent channel flow: streamwise (a), wall-normal and spanwise (b) Reynolds stress plot for the reference DNS computation [13] and both direct-forcing and penalization methods.

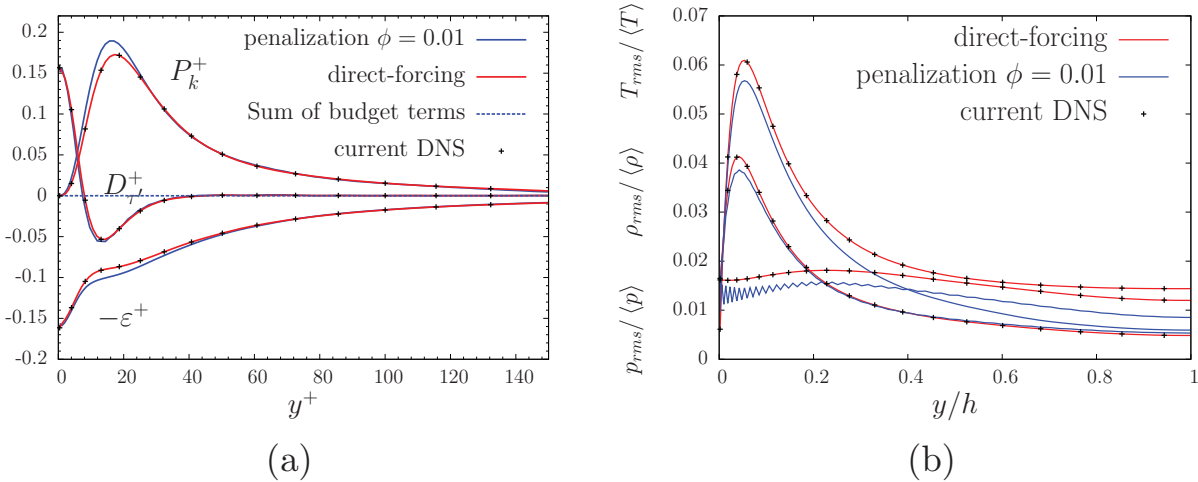


Fig. 16. Turbulent channel flow: normalized turbulent budget (a) and normalized RMS (b) plot for both direct-forcing and penalization methods. The subscript + stands for normalized wall quantities by the factor $\rho_w^+ u_w^+ / \mu_w$.

Acknowledgments

The authors would like to thank Prof. O. Vasilyev, from the University of Colorado, for fruitful discussions on the Brinkman penalization. This work was granted by the ANR (Agence Nationale de la Recherche) - MAPIE project, ANR-13-MONU-002. The first author is supported by a Ph.D. scholarship from the UK-France Ph.D. programme, jointly managed by DSTL (Defence Science and Technology Laboratory) and DGA (Direction Générale de l'Armement). The access to the European PRACE resources TGCC Curie-CEA, under allocation “2014102285”, and to the French GENCI resources, under allocation “t20152a7544”, is acknowledged.

References

[1] Angot P. Analysis of singular perturbations on the Brinkman problem for fictitious domain models of viscous flows. *Math meth appl sci* 1999;22(16):1395–412.
 [2] Angot P, Bruneau C-H, Fabrie P. A penalization method to take into account obstacles in incompressible flows. *Numer Math* 1999;81:497–520.
 [3] Arquies E, Caltagirone J. Sur les conditions hydrodynamiques au voisinage d'une interface milieu fluide-milieu poreux: application à la convection naturelle. *CR Acad Sci Paris II* 1984;299:1–4.
 [4] Ben-Dor G, Igra O, Elperin T. *Handbook of shock waves*, vol. 1. Academic Press; 2000.

[5] Boiron O, Chiavassa G, Donat R. A high-resolution penalization method for large Mach number flows in the presence of obstacles. *Comp Fluids* 2009;38(3):703–14.
 [6] Brown-Dymkoski E, Kasimov N, Vasilyev OV. A characteristic based volume penalization method for general evolution problems applied to compressible viscous flows. *J Comput Phys* 2014;262:344–57.
 [7] Bryson A, Gross R. Diffraction of strong shocks by cones, cylinders, and spheres. *J Fluid Mech* 1961;10(01):1–16.
 [8] Chaudhuri A, Hadjadj A, Chinnayya A. On the use of immersed boundary methods for shock/obstacle interactions. *J Comput Phys* 2011;230(5):1731–48.
 [9] Chaudhuri A, Hadjadj A, Chinnayya A. On the use of immersed boundary methods for shock/obstacle interactions. *J Comput Phys* 2011;230(5):1731–48.
 [10] Chaudhuri A, Hadjadj A, Sadot O, Glazer E. Computational study of shock-wave interaction with solid obstacles using immersed boundary methods. *Int J Numer Meth Eng* 2012;89(8):975–90.
 [11] Daru V, Tenaud C. Evaluation of TVD high resolution schemes for unsteady viscous shocked flows. *Comp Fluids* 2001;30:89–113.
 [12] Fadlun E, Verzicco R, Orlandi P, Mohd-Yusof J. Combined immersed-boundary finite-difference methods for three-dimensional complex flow simulations. *J Comput Phys* 2000;161(1):35–60.
 [13] Foysi H, Sarkar S, Friedrich R. Compressibility effects and turbulence scalings in supersonic channel flow. *J Fluid Mech* 2004;509:207–16.
 [14] Glass I, Kaca J, Zhang D. Shock wave diffractions over semi-circular and half-diamond cylinders. In: *Twelfth Canadian congress of applied mechanics*, vol. 1; 1989. p. 596–7.
 [15] Glazer E, Sadot O, Hadjadj A, Chaudhuri A. Velocity scaling of a shock wave reflected off a circular cylinder. *Phys Rev E* 2011;83(6):066317.
 [16] Goldstein D, Handler R, Sirovich L. Modeling a no-slip flow boundary with an external force field. *J Comput Phys* 1993;105(2):354–66.

- [17] Hirsch C. Numerical computation of internal and external flows, vol. 2. John Wiley and Sons; 1990.
- [18] Iaccarino G, Verzicco R. Immersed boundary technique for turbulent flow simulations. *Appl Mech Rev* 2003;56(3):331–47.
- [19] Jiang GS, Shu CW. Efficient implementation of weighted ENO schemes. *J Comput Phys* 1996;12:202–28.
- [20] Kadoch B, Kolomenskiy D, Angot P, Schneider K. A volume penalization method for incompressible flows and scalar advection–diffusion with moving obstacles. *J Comput Phys* 2012;231(12):4365–83.
- [21] Kevlahan NK-R, Ghidaglia J-M. Computation of turbulent flow past an array of cylinders using a spectral method with Brinkman penalization. *Eur J Mech B/Fluids* 2001;20(3):333–50.
- [22] Nguyen van yen R, Kolomenskiy D, Schneider K. Approximation of the laplace and stokes operators with dirichlet boundary conditions through volume penalization: a spectral viewpoint. *Numerische Mathematik* 2014;128(2):301–38.
- [23] Kolomenskiy D, Nguyen van yen R, Schneider K. Analysis and discretization of the volume penalized laplace operator with neumann boundary conditions. *Appl Numer Math* 2015;95:238–49.
- [24] Liu Q, Vasilyev OV. A Brinkman penalization method for compressible flows in complex geometries. *J Comput Phys* 2007;227(2):946–66.
- [25] Liu X, Osher S, Chan T. Weighted essentially non-oscillatory schemes. *J Comput Phys* 1994;115(1):200–12.
- [26] M Klein AS, Janicka J. A digital filter based generation of inflow data for spatially developing direct numerical or large eddy simulation. *J Comput Phys* 2003;186:652–65.
- [27] Majumdar S, Iaccarino G, Durbin P. Rans solvers with adaptive structured boundary non-conforming grids. In: Annual research briefs. Center for Turbulence Research, Stanford University; 2001. p. 353–466.
- [28] Mittal R, Iaccarino G. Immersed boundary methods. *Annu Rev Fluid Mech* 2005;37:239–61.
- [29] Mohd-Yusof J. Combined immersed-boundary/b-spline methods for simulations of ow in complex geometries. In: Annual Research Briefs NASA Ames Research Center. Stanford: Stanford University Center of Turbulence Research; 1997. p. 317–27.
- [30] Nam J, Lien F. A ghost-cell immersed boundary method for large-eddy simulations of compressible turbulent flows. *Int J Comput Fluid Dyn* 2014;28(1-2).
- [31] Peskin CS. Flow patterns around heart valves: a numerical method. *J Comput Phys* 1972;10(2):252–71.
- [32] Pirozzoli S. Generalized conservative approximations of split convective derivative operators. *J Comput Phys* 2010;229(19):7180–90.
- [33] Roe PL. Approximate Riemann solvers, parameter vectors, and difference schemes. *J Comput Phys* 1981;43:357–72.
- [34] Saiki E, Biringen S. Numerical simulation of a cylinder in uniform flow: application of a virtual boundary method. *J Comput Phys* 1996;123(2):450–65.
- [35] Sotiropoulos F, Yang X. Immersed boundary methods for simulating fluid–structure interaction. *Prog Aerosp Sci* 2014;65:1–21.
- [36] Taieb D. Simulation numérique des écoulements turbulents dans les canaux de refroidissement. Application aux moteurs-fusées. Université de Rouen; 2010. Ph.D. thesis.
- [37] Taieb D, Ribert G. Direct numerical simulation and large-eddy simulation of supersonic channel flow. *J Propul Power* 2013;29(5):1064–75.
- [38] Taieb D, Ribert G, Hadjadj A. DNS and LES of wall-bounded compressible turbulent flows in narrow cooling channels. In: 48th AIAA aerospace sciences meeting including the new horizons forum and aerospace exposition, vol. 638; 2010. p. 2010.
- [39] Uhlmann M. An immersed boundary method with direct forcing for the simulation of particulate flows. *J Comput Phys* 2005;209(2):448–76.
- [40] Whitham G. A new approach to problems of shock dynamics part i two-dimensional problems. *J Fluid Mech* 1957;2(02):145–71.
- [41] Yang J, Liu Y, Lomax H. Computation of shock wave reflection by circular cylinders. *AIAA J* 1987;25(5):683–9.
- [42] Zóltak J, Drikakis D. Hybrid upwind methods for the simulation of unsteady shock-wave diffraction over a cylinder. *Comput Methods Appl Mech Eng* 1998;162(1):165–85.

List of Figures

1.1	Rocket engine diagram	2
1.2	Nozzle flow regime during flight.	3
1.3	Ariane 5 launch.	3
1.4	Shock patterns in over-expanded nozzle flow; S: separation, SS: separated shock, RS: reflected shock, TP: triple point, IS: internal shock, MS: Mach stem, RB: recirculation bubbles, J: supersonic jet, SL: slip line.	5
1.5	Typical wall-pressure distribution (<i>left</i>) and schematic representation of SWBLI (<i>right</i>); I: start of interaction, S: separation point, P: plateau point, R: reattachment point, L_s : separation length.	7
1.6	Typical rms wall-pressure distribution.	8
1.7	Topology of shock unsteadiness in over-expanded nozzle flow (FSS).	9
1.8	Representation of Kelvin-Helmholtz instability observed downstream of the separation over an airfoil; Extracted from Yarusevych et al. (2006).	11
1.9	Representation of the recirculating area captured in a backward facing step; Extracted from Rajasekaran (2011).	12
1.10	Parametric study of the flange width effects on lip vortices; Extracted from Olson & Lele (2013).	13
2.1	Transformation between physical and computational space.	21
2.2	Strong scaling on the TGCC-Curie with a constant grid of 16.7 millions cells.	33
2.3	Weak scaling on the TGCC-Curie with a constant grid size per process of 48^3	33
2.4	Immersed Boundary Method for a pipe geometry; Black, grey and white color represent pure solid cells, ghost cells and fluid cells, respectively.	35
2.5	Bi-linear interpolation for the IBM demonstrating the two interpolations method (ghost cells close to the wall).	35
2.6	Representation of the domain decomposition method showing every 5th grid line.	41

2.7	Global discretization of the DD method; <i>Orange</i> : overlapping ghost point from subdomain Ω_1 , <i>Yellow</i> : overlapping ghost point from subdomain Ω_2 .	41
2.8	Example of MPI discretization of the DD method; <i>Orange</i> : overlapping ghost point from subdomain Ω_1 , <i>Yellow</i> : overlapping ghost point from subdomain Ω_2 .	42
2.9	Example of <i>Send/Recv</i> request for the DD method. View from process 3.	43
3.1	Grid of the vortex test case	46
3.2	Comparison of centered schemes with different order of accuracy; $-$: 2th order, $-$: 4th order, $-$: 6th order, $-$: 8th order, \cdot : Exact solution.	47
3.3	Grid of the cylindrical vortex test case (<i>left</i>) and shifted pressure distribution at different time step (<i>right</i>); $-$: $t^* = 0$, $-$: $t^* = 5.9$, $-$: $t^* = 11.8$.	48
3.4	Pressure field contour at different time step.	49
3.5	Grid of the compressible flow over a circular cylinder test case	50
3.6	Mach number contours; <i>Left</i> : current simulation, <i>Right</i> : Burbeau & Sagaut (2002)	51
3.7	Grid representation for Mesh 1 (<i>left</i>) and Mesh 2 (<i>right</i>) showing every 4th grid-line	52
3.8	Streamwise velocity solution (<i>left</i>) and temperature solution (<i>right</i>) along the spanwise direction; $-$: Poiseuille analytical solution, \bullet : Mesh 1, \times : Mesh 2.	52
3.9	Configuration of the channel flow.	53
3.10	Averaged velocity profile along the wall-normal direction; \bullet : H. Foysi & Friedrich (2004).	54
3.11	Averaged temperature ($-$), pressure ($-$) and density ($-$) profile along the wall-normal direction; \bullet : H. Foysi & Friedrich (2004).	54
3.12	Van Driest velocity profile along the wall-normal direction; \bullet : H. Foysi & Friedrich (2004), $--$: viscous sublayer and logarithmic law.	55
3.13	Instantaneous contours in the x - y plane at $z = L_z/2$; <i>Top left</i> : Streamwise velocity, <i>Top right</i> : Temperature, <i>Bottom left</i> : Pressure, <i>Bottom right</i> : Mach number.	56
3.14	Scatter plots of different fluctuating quantities at different y^+ . <i>Left</i> : Temperature fluctuation; <i>Right</i> : Density fluctuation, <i>Top</i> : $y^+ \sim 1$, <i>Middle</i> : $y^+ \sim 10$, <i>Bottom</i> : $y^+ \sim 200$.	57
3.15	Instantaneous contours of the fluctuating streamwise velocity in x - z plane at $t^* \approx 150$ for different y^+	58
3.16	Outer/inter process interaction near the wall	59

3.17 Reynolds stress tensor along y-direction along the wall-normal direction; $-\cdot$: $\langle \rho \rangle \widetilde{u''u''}/\tau_w$, $-$: $\langle \rho \rangle \widetilde{v''v''}/\tau_w$, $-$: $\langle \rho \rangle \widetilde{w''w''}/\tau_w$, \bullet : H. Foysi & Friedrich (2004).	59
3.18 Velocity profiles with the Van Driest transformation; $-$: channel flow, $-$: pipe flow.	63
3.19 Profiles of $\gamma^+ = y^+(du^+/dy^+)$ according to the log-law definition (<i>left</i>) and $\beta^+ = (y^+/u^+)(du^+/dy^+)$ according to the power-law definition (<i>right</i>); Line types as in figure 3.18.	63
3.20 Averaged temperature (<i>left</i>) and pressure (<i>right</i>) along the wall-normal direction; Line colors as in figure 3.18, \bullet : Channel flow of Foysi et al. (2004).	64
3.21 Reynolds stress tensor along the wall-normal direction, streamwise (<i>left</i>), wall-normal and spanwise (<i>right</i>); Line colors as in figure 3.18, $--$: R_{22}^+	65
3.22 Shear stress tensor along the wall-normal direction; Line colors as in figure 3.18; $-$: $-R_{12}^+$; $---$: $\frac{\langle \mu \rangle}{\mu_w} \frac{\partial u^+}{\partial y^+}$	65
3.23 Normalized pressure rms ($--$) and temperature rms ($-$); Line colors as in figure 3.18.	65
3.24 Energy transfer of compressible turbulent flow between internal, mean kinetic and turbulent kinetic energy. The dashed lines represent the compressible terms.	66
3.25 Turbulent kinetic budget; Line colors as in figure 3.18; $-$: P_k^+ , $---$: D_k^+ , $- \cdot -$: ε_k^+	67
3.26 Compressible terms of TKE; Line colors as in figure 3.18; $-$: C_{k1}^+ , $---$: C_{k2}^+ , $- \cdot -$: C_{k3}^+	67
3.27 Grid representation for the cartesian coordinates (IBM) showing every 9th grid-lines (<i>left</i>), the fully-cylindrical coordinates showing every 4th grid-lines (<i>middle</i>) and the DD method showing every 3rd grid-lines (Ω_1) and 4th grid-lines (Ω_2) (<i>right</i>).	69
3.28 Mean velocity (<i>left</i>) and mean temperature (<i>right</i>) profile along the wall-normal direction; $-$: DD method ($-$: Ω_1 and $-$: Ω_2), $-$: Fully-cylindrical method, \bullet : Ghosh et al. (2010).	69
3.29 Normalized Reynolds stress tensor along the wall-normal direction; Line colors as in figure 3.28, $-$: R_{11}^+ , $--$: R_{22}^+ , $- \cdot -$: R_{33}^+	70
4.1 Computational domain for the DNS of the transition laminar/turbulent, perturbation model extends from $x = 4.5''$ to $x = 5''$	72
4.2 Side view of Mach number contour field; Linear black/blue colormap from $M = 0$ to $M = 2.25$, reverse linear colormap for $A - A$ view.	73

4.3	Mach number contour field at $y^+ = 15$ at different x -locations; <i>top</i> : closed to the perturbation model, <i>middle</i> : at the transition, <i>bottom</i> : in the fully-turbulent zone; Linear blue/black colormap from $M = 0$ to $M = 1$	73
4.4	Friction coefficient along the x -direction for different convective schemes; $-$: Hybrid scheme, $-$: WENO-5th, $-$: Centered-6th, $-$: Pirozzoli et al. (2004), \bullet : Theoretical friction coefficient.	75
4.5	Friction coefficient along the x -direction for different parameters of the perturbation model; $-$: $A = 0.04$ and $f = 75$ kHz, $-$: $A = 0.08$ and $f = 75$ kHz, $-$: $A = 0.04$ and $f = 150$ kHz, $-$: Pirozzoli et al. (2004), \bullet : Theoretical friction coefficient.	75
4.6	Van Driest normalized velocity at $Re_x = 5 \times 10^6$; \bullet : Pirozzoli et al. (2004), \blacksquare : Gatski & Erlebacher (2002), $-$: Log-wall with $C^+ = 5.5$	76
4.7	Averaged temperature at $Re_x = 5 \times 10^6$; \bullet : Pirozzoli et al. (2004).	77
4.8	Averaged pressure at $Re_x = 5 \times 10^6$	77
4.9	Streamwise, wall-normal and spanwise Reynolds stress tensor (<i>left</i>) and normalized shear tensor terms (<i>right</i>) at $Re_x = 5 \times 10^6$; \bullet : Pirozzoli et al. (2004).	77
4.10	Turbulent kinetic energy budget at $Re_x = 5 \times 10^6$; \bullet : Pirozzoli et al. (2004).	77
4.11	Temperature field contour (Case 1) (<i>top</i>) and associated diagram of shock pattern (<i>bottom</i>).	80
4.12	Mach number field contour in the x - y plane; <i>top</i> : strong pressure gradient (Case 1), <i>bottom</i> : moderate pressure gradient (Case 2).	81
4.13	Additional force distribution along the x -direction; $-$: Case 1, $-$: Case 2	82
4.14	Navier-Stokes terms in the freestream zone along the x -direction (Case 2); $-$: $d\bar{p}/dx$, $-$: $d\bar{\rho}\bar{u}\bar{u}/dx$, $-$: $d\bar{p}/dx + d\bar{\rho}\bar{u}\bar{u}/dx$	83
4.15	Friction coefficient along the x -direction; Line types as in figure 4.13.	83
4.16	Pressure gradient parameter along the x -direction.	84
4.17	Van Driest velocity along the wall-normal direction; $-$: zero-pressure gradient $\Delta p^+ = 0$, $-$: adverse pressure gradient $\Delta p^+ = 0.0075$, $-$: favorable pressure gradient $\Delta p^+ = -0.0025$	85
4.18	Non-dimensional parameter γ^+ along the wall-normal direction; Line types as in figure 4.17	86
4.19	Log-law coefficient κ^+ (<i>left</i>) and C^+ (<i>right</i>) computed at $y^+ = 100$ along the x -direction.	86
4.20	Log-law coefficients K_i (<i>left</i>) and C_i (<i>right</i>) at $y^+ = 100$ along the pressure parameter Δp^+ in the ZPG and APG region.	87

4.21	Modified non-dimensional parameter γ_{mod}^+ along the wall-normal direction; Line types as in figure 4.17	88
4.22	Van Driest velocity along the y -direction; Line types as in figure 4.17, --- : Modified log-law (McDonald 1969).	89
4.23	Modified log-law coefficient κ_{mod}^+ (<i>left</i>) and C_{mod}^+ (<i>right</i>) at $y^+ = 100$ along the x -direction.	89
4.24	Van Driest velocity field u_{VD}^+ in x - y plane	90
4.25	Representation of the STBLE model coupling with LES compared to DNS.	94
4.26	Wall-shear stress over time with zero-pressure gradient (<i>left</i>) and adverse pressure gradient (<i>right</i>); —: Wall-resolved data, —: Reconstructed data using the STBLE model.	94
4.27	Van Driest velocity along the wall-normal direction with zero-pressure gradient (<i>left</i>) and adverse pressure gradient (<i>right</i>); —: Wall-resolved data (: Subtracted data), •: Reconstructed data using the STBLE model showing every 4th-grid line.	95
4.28	Normalized velocity along the wall-normal direction, zero-pressure gradient (<i>left</i>) and adverse pressure gradient (<i>right</i>); —: WM-LES, —: DNS.	98
4.29	Normalized velocities RMS along the wall-normal direction, zero-pressure gradient (<i>left</i>) and adverse pressure gradient (<i>right</i>); —: WM-LES, —: DNS.	98
5.1	Schematic of the planar nozzle test section from Papamoschou & Johnson (2006).	102
5.2	Schematic representation of the planar nozzle flow.	104
5.3	Grid representation from the Wall-Resolved case showing every 10th grid-line.	105
5.4	Separation location vs. time; —: Upper wall, —: Lower wall.	108
5.5	Asymmetric parameter $x_s^{\text{top}}/x_s^{\text{bottom}}$ (—) and dimensionless separation velocity speed $u_s/u_{i,\infty}$ (—) over time.	108
5.6	z -averaged numerical “Schlieren” imaging contour $ \nabla\rho $ in the x - y plane at different times.	109
5.7	Longitudinal pressure distribution at the nozzle centerline (<i>left</i>) and pressure distribution at the lower wall (<i>right</i>); —: Total time average, —: Conditional averaging $x_s/\delta_i \sim 0$, -- : Conditional averaging showing the maximal position $x_s/\delta_i \sim 10$, -·-: Conditional averaging showing the minimal position $x_s/\delta_i \sim -10$, •: WR-LES from Olson & Lele (2011), ■: Experimental results from Johnson & Papamoschou (2010).	110
5.8	Wall-unit length Δy^+ at the first cell near the wall along the x -direction.	111

5.9	Normalized boundary layer thicknesses along the x -direction; $-$: boundary-layer thickness δ/δ_i (at 99%), $-$: momentum thickness θ/θ_i , $-$: displacement thickness δ^*/δ_i^*	111
5.10	Instantaneous velocity fluctuations in the x - z plane at $y^+ \sim 20$	112
5.11	Normalized pressure gradient along the x -direction; $-$: present LES, $-$: WR-LES from Olson & Lele (2011), \blacksquare : Experimental results from Johnson & Papamoschou (2010).	112
5.12	Van Driest velocity along the wall-normal direction at $x/\delta_i = -10$; $-$: $u^+ = y^+$ and the log-law with $\kappa = 0.41$ and $C^+ = 6.2$, $-$: present LES, \bullet : WR-LES from Olson & Lele (2011).	112
5.13	Normalized rms velocities along the wall-normal direction at $x/\delta_i = -10$; $-$: u_{rms}^+ , $-$: v_{rms}^+ , $-$: w_{rms}^+ , \bullet : WR-LES from Olson & Lele (2011).	113
5.14	Normalized rms x -velocity u_{rms}^+ along the wall-normal direction at $x/\delta_i = -10$; $-$: Present DNS, $-$: WR-LES from Olson & Lele (2011), DNS from Spalart & Watmuff (1993) at \blacksquare : throat, \blacksquare : FPG.	113
5.15	Two-point correlations function of wall pressure fluctuations along the span-wise direction at $x/\delta_i = 0$; $-$: Results at different x -location in the pre-shock boundary layer zone, \bullet : WR-LES from Olson & Lele (2011).	114
5.16	Pre-multiplied power spectral density of the two-point pressure fluctuations correlation function; $-$: at the throat, $-$: in the separated shear layer.	114
5.17	Normalized pressure forces over time; $-$: x -direction (F_x), $-$: y -direction (F_y).	114
5.18	Angle of the resultant pressure force \vec{F} on the nozzle wall in degrees ($-$) and lower-wall separation location x_s/δ_i ($-$).	114
5.19	Representation of the lambda shock pattern (<i>left</i>) and the separation area (<i>right</i>); <i>MS</i> : Mach stem, <i>IS</i> : incident shock or separated shock, <i>RS</i> : reflected shock, <i>TP</i> : triple point, <i>SL</i> : slip line, <i>SJ</i> : supersonic jet, <i>s</i> : separation location, <i>I</i> : interaction location.	116
5.20	Representation of the shock pattern at $t^* = 1456$ when the shock is moving downstream (<i>left</i>) and at $t^* = 1692$ when the shock is moving upstream (<i>right</i>); Subscript as in figure 5.19, <i>CW</i> : compression waves, <i>RB</i> : recirculation bubbles.	117
5.21	Mean Mach number $\langle M \rangle$ contour in the x - y plane.	118
5.22	Mean temperature $\langle T \rangle / T_a$ contour in the x - y plane.	118
5.23	Mean wall-normal velocity $\langle v \rangle / u_{i,\infty}$ contour in the x - y plane.	118
5.24	Mean pressure $\langle p \rangle / p_a$ contour in the x - y plane.	118
5.25	Rms velocity $u_{rms} / u_{i,\infty}$ contour in the x - y plane.	119

5.26	Instantaneous velocity fluctuations contour for the upper wall (<i>top</i>) and the lower wall (<i>bottom</i>) in the x - z plane at $y^+ \sim 5$ when the shock is moving downstream, <i>i.e.</i> $u_s > 0$ ($t^* = 1456$).	120
5.27	Instantaneous velocity fluctuations contour for the upper (<i>top</i>) and lower walls (<i>bottom</i>) in the x - z plane at $y^+ \sim 5$ when the shock is moving upstream, <i>i.e.</i> $u_s < 0$ ($t^* = 1692$).	120
5.28	Representation of the shock locator (<i>left</i>) and diagram of the wall-model implementation in curvilinear coordinates (<i>right</i>).	123
5.29	Separation location over time; $-$: Upper wall, $-$: Lower wall.	124
5.30	Asymmetry parameter $x_s^{\text{top}}/x_s^{\text{bottom}}$ ($-$) and shock speed $u_s/u_{i,\infty}$ ($-$) over time.	124
5.31	Pressure distribution at the center of the nozzle (<i>left</i>) and pressure distribution at the lower wall (<i>right</i>) along the x -direction; $-$: WM-LES (conditional averaging at $x_s/\delta_i \sim 0$), $-$: WR-LES (conditional averaging at $x_s/\delta_i \sim 0$), \bullet : WR-LES from Olson & Lele (2011), \blacksquare : Experimental results from Johnson & Papamoschou (2010).	125
5.32	Normalized pressure gradient along the x -direction; $-$: WM-LES, $-$: WR-LES, \bullet : WR-LES from Olson & Lele (2011), \blacksquare : Experimental results from Johnson & Papamoschou (2010).	125
5.33	Van Driest velocity along the wall-normal direction at $x/\delta_i = -10$; $-$: WM-LES, $--$: WR-LES, $--$: $u^+ = y^+$ and the log-law with $\kappa = 0.41$ and $C^+ = 6.2$, \bullet : WR-LES from Olson & Lele (2011).	125
5.34	Normalized forces for the WM-LES; $-$: x -direction (F_x), $-$: y -direction (F_y). 127	
5.35	Comparison of forces between WM-LES ($-$) and WR-LES (\bullet); Line colors as in figure 5.34.	127
5.36	Pre-multiplied spectra of the normalized fluctuating forces in x -direction (<i>left</i>) and y -direction (<i>right</i>); $-$: WM-LES, $-$: WR-LES.	127
5.37	Normalized pre-multiplied spectra of the pressure fluctuations at the wall in the incoming boundary layer, <i>i.e.</i> $x/\delta_i = 0$	129
5.38	Normalized pre-multiplied spectra of the pressure fluctuations at the exit of the nozzle, <i>i.e.</i> $x/\delta_i \sim 66$; $-$: lower wall, $-$: upper wall.	129
5.39	Normalized pre-multiplied spectra of the pressure fluctuations $St \mathcal{F}(p'/p_{rms})^*$ at the lower wall along the x -direction.	130
5.40	Space-time correlation of the normalized pressure field in the boundary layer centered at $x/\delta_i = 0$	130
5.41	Space-time correlation of the normalized pressure field in the separated zone at the upper (<i>left</i>) and lower wall (<i>right</i>).	130

5.42	z -averaged numerical ‘‘Schlieren’’ pictures contour $ \nabla\rho $ in the x - y plane at different times.	132
5.43	Highlight of the delay phenomenon between the effective exit area A_e^* (–) and the separation location x_s (–).	134
5.44	Highlight of the anti-correlation between the exit pressure p_e (–) and the separation location x_s (–).	134
5.45	Shock excursion over one resonant tone period St_1 for different time step using the WR-LES; z -averaged Schlieren pictures are shown in grayscale, blue regions highlight negative x -velocity, orange arrows represent the velocity of the shock, black arrows the backflow and purple arrows the suction effect from the ambient pressure.	136
5.46	Averaged Mach number $\langle M \rangle$ contour in the x - y plane.	136
5.47	Averaged temperature $\langle T \rangle / T_a$ contour in the x - y plane.	137
5.48	Averaged wall-normal velocity $\langle v \rangle / u_{i,\infty}$ contour in the x - y plane.	137
5.49	Averaged pressure $\langle p \rangle / p_a$ contour in the x - y plane.	137
5.50	Rms velocity $u_{rms} / u_{i,\infty}$ contour in the x - y plane.	138
5.51	Planar WR-LES: The separated shock is moving upstream towards the throat, MS: Mach stem, SS: separated shock, RS: reflected shock; grayscale surface: Schlieren imaging in the x - y plane, grayscale volume: iso-volume of $\nabla u $, jet color: iso-contour of Q criterion colored by the velocity field (blue: slow, red: fast).	139
5.52	Planar WR-LES: The separated shock is moving downstream towards the exit; for the legend see figure 5.51.	140
6.1	Grid representation from the Wall-Resolved case showing every 10th grid-line from half of the domain in z -direction or θ -direction. <i>Top</i> : Internal mesh Ω_1 (cartesian coordinates), <i>Bottom</i> : External mesh Ω_2 (cylindrical coordinates)	144
6.2	Van Driest velocity profiles along the wall-normal direction at $x/\delta_i = -10$; –: cylindrical WR-LES, –: planar WR-LES, --: $u^+ = y^+$ and the log-law.	145
6.3	WR-LES: Normalized Reynolds stress along the wall-normal direction at $x/\delta_i = -10$; –: R_{11}^+ , –: R_{22}^+ , –: R_{33}^+ , --: planar WR-LES.	145
6.4	WR-LES: Normalized velocity RMS along the wall-normal direction at $x/\delta_i = -10$; –: u_{rms}^+ , –: v_{rms}^+ , –: w_{rms}^+ , -: planar WR-LES.	146
6.5	WR-LES: Normalized shear stress, turbulent (–) and viscous (–) terms, along the wall-normal direction at $x/\delta_i = -10$; --: planar WR-LES.	146
6.6	WR-LES: Instantaneous velocity fluctuations in x - θ plane at $y^+ \sim 20$	146

6.7	WR-LES: Boundary layer thickness along the x -direction; —: planar WR-LES, —: cylindrical WR-LES.	147
6.8	WR-LES: Normalized pressure gradient along the x -direction; —: planar WR-LES, -- : planar WR-LES from Olson & Lele (2011), —: cylindrical WR-LES, ■: planar experimental results from Johnson & Papamoschou (2010).	147
6.9	WR-LES: Wall-unit length Δy^+ at the first near-wall cell along the x -direction; —: planar WR-LES, —: cylindrical WR-LES.	148
6.10	Normalized wall pressure along the x -direction; —: WM-LES, —: WR-LES.	148
6.11	WM-LES: Normalized pressure RMS at the wall along the x -direction.	148
6.12	Normalized pressure RMS centered in the separation area; —: present WM-LES, -- : theoretical function.	148
6.13	Separation location over time; —: WM-LES, —: WR-LES.	149
6.14	Normalized pre-multiplied spectrum of the separation location from the time-resolved WM-LES.	149
6.15	WM-LES: Forces over time; —: streamwise direction F_x , —: wall-normal direction $F_{\vec{n}}$	151
6.16	WM-LES: Polar plot of the side-loads over time.	151
6.17	WM-LES: Normalized pre-multiplied spectrum of the streamwise force $F_x/F_{x,rms}$	152
6.18	WM-LES: Normalized pre-multiplied spectra of the side-loads; —: $F_y/F_{y,rms}$, —: $F_z/F_{z,rms}$	152
6.19	Probability Density Function of the side-loads $F_{\vec{n}}$; —: current WM-LES, -- : Rayleigh distribution, ●: experiment from Deck & Nguyen (2004), ■: URANS from Deck & Nguyen (2004).	152
6.20	WM-LES: Normalized pre-multiplied spectra of the pressure field at the wall; —: in the incoming boundary layer $x/\delta_i = 0$, —: at the separation $x/\delta_i \sim 37.1$, —: at the exit $x/\delta_i = 66$	152
6.21	WM-LES: Frequency analysis in the x - y plane showing the Strouhal number associated with the maximal energy extracted from the normalized pressure field spectra $\mathcal{F}(p'/p_{rms})$; boundary-layer turbulence ($St \sim 1$), mixing layer unsteadiness ($St \sim 0.1$), trailing-edge noises ($St \sim 0.04$), recirculation bubbles ($St \sim 0.016$), resonant tone ($St \sim 0.0067$).	154
6.22	WM-LES: Normalized pressure fluctuations spectra $St\mathcal{F}(p'_w/p_{rms})^*$ along x -direction.	155
6.23	WR-LES: Averaged Mach number $\langle M \rangle$ contour in the x - y plane.	155
6.24	WR-LES: Averaged temperature $\langle T \rangle/T_a$ contour in the x - y plane.	155

6.25	WR-LES: Averaged pressure $\langle p \rangle / p_a$ contour in the x - y plane.	156
6.26	WR-LES: RMS velocity $u_{rms} / u_{i,\infty}$ contour in the x - y plane.	156
6.27	WR-LES: Instantaneous density gradient contour $\nabla \rho$ (<i>top</i>) and temperature field (<i>top</i>) in the x - y plane at $t^* = 1025$	156
6.28	WR-LES: Instantaneous temperature contour T in the x - y plane (<i>top</i>) and in the θ - r plane (<i>bottom</i>) for different x -position: in the upstream boundary layer, at the separation, downstream of separation and at the exit (<i>from left to right</i>).	157
6.29	WM-LES: Averaged Mach number $\langle M \rangle$ contour in the x - y plane.	157
6.30	WM-LES: Averaged temperature $\langle T \rangle / T_a$ contour in the x - y plane.	157
6.31	WM-LES: Averaged pressure $\langle p \rangle / p_a$ contour in the x - y plane.	158
6.32	WM-LES: RMS velocity $u_{rms} / u_{i,\infty}$ contour in the x - y plane.	158
6.33	WM-LES: Instantaneous density gradient contour $\nabla \rho$ (<i>top</i>) and temperature field (<i>top</i>) in the x - y plane at $t^* = 8190$	158
6.34	Cylindrical WR-LES: iso-contour of Q criterion colored by the velocity field (blue: slow, red: fast); MS: Mach stem, SS: separated shock, RS: reflected shock, A_e^* : effective exit area; grayscale surface: Schlieren imaging at $\theta = 0$, white volume: iso-volume of $\nabla u $	159
6.35	Cylindrical WR-LES: 3D representation of the different phenomenon observed in cylindrical nozzle flow; legend as in figure 6.34, box 2: iso-contour of temperature $T/T_\infty \sim 0.9$ colored by velocity (blue/black) and streamline near the nozzle lip (yellow), box 3: jet color represents the supersonic field while b/w color represents the subsonic part.	160
A.1	2D grid representation of the planar nozzle flow with the ambient domain.	166
A.2	Grid representation of the planar nozzle flow in the x - y direction showing the exit of the nozzle.	167
A.3	Grid representation of the cylindrical nozzle showing the internal mesh Ω_1 and the contour of the external mesh Ω_2	169
A.4	Grid representation of the planar cylindrical showing both internal Ω_1 and external Ω_2 meshes; View of the ambient domain.	170
A.5	Grid representation of the cylindrical nozzle showing half-domain of the external mesh Ω_2 and the contour of the internal mesh Ω_1	171
A.6	Grid representation of the cylindrical nozzle showing half-domain of the external mesh Ω_2 and the contour of the internal mesh Ω_1 ; View from the inlet.	172

B.1	WM-LES: Normalized pre-multiplied spectrum of the non-filtered separation location from the time-resolved WM-LES; —: original data, —: with NSCBC.	176
-----	--	-----

List of Tables

2.1	Strong scalability test of the curvilinear code.	32
2.2	Grid size per process scaling.	32
2.3	Weak scaling test of the curvilinear code	33
3.1	Channel flow domain properties	53
3.2	Channel flow properties	54
3.3	Computational domains and grids	62
3.4	Flow parameters for channel/pipe flows	62
3.5	Differences between the pipe flow from section 3.5.1 and Ghosh et al. (2010) simulation.	67
3.6	Details of computational domains and time step values.	68
4.1	Pressure gradient specifications for each case.	79
4.2	Results of the <i>a priori</i> test using the DNS of section 4.2.	95
4.3	Grid requirements for the WM-LES	96
5.1	The geometrical parameters of Papamoschou et al.'s planar nozzle.	102
5.2	Grid parameters for the WR-LES of the planar nozzle flow.	105
5.3	Physical parameters for the WR-LES of the planar nozzle flow.	106
5.4	Grid parameters for the WM-LES of the planar nozzle flow.	121
5.5	Results of the planar WM-LES compared to WR-LES.	124
5.6	Averaged/rms forces of the planar WM-LES compared to WR-LES scaled by the isentropic normal force.	126
6.1	Grid parameters of the cylindrical nozzle flows.	143
6.2	Averaged/rms forces of the cylindrical WM-LES compared to WR-LES scaled by the isentropic normal force.	151
6.3	Effects of different nozzle unsteadiness.	154
A.1	Grid parameters of the planar nozzle.	168
A.2	Grid parameters of the planar nozzle.	168

- B.1 Wave amplitude treatment for various non-reflecting boundary conditions.
Wave subscript 1 corresponds to $u - c$ wave, 2-4 to u and 5 to $u + c$ 176

Bibliography

- Abu-Ghannam, B. & Shaw, R. (1980), ‘Natural transition of boundary layers - the effects of turbulence, pressure gradient, and flow history’, *Journal of Mechanical Engineering Science* **22**(5), 213–228. (Cited on page 78).
- Adrian, R., Meinhart, C. & Tomkins, C. (2000), ‘Vortex organization in the outer region of the turbulent boundary layer’, *Journal of Fluid Mechanics* **422**, 1–54. (Cited on page 10).
- Alving, A. E. & Fernholz, H. (1995), ‘Mean-velocity scaling in and around a mild, turbulent separation bubble’, *Physics of Fluids (1994-present)* **7**(8), 1956–1969. (Cited on page 83).
- Arens, M. & Spiegler, E. (1963), ‘Shock-induced boundary layer separation in over-expanded conical exhaust nozzles’, *AIAA Journal* **1**(3), 578–581. (Cited on page 7).
- Baars, W. & Tinney, C. (2013), ‘Transient wall pressures in an overexpanded and large area ratio nozzle’, *Experiments in Fluids* **54**(2), 1–17. (Cited on page 7).
- Balaras, E., Benocci, C. & Piomelli, U. (1996), ‘Two-layer approximate boundary conditions for large-eddy simulations’, *AIAA journal* **34**(6), 1111–1119. (Cited on page 92).
- Barenblatt, G., Chorin, A. & Prostokishin, V. (1997), ‘Scaling laws for fully developed turbulent flow in pipes’, *Applied Mechanics Reviews* **50**(7), 413–429. (Cited on pages 61, 62 & 143).
- Ben-Dor, G., Ivanov, M., Vasilev, E. & Elperin, T. (2002), ‘Hysteresis processes in the regular reflection, \hat{U} mach reflection transition in steady flows’, *Progress in Aerospace Sciences* **38**(4), 347–387. (Cited on page 5).
- Boccaletto, L. (2011), Maîtrise du décollement de tuyère. Analyse du comportement d’une tuyère de type TOC et définition d’un nouveau concept: le BOCCAJET, PhD thesis, Aix Marseille 1. (Cited on page 12).

- Bodony, D. J. & Lele, S. K. (2008), ‘Current status of jet noise predictions using large-eddy simulation’, *AIAA journal* **46**(2), 364–380. (Cited on page 152).
- Bogar, T., Sajben, M. & Kroutil, J. (1983), ‘Characteristic frequencies of transonic diffuser flow oscillations’, *AIAA journal* **21**(9), 1232–1240. (Cited on pages 6, 15, 129 & 131).
- Brown, G. L. & Roshko, A. (1974), ‘On density effects and large structure in turbulent mixing layers’, *Journal of Fluid Mechanics* **64**(04), 775–816. (Cited on page 10).
- Brown, K. & Joubert, P. (1969), ‘The measurement of skin friction in turbulent boundary layers with adverse pressure gradients’, *Journal of Fluid Mechanics* **35**(04), 737–757. (Cited on page 85).
- Bühler, S., Kleiser, L. & Bogey, C. (2014), ‘Simulation of subsonic turbulent nozzle jet flow and its near-field sound’, *AIAA Journal* **52**(8), 1653–1669. (Cited on pages 152 & 153).
- Burbeau, A. & Sagaut, P. (2002), ‘Simulation of a viscous compressible flow past a circular cylinder with high-order discontinuous galerkin methods’, *Computers & Fluids* **31**(8), 867–889. (Cited on pages 49, 51 & 200).
- Cabot, W. & Moin, P. (2000), ‘Approximate wall boundary conditions in the large-eddy simulation of high Reynolds number flow’, *Flow, Turbulence and Combustion* **63**(1–4), 269–291. (Cited on pages 90 & 95).
- Chapman, D. R., Kuehn, D. M. & Larson, H. K. (1958), ‘Investigation of separated flows in supersonic and subsonic streams with emphasis on the effect of transition’. (Cited on pages 7 & 131).
- Chen, C., Chakravarthy, S. & Hung, C. (1994), ‘Numerical investigation of separated nozzle flows’, *AIAA journal* **32**(9), 1836–1843. (Cited on pages 6 & 7).
- Chpoun, A., Passerel, D., Li, H. & Ben-Dor, G. (1995), ‘Reconsideration of oblique shock wave reflections in steady flows. part 1. experimental investigation’, *Journal of Fluid Mechanics* **301**, 19–35. (Cited on page 5).
- Clemens, N. T. & Narayanaswamy, V. (2014), ‘Low-frequency unsteadiness of shock wave/turbulent boundary layer interactions’, *Annual Review of Fluid Mechanics* **46**, 469–492. (Cited on page 15).
- Coles, D. (1968), The young person’s guide to the data, Technical report, DTIC Document. (Cited on page 85).

- Constantinescu, G. S. & Lele, S. (2002), ‘A highly accurate technique for the treatment of flow equations at the polar axis in cylindrical coordinates using series expansions’, *Journal of Computational Physics* **183**(1), 165–186. (Cited on page 39).
- Damgaard, T., Östlund, J. & Frey, M. (2004), ‘Side-load phenomena in highly overexpanded rocket nozzles’, *Journal of Propulsion and Power* **20**(4), 695–704. (Cited on page 115).
- Deck, S. (2009), ‘Delayed detached eddy simulation of the end-effect regime and side-loads in an overexpanded nozzle flow’, *Shock Waves* **19**(3), 239–249. (Cited on page 16).
- Deck, S. & Nguyen, A. T. (2004), ‘Unsteady side loads in a thrust-optimized contour nozzle at hysteresis regime’, *AIAA journal* **42**(9), 1878–1888. (Cited on pages 150, 152 & 207).
- Deng, X. & Zhang, H. (2000), ‘Developing high-order weighted compact nonlinear schemes’, *Journal of Computational Physics* **165**(1), 22–44. (Cited on pages 27 & 28).
- Ducros, F., Ferrand, V., Nicoud, F., Weber, C., Darracq, D., Gacherieu, C. & Poinso, T. (1999), ‘Large-eddy simulation of the shock/turbulence interaction’, *Journal of Computational Physics* **152**(2), 517–549. (Cited on page 29).
- Dumnov, G. et al. (1996), Unsteady side-loads acting on the nozzle with developed separation zone, in ‘32nd Joint Propulsion Conference and Exhibit, AIAA Paper’, number 96-3220. (Cited on page 150).
- Dupont, P., Haddad, C. & Debiève, J. (2006), ‘Space and time organization in a shock-induced separated boundary layer’, *Journal of Fluid Mechanics* **559**, 255–277. (Cited on pages 8, 9, 12, 15, 151 & 153).
- Duprat, C., Balarac, G., Métais, O., Congedo, P. M. & Brugière, O. (2011), ‘A wall-layer model for large-eddy simulations of turbulent flows with/out pressure gradient’, *Physics of Fluids (1994-present)* **23**(1), 015101. (Cited on pages i, ii, 91, 93, 95, 97 & 99).
- Dussauge, J.-P. & Piponniau, S. (2008), ‘Shock/boundary-layer interactions: Possible sources of unsteadiness’, *Journal of Fluids and Structures* **24**(8), 1166–1175. (Cited on page 10).
- Eaton, J. & Johnston, J. (1981), ‘A review of research on subsonic turbulent flow reattachment’, *AIAA journal* **19**(9), 1093–1100. (Cited on page 12).

- Eckhardt, B., Schneider, T. M., Hof, B. & Westerweel, J. (2007), ‘Turbulence transition in pipe flow’, *Annu. Rev. Fluid Mech.* **39**, 447–468. (Cited on page 143).
- Eggels, J., Unger, F., Weiss, M., Westerweel, J., Adrian, R., Friedrich, R. & Nieuwstadt, F. (1994), ‘Fully developed turbulent pipe flow: a comparison between direct numerical simulation and experiment’, *Journal of Fluid Mechanics* **268**, 175–210. (Cited on pages 60, 142 & 143).
- Eggels, J., Westerweel, J., Nieuwstadt, F. & Adrian, R. (1993), ‘Direct numerical simulation of turbulent pipe flow’, *Applied Scientific Research* **51**(1-2), 319–324. (Cited on page 143).
- Foysi, H., Sarkar, S. & Friedrich, R. (2004), ‘Compressibility effects and turbulence scalings in supersonic channel flow’, *Journal of Fluid Mechanics* **509**, 207–216. (Cited on pages 60, 61, 64 & 201).
- Frey, M. & Hagemann, G. (1998), ‘Status of flow separation prediction in rocket nozzles’, *AIAA paper* **3619**, 1998. (Cited on pages 5, 6, 7 & 117).
- Frey, M. & Hagemann, G. (2000), ‘Restricted shock separation in rocket nozzles’, *Journal of Propulsion and Power* **16**(3), 478–484. (Cited on page 117).
- Fukagata, K. & Kasagi, N. (2002), ‘Highly energy-conservative finite difference method for the cylindrical coordinate system’, *Journal of Computational Physics* **181**(2), 478–498. (Cited on page 60).
- Ganapathisubramani, B., Clemens, N. & Dolling, D. (2007), ‘Effects of upstream boundary layer on the unsteadiness of shock-induced separation’, *Journal of Fluid Mechanics* **585**, 369–394. (Cited on page 15).
- Gatski, T. & Erlebacher, G. (2002), ‘Numerical simulation of a spatially evolving supersonic turbulent boundary layer’, *NASA Technical Reports* . (Cited on pages 74, 76 & 202).
- Ghosh, S., Foysi, H. & Friedrich, R. (2010), ‘Compressible turbulent channel and pipe flow: similarities and differences’, *Journal of Fluid Mechanics* **648**, 155–181. (Cited on pages 60, 67, 68, 69, 70, 145, 201 & 211).
- Ghosh, S., Sesterhenn, J. & Friedrich, R. (2008), ‘Large-eddy simulation of supersonic turbulent flow in axisymmetric nozzles and diffusers’, *International Journal of Heat and Fluid Flow* **29**(3), 579–590. (Cited on page 60).

- G.N. Coleman, J. K. & Moser, R. (1995), ‘A numerical study of turbulent supersonic isothermal-wall channel flow’, *Journal of Fluid Mechanics* **305**, 159–183. (Cited on page 56).
- Grötzbach, G. (1987), ‘Direct numerical and large eddy simulation of turbulent channel flows’, *Encyclopedia of Fluid Mechanics. West Orange NJ* **13**. (Cited on page 90).
- Guarini, S. E., Moser, R. D., Shariff, K. & Wray, A. (2000), ‘Direct numerical simulation of a supersonic turbulent boundary layer at Mach 2.5’, *Journal of Fluid Mechanics* **414**, 1–33. (Cited on page 74).
- Guo, Y. & Adams, N. (1994), ‘Numerical investigation of supersonic turbulent boundary layers with high wall temperature’. (Cited on page 72).
- H. Foysi, S. S. & Friedrich, R. (2004), ‘Compressibility effects and turbulence scalings in supersonic channel flow’, *Journal of Fluid Mechanics* **509**, 207–216. (Cited on pages 53, 54, 55, 58, 59, 200 & 201).
- Hadjadj, A. (2012), ‘Large-eddy simulation of shock/boundary-layer interaction’, *AIAA journal* **50**(12), 2919–2927. (Cited on page 8).
- Hagstrom, T. & Hariharan, S. (1988), ‘Accurate boundary conditions for exterior problems in gas dynamics’, *Mathematics of Computation* **51**(184), 581–597. (Cited on page 175).
- Handa, T., Masuda, M. & Matsuo, K. (2003), ‘Mechanism of shock wave oscillation in transonic diffusers’, *AIAA journal* **41**(1), 64–70. (Cited on page 15).
- Hickel, S. & Adams, N. (2008), ‘Implicit les applied to zero-pressure-gradient and adverse-pressure-gradient boundary-layer turbulence’, *International Journal of Heat and Fluid Flow* **29**(3), 626–639. (Cited on page 78).
- Hinze, J. (1959), ‘Turbulence, 1975’, *New York* . (Cited on page 61).
- Huang, P. & Bradshaw, P. (1995), ‘Law of the wall for turbulent flows in pressure gradients’, *AIAA journal* **33**(4), 624–632. (Cited on page 83).
- Hunter, C. A. (2004), ‘Experimental investigation of separated nozzle flows’, *Journal of Propulsion and Power* **20**(3), 527–532. (Cited on pages 115 & 116).
- Inoue, M., Pullin, D., Harun, Z. & Marusic, I. (2013), ‘LES of the adverse-pressure gradient turbulent boundary layer’, *International Journal of Heat and Fluid Flow* **44**, 293–300. (Cited on page 78).

- Ivanov, I., Kryukov, I. & Semenov, V. (2009), Numerical simulation of separated flow in nozzle with slots, *in* ‘Shock Waves’, Springer, pp. 973–978. (Cited on page 7).
- Jameson, A., Schmidt, W., Turkel, E. et al. (1981), ‘Numerical solutions of the Euler equations by finite volume methods using runge-kutta time-stepping schemes’, *AIAA paper* **1259**, 1981. (Cited on page 29).
- Johnson, A. D. & Papamoschou, D. (2010), ‘Instability of shock-induced nozzle flow separation’, *Physics of Fluids (1994-present)* **22**(1), 016102. (Cited on pages 101, 102, 103, 107, 110, 112, 116, 117, 123, 125, 129, 147, 203, 204, 205 & 207).
- Kawai, S. & Larsson, J. (2012), ‘Wall-modeling in large eddy simulation: Length scales, grid resolution, and accuracy’, *Physics of Fluids (1994-present)* **24**(1), 015105. (Cited on pages 91, 96 & 121).
- Kawai, S. & Larsson, J. (2013), ‘Dynamic non-equilibrium wall-modeling for large eddy simulation at high Reynolds numbers’, *Physics of Fluids (1994-present)* **25**(1), 015105. (Cited on pages i, ii, 91, 93, 96 & 99).
- Kawai, S. & Lele, S. K. (2008), ‘Localized artificial diffusivity scheme for discontinuity capturing on curvilinear meshes’, *Journal of Computational Physics* **227**(22), 9498–9526. (Cited on page 45).
- Keller, J. B. & Givoli, D. (1989), ‘Exact non-reflecting boundary conditions’, *Journal of Computational Physics* **82**(1), 172–192. (Cited on page 175).
- Kistler, A. (1964), ‘Fluctuating wall pressure under a separated supersonic flow’, *The Journal of the Acoustical Society of America* **36**(3), 543–550. (Cited on pages 7, 8 & 148).
- Kitsios, V., Atkinson, C., Sillero, J., Borrell, G., Gungor, A., Jiménez, J. & Soria, J. (2015), ‘Boundary condition development for an adverse pressure gradient turbulent boundary layer at the verge of separation’, *Advances in Computation, Modeling and Control of Transitional and Turbulent Flows* p. 269. (Cited on page 78).
- Kiya, M. & Sasaki, K. (1983), ‘Structure of a turbulent separation bubble’, *Journal of Fluid Mechanics* **137**, 83–113. (Cited on pages 12 & 13).
- Klein, M., Sadiki, A. & Janicka, J. (2003), ‘A digital filter based generation of inflow data for spatially developing direct numerical or large eddy simulations’, *Journal of Computational Physics* **186**(2), 652–665. (Cited on page 61).

- Knopp, T., Schanz, D., Schröder, A., Dumitra, M., Cierpka, C., Hain, R. & Kähler, C. (2014), ‘Experimental investigation of the log-law for an adverse pressure gradient turbulent boundary layer flow at $re_\theta = 10000$ ’, *Flow, Turbulence and Combustion* **92**(1-2), 451–471. (Cited on page 87).
- Kwan, W. & Stark, R. (2002), ‘Flow separation phenomena in subscale rocket nozzles’, *AIAA Paper* **4229**, 2002. (Cited on page 6).
- Landmann, B., Haselbacher, A., Chao, J. & Yu, C. (2010), Characteristic boundary conditions for compressible viscous flows on curvilinear grids, in ‘48th AIAA Aerospace Sciences Meeting Including the New Horizons Forum and Aerospace Exposition’, p. 1084. (Cited on page 175).
- Lasheras, J. & Choi, H. (1988), ‘Three-dimensional instability of a plane free shear layer: an experimental study of the formation and evolution of streamwise vortices’, *Journal of Fluid Mechanics* **189**, 53–86. (Cited on pages 10 & 11).
- Lee, J.-H. & Sung, H. J. (2009), ‘Structures in turbulent boundary layers subjected to adverse pressure gradients’, *Journal of Fluid Mechanics* **639**, 101–131. (Cited on pages 83 & 84).
- Lesieur, M. (2012), *Turbulence in Fluids*, Vol. 40, Springer Science & Business Media. (Cited on pages 10 & 11).
- Lodato, G., Domingo, P. & Vervisch, L. (2008), ‘Three-dimensional boundary conditions for direct and large-eddy simulation of compressible viscous flows’, *Journal of Computational Physics* **227**(10), 5105–5143. (Cited on page 175).
- Loulou P., Moser R. D., M. N. N. . C. B. J. (1997), ‘Direct numerical simulation of incompressible pipe flow using a b-spline spectral method’, *NASA Technical Memo* . (Cited on page 60).
- Lund, T. S., Wu, X. & Squires, K. D. (1998), ‘Generation of turbulent inflow data for spatially-developing boundary layer simulations’, *Journal of Computational Physics* **140**(2), 233–258. (Cited on pages 103 & 106).
- M. Klein, A. S. & Janicka, J. (2003), ‘A digital filter based generation of inflow data for spatially developing direct numerical or large eddy simulation’, *Journal of Computational Physics* **186**, 652–665. (Cited on pages 36 & 37).
- Maeder, T., Adams, N. A. & Kleiser, L. (2001), ‘Direct simulation of turbulent supersonic boundary layers by an extended temporal approach’, *Journal of Fluid Mechanics* **429**, 187–216. (Cited on pages 72 & 75).

- Manhart, M., Peller, N. & Brun, C. (2008), ‘Near-wall scaling for turbulent boundary layers with adverse pressure gradient’, *Theoretical and Computational Fluid Dynamics* **22**(3-4), 243–260. (Cited on pages 90, 91 & 92).
- Martelli, E., Ciottoli, P. P., Bernardini, M., Nasuti, F. & Valorani, M. (2016), ‘Detached eddy simulation of shock unsteadiness in an over-expanded planar nozzle’, *arXiv preprint arXiv:1606.05114*. (Cited on page 16).
- Martelli, E., Nasuti, F. & Onofri, M. (2010), ‘Numerical calculation of FSS/RSS transition in highly overexpanded rocket nozzle flows’, *Shock Waves* **20**(2), 139–146. (Cited on pages 6 & 117).
- Marusic, I., Monty, J. P., Hultmark, M. & Smits, A. J. (2013), ‘On the logarithmic region in wall turbulence’, *Journal of Fluid Mechanics* **716**, R3. (Cited on pages 82 & 143).
- Marušić, I. & Perry, A. (1995), ‘A wall-wake model for the turbulence structure of boundary layers. part 2. further experimental support’, *Journal of Fluid Mechanics* **298**, 389–407. (Cited on page 78).
- Matsumoto, M. & Nishimura, T. (1998), ‘Mersenne twister: a 623-dimensionally equidistributed uniform pseudo-random number generator’, *ACM Transactions on Modeling and Computer Simulation (TOMACS)* **8**(1), 3–30. (Cited on page 37).
- Matsuo, K., Miyazato, Y. & Kim, H.-D. (1999), ‘Shock train and pseudo-shock phenomena in internal gas flows’, *Progress in Aerospace Sciences* **35**(1), 33–100. (Cited on page 115).
- Mcdonald, H. (1969), ‘The effect of pressure gradient on the law of the wall in turbulent flow’, *Journal of Fluid Mechanics* **35**(02), 311–336. (Cited on pages 87, 89 & 203).
- McKeon, B., Li, J., Jiang, W., Morrison, J. & Smits, A. (2004), ‘Further observations on the mean velocity distribution in fully developed pipe flow’, *Journal of Fluid Mechanics* **501**, 135–147. (Cited on pages 62 & 143).
- Mellor, G. & Gibson, D. (1966), ‘Equilibrium turbulent boundary layers’, *Journal of Fluid Mechanics* **24**(02), 225–253. (Cited on page 78).
- Mohseni, K. & Colonius, T. (2000), ‘Numerical treatment of polar coordinate singularities’, *Journal of Computational Physics* **157**(2), 787–795. (Cited on page 39).
- Morgan, B., Duraisamy, K., Nguyen, N., Kawai, S. & Lele, S. (2013), ‘Flow physics and RANS modelling of oblique shock/turbulent boundary layer interaction’, *Journal of Fluid Mechanics* **729**, 231–284. (Cited on page 8).

- Morkovin, M. (1962), *Effects of compressibility on turbulent flows*, Ed. A. Favre. (Cited on page 56).
- Na, Y. & Moin, P. (1998), ‘The structure of wall-pressure fluctuations in turbulent boundary layers with adverse pressure gradient and separation’, *Journal of Fluid Mechanics* **377**, 347–373. (Cited on page 78).
- Nagano, Y., Tagawa, M. & Tsuji, T. (1993), Effects of adverse pressure gradients on mean flows and turbulence statistics in a boundary layer, in ‘Turbulent Shear Flows 8’, Springer, pp. 7–21. (Cited on pages 78, 83 & 84).
- Nagib, H. M. & Chauhan, K. A. (2008), ‘Variations of von kármán coefficient in canonical flows’, *Physics of Fluids* **20**(10), 1518. (Cited on pages 83, 84, 86 & 87).
- Nam, J. & Lien, F. (2014), ‘A ghost-cell immersed boundary method for large-eddy simulations of compressible turbulent flows’, *International Journal of Computational Fluid Dynamics* **28**(1-2). (Cited on pages 34 & 35).
- Nave, L. & Coffey, G. (1973), ‘Sea level side loads in high-area-ratio rocket engines’, *9th Propulsion Conference*. (Cited on pages 6, 14 & 117).
- Neves, J. C., Moin, P. & Moser, R. D. (1994), ‘Effects of convex transverse curvature on wall-bounded turbulence. part 1. the velocity and vorticity’, *Journal of Fluid Mechanics* **272**, 349–382. (Cited on page 122).
- Nguyen, A. T., Deniau, H., Girard, S. & de Roquefort, T. A. (2003), ‘Unsteadiness of flow separation and end-effects regime in a thrust-optimized contour rocket nozzle’, *Flow, Turbulence and Combustion* **71**(1-4), 161–181. (Cited on pages 6, 7 & 117).
- Nickels, T. (2004), ‘Inner scaling for wall-bounded flows subject to large pressure gradients’, *Journal of Fluid Mechanics* **521**, 217–239. (Cited on pages 85, 86 & 87).
- Nicoud, F. & Ducros, F. (1999), ‘Subgrid-scale stress modelling based on the square of the velocity gradient tensor’, *Flow, turbulence and Combustion* **62**(3), 183–200. (Cited on page 25).
- Nieuwstadt, F. & Bradshaw, P. (1997), ‘Similarities and differences of turbulent boundary-layer, pipe and channel flow’. (Cited on page 60).
- Nituch, M., Sjolander, S. & Head, M. (1978), ‘An improved version of the Cebeci-Smith eddy-viscosity model’, *Aeronautical Quarterly* **29**, 207–225. (Cited on pages 92 & 95).

- Nonomura, T. & Fujii, K. (2013), ‘Robust explicit formulation of weighted compact nonlinear scheme’, *Computers & Fluids* **85**, 8–18. (Cited on page 27).
- Nonomura, T., Iizuka, N. & Fujii, K. (2010), ‘Freestream and vortex preservation properties of high-order weno and wcns on curvilinear grids’, *Computers & Fluids* **39**(2), 197–214. (Cited on pages 27 & 28).
- Nonomura, T., Terakado, D., Abe, Y. & Fujii, K. (2015), ‘A new technique for freestream preservation of finite-difference weno on curvilinear grid’, *Computers & Fluids* **107**, 242–255. (Cited on page 27).
- Olson, B. J. (2012), Large-eddy simulation of multi-material mixing and over-expanded nozzle flow, Master’s thesis, Stanford university. (Cited on pages 13, 103 & 104).
- Olson, B. J. & Lele, S. K. (2011), ‘Large-eddy simulation of an over-expanded planar nozzle’, *AIAA Paper* **3908**, 2011. (Cited on pages iv, 101, 102, 103, 104, 106, 107, 110, 111, 112, 113, 114, 123, 125, 138, 147, 154, 203, 204, 205 & 207).
- Olson, B. J. & Lele, S. K. (2013), ‘A mechanism for unsteady separation in over-expanded nozzle flow’, *Physics of Fluids (1994-present)* **25**(11), 110809. (Cited on pages 7, 13, 16, 129, 133, 134, 163, 164 & 199).
- Orlandi, P. & Fatica, M. (1997), ‘Direct simulations of turbulent flow in a pipe rotating about its axis’, *Journal of Fluid Mechanics* **343**, 43–72. (Cited on page 60).
- Örlü, R., Fransson, J. H. & Alfredsson, P. H. (2010), ‘On near wall measurements of wall bounded flows - the necessity of an accurate determination of the wall position’, *Progress in Aerospace Sciences* **46**(8), 353–387. (Cited on pages 82, 84 & 85).
- Östlund, J. (2002), ‘Flow processes in rocket engine nozzles with focus on flow separation and side-loads’. (Cited on pages 6, 7, 14 & 115).
- P. Huang, G. C. & Bradshaw, P. (1995), ‘Turbulence statistics in fully developed channel flow at low Reynolds number’, *Journal of Fluid Mechanics* **177**, 133–166. (Cited on page 56).
- Papamoschou, D. & Johnson, A. (2006), ‘Unsteady phenomena in supersonic nozzle flow separation’, *AIAA Paper* **3360**, 2006. (Cited on pages 15, 16, 101, 102, 133, 163 & 203).
- Papamoschou, D., Zill, A. & Johnson, A. (2009), ‘Supersonic flow separation in planar nozzles’, *Shock Waves* **19**(3), 171–183. (Cited on page 101).

- Peskin, C. S. (1972), ‘Flow patterns around heart valves: a numerical method’, *Journal of Computational Physics* **10**(2), 252–271. (Cited on page 33).
- Pilinski, C. (2002), Etude numérique du décollement en tuyères supersoniques, PhD thesis, INSA de Rouen. (Cited on page 13).
- Piomelli, U. & Balaras, E. (2002), ‘Wall-layer models for large-eddy simulations’, *Annual Review of Fluid Mechanics* **34**(1), 349–374. (Cited on pages 90 & 91).
- Piponniau, S., Dussauge, J., Debieve, J. & Dupont, P. (2009), ‘A simple model for low-frequency unsteadiness in shock-induced separation’, *Journal of Fluid Mechanics* **629**, 87–108. (Cited on pages 8, 9, 12 & 153).
- Piquet, A., Roussel, O. & Hadjadj, A. (2016), ‘A comparative study of brinkman penalization and direct-forcing immersed boundary methods for compressible viscous flows’, *Computers & Fluids* **136**, 272 – 284. (Cited on page 34).
- Pirozzoli, S. (2010), ‘Generalized conservative approximations of split convective derivative operators’, *Journal of Computational Physics* **229**(19), 7180–7190. (Cited on page 27).
- Pirozzoli, S. (2011a), ‘Numerical methods for high-speed flows’, *Annual Review of Fluid Mechanics* **43**, 163–194. (Cited on page 29).
- Pirozzoli, S. (2011b), ‘Stabilized non-dissipative approximations of Euler equations in generalized curvilinear coordinates’, *Journal of Computational Physics* **230**(8), 2997–3014. (Cited on page 46).
- Pirozzoli, S., Bernardini, M. & Grasso, F. (2010), ‘Direct numerical simulation of transonic shock/boundary layer interaction under conditions of incipient separation’, *Journal of Fluid Mechanics* **657**, 361–393. (Cited on page 9).
- Pirozzoli, S., Grasso, F. & Gatski, T. (2004), ‘Direct numerical simulation and analysis of a spatially evolving supersonic turbulent boundary layer at $M=2.25$ ’, *Physics of Fluids (1994-present)* **16**(3), 530–545. (Cited on pages 38, 71, 72, 74, 75, 76, 77 & 202).
- Poinsot, T. J. & Lele, S. (1992), ‘Boundary conditions for direct simulations of compressible viscous flows’, *Journal of Computational Physics* **101**(1), 104–129. (Cited on page 175).
- Ponton, M. & Seiner, J. (1992), ‘The effects of nozzle exit lip thickness on plume resonance’, *Journal of Sound and Vibration* **154**(3), 531–549. (Cited on pages 13 & 152).

- Pope, S. B. (2000), *Turbulent Flows*, Cambridge University Press. (Cited on page 9).
- Rai, M., Gatski, T. & Erlebacher, G. (1995), Direct simulation of spatially evolving compressible turbulent boundary layers, in ‘33rd Aerospace Sciences Meeting and Exhibit’, p. 583. (Cited on page 38).
- Rai, M. M. & Moin, P. (1993), ‘Direct numerical simulation of transition and turbulence in a spatially evolving boundary layer’, *Journal of Computational Physics* **109**(2), 169–192. (Cited on page 71).
- Rajasekaran, J. (2011), On the flow characteristics behind a backward-facing step and the design of a new axisymmetric model for their study, PhD thesis, University of Toronto. (Cited on pages 12 & 199).
- Reijasse, P. (2005), *Aérodynamique des tuyères propulsives en sur-détente: décollement libre et charges latérales en régime stabilisé*, PhD thesis, Paris 6. (Cited on page 7).
- Roe, P. L. (1981), ‘Approximate Riemann solvers, parameter vectors, and difference schemes’, *Journal of Computational Physics* **43**(2), 357–372. (Cited on pages 28 & 29).
- Rudman, M. & Blackburn, H. M. (1999), Large eddy simulation of turbulent pipe flow, in ‘Second International Conference on CFD in the Minerals and Process Industries, Melbourne, Australia, Dec’, pp. 6–8. (Cited on page 143).
- Rudy, D. H. & Strikwerda, J. C. (1980), ‘A nonreflecting outflow boundary condition for subsonic navier-stokes calculations’, *Journal of Computational Physics* **36**(1), 55–70. (Cited on page 175).
- Sajben, M., Bogar, T. & Kroutil, J. (1984), ‘Forced oscillation experiments in supercritical diffuser flows’, *AIAA journal* **22**(4), 465–474. (Cited on page 15).
- Sajben, M. & Kroutil, J. (1980), Effects of approach boundary-layer thickness on oscillating, transonic diffuser flows including a shock, in ‘AIAA, 18th, Aerospace Sciences Meeting, Pasadena, CA’, p. 1980. (Cited on pages 6, 131 & 163).
- Salmon, J., Bogar, T. & Sajben, M. (1983), ‘Laser doppler velocimeter measurements in unsteady, separated, transonic diffuser flows’, *AIAA journal* **21**(12), 1690–1697. (Cited on page 15).
- Satake, S.-i., Kunugi, T. & Himeno, R. (2000), High Reynolds number computation for turbulent heat transfer in a pipe flow, in ‘High Performance Computing’, Springer, pp. 514–523. (Cited on page 60).

- Schlichting, H. & Gersten, K. (2003), *Boundary-layer theory*, Springer Science and Business Media. (Cited on page 50).
- Schmucker, R. (1974), ‘Status of flow separation prediction in liquid propellant rocket nozzles’, *NASA Technical Reports* . (Cited on page 7).
- Schumann, U. (1975), ‘Subgrid scale model for finite difference simulations of turbulent flows in plane channels and annuli’, *Journal of Computational Physics* **18**(4), 376–404. (Cited on page 90).
- Sé, Deck, b. & Guillen, P. (2002), ‘Numerical simulation of side loads in an ideal truncated nozzle’, *Journal of Propulsion and Power* **18**(2), 261–269. (Cited on page 150).
- Shimizu, T., Miyajima, H. & Kodera, M. (2006), ‘Numerical study of restricted shock separation in a compressed truncated perfect nozzle’, *AIAA journal* **44**(3), 576–584. (Cited on page 117).
- Shmyglevsky, Y. D. (1957), ‘A variation problem in the gas dynamics of axially symmetrical supersonic flows’, *DOKLADY AKADEMII NAUK SSSR* **113**(3), 520–522. (Cited on page 7).
- Simon, F., Deck, S., Guillen, P., Sagaut, P. & Merlen, A. (2007), ‘Numerical simulation of the compressible mixing layer past an axisymmetric trailing edge’, *Journal of Fluid Mechanics* **591**, 215–253. (Cited on page 12).
- Simpson, R. L. (1983), ‘A model for the backflow mean velocity profile’, *AIAA journal* **21**(1), 142–143. (Cited on page 92).
- Simpson, R. L. (1989), ‘Turbulent boundary-layer separation’, *Annual Review of Fluid Mechanics* **21**(1), 205–232. (Cited on page 10).
- Skote, M. & Henningson, D. S. (2002), ‘Direct numerical simulation of a separated turbulent boundary layer’, *Journal of Fluid Mechanics* **471**, 107–136. (Cited on page 83).
- Smalley, K. B., Brown, A. M., Ruf, J. & Gilbert, J. (2007), ‘Flow separation side loads excitation of rocket nozzle fem’, *48th AIAA/ASME/ASCE/AHS/ASC Structures, Structural Dynamics, and Materials Con., Honolulu, Hawaii, USA* . (Cited on page 7).
- So, R., Zhang, H., Gatski, T. & Speziale, C. (1994), ‘Logarithmic laws from compressible turbulent boundary layers’, *AIAA journal* **32**(11), 2162–2168. (Cited on page 85).

- Souverein, L. J. (2010), *On the scaling and unsteadiness of shock induced separation*, TU Delft, Delft University of Technology. (Cited on page 96).
- Spalart, P. R. & Watmuff, J. H. (1993), ‘Experimental and numerical study of a turbulent boundary layer with pressure gradients’, *Journal of Fluid Mechanics* **249**, 337–371. (Cited on pages 111, 113 & 204).
- Spalding, D. (1961), ‘A single formula for the law of the wall’, *Journal of Applied Mechanics* **28**(3), 455–458. (Cited on page 90).
- Stratford, B. (1959), ‘The prediction of separation of the turbulent boundary layer’, *Journal of Fluid Mechanics* **5**(01), 1–16. (Cited on pages 83 & 87).
- Summerfield, M., Foster, C. R. & Swan, W. C. (1954), ‘Flow separation in overexpanded supersonic exhaust nozzles’. (Cited on page 6).
- Taieb, D. (2010), Simulation numérique des écoulements turbulents dans les canaux de refroidissement, Master’s thesis, INSA de Rouen. (Cited on page 54).
- Tanna, H. (1977), ‘An experimental study of jet noise part ii: shock associated noise’, *Journal of Sound and Vibration* **50**(3), 429–444. (Cited on page 152).
- Terhardt, M., Hagemann, G. & Frey, M. (2001), ‘Flow separation and side-load behavior of truncated ideal rocket nozzles’, *AIAA paper* **3686**, 2001. (Cited on page 150).
- Tomita, T., Takahashi, M., Sasaki, M., Sakamoto, H., Takahashi, M. & Tamura, H. (2009), ‘Experimental evaluation of side-loads in LE-7A prototype engine nozzle’, *Shock Waves* **19**(3), 213–228. (Cited on page 7).
- Touber, E. & Sandham, N. D. (2009), ‘Large-eddy simulation of low-frequency unsteadiness in a turbulent shock-induced separation bubble’, *Theoretical and Computational Fluid Dynamics* **23**, 79–107. (Cited on pages 36, 37, 128, 151 & 153).
- Touber, E. & Sandham, N. D. (2011), ‘Low-order stochastic modelling of low-frequency motions in reflected shock-wave/boundary-layer interactions’, *Journal of Fluid Mechanics* **671**, 417–465. (Cited on pages 8, 9 & 12).
- Unger, F. & Friedrich, R. (1993), ‘Numerical simulation of fully developed turbulent pipe flow’, *Notes on Numerical Fluid Mechanics* **38**, 201–201. (Cited on pages 142 & 143).
- Veenman, M. P. B. (2004), *Statistical analysis of turbulent pipe flow: A numerical approach*, Tue Universiteitsbibliotheek. (Cited on page 60).

- Verma, S. & Manisankar, C. (2014), ‘Origin of flow asymmetry in planar nozzles with separation’, *Shock Waves* **24**(2), 191–209. (Cited on pages [10](#), [116](#) & [117](#)).
- Verzicco, R. & Orlandi, P. (1996), ‘A finite-difference scheme for three-dimensional incompressible flows in cylindrical coordinates’, *Journal of Computational Physics* **123**(2), 402–414. (Cited on page [39](#)).
- Viets, H. (1975), ‘Flip-flop jet nozzle’, *AIAA journal* **13**(10), 1375–1379. (Cited on page [12](#)).
- Visbal, M. R. & Gaitonde, D. V. (1999), ‘High-order-accurate methods for complex unsteady subsonic flows’, *AIAA journal* **37**(10), 1231–1239. (Cited on page [26](#)).
- Visbal, M. R. & Gaitonde, D. V. (2002), ‘On the use of higher-order finite-difference schemes on curvilinear and deforming meshes’, *Journal of Computational Physics* **181**(1), 155–185. (Cited on pages [26](#) & [45](#)).
- Wagner, C., Huttl, T. & Friedrich, R. (2001), ‘Low-Reynolds-number effects derived from direct numerical simulations of turbulent pipe flow’, *Computers & Fluids* **30**(5), 581–590. (Cited on page [60](#)).
- Waltrup, P. & Billig, F. (1973), ‘Structure of shock waves in cylindrical ducts’, *AIAA journal* **11**(10), 1404–1408. (Cited on page [115](#)).
- Wang, M. & Moin, P. (2002), ‘Dynamic wall modeling for large-eddy simulation of complex turbulent flows’, *Physics of Fluids (1994-present)* **14**(7), 2043–2051. (Cited on pages [91](#) & [95](#)).
- Wang, T.-S. (2009), ‘Transient three-dimensional startup side load analysis of a regeneratively cooled nozzle’, *Shock Waves* **19**(3), 251–264. (Cited on page [7](#)).
- Watanabe, Y., Sakazume, N. & Tsuboi, M. (2002), ‘LE-7A engine nozzle problems during the transient operations’, *AIAA paper* **3841**, 2002. (Cited on page [7](#)).
- Weiss, A., Grzona, A. & Olivier, H. (2010), ‘Behavior of shock trains in a diverging duct’, *Experiments in fluids* **49**(2), 355–365. (Cited on pages [15](#) & [115](#)).
- White, F. M. & Corfield, I. (2006), *Viscous fluid flow*, Vol. 3, McGraw-Hill New York. (Cited on page [72](#)).
- Wille, R. & Fernholz, H. (1965), ‘Report on the first european mechanics colloquium, on the coanda effect’, *Journal of Fluid Mechanics* **23**(04), 801–819. (Cited on page [116](#)).

- Williamson, J. (1980), ‘Low-storage Runge-Kutta schemes’, *Journal of Computational Physics* **35**(1), 48–56. (Cited on page 30).
- Wong, H. Y. (2006), ‘Overview of flow oscillations in transonic and supersonic nozzles’, *Journal of Propulsion and Power* **22**(4), 705–720. (Cited on page 131).
- Wosnik, M., Castillo, L. & George, W. K. (2000), ‘A theory for turbulent pipe and channel flows’, *Journal of Fluid Mechanics* **421**, 115–145. (Cited on page 60).
- Wu, X. & Moin, P. (2008), ‘A direct numerical simulation study on the mean velocity characteristics in turbulent pipe flow’, *Journal of Fluid Mechanics* **608**, 81–112. (Cited on pages 60, 142 & 143).
- Xiao, Q., Tsai, H.-M. & Papamoschou, D. (2007), ‘Numerical investigation of supersonic nozzle flow separation’, *AIAA journal* **45**(3), 532–541. (Cited on page 7).
- Xie, Z.-T. & Castro, I. P. (2008), ‘Efficient generation of inflow conditions for large eddy simulation of street-scale flows’, *Flow, Turbulence and Combustion* **81**(3), 449–470. (Cited on pages 37, 106, 110 & 145).
- Xu, X. (2003), Large eddy simulation of compressible turbulent pipe flow with heat transfer, Master’s thesis, Iowa State University. (Cited on pages 142 & 143).
- Yarusevych, S., Sullivan, P. E. & Kawall, J. G. (2006), ‘Coherent structures in an airfoil boundary layer and wake at low Reynolds numbers’, *Physics of Fluids (1994-present)* **18**(4), 044101. (Cited on pages 11 & 199).
- Zagarola, M. V. & Smits, A. J. (1998), ‘Mean-flow scaling of turbulent pipe flow’, *Journal of Fluid Mechanics* **373**, 33–79. (Cited on pages 62 & 143).
- Zaman, K., Dahl, M., Bencic, T. & Loh, C. (2002), ‘Investigation of a transonic resonance with convergent–divergent nozzles’, *Journal of Fluid Mechanics* **463**, 313–343. (Cited on pages 6, 15, 16, 131, 133, 134, 149, 153 & 163).